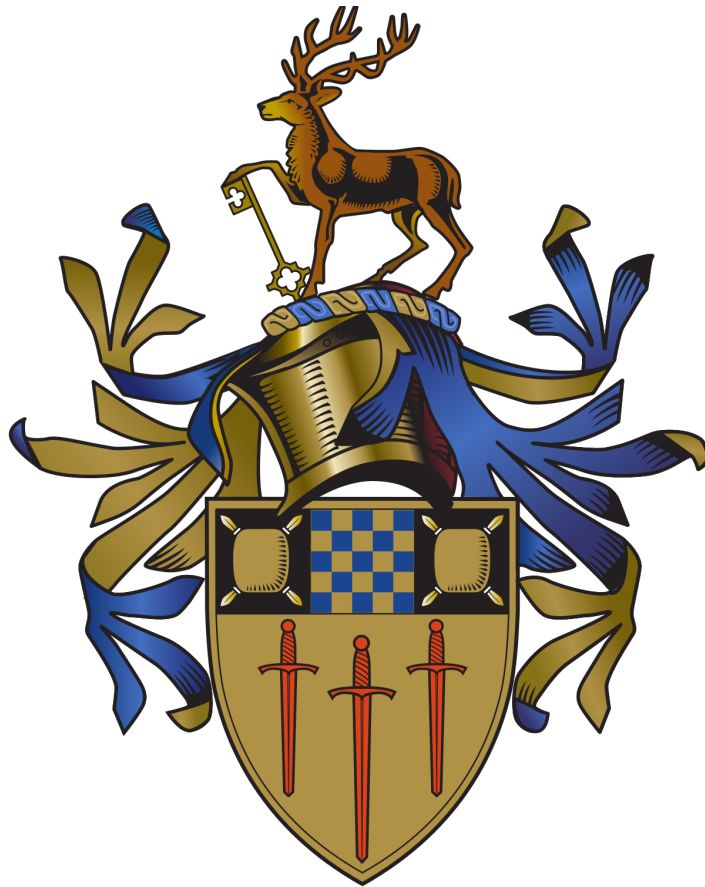


UNIVERSITY OF SURREY

PHD THESIS

Investigations into Nuclear Astrophysical Reactions using Single Nucleon Transfer Reactions



Author:

Sam HALLAM

Supervisors:

Prof. Wilton CATFORD

Dr. Gavin LOTAY

Department of Physics,
Faculty of Engineering and Physical Sciences,
University of Surrey, Guildford, Surrey, GU2 7XH

July 2020

Declaration

“This thesis and the work to which it refers are the results of my own efforts. Any ideas, data, images or text resulting from the work of others (whether published or unpublished) are fully identified as such within the work and attributed to their originator in the text, bibliography or in footnotes. This thesis has not been submitted in whole or in part for any other academic degree or professional qualification. I agree that the University has the right to submit my work to the plagiarism detection service TurnitinUK for originality checks. Whether or not drafts have been so-assessed, the University reserves the right to require an electronic version of the final document (as submitted) for assessment as above ”

Signature: _____ Date: _____

S. J. Hallam

Abstract

The $^{26m}\text{Al}(p,\gamma)^{27}\text{Si}$ reaction is thought to have a significant impact on the nucleosynthesis of both ^{26}Mg and ^{27}Al in explosive stellar environments, where $T > 0.3$ GK. The isomeric component of ^{26}Al forms part of the $T = 1$, isospin triplet ^{26}Si - ^{26m}Al - ^{26}Mg . As such, the $^{26}\text{Si}(d,p)^{27}\text{Si}$ transfer acts as a novel surrogate reaction that populates the final states within ^{27}Si . No γ -ray transitions were observed for proton-unbound states, suggesting the absence of strong single-particle states within the energy range $E_r = 100 - 500$ keV. Stellar reaction rate upper limits were placed on known resonances at 146, 218, 378, 448 and 492 keV, based on excess counts observed within respective γ -ray transition energy regions. These indicate that a single resonance dominates the reaction rate at a given temperature, the 218 keV resonance at $T < 0.3$ GK and the 448 keV resonance at $T > 0.3$ GK. Most importantly these reaction rates are much smaller than previously estimated.

The $^{22}\text{Ne}(\alpha,\gamma)^{26}\text{Mg}$ reaction is a n -poison reaction within the weak s -process of massive stars. It is thought that the reaction rate will be dominated by resonant capture to natural-parity excited states between the α -emission and n -emission thresholds within ^{26}Mg , at energies of 10614.75 keV and 11093.09 keV respectively. The indirect reaction $^{25}\text{Mg}(d,p)^{26}\text{Mg}$ was performed to investigate possible γ -ray decaying states above these thresholds. No states above the n -emission threshold were observed, suggesting that there are no strong γ -ray decaying single particle states in this system. Mirror analogue states for the astrophysical $^{25}\text{Al}(p,\gamma)^{26}\text{Mg}$ resonant-capture reaction were analysed, extracted spectroscopic factors were compared to shell-model calculations and literature values. Of note was the re-assertion of a possible low-lying negative parity state, with energy of 5.710 MeV, within the ^{26}Mg system as noted by previous (d,p) transfer reaction studies. Whilst no measurements of this state could be made within this study the need for further study was re-affirmed.

Acknowledgements

The first people I would like to thank for their contributions to this research, are my supervisors, Professor Wilton Catford and Dr. Gavin Lotay. Without them this thesis simply would not have become a reality. Their expertise, knowledge and most importantly patience have helped me to become the researcher that I am today. From endless Starbucks trips, 3 AM visits to Denny's, possible ducks in motel rooms, Coronaritas and various social gatherings in Guildford and across North America, they have made me feel welcome as part of their team and made the entire experience as enjoyable as it was. A no lesser thanks is extended to Dr. Daniel Doherty who whilst not an official supervisor was an integral part of this team and commonly provided a much needed perspective.

I would also like to extend my thanks to Professor Gregory Christian, Professor Alex Gade, Dr. Dirk Weishar and Dr. Antti Saastamoinen and for all of their assistance in making the experiments within this thesis happen. For all of the physics insight they have provided into this work and for their efforts at their respective institutions as local spokespeople.

My gratitude also goes to all of the post-doctoral researchers I had the pleasure of working with during this research, Dr. Adrien Matta, Dr. Mohamad Moukaddam, Dr. Peter Bender and Dr. Shuya Ota, there was most certainly good reason for all of you to earned permanent positions. Their experience and knowledge with detection systems and analysis software have been invaluable.

A large thanks to Professor Alex Brown and Dr. Natasha Timofeyuk for their theoretical contributions to the analysis within this work. Special thanks to Natasha for her patience in explaining key parts of nuclear reaction theory to me in a way a young experimentalist can understand.

To all of my fellow PhD students I had the pleasure of working or socialising with during this time, a massive thank you. From the working side a special thank you to the PhD students in both College Station and East Lansing for their help with the experiments within this work, from sitting shifts to providing analysis code help. To all of the Surrey PhD students, I have always felt welcome because of your friendship. Special thanks to Ryan (the good Ag!), Lisa (my office sister) Andy, Callum, Laila, Dan, Chantal, Tom, Rob, Rhiann, Matt, Adam, Shaheen, Tom and Ben for your office

shenanigans and chat. A special mention to the Radiation, Soft Matter and Astro groups who collectively have provided many lunchtime and after work conversations and fun.

A collective thanks to all of my friends who have kept me sane through the last few years. For the weekends of fun with the Soccer Saturday boys who provided much needed stress relief through our collective antics. For the collection of people I met through the Student's Union who sat and drank with me on many an evening. A special thank you to Ferdia who's friendship was invaluable within our Percy Road house.

A massive thank you to Mum and Dad for all their support and work to get me where I am today. You have helped me through the worst of these periods both emotionally and financially and for that I am ever grateful. I would like to extend this thank you to my brothers and extended family for their part in this journey, with their tough science and life questions that kept pushing me to the end. A huge thank you to my adopted Doughty clan, who for the last four years have treated me as one of their own and provided many a roast dinner and pub dinner throughout this work. A "small" thank you to Hamlet, who was a brilliant writing companion for those late nights on the sofa as this thesis finally came together.

Finally, Danielle, it is hard to encompass the amount of support you have provided through this work. You have dealt with me disappearing for weeks or months at a time with relatively short notice on top of dealing with all of my moans and groans as I struggled to get code and analysis to work. I only hope I can repay you for all of your support, time and patience whilst I went through this journey.

Contents

Declaration	i
Abstract	ii
Acknowledgements	iii
List of Figures	xii
List of Tables	xiv
1 Introduction & Astrophysical Background	1
1.1 Evidence for Nucleosynthesis	2
1.1.1 Solar System Abundances	3
1.1.2 Stellar Populations & Hertzsprung-Russell Diagram	4
1.2 The Evolution of Single Stars	6
1.2.1 The Birth of Stars	6
1.2.2 The Main Sequence	6
1.2.3 The Fate of Stars	11
1.3 <i>s</i> -process	16
1.3.1 Main <i>s</i> -process	17
1.3.2 Weak <i>s</i> -process	19
1.4 Nuclear Reactions of Interest	20
1.4.1 $^{22}\text{Ne}(\alpha,\gamma)^{26}\text{Mg}$ within the <i>s</i> -process	20
1.4.2 $^{26m}\text{Al}(p,\gamma)^{27}\text{Si}$ within Core-Collapse Supernovae	21
2 Thermonuclear Reaction Rates and Transfer Reactions	25
2.1 Kinematics and Energetics	25
2.2 Cross Sections and Stellar Reaction Rates	27

2.3	Non-resonant and Resonant Reactions	29
2.3.1	Charged Particle-Induced Non-resonant Reactions	29
2.3.2	Narrow-Resonance Reaction Rates	34
2.4	Direct Measurements of Resonances	37
2.5	Indirect Determination of Resonance Strengths	38
2.5.1	Mirror Nuclei	40
2.6	Nuclear Shell Model	41
2.7	Nucleon Transfer Reactions	44
2.8	Theoretical Analysis of Transfer Reactions	45
2.8.1	Plane Wave Born Approximation (PWBA)	45
2.8.2	Distorted Wave Born Approximation (DWBA)	46
2.8.3	Adiabatic Distorted Wave Approximation (ADWA)	48
3	Investigation of the $^{25}\text{Mg}(d,p)^{26}\text{Mg}$ Reaction	49
3.1	Previous Research	51
3.2	Beam Production & Acceleration	53
3.3	Detection Systems	53
3.3.1	The TIARA Array	53
3.3.2	The Oxford MDM-2 Magnetic Spectrometer	57
3.3.3	Germanium Array	59
3.3.4	Signal Processing & Data Acquisition System	61
3.4	Detector Calibrations	62
3.4.1	Pulsar Calibrations	62
3.4.2	Charged Particle Energy Loss Corrections	64
3.4.3	Hyball Calibration	64
3.4.4	Barrel Calibration	66
3.4.5	Germanium Calibrations	73
3.4.6	Focal Plane Calibrations	74
3.5	Particle Identification	76
3.5.1	Si-FPD TAC Data	77
3.5.2	Oxford-2 Data	78
3.6	Beam Spot Corrections	80
3.7	Constructing Particle Excitation Spectra	81

3.8	Determining State Population and Decay	83
3.8.1	$1.6 < E_x < 2.1$	85
3.8.2	$2.6 < E_x < 3.2$	87
3.8.3	$3.3 < E_x < 4.15$	89
3.8.4	$4.15 < E_x < 4.55$	90
3.8.5	$4.6 < E_x < 5.1$	91
3.8.6	$5.1 < E_x < 5.85$	93
3.8.7	$5.9 < E_x < 6.3$	94
3.8.8	$6.4 < E_x < 7.0$	95
3.8.9	$7.0 < E_x < 7.45$	97
3.8.10	$7.45 < E_x < 8.0$	98
3.8.11	$8.0 < E_x < 8.4$	100
3.8.12	$8.5 < E_x < 9.7$	101
3.8.13	$9.9 < E_x < 11.5$	102
3.8.14	State Population Summary	103
3.9	Constructing Proton Angular Distributions	104
3.9.1	Beam Normalisation	105
3.9.2	Calculating $d\Omega'$	109
3.9.3	Calculating N_{det}	110
3.9.4	Angular Distributions	111
3.10	Spectroscopic Factors	124
3.10.1	d -wave Sensitivity	128
3.10.2	Relation to $^{25}\text{Al}(p,\gamma)^{26}\text{Si}$ proton spectroscopic factors	129
4	Investigation of the $^{26m}\text{Al}(p,\gamma)^{27}\text{Si}$ Reaction through a Novel Isospin Analogue Reaction	133
4.1	Previous Research	133
4.2	^{26}Si Beam Production & Acceleration	137
4.2.1	Primary Beam Production	137
4.2.2	A1900 & Secondary Beam Production	138
4.3	Detection Systems	140
4.3.1	The S800 Spectrograph	140
4.3.2	S800 Focal Plane Particle Detectors	141

4.3.3	Gamma-Ray Detection - GRETINA	146
4.3.4	Electronics	148
4.4	Detector Calibrations	149
4.4.1	CRDC Calibrations	149
4.4.2	Ion Chamber Calibrations	151
4.4.3	GRETINA Calibrations	152
4.4.4	Time of Flight Corrections	153
4.4.5	Doppler Correction	155
4.4.6	Target Placement Correction	156
4.5	^{27}Si Particle and State Identification	157
4.5.1	^{27}Si Particle Identification	157
4.5.2	^{27}Si State Identification	159
4.5.3	Reaction Mechanism Determination	162
4.6	Determining Cross Section	163
4.6.1	Determining N_R	164
4.6.2	Determining N_B	168
4.6.3	Determining N_T/A	170
4.6.4	Summary of measured cross sections	171
4.7	Determining Spectroscopic Factors	172
4.7.1	Comparison of non-resonant state spectroscopic factors	172
4.7.2	Relating resonant spectroscopic factors to the $^{26}\text{Al}(p,\gamma)^{27}\text{Si}$	175
4.8	Determining Resonance Reaction Rate	177
5	Conclusion	180
A	Semiconductor Detectors	184
A.1	Charged Particles Detectors	184
A.1.1	Energy Loss of Charged Particles in Matter	184
A.1.2	Semiconductor Diode Detectors	185
A.2	Gamma-ray Detectors	189
A.2.1	Interactions of Gamma Rays with Matter	189
A.2.2	Germanium Detectors	191
A.2.3	Add-back	193
A.2.4	Doppler Effects	193

List of Figures

1.1	Present Day Solar System Abundances	3
1.2	Hertzsprung-Russell diagram	5
1.3	<i>pp</i> -chain reaction pathways	8
1.4	CNO cycle pathways.	9
1.5	NeNa cycle pathways.	10
1.6	Cross section of a super giant phase star.	15
1.7	Example of <i>s</i> -process	16
1.8	Examples of SiC type presolar grains	21
1.9	Schematic of ^{26}Al decay	22
1.10	COMPTEL sky-map	23
2.1	Combined nuclear, centriufugal and coulombic potential	30
2.2	Cross section and $S(E)$ -factor as functions of beam energies.	32
2.3	Diagram of Gamow window.	33
2.4	Cross section of resonannt and non-resonant reactions.	36
2.5	Schematic illustration of a Woods-Saxon potential.	42
2.6	Energy Levels from Shell Model.	43
2.7	Three-body model of a $d + X$ reaction.	47
3.1	Angular Coverage of TIARA	50
3.2	Schematic diagram of the detector set up.	51
3.3	3D layout of Cyclotron Institute.	54
3.4	TIARA Array surrounded by HPGe detectors.	55
3.5	TIARA Silicon Detectors.	55
3.6	Oxford Detector.	58
3.7	Clover Segmentation Schematic	60
3.8	“Matchstick” spectrum.	63

3.9	Matchstick Residual Voltages	63
3.10	Hyball triple-alpha energy spectrum.	65
3.11	Barrel Upstream vs Downstream	66
3.12	Raw Barrel E vs P	67
3.13	Barrel strip end projections.	68
3.14	Barrel Charge without Energy Calibrations	69
3.15	Barrel Energy without Ballistic Deficit	71
3.16	Barrel Energy with Ballistic Deficit	72
3.17	Triple-alpha spectrum within the Barrel.	73
3.18	HPGe Calibration	74
3.19	Functional forms and residuals of the Avalance Wires.	75
3.20	Si-FPD TAC signal.	77
3.21	Focal plane data ^{27}Si software gates.	79
3.22	TIARA Target Position Optimization	81
3.23	Application of software gates upon the kinematic plots.	82
3.24	Observed ^{26}Mg excitation spectrum from TIARA.	82
3.25	Energy calibrated γ -ray spectrum for $^{25}\text{Mg}(d,p)^{26}\text{Mg}$	83
3.26	Excitation energy of ^{26}Mg as a function of coincident γ -ray events.	84
3.27	γ -ray energy spectrum for $1.6 < E_x < 2.1$ MeV.	85
3.28	Determination of γ -ray efficiency of $E_\gamma = 1.808$ MeV.	87
3.29	γ -ray energy spectrum for $2.6 < E_x < 3.2$ MeV.	88
3.30	γ -ray energy spectrum for $3.3 < E_x < 4.15$ MeV.	89
3.31	γ -ray energy spectrum for $4.15 < E_x < 4.55$ MeV.	91
3.32	γ -ray energy spectrum for $4.6 < E_x < 5.1$ MeV.	92
3.33	γ -ray energy spectrum for $5.1 < E_x < 5.85$ MeV.	94
3.34	γ -ray energy spectrum for $5.9 < E_x < 6.3$ MeV.	95
3.35	γ -ray energy spectrum for $6.4 < E_x < 7.0$ MeV.	96
3.36	γ -ray energy spectrum for $7.0 < E_x < 7.45$ MeV.	98
3.37	γ -ray energy spectrum for $7.5 < E_x < 8.0$ MeV.	99
3.38	γ -ray energy spectrum for $8.0 < E_x < 8.4$ MeV.	101
3.39	γ -ray energy spectrum for $8.5 < E_x < 9.7$ MeV.	102
3.40	γ -ray energy spectrum for $9.9 < E_x < 11.3$ MeV.	103
3.41	E_{LAB} vs θ_{LAB} of $^{25}\text{Mg}(d,d)^{25}\text{Mg}$ scattering reaction.	106

3.42	Differential cross sections of $^{25}\text{Mg}(d,d)^{25}\text{Mg}$ reaction.	108
3.43	Geometric efficiency as a function of laboratory angle for the Hyball.	110
3.44	Excitation spectrum for differing angular ranges.	111
3.45	Angular distribution for the ground state.	112
3.46	Angular distribution for the state at $E_x = 1.808$ MeV.	113
3.47	Angular distribution for the state at $E_x = 2.928$ MeV.	115
3.48	Angular distribution for the state at $E_x = 3.588$ MeV.	116
3.49	Angular distribution for the state at $E_x = 3.941$ MeV.	117
3.50	Angular distribution for the state at $E_x = 4.350$ MeV.	118
3.51	Angular distribution for the state at $E_x = 5.291$ MeV.	119
3.52	Angular distribution for the state at $E_x = 5.476$ MeV.	120
3.53	Angular distribution for the state at $E_x = 5.715$ MeV.	121
3.54	Angular distribution for the state at $E_x = 6.125$ MeV.	122
3.55	Angular distribution for the state at $E_x = 10.949$ MeV.	123
3.56	Effects of d -wave on the angular distribution of the 3.941, 3^+ state.	128
4.1	The coupled-cyclotron fragmentation facility at NSCL.	138
4.2	Schematic of the A1900 Fragment Separator	139
4.3	The S800 Spectrograph.	140
4.4	S800 Modes.	141
4.5	S800 Focal Plane Detectors.	142
4.6	CRDC Detector Layout.	143
4.7	GRETINA Modules.	147
4.8	CRDC Calibration.	150
4.9	CRDC Mask Position Spectra.	151
4.10	Ion Chamber Calibration	151
4.11	GRETINA Energy Calibration.	152
4.12	Time of Flight Corrections	154
4.13	GRETINA Beta Minimisation.	155
4.14	Target Placement Effect.	156
4.15	Corrected spectrum as function of phi.	157
4.16	Secondary Beam Composition.	158
4.17	Secondary beam reaction products.	159

4.18	^{27}Si γ -ray spectrum.	160
4.19	Level Structure of ^{27}Si	161
4.20	Particle identification using CH_2 target.	162
4.21	γ -ray information gated on the CH_2 ^{27}Si ROI.	163
4.22	Example fit of the 2.866 MeV decay.	164
4.23	Simulated efficiency curves.	167
4.24	CRDC 1 X position of ^{27}Si ions.	168
4.25	Mass Calibration PID.	169
4.26	$^{26m}\text{Al}(p,\gamma)^{27}\text{Si}$ resonant reaction rate as a function of temperature. . .	179
A.1	γ -ray interactions with matter and regions of dominance.	189
A.2	Schematic diagram of HPGe.	192

List of Tables

3.1	Nuclides contained within the triple- α source used to calibrate the TIARA detection systems. Shown with their dominant α -decay branch energies.	65
3.2	Table summarising the states populated within this experiment. Only states with clear direct transitions from the excited state observed are presented. States without clear γ -ray information were excluded from this table.	104
3.3	Table outlining relevant values in determining the solid angle corrected for non-contributing regions of the annulus, due to non-functioning detectors or space between neighbouring detectors.	107
3.4	Table outlining the values used to determine C , or the normalisation factor, and the final extracted values.	108
3.5	Spectroscopic factors obtained for all previously discussed excitations from the $^{25}\text{Mg}(d,p)^{26}\text{Mg}$ reaction in Section 3.9.4. Also, shown is related spectroscopic factors determined in historical studies and from shell-model calculations.	127
3.6	Effects on the determined l -transfer value spectroscopic contributions when specifically increasing/decreasing the d -wave component by 50%.	129
3.7	Summary of previously measured spectroscopic factors of note for this mirror reaction.	130
3.8	Comparison between the reaction strength variables between that determined within this study and those published by previous investigations.	131
4.1	γ -ray reference energies.	153
4.2	Summary of the measured number of recoil ^{27}Si ions with a given excitation energy, determined using γ -ray information from GRETINA.	165
4.3	Information determined from mass calibration runs.	169

4.4	Quantities used to determine the deuterium density within the target for cross section calculation.	170
4.5	Summary of the measured cross sections of recoil ^{27}Si ions with a given excitation energy, determined using γ -ray information from GRETINA.	171
4.6	Summary of the calculated spectroscopic factors.	173
4.7	Properties of observed excited states in ^{27}Si	174
4.8	Properties of resonant states in $^{26m}\text{Al}(p,\gamma)^{27}\text{Al}$ system.	176
4.9	Resonance strengths of states in $^{26m}\text{Al}(p,\gamma)^{27}\text{Al}$ system.	178

Chapter 1

Introduction & Astrophysical Background

Just seconds following the Big Bang, the five lightest stable nuclei; ^1H , ^2H , ^3He , ^4He and ^6Li were formed. Heavier elements, however, were not created as a result of the Big Bang. In 1957, Burbidge, Burbidge, Fowler and Hoyle published a paper titled “Synthesis of Elements in Stars” which demonstrated that instead these elements were forged within the hearts of stars and in explosive stellar environments [1]. The field of nuclear astrophysics, where the microscopic universe of nuclear physics and the macroscopic realms of astrophysics and astronomy combine, studies the nuclear reactions and processes responsible for stellar nucleosynthesis. The key goal of this field is to answer the massive question: What is the origin of the chemical elements that surround us within the universe?

Throughout the life of a star matter is ejected via various processes, these ejected nuclei enrich the interstellar medium and become the seeds for everything non-stellar, and new stars. Nucleosynthesis is the process that describes how stars generate energy and work as elemental factories. Observations using an ever-increasing range of the electromagnetic spectrum are shining light on the evidence for this process. By measuring the chemical elemental abundances at various astrophysical sights, such as the ejecta of explosive nova and supernova or the stellar winds of massive stars, direct links between the two can be formed. Abundances measured on Earth can contribute to the picture through meteoric remains and interstellar solid grains that formed before the Sun, known as presolar grains. All of this is fed into progressively more complex and

sophisticated nucleosynthesis and hydrodynamical models, which have the combined aim of providing a detailed understanding of the astrophysical events occurring within the universe. The predictions from these models can be compared to the observations made, however, the input data for these models have considerable uncertainties. In order for these models to improve a detailed understanding of the nuclear reactions involved and their corresponding processes is required.

The focus of this work is on two key nuclear reactions in two different stellar environments, through indirect experimental investigations. The weak s -process, which predominantly occurs in Asymptotic Giant Branch stars, is thought to be responsible for the creation of s -nuclei with masses $A \leq 90$. The $^{22}\text{Ne}(\alpha,\gamma)^{26}\text{Mg}$ and the $^{22}\text{Ne}(\alpha,n)^{25}\text{Mg}$ are key confrontational reactions to the available neutron flux within this process, the former reducing the number of neutrons available whilst the latter is neutron producing. The $^{22}\text{Ne}(\alpha,\gamma)^{26}\text{Mg}$ reaction was studied by investigating the $^{25}\text{Mg}(d,p)^{26}\text{Mg}$ reaction to determine the spin and parity of resonant states between the α -threshold and the n -threshold. The second reaction studied was the $^{26m}\text{Al}(p,\gamma)^{27}\text{Si}$ reaction via the $^{26}\text{Si}(d,p)^{27}\text{Si}$ reaction. The rate at which this reaction occurs may have significant effects on the abundance of ^{26g}Al and overall flux of cosmic γ -ray emissions from Core-Collapse Supernovae (CSSN) events.

The following sections provide a general background to nuclear astrophysics, introduce the relevant astrophysical sites of interest and discuss the important roles of the $^{22}\text{Ne}(\alpha,n)^{25}\text{Mg}$ and $^{26m}\text{Al}(p,\gamma)^{27}\text{Si}$ nuclear reactions.

1.1 Evidence for Nucleosynthesis

Nucleosynthesis is the theory explaining the creation of elements and is the cornerstone of nuclear astrophysics. It has been widely accepted since the 1930s that the fusion of light nuclei is the fuel that powers the stars throughout the universe [2–4]. The creation of heavier metallic nuclei was attributed to the stars and their nuclear processes a few years after that [5–7]. In order to develop a theory, observational data is needed to test against it.

1.1.1 Solar System Abundances

The most important piece of evidence for nucleosynthesis currently available is the chemical elemental abundance data of the solar system. Most of the mass within the Solar System is contained within the Sun, therefore, the chemical abundance of the Sun can be treated as representative of the entire solar system. Measurements of the solar spectra can allow the composition of the Solar System to be determined. It is also possible to collect data from presolar grains, a specific class of meteorites known as CI carbonaceous chondrites [8–12]. These are thought to be time capsules from the original solar nebula before the formation of the present Solar System. The Solar System was created after the collapse of a gaseous nebula with an approximately uniform elemental and isotopic distribution. Some objects within the Solar System can therefore be treated as representative of the abundances from our local region of the Milky Way at the time of their formation.

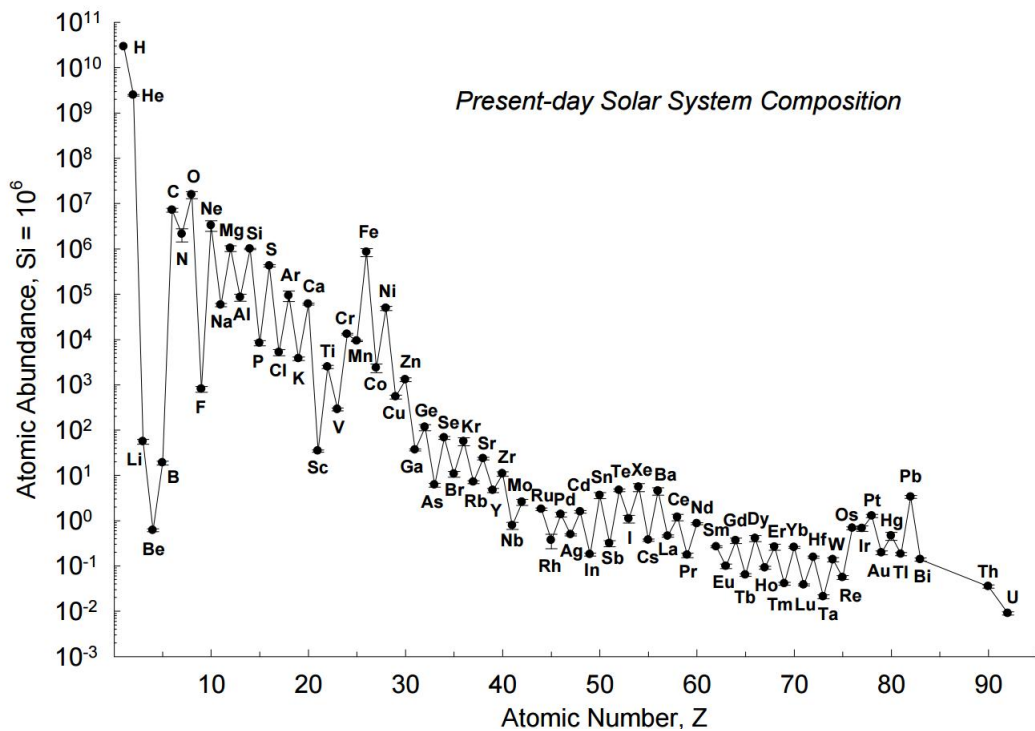


Figure 1.1: Abundances of nuclides in the present day solar system normalized to the number of silicon nuclei [13].

In 1956 the first major study using a combination of both meteoritic and solar spectra data was published by Suess and Urey [14]. This paper laid out the schematic for the abundance tables in use today. It is now possible to investigate the various nu-

cleosynthesis processes that leave clear signatures within the observed Solar System abundance data. Taking this method further allows a direct link between these processes to the stellar environments in which they occur. Figure 1.1 displays the solar system abundances of nuclides, normalized to the number of silicon atoms, versus their mass number. There is no random scatter of the abundances, instead there is a regular and systematic pattern within the maxima/minima of the abundance. It is commonly accepted that the abundances of a particular nuclides group/subgroup can be connected to a specific system of nucleosynthesis.

1.1.2 Stellar Populations & Hertzsprung-Russell Diagram

It is currently accepted within astronomy that there are three generations of stars within the universe, referred to as stellar populations. These are known as Population I, Population II and Population III stars. The categorization of stars into these population groups is based mostly on the metallicity of the star [15]. Population III stars are thought to be the first chemical evolution of stars, they are extremely metal poor and formed of the primordial gas of the universe [16–18]. Any of these stars still in existence would have to be of small mass $\leq 0.8 M_{\odot}$, otherwise they would long be extinct. Population I stars, including the Sun, are metal rich and so contain elements heavier than hydrogen or helium. Population II stars lie in between these two, they are more metal poor than Population I but unlike Population III stars they contain some metallic elements. Approximately Population I stars contain less metallic element by a factor of 100 or more, relative to Population II stars.

Population I stars can commonly be found within the spiral arms of the Milky Way whilst Population II stars are found in the halo and bulge of the Galaxy. Population III stars are difficult to identify within the Milky Way and not many are believed to still be burning. In fact there are very few candidates for Population III stars, one of these candidates is the “COSMOS Redshift 7” [19]. Making a presumption that the Milky Way began as uniform and metal poor, with no method of concentrating the metallic elements within the disk, then the Galaxy must have synthesized the majority of its metallic elements. When considering the various metallicity of the star populations, a timeline of the populations can be concluded. This timeline follows that the Population III stars were the first generation stars within the Universe. Population

II stars followed the death and pollination of these stars and Population I stars formed significantly further on in history [20, 21].

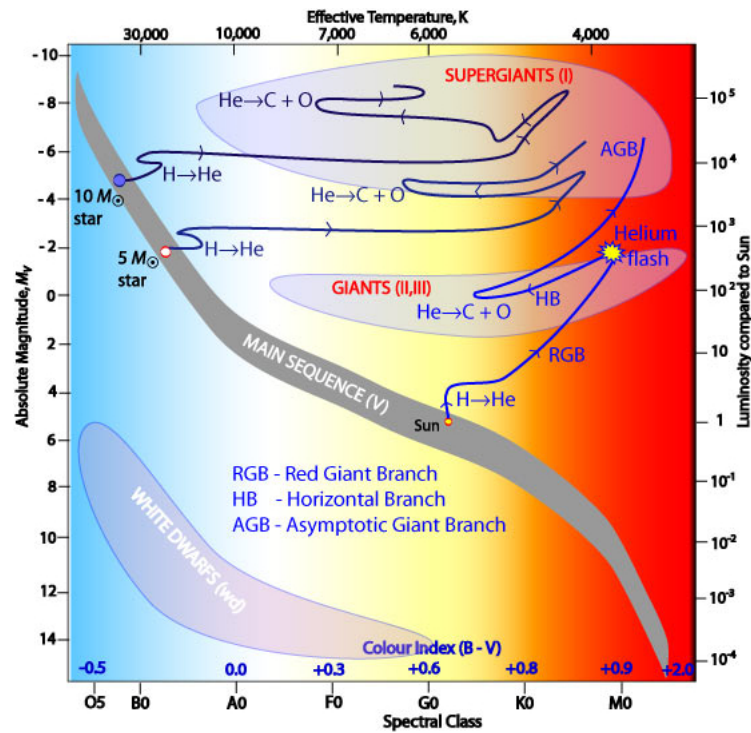


Figure 1.2: A Hertzsprung-Russell diagram showing the evolutionary pathways for main-sequence stars, including the evolution pathway into the AGB classification. Image Credit: Australian Telescope National Facility [22].

Hertzsprung and Russell were the first people to make the significant comparison of a star's surface temperature and luminosity [23, 24]. Plotting these two variables against each other for several observed stellar clusters displayed how instead of a random scattering, there are a distinct number of stellar groups. The graphical display of this comparison became known as the Hertzsprung-Russell diagram, Figure 1.2. It can be seen that the majority of stars lay along a narrow curved band running along from the lower right-hand corner to the upper left-hand corner. This band has become known as the “main sequence”. In the lower left-hand corner is a small group of stars known as “white-dwarfs”. Most of the remaining stars are divided into two groups within the upper right-hand corner. These are the “red giants” and “red super-giants”

1.2 The Evolution of Single Stars

Understanding the Hertzsprung-Russell diagram and the specific clustering of stars within it is a key goal of stellar astrophysics. The evolution of stars from one region to another and the effect of this evolution on the stellar structure is of key importance. The main stages of the stellar life cycle will be discussed in the following subsections.

1.2.1 The Birth of Stars

Stars form within nebulae, throughout the interstellar medium, when a large cool cloud of gas gravitationally collapses. During this gravitational free fall the internal heat is easily radiated away due to the significant transparency of the gas cloud [25]. A protostar is finally formed when the cloud reaches a critical density, due to random turbulent process, such that the cloud becomes opaque to radiation and rapidly undergoes a heating process [26]. Protostars will eventually reach a peak temperature as a result of this contraction, this will determine the life cycle the star will follow. In order to ignite nuclear fusion reactions, and become a main sequence star, a protostar must reach a core temperature in excess of 10^6 K. When this temperature is reached stable hydrogen burning can begin and further gravitational contraction is prevented. Those protostars without the sufficient mass ($\lesssim 0.8 M_{\odot}$) to reach these core temperatures evolve into “black” or “brown” dwarf stars [27].

It is common to find clusters of young stars in close proximity to each other. The theorized cause of this is a phenomenon known as supernova-induced star formation. In this process the shock waves from a nearby supernova is incident on the molecular gas cloud, causing the gas cloud to compress and clump [28]. This compression acts as a trigger for gravitational collapse and eventual star formation to occur.

1.2.2 The Main Sequence

When a protostar achieves hydrostatic hydrogen burning within its core, it begins its life as a main sequence star. This stage can be loosely defined as an extended period of stable hydrogen burning that composes the majority of a star’s lifespan. There are two conditions for a star to maintain this stability and continue its evolution, these are hydrostatic equilibrium and thermal equilibrium.

Within the context of stars, thermal equilibrium is when the thermal energy being created by nuclear reactions throughout its interior is equal to the energy being lost through its surface. It is not that the star is a constant temperature throughout its structure. In a mathematical format this condition can be transcribed as

$$\frac{dL(r)}{dr} = 4\pi r^2 \rho(r) \epsilon(r), \quad (1.1)$$

where $L(r)$ is the flux of energy through a sphere of radius r and $\epsilon(r)$ is the released energy from the star per gram of stellar matter per second. Any energy gradients within the star could lead to instabilities within the stellar interior and possibly gravitational collapse. As a result, an energy balance is required throughout the entirety of the stellar interior.

The second condition is known as hydrostatic equilibrium, the internal pressure at any given spatial point must be large enough to counteract the gravitational weight of the layers outside of that point and prevent gravitational collapse. The mass and density of a star are functions of the distance r from the centre of the star. Both variables decrease as r tends towards the radius of the star. The internal pressure is also a function of r and will decrease proportionally to the mass supported at that distance. This condition can be expressed mathematically in the following way:

$$\frac{dP(r)}{dr} = -\frac{GM(r)\rho(r)}{r^2}, \quad (1.2)$$

where $P(r)$ is the total gas pressure at a distance r , G is the gravitational constant, $\rho(r)$ is the density at the radial distance r and $M(r)$ is the mass contained within the sphere demarcated by the distance r .

With these two conditions satisfied, a star begins its main sequence and hydrostatic hydrogen burning is achieved within the core. The basic principle process is the conversion of four ^1H nuclei into a singular ^4He nucleus via nuclear fusion, releasing a net energy of 26.731 MeV. However, the probability of four protons within the stellar plasma interacting simultaneously is far too low to explain the observed luminosity of stars [29].

There are two key nuclear pathways, both utilising two particle entrance channels, which are responsible for this fusion process. The mass of a given star determines the specific hydrogen burning pathway. A star with mass smaller than $\sim 2M_{\odot}$ burns

hydrogen through the pp chains. Stars with larger masses primarily burn hydrogen via a series of reactions known as the CNO cycles. These nuclear reaction series will govern the energy production of a star until a significant proportion of its hydrogen has been exhausted.

1.2.2.1 The pp Chain

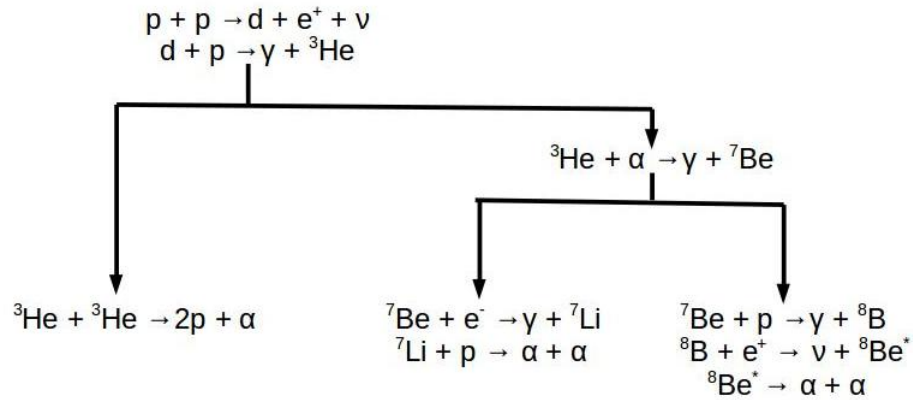


Figure 1.3: A schematic of the three dominant pp -chain reaction pathways.

The proton-proton (pp) chain is a formalism used to encapsulate four predominate reaction pathways, all of which share the initial creation method of ${}^3\text{He}$. ${}^3\text{He}$ is created via the fusion of three ${}^1\text{H}$ nuclei with an intermediary β^+ decay. After this, the four reaction pathways diverge to enable the destruction of ${}^3\text{He}$ culminating in the creation of ${}^4\text{He}$. The dominance of an individual process is determined by the temperature of the star and the quantity of seeded ${}^4\text{He}$ within the star. The pp -I chain is the simplest reaction process with a single step reaction of ${}^3\text{He}({}^3\text{He}, 2\text{p}){}^4\text{He}$ and is dominant in stars with a temperature < 18 MK. If a star has significant seeding of ${}^4\text{He}$ on formation, or the ability to synthesize large quantities, the ${}^3\text{He}({}^4\text{He}, \gamma){}^7\text{Be}$ capture reaction can occur and make possible the pp -II and pp -III chain pathways. These two pathways destroy ${}^7\text{Be}$ creating two ${}^4\text{He}$ nuclei, via ${}^7\text{Li}$ and ${}^8\text{Be}$ respectively. The pp -II chain is dominant over the temperature range of 14 to 23 MK whilst the pp -III chain is dominant at temperatures above 23 MK [30, 31]. Lastly, the the least probabilistic pp -IV chain relies upon the direct capture reaction of ${}^3\text{He}({}^1\text{H}, \text{e}^+){}^4\text{He}$ [32]. The four pathways have the same net energy production, however, the neutrinos created within

each chain removes a different maximum energy value. All four of these chains can operate simultaneously within stars with varying contributions as discussed above.

1.2.2.2 The CNO Cycles

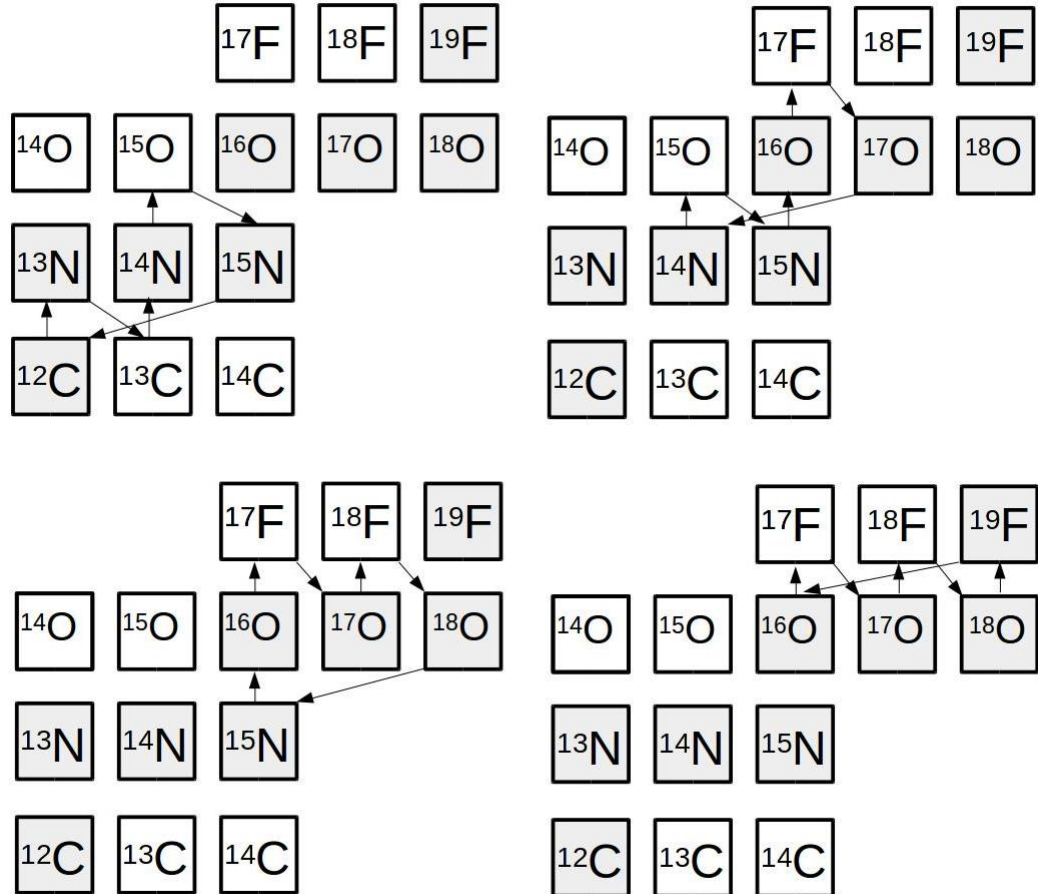


Figure 1.4: Schematical representation of the four separate CNO cycle pathways. Stable nuclei are shaded.

When stars contain more than just hydrogen and helium, other methods of hydrogen burning become available to the star. It is common for the composition of stars beyond population III (i.e. population I or II) to include heavier metallic elements, where metallic refers to elements heavier than helium. The elements Carbon, Nitrogen and Oxygen can be used as catalyst nuclei for the hydrostatic burning of hydrogen. The CNO cycles refers to four nuclear pathways, which similar to the *pp* chains, convert hydrogen into helium. These pathways have an identical conclusion as the *pp* chains and

the amount of energy released by each cycle is the same. The abundance of these catalyst nuclei remain relatively unchanged through this process, with each cycle returning back to the original nuclei. These cycles allow for substantial quantities of energy to be produced even if the amount of metallic nuclei is relatively low. The dominant timescale restraint to this process is the proton capture of hydrogen is typically much longer than for the β -decays [33]. The four separate reaction pathways are displayed in Figure 1.4.

1.2.2.3 Other Cycles

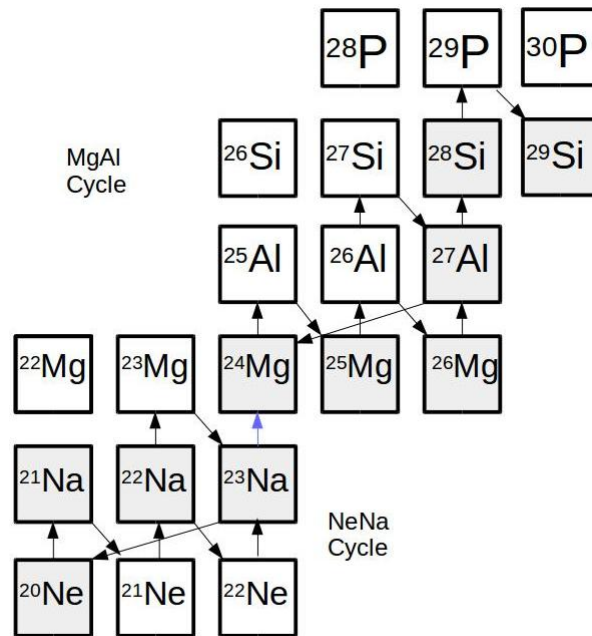


Figure 1.5: Schematical representation of the NeNa and MgAl reaction pathways. A blue arrow represents the proton capture reaction linking the two. Stable nuclei are shaded.

There exists other nuclear pathways to convert hydrogen into helium for stars with circumstances different to those previously discussed. Two notable examples of this are the NeNa and MgAl cycles. These can occur in stars that contain seed nuclei with mass $A \geq 20$ upon formation and a sufficiently high core temperature. The most common site is within massive population I stars. Similar to the CNO cycles these two pathways use heavy metallic nuclei as catalysts. It is of note that these two cycles do not provide large quantities of energy due to the higher Coulomb barriers involved, therefore they are relatively unimportant as an energy source. These pathways play an

important role in the nucleosynthesis of the elements between ^{20}Ne and ^{27}Al [33]. The nuclear reactions involved in these cycles are shown in Figure 1.5.

1.2.3 The Fate of Stars

The conclusion of a star's life is heavily dependent on its initial mass. A star begins towards its death after the completion of its hydrostatic hydrogen burning. After a significant proportion of a star's hydrogen has been burnt, the star enters a volatile series of burning phases, complemented with a sequence of contraction and expansion phases. The “turn-off point” is the moment of a stars life when it is the bluest and hottest within the main sequence, and is also the end of the main sequence.

1.2.3.1 Initial Mass $0.4 M_{\odot} \lesssim M \lesssim 2 M_{\odot}$

Once the main sequence is over most of the hydrogen within the core has been burnt and the star's core is composed mostly of helium. There are no longer nuclear reactions providing the necessary energy to stave off the gravitational pull of the star's mass. The star begins to spatially contract and the gravitational pressure and therefore the temperature increases. This contraction continues until a thin shell of hydrogen that surrounds the helium core is ignited. This layer of nuclear burning prevents all of the energy produced by the core from radiating away. The layers surrounding the core expand and cool such that the star enters onto the “red giant branch” or RGB. The luminosity of the star continuously increases until a maximum T value of ~ 0.6 Gy is achieved at the tip of the RGB. During this phase of evolution the star goes through significant changes. The star sheds material from its surface and loses a significant amount of mass. Also during this phase the core contracts with a sharp increase in its central temperature and density, by several orders of magnitude, up to a 10^4 increase. Eventually, the helium core becomes electron degenerate.

At this point non-hydrogen burning begins within a star for the first time. The core temperature still increases reaching ~ 0.1 GK, at this point helium begins to fuse into carbon, via the triple α -reaction. The triple α -reaction is a two-step process, the first is the fusion of two α -particles into the ground state of ^8Be , see Equation 1.3 [34–36]. An additional complication to this process is the instability of the ^8Be nucleus, which decays into two individual α -particles with a half life of $6.7 \times 10^{-17}\text{s}$.

Eventually the decay rate of ${}^8\text{Be}$ equalises with its formation rate and small pockets of ${}^8\text{Be}$ concentrations build up. The second step within this process is for a third α -particle to fuse with a formed ${}^8\text{Be}$ nuclei. This resonant capture reaction forms nuclei of ${}^{12}\text{C}$, see Equation 1.4 [37].



This ${}^{12}\text{C}$ nuclei acts like a gateway for a series of helium capture reactions, all of which create heavier nuclei. Whilst the main products of this reaction series are ${}^{12}\text{C}$ and ${}^{16}\text{O}$, a number of other heavier isotopes can be produced via subsequent α -capture reactions such as; ${}^{20}\text{Ne}$, ${}^{24}\text{Mg}$, ${}^{28}\text{Si}$ and more. The greater abundance of ${}^{12}\text{C}$ and ${}^{16}\text{O}$ is determined by the low cross section of the alpha capture reaction ${}^{16}\text{O}(\alpha,\gamma){}^{20}\text{Ne}$. These α -capture reactions within the helium core are collectively described as the “helium burning” phase. In this phase of a star’s life there is a strong dependency between the temperature of the core and the energy generation of the star from helium burning. In previous phases of the star’s life any increase in temperature would cause an expansion and cooling of the star. However, the helium core is now a degenerate gas and there is no temperature dependence to the pressure within the core. Without this increasing pressure, there is no force to drive spatial expansion of the star. Another point of note for this particular phase is the occurrence of “helium flashes”. These are detonations within the core, brief thermonuclear runaways caused by the explosive nature of this hot degenerate helium gas core. Helium fusion is much less energy efficient relative to hydrogen fusion. As such the length of time a star will burn helium for is much shorter. A given star will burn helium within its core with some stability for approximately 0.1 Gy, this time is known as the “horizontal branch”.

At the end of the “horizontal branch”, a star ascends onto the “asymptotic giant branch” (AGB) when all of the helium within the core is exhausted and the star has a core composed of carbon and oxygen. The core contracts once again without the energy from a nuclear reaction to support the gravitational pull, and the star’s temperature rises. At this point two shells become the predominant energy suppliers for the star, these are a helium shell surrounding the core and a hydrogen shell that encases the

helium shell. Energy production within these shells does not occur at a stable constant rate, the star will go through periodic phases of contraction and expansion corresponding to different burning process dominance. First hydrogen burning is dominant and continuously seeds helium nuclei into the helium shell. The increasing quantity of helium is coupled to an increasing temperature and density. It is possible for the energy generation rate to rise rapidly, such that it surpasses the energy diffusion rate from this shell. At a critical point thermonuclear runaway begins, the helium shell energy production increases quickly becoming the dominant source of energy. Driven by the push of energy from this helium flash the hydrogen shell expands and cools such that the nuclear fusion of hydrogen is quenched. This expansion continues until the helium reactions are quenched and the star contracts again [38]. This contraction reignites the hydrogen burning shell, again becoming the main source of energy generation. This cycle repeats multiple times whilst the star is within the Asymptotic Giant Branch. Helium flashes can reoccur as frequently as every 0.1 ky for a total of approximately 20 My when the star leaves the AGB.

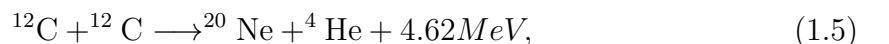
The AGB typically finishes because of a period of destructive stellar winds. These winds allow for a significant amount of mass to escape into the interstellar medium, such that there is not enough mass to cause the thermal pulses driving this branch. The next phase of stellar life is known as the post-asymptotic giant branch, or P-AGB. Stellar winds still drive the release of the star's hydrogen envelope, which in turn reveal the inner layers of the star. The deeper the layer revealed the higher the surface temperature of the star becomes. It is possible for the surface temperature to be such that intense ultraviolet radiation is emitted. This radiation ionizes the ejected matter from the star causing the material to fluoresce as a "planetary nebula". The penultimate stage of a star with mass less than $2 M_{\odot}$ is a "white dwarf" star. This begins when the remaining hydrogen envelope has been ejected and any late hydrogen burning processes have ceased. Left is a hot carbon and oxygen core remanent with no thermonuclear reactions occurring. With no energy being generated, this core remnant enters an extended cooling phase, lasting approximately 500 Gy, until finally the star is left cold and "dead" as a "black dwarf".

1.2.3.2 Initial Mass $2 M_{\odot} \lesssim M \lesssim 11 M_{\odot}$

The key difference for stars with mass $2 M_{\odot} \lesssim M \lesssim 11 M_{\odot}$ relative to stars with mass $\lesssim 2 M_{\odot}$, is the entry of these stars into the RGB phase. These stars do not become electron degenerate within their helium cores, thereby preventing helium flashes as described above. Instead these stars begin their stable helium burning quiescently. Apart from this, stars within this mass region follow approximately the same evolutionary path. However, the progression rate of these stars along this path is much faster than those of the smaller mass bracket.

1.2.3.3 Initial Mass $\gtrsim 11 M_{\odot}$

The initial phases are very similar for stars with mass $\gtrsim 11 M_{\odot}$ to the smaller masses, a key difference is the shorter timescale of evolution within more massive stars. The total nuclear burning lifetime for these stars is currently thought to be ~ 7 My. After the initial hydrogen burning phases, helium ignites within the core in a non-degenerative way, so no helium flash. But the stars outer layer expand greatly to such an extent that it is differentiated to the RGB phase of smaller stars and is known as a “super giant”. Their sheer size can lead to temperatures large enough to begin carbon burning, the fusion of carbon nuclei within the core. The principle reactions from this carbon burning are shown below:



Alongside the processes above are a number of minor reactions not discussed within this thesis. Carbon is not the only heavy element fusion process that can be ignited within the core of these high temperature stars. A series of heavy element burning process can take place using the ash created by the previous nuclear reactions as fuel. This includes the fusion of neon, oxygen, magnesium and silicon nuclei. Nucleosynthesis from nuclear fusion processes culminates with the creation of iron nuclei, where the fusion process is no longer energetically favourable. It is also possible within this “super giant” phase to synthesize nuclei with mass $A \geq 60$ through the s -process,

which will be discussed in more detail in a later section. [39]

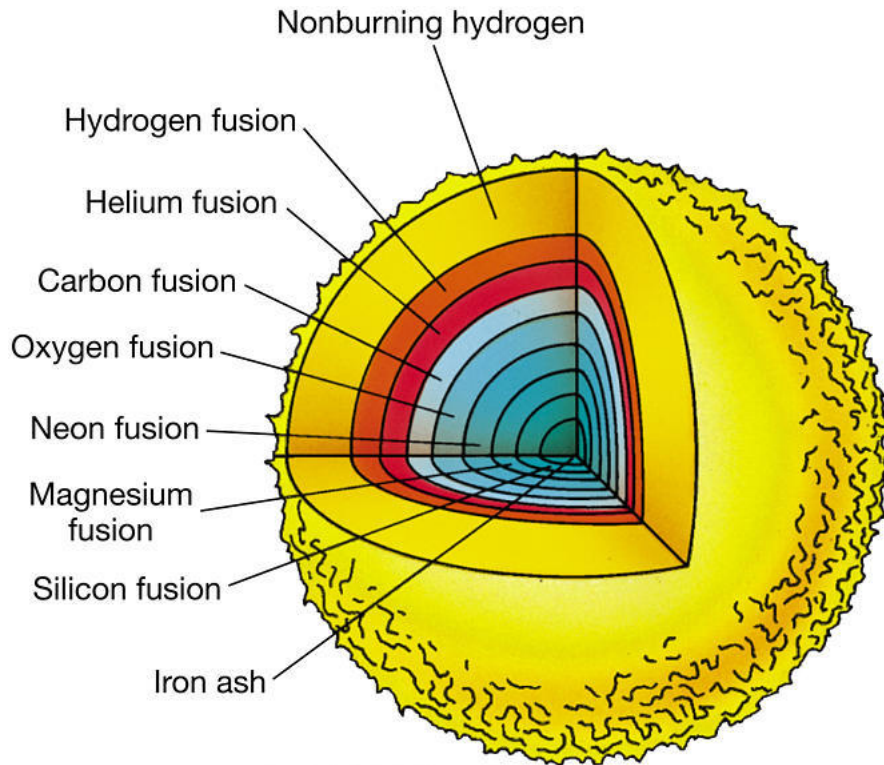


Figure 1.6: Cross section of a super giant phase star, displaying the various layers of fusion reaction burning [40].

After silicon burning within the core has finished, the star has a structure similar to that within Figure 1.6, commonly known as an “onion star” due to its layered structure. In this “super giant” phase the star’s luminosity is so large that strong stellar winds blow away a significant amount of the stars mass. The larger the mass of the star the more pronounced this effect is. In fact, stars with masses $\gtrsim 30 M_{\odot}$ can lose nearly the entirety of their hydrogen envelope.

At this stage of a large star’s evolution there is no longer a nuclear burning energy source within the core. Within the shells surrounding the core some nuclear burning continues and the ashes diffuse into the core. The core becomes electron degenerate and grows in mass until it exceeds the Chandrasekhar limit, approximately $1.4 M_{\odot}$. At this mass limit the electron degeneracy pressure no longer prevents the gravitational collapse of the core. During this collapse, large quantities of photo-disintegration and electron capture upon iron nuclei occurs. These two processes can remove electrons and consumes energy from the gas, both accelerating the collapse [41].

It is of note that vast quantities of energy escapes from the collapsing core through

neutrino release. The energy removed by neutrinos is counterbalanced by the accelerating collapse of the iron core. An extremely violent explosion, or “supernova”, follows this collapse resulting in the near total destruction of the star, with the majority of the star being ejected into the interstellar medium. Only the high-density core is left as a remnant either as a neutron star or a black hole, dependent on the mass of the star. The above scenario accounts for the majority of supernova types, i.e. types II, Ib and Ic. The classification of these supernova types are based on the spectral observations of these events.

1.3 *s*-process

The *s*-process is a neutron capture process responsible for the creation of elements $A \geq 60$. This process is entirely dependent on two nuclear processes, the neutron capture reaction, $X(n, \gamma)Y$, and β^- -decay, $n \rightarrow p + e^- + \bar{\nu}_e$. This process relies on there existing a high free neutron density, on the order of $\sim 10^8$ neutrons per cm^3 , and that the star is seeded with a relatively high abundance of Fe nuclei. This nucleosynthesis occurs along the “valley of stability”, as the neutron capture cross section and time-scale is slow enough for unstable nuclei to β^- -decay before the capture of another neutron. This is especially true at nuclei with a magic number of neutrons, which act as bottlenecks and help to explain for *s*-process abundance peaks.

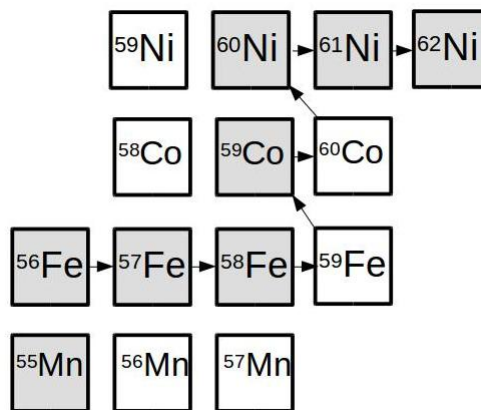
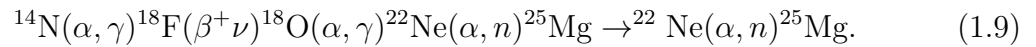
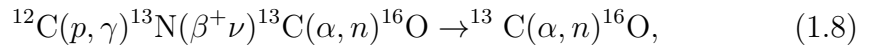


Figure 1.7: A schematical representation of the *s*-process, beginning with a seed nuclei of ^{56}Fe . Stable nuclei that form part of the “valley of stability” are shaded.

Two important reaction pathways [42] are thought to provide the necessary free neutrons to ignite the *s* process, shown below alongside their shortened versions:



The most important part of the *s*-process is the “neutron economy” of the nucleosynthesis. There are three key elements to this economy, these are listed below:

- The abundance of neutron providing nuclei (i.e. ^{13}C or ^{22}Ne).
- The abundance of seed *s*-nuclei (such as iron isotopes).
- The “neutron poisons” that occur throughout the nuclear pathways.

. The balance of the above three items control the final abundance production of *s*-nuclei from any given star. “Neutron poison” is a term to describe any reaction which does not produce *s*-nuclei and removes the availability of free neutrons. A relevant and textbook example of a neutron poison is the so-called “self-poisoning” $^{22}\text{Ne}(\alpha, n)^{25}\text{Mg}$ reaction, because the ^{25}Mg product has a high neutron capture cross section [37]. Competitive reactions are also a source of neutron poisoning, for instance the $^{22}\text{Ne}(\alpha, \gamma)^{26}\text{Mg}$ reaction competes with the neutron producing $^{22}\text{Ne}(\alpha, n)^{25}\text{Mg}$ reaction. The ratio of cross sections between the two reactions defines the available neutrons for the *s*-process [43]. Some individual reactions can appear to be neutron poisons until the larger nuclear pathway is examined, as neutrons can be recycled further down the path. For example, $^{16}\text{O}(n, \gamma)^{17}\text{O}$ appears to absorb neutron flux but is followed by the neutron producing reaction $^{17}\text{O}(\alpha, n)^{20}\text{Ne}$ and so the path “neutron neutral”.

The *s*-process can be divided into two constituent parts, the “main” and “weak” *s*-processes. These will be discussed in more detail in the following sections.

1.3.1 Main *s*-process

The main *s*-process is responsible for the synthesis of elements with $A \gtrsim 90$ occurs within low mass AGB stars. More specifically within thermally pulsing AGB stars, or TP-ABG, with masses of the order 1.5 - 3 M_{\odot} [44]. Both of the neutron producing reactions described in Section 1.3 are accessible within this stellar environment. After the completion of a helium flash, or thermal pulse, the He-burning shell is quenched.

Protons from the hydrogen/helium envelope of the star are dragged down into the intershell region between the previously burning C/O core and the envelope. The intershell is composed of ^4He and ^{12}C with an approximate mass ratio of 3:1. As the thermal pulse ends the star begins to cool and contract again. The H shell re-ignites and newly mixed protons within the intershell region create the following reaction pathway:



This reaction creates two pockets of individual nuclei within this intershell region, one pocket of ^{13}C and one of ^{14}N . As the temperature of the star increases it is possible for the mean lifetime of the $^{13}\text{C}(\alpha, n)^{16}\text{O}$ destruction path to be smaller than the inter-thermal pulse timespan [45]. This temperature is approximately 0.09 GK, or $kT \approx 8$ keV. The free neutrons that escape from these reactions can interact with the seed nuclei within the star, and importantly the Fe seed nuclei. The neutron density produced by this reaction is relatively low, $N_n \approx 10^7$ cm $^{-3}$, but is maintained for ≈ 10 -20 ky and can produce local neutron exposures of ≈ 0.1 mb $^{-1}$ [46]. The entirety of this ^{13}C pocket is consumed in this inter-pulse time period, but the temperature does not rise significantly enough at this point to affect the ^{14}N pocket.

As the H-shell continues to burn, more ash falls into the intershell region increasing its mass, temperature and density. At a critical point the He-region at the bottom of the intershell region can ignite and begin a new thermal pulse. This thermal pulse expands and engulfs the intershell region, including the ^{14}N pocket, reaching close to the H-shell and extinguishing the burning within this shell. This pulse increases the temperature enough ($T \approx 0.27$ GK) to ignite the sequence:



within the ^{14}N pocket. This chain enables the production of neutrons from the secondary equation described previously, $^{22}\text{Ne}(\alpha, n)^{25}\text{Mg}$. The peak neutron density reaches $N_n \approx 10^{10}$ cm $^{-3}$, slightly higher than the ^{13}C neutron source. However, the period of time this reaction occurs over is much shorter, ≈ 10 years, leaving a much lower neutron exposure of ≈ 0.01 mb $^{-1}$ [42]. The consequence of this reaction does not significantly change the overall production of the *s*-process but does affect the branching the *s*-process can take. The higher temperature during this pulse increases the

efficiency of branching away from the valley of stability [47]. After the pulse reaches crescendo it will cool and the star will contract, restarting the cycle which can repeat many times.

1.3.2 Weak *s*-process

The main *s*-process does not account for elemental abundances of nuclei with $A \lesssim 90$. The difference in these abundances is made up by the creation of elements by the weak *s*-process. This process is dominant in two stellar environments, one of them is within the He-burning core and C-burning shells within massive stars with mass $\geq 13 M_{\odot}$ and the other is within the TP-AGB phase of stars with masses $\gtrsim 3 M_{\odot}$ [48, 49].

For the He-burning phase of massive stars ($\geq 13 M_{\odot}$) the weak *s*-process is preceded by the CNO cycle and a He-burning reaction pathway. Of note from the CNO cycle is the production of ^{14}N , the important seed nuclei for the He-fusion reaction pathway. The ^{14}N is rapidly converted into ^{22}Ne through the $^{14}\text{N}(\alpha, \gamma)^{18}\text{F}(\beta^+\nu)^{18}\text{O}(\alpha, \gamma)^{22}\text{Ne}$ pathway, similar to the production within AGB stars [49]. During the helium core burning the core temperature rises. At a temperature of ≈ 0.25 GK ($kT \geq 22$ keV) the star can ignite the $^{22}\text{Ne}(\alpha, n)^{25}\text{Mg}$ reaction and release neutrons for the weak *s*-process. This temperature is reached towards the end of the He-burning core lifetime for most stars, larger stars reach this temperature sooner and as a result are a lot more efficient at burning ^{22}Ne . Above mass $\gtrsim 30 M_{\odot}$ this process is efficient enough to completely burn the ^{22}Ne produced by the He-burning core.

For massive stars with remanent ^{22}Ne after the end of the helium core burning there is the possibility for a second burst of *s*-process within the carbon burning shell. Within this shell the temperatures are high enough to ignite the neutron releasing reaction that feeds the weak *s*-process. The α -particles for this reaction are provided by the reaction:



Temperatures within this site are large enough to create a peak neutron density of $\approx 10^{11} \text{ cm}^{-3}$, dependant on the iron seeding this can significantly affect the abundance pattern. It should be noted that carbon burning within the cores of these massive stars are not believed to be a source of *s*-process nuclei. The elements created within the

core are unlikely to escape in the event of a supernova and during the core oxygen burning phase s -nuclei would likely be destroyed via photodisintegration.

The production of s -nuclei within large AGB stars ($M \gtrsim 3.0 M_{\odot}$) is similar to that within smaller stars, i.e. smaller than $3.0 M_{\odot}$. However, the rate and timescale is dramatically increased within these large stars. The key difference for these large AGB stars is the level of dominance between the two available neutron sources, $^{13}\text{C}(\alpha, n)^{16}\text{O}$ and $^{22}\text{Ne}(\alpha, n)^{25}\text{Mg}$ [50]. With low mass stars the former reaction process is the dominant neutron source, however, in the larger AGB stars the latter is the dominant source.

1.4 Nuclear Reactions of Interest

Understanding the observed elemental abundances throughout the cosmos is a key goal of nuclear astrophysics. Identifying the astrophysical sites and investigating the properties of individual reactions are vital components. The s -process has a large contribution to the abundance of isotopes with $A \gtrsim 60$ and occurs within a significant proportion of stars. Supernova and Wolf-Rayet stars are probable sites to explain a number of observed cosmic γ rays throughout the universe. In the present work we have investigated the astrophysical $^{22}\text{Ne}(\alpha, \gamma)^{26}\text{Mg}$ and $^{26m}\text{Al}(p, \gamma)^{27}\text{Si}$ reactions, the former of which plays a key role in the neutron flux available within the weak s -process whilst the latter provides a competitive version to the $^{26g}\text{Al}(p, \gamma)^{27}\text{Si}$ reaction, both of which are destructive reactions of ^{26}Al .

1.4.1 $^{22}\text{Ne}(\alpha, \gamma)^{26}\text{Mg}$ within the s -process

As discussed previously, the weak s -process is a major source for the elemental abundances with $60 \leq A \leq 90$. This is dominant within high mass AGB stars ($M \gtrsim 3 M_{\odot}$) and in the He-core and C-burning shell burning of massive stars ($M \gtrsim 13 M_{\odot}$). The lynchpin of this process is the free neutron density, which in this scenario is predominately provided by $^{22}\text{Ne}(\alpha, n)^{25}\text{Mg}$ reaction. The free neutrons produced within this reaction can be captured by heavier seed nuclei, such as iron isotopes. Due to the relatively low neutron densities within these environments the capture timescales are much smaller than the β -decay lifetimes. As a result the process follows the valley of

stability up the chart of nuclides.

The neutron economy in the first instance is reliant upon the rates of neutron producing reactions and the poison reactions that remove/prevent neutrons. In high mass AGB stars the main neutron producing reaction is $^{22}\text{Ne}(\alpha, n)^{25}\text{Mg}$. This has a number of corresponding poison reactions that need to be understood to account for the true number of free neutrons released. It has been previously mentioned in Section 1.3.2 that one such poison is the relatively high neutron capture cross section upon the ^{25}Mg product. Another such poison, which this work investigates, is the $^{22}\text{Ne}(\alpha, \gamma)^{26}\text{Mg}$ reaction. This is a competitive reaction to the neutron producing $^{22}\text{Ne}(\alpha, n)^{25}\text{Mg}$ reaction which could significantly alter the flux of free neutrons available.

It is expected that this competitive reaction rate will be dominated by resonant capture rates to excited states in-between the α -emission and n -emission thresholds within ^{26}Mg . These thresholds are at energies of 10614.75 keV and 11093.09 keV respectively. The dominant excited states in this region are expected to be natural parity states due to the 0^+ ground states of both incident particles, i.e. the ^4He and ^{22}Ne isotopes.

1.4.2 $^{26m}\text{Al}(p, \gamma)^{27}\text{Si}$ within Core-Collapse Supernovae

The nucleus ^{26}Al has a relatively short lifetime ($t_{1/2} \approx 7.2 \times 10^5$ years) and so present-day evidence cosmological decay provides direct evidence for continuing nucleosynthesis. There are two cosmological studies that provide suitable evidence for the stellar production of ^{26}Al .

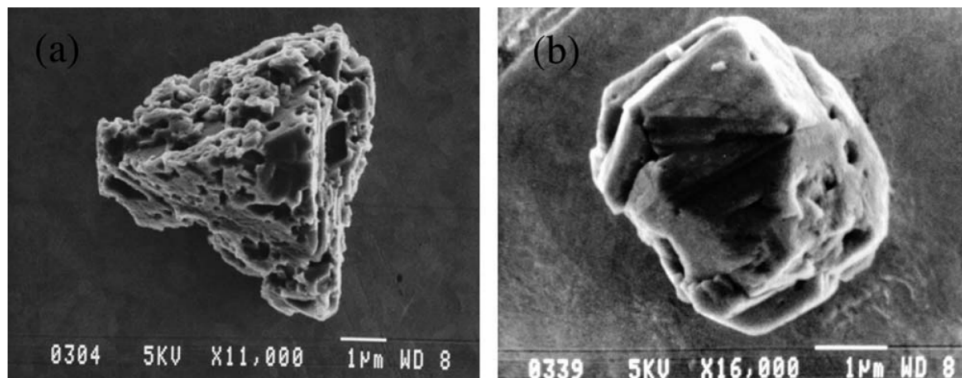


Figure 1.8: Examples of SiC type presolar grains, such as those containing evidence of the ^{26}Al nucleosynthesis [51]

Historically speaking, the first piece of evidence of the nucleosynthesis of ^{26}Al came from the study of meteorites. More specifically the isotopic abundance distribution of presolar grains, primitive meteorites that survived the formation of the solar system [52]. These meteorites predate the solar system and have been excluded from nucleosynthetic processes for enough time that ^{26}Al nuclei have become extinct. There should be no isotopic abundance of ^{26}Al within these meteorites as a result. The previous presence of ^{26}Al can be inferred from a relative overabundance of its daughter nuclei ^{26}Mg . This was seen using detailed mass spectrometry techniques in a study in 1978 by Lee *et al* [53]. This was one of the first studies to conclusively prove that meteorites of this class once contained a significant quantity of ^{26}Al . More recent techniques have discovered that this property may be enhanced within grains from supernovae [54]. Separately, it has been suggested that the in-situ decay of ^{26}Al may affect the life supporting conditions of planetary systems by heating/melting icy planetesimals in protoplanetary disk [55].

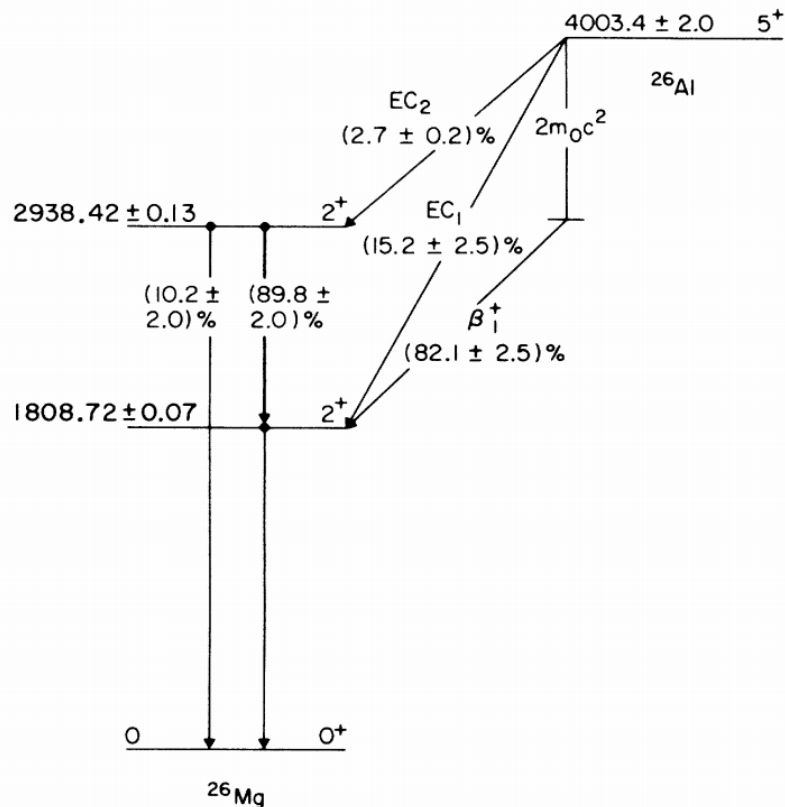


Figure 1.9: Schematic of ^{26}Al decay showing the 1.809 MeV γ -ray decay within ^{26}Mg [56].

In 1983, the HEAO-3 satellite, with a cluster of four coaxial high purity germa-

mium detectors, detected a cosmic γ -ray transition line at 1.809 MeV the characteristic energy for the γ -decay for the β -decay daughter of ^{26}Al [57, 58]. For the first time, there was direct evidence of present day ongoing nucleosynthesis and of γ -ray sources within the interstellar medium [59, 60]. Since this discovery more state-of-the-art γ -ray satellite observatories have been launched into orbit, part of their missions have been to determine the galactic origin of ^{26}Al . These include the satellites: COMPTEL (double-scattering Compton telescope consisting of NE 213A organic liquid scintillators and NaI(Tl) crystals), RHESSI (nine high-purity germanium crystals) and INTEGRAL (nineteen high-purity germanium crystals) [61–63]. A galactic plane all-sky map of the 1.809 MeV γ -ray line was created by the COMPTEL satellite, see Figure 1.10. This sky map displays in detail the inhomogeneous emission of the 1.809 MeV γ -ray across the galactic plane. Together with information from surveys by the INTEGRAL satellite it is thought the origin of this emission is dominated by high-mass stellar environments, such as Wolf-Rayet stars and core-collapse supernovae (CCSN) [64–66]. Using a comparison of the γ -ray flux of ^{60}Fe and ^{26}Al nuclei, using the RHESSI satellite, and with information from theoretical nucleosynthetic studies it has been determined that, Wolf-Rayet stars are the dominant ^{26}Al producing stellar environment within the cosmos [67–69]

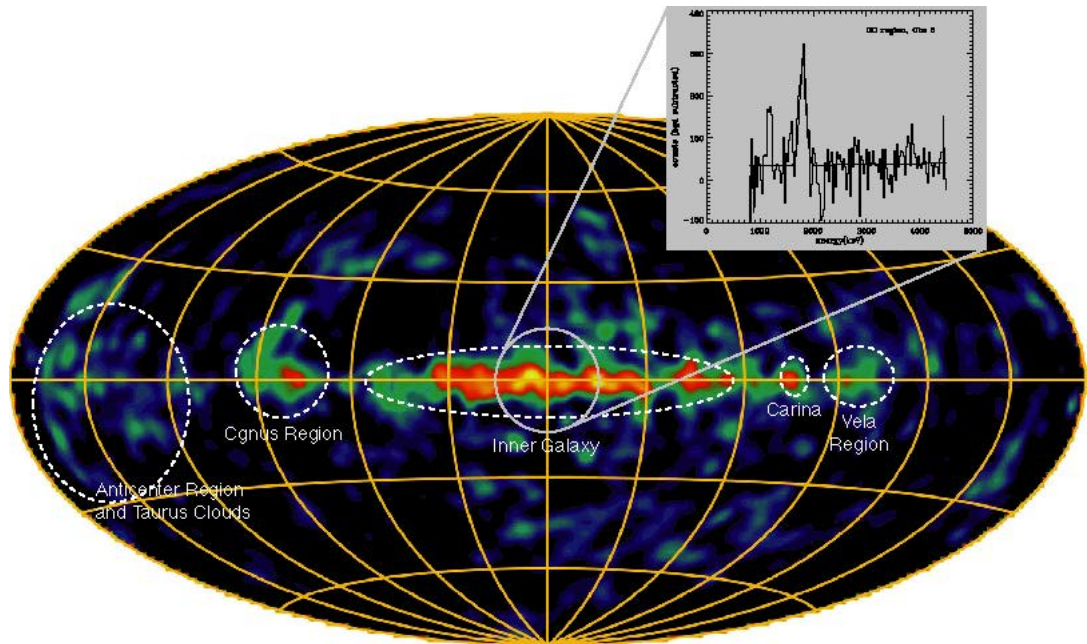


Figure 1.10: COMPTEL satellite sky-map of the ^{26}Mg γ -decay line at 1.809 MeV. Inset: INTEGRAL energy spectrum containing the ^{26}Mg γ -decay line at 1.809 MeV [70].

The destruction of ^{26}Al within Wolf-Rayet state is expected to be dominated by the $^{26g}\text{Al}(p,\gamma)^{27}\text{Si}$ reaction, therefore skipping its β -decay and subsequent 1.809 MeV γ -decay. Core-collapse supernovae are more complex than Wolf-Rayet stars. The ^{26}Al nucleus exhibits a spin isomer, ^{26m}Al ($J^\pi = 0^+$, $t_{1/2} = 6.3460$ s), located 228.305(13) keV above the ground state. This isomer has a super-allowed β^+ -decay directly to the ^{26}Mg ground state ($0^+ \rightarrow 0^+$) excluding the 1.809 MeV γ -ray decay [71]. Theoretical models of nucleosynthesis currently treat this isomer as a separate nucleus within Wolf-Rayet stellar environments [72]. However, within CCSN the high temperatures allow for thermal excitations between the ground and isomeric states of ^{26}Al via higher-lying levels [73]. The rate at which this isomeric state is created and destroyed will therefore affect the overall abundance of ^{26g}Al and have a role in the flux of the 1.809 MeV cosmic γ -ray line. Similarly within these high temperature environments the $^{25}\text{Al}(p,\gamma)^{26}\text{Si}$ reaction is prevalent. The β -decay of ^{26}Si exclusively populates the isomeric state of ^{26m}Al . Therefore, this isomer has a role in the measured isotopic abundance of ^{26}Mg in presolar grains originating from supernovae [74].

Chapter 2

Thermonuclear Reaction Rates and Transfer Reactions

In order to fully understand the nucleosynthetic processes within stellar environments a comprehensive understanding of the of thermonuclear reactions that occur is needed. Of particular note is understanding the nuclear reaction rates. Working knowledge of all these individual reactions creates an in-depth model for the chemical evolution of stars and the energy generation of stars.

In this chapter, a general overview of resonant and non-resonant reaction mechanisms is discussed and an analytical formalism for determining stellar reaction rates is presented.

2.1 Kinematics and Energetics

The simplest nuclear reaction mechanism is where a particle “ a ” strikes a nucleus “ X ” producing a product nucleus “ Y ” and an ejectile “ b ”. This can be expressed as:



or simply as:



The energy released, or associated reaction Q value, is defined by masses of the particles involved within the reaction, this can be expressed as:

$$Q = (M_X + M_a - M_Y - M_b)c^2, \quad (2.3)$$

where M_X and M_a are the ground state masses of the entrance channel particles and M_Y and M_b are the ground state masses of the exit channel particles. The polarity of this Q -value provides insight into the reaction energetics. If the Q -value is positive then the reaction is exothermic and there is a net production of energy. Conversely, if the Q -value is negative then the reaction is endothermic and a minimum amount of energy is required for the reaction. This energy must be brought into the reaction by the entrance channel particles.

Equation 2.3 represents the exit channel particles in their respective ground state configurations. In the case where, for example, the exit channel particle Y is produced in an excited configuration (with energy E_Y^*) then the Q -value equation must be modified in the following manner:

$$Q_{ex} = (M_X + M_a - M_Y - M_b)c^2 - E_Y^* = Q - E_Y^*, \quad (2.4)$$

where Q_{ex} is the Q -value for the excited state and Q is the Q -value as defined in Equation 2.3. E_Y^* can also be defined in terms of the ground state mass, M_Y , and excited state mass, M_Y^* as:

$$E_Y^* = (M_Y^* - M_Y)c^2. \quad (2.5)$$

Known Q -values are regularly tabulated, the most recent of which was the 2016 atomic mass table evaluation [75, 76].

Three additional nuclear properties are tabulated similarly to the Q -value. These are the particle separation energies for nuclei, specifically those for neutron, proton and alpha separation, typically denoted S_n , S_p and S_α respectively. These can be defined as:

$$S_n = (M({}_{Z}^{A-1}X_{N-1}) + M_n - M({}_{Z}^AX_N))c^2, \quad (2.6)$$

$$S_p = (M({}_{Z-1}^{A-1}X_N) + M_p - M({}_{Z}^AX_N))c^2, \quad (2.7)$$

$$S_\alpha = (M({}_{Z-2}^{A-4}X_{N-2}) + M_\alpha - M({}_{Z}^AX_N))c^2, \quad (2.8)$$

where A_ZX_N is the standard nomenclature for defining a nucleus of mass number A , atomic number Z and neutron number N , and M_n , M_p and M_α are the neutron, proton and alpha masses respectively.

In this work, the experimental focus is on neutron transfer reactions using the deuteron as an entrance particle and the proton as an exit channel particle. These reactions are typically denoted as $X(d,p)Y$, relative to Equation 2.2. This reaction is atypical within the astrophysical environments, however is used commonly to indirectly extract information relevant to like astrophysical reactions.

2.2 Cross Sections and Stellar Reaction Rates

The Q -value quantifies the amount of energy released by a given nuclear reaction. Unfortunately, the important property within stellar environments is the total nuclear energy released within the stellar plasma per unit volume. The probability of a reaction happening per unit time and per unit volume is needed to determine this quantity. The quantitative measurement of this probability is known as the nuclear reaction cross section, σ , and is dependant on the relative velocity of the target-plus-projectile system, $\sigma = \sigma(v)$. The occurrence of the previously mentioned example reaction, $X(a,b)Y$, within a stellar gas containing a number, N_a , particles of type a per cm^3 and number, N_X , particles of type X per cm^3 , then the reaction rate, r_{aX} is :

$$r_{aX} = N_a N_X v \sigma(v), \quad (2.9)$$

where v is the relative velocity between the particles and $\sigma(v)$ is the reaction cross section. This can be separated into the projectile particle flux ($N_a \cdot v$) and the product of the effective reaction area in the volume ($N_X \cdot \sigma(v)$).

In stellar plasmas (and other gases) there is a spread of relative velocities between the interacting nuclei, this is described by the probability function $P(v)$, where

$$\int_0^\infty P(v) dv = 1. \quad (2.10)$$

Here, the quantity $P(v)dv$ represents the probability that the relative velocity between the particle pair, v , has a value between $v + dv$. This leads to an expression for the reaction rate per particle pair which is averaged over the velocity distribution, $\langle \sigma v \rangle$,

in the following manner:

$$\langle \sigma v \rangle = \int_0^{\infty} P(v) v \sigma(v) dv. \quad (2.11)$$

Combined with equation 2.9, the total reaction rate can be presented as:

$$r_{aX} = N_a N_X \langle \sigma v \rangle_{aX}, \quad (2.12)$$

where $N_a N_X$ is the total number density of non-identical pairs of “ a ” and “ X ” particles and $\langle \sigma v \rangle_{aX}$ is the reaction rate per particle pair. In practise, this equation becomes:

$$r_{aX} = N_A \langle \sigma v \rangle_{aX}, \quad (2.13)$$

where N_A is the Avogadro constant and r_{aX} is expressed in units of $\text{cm}^3 \text{mol}^{-1} \text{s}^{-1}$.

Particles within a typical stellar gas are non-degenerate and move at non-relativistic velocities. The energy available to these particles originates from their thermal motion, hence reactions in this environment are referred to as thermonuclear reactions. The relative velocities of the particles within the nuclear reactions can be modelled by a Maxwell-Boltzmann distribution:

$$P(v) = 4\pi v^2 \left(\frac{\mu}{2\pi kT} \right)^{3/2} \exp \left(-\frac{\mu v^2}{2kT} \right), \quad (2.14)$$

where μ is the reduced mass of the particles within the interaction, $\mu = m_a m_X / (m_a + m_X)$, T is to the temperature of the plasma and k is the Boltzmann constant. Within the exponential term, the numerator represents twice the kinetic energy of the nuclei within the reaction. Equation 2.14 can therefore be expressed as a function of the kinetic energy:

$$P(E) \propto E \cdot \exp \left(-\frac{E}{kT} \right). \quad (2.15)$$

Incorporating the Maxwellian velocity and energy distributions into equation 2.11, the reaction rate per particle pair becomes:

$$\langle \sigma v \rangle = \int_0^{\infty} P(v) \sigma(v) v dv = \int P(E) \sigma(E) v dE, \quad (2.16)$$

$$= \left(\frac{8}{\pi \mu} \right)^{1/2} \frac{1}{(kT)^{3/2}} \int_0^{\infty} \sigma(E) \cdot E \cdot \exp \left(-\frac{E}{kT} \right) dE. \quad (2.17)$$

Lastly, the total reaction rate r_{aX} can be expressed as:

$$r_{aX} = N_a N_X \left(\frac{8}{\pi \mu} \right)^{1/2} \frac{1}{(kT)^{3/2}} \int_0^\infty \sigma(E) \cdot E \cdot \exp\left(-\frac{E}{kT}\right) dE. \quad (2.18)$$

From the discussion above, it can be seen that the reaction rate has a strong dependence on the energy dependent cross section, $\sigma(E)$. This property is heavily linked to the independent reaction mechanisms for each reaction.

2.3 Non-resonant and Resonant Reactions

Equation 2.18 can be determined numerically or analytically depending on the behaviour of the energy dependent cross section, $\sigma(E)$. With a measurement or theoretical estimation of the energy dependent cross section, ($\sigma(E)$), the reaction rate $\langle \sigma v \rangle$ can be calculated numerically. If the behaviour of the energy dependent cross section is complicated then this is the only viable option for determination. A relatively simple cross section energy dependence allows for an analytical approach.

There are several benefits from determining the reaction rate with an analytical expression. Most importantly, it is possible for a numerical approach to not encapsulate the reality of the reaction rate. If the energy dependent cross section is not known then the rate cannot be integrated numerically. This can happen in situations where narrow resonances exist within the cross section. Another benefit for analytical descriptions is in cases where the reaction rate has to be extrapolated to the region of interest, analytical approaches allow for an improved estimation of the rate.

2.3.1 Charged Particle-Induced Non-resonant Reactions

Energy generation within stars is provided primarily by the fusion of hydrogen nuclei into helium, which can only occur when a minimum temperature is reached, $\approx 10^7$ K. This high temperature is required to overcome the potential energy barrier ($V(r)$) separating two charged particles. This barrier is composed of two components. The first is a Coulomb barrier, $V_C(r)$, created by the positive charge of nuclei, expressed using the nomenclature from equation 2.2:

$$V_C(r) = \frac{Z_a Z_X e^2}{r}, \quad (2.19)$$

where Z_a and Z_X are the charges of the interacting particles, e is the electron charge and r is the distance between the pair. The second component is the centrifugal potential, $V_{cf}(r)$ arising from the relative orbital angular momentum between the particle pair, this is expressed as:

$$V_{cf}(r) = \frac{l(l+1)\hbar^2}{2\mu r}, \quad (2.20)$$

where l is the orbital angular momentum quantum number. This gives rise to a functional form for the potential barrier, given by:

$$V(r) = V_C(r) + V_{cf}(r) = \frac{Z_a Z_X e^2}{r} + \frac{l(l+1)\hbar^2}{2\mu r}. \quad (2.21)$$

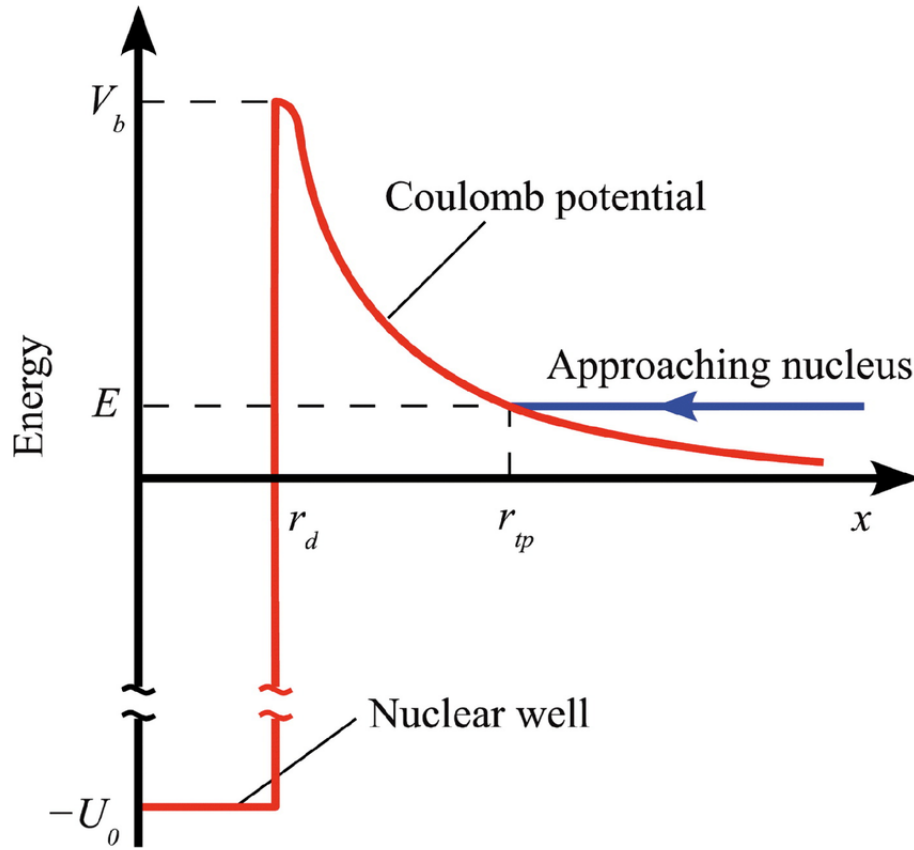


Figure 2.1: Schematic of the combined nuclear, centrifugal and Coulombic potentials in 1-dimension. In this representation $V_b = V(r)$. A projectile with $E < V_b$ has to tunnel through this combined centrifugal and Coulombic potential to reach the nuclear force [77].

A schematic of this barrier is displayed in Figure 2.1. For the case of two protons, the effective height of the potential is 550 keV. In a classical sense, only when the particle pair interaction surpasses this energy can a reaction take place. This energy barrier

for thermal motion corresponds to a stellar temperature of 6.4 GK. Theoretically, under these circumstances it would be possible for all particle pairs to react instantaneously. If this happened then the star would explode catastrophically rather than burn with stability for billions of years.

Quantum mechanically, there is a finite probability for a projectile to tunnel through this potential barrier, even with an energy less than the potential height of the barrier, $E < V(r)$. If the particle can tunnel to a radius, r_0 , whereby the nuclear force is dominant, the reaction can take place. The probability of barrier penetration, with $E_{\text{projectile}} \ll V(r)$, via this tunnelling effect is quantified by the ‘‘Gamow factor’’ (P):

$$P = e^{-2\pi\eta}, \quad (2.22)$$

where η is the ‘‘Sommerfeld Parameter’’, defined as:

$$2\pi\eta = 31.29Z_aZ_X \left(\frac{\mu}{E} \right)^{1/2}, \quad (2.23)$$

where E is the centre-of-mass energy E in units of keV and μ is the reduced mass in units of amu.

The tunnelling probability is directly proportional to the energy dependent cross section, $\sigma(E)$, for charged particle reactions. As a result, the total cross section for these reactions is significantly quenched for energies less than the potential barrier (V_b from Figure 2.1) between the particles. Experiments aimed at measuring cross sections must account for astrophysical energies lower than this potential barrier. Consequently, cross section at astrophysical energies can be too low to measure with current techniques/technologies. The minimum achievable beam energy may be larger than the astrophysical energy of interest. This is of particular importance in direct measurement experiments. This experimental limitation requires models to extrapolate current data into astrophysically relevant energy regions, as shown in Figure 2.2(a). However, at these low beam energies the cross section can vary dramatically with beam energy and are unreliable.

The astrophysical S-factor, $S(E)$, encapsulates all of the nuclear components of the probability. This property is defined as:

$$\sigma(E) = \frac{1}{E} \exp(-2\pi\eta)S(E), \quad (2.24)$$

where the $1/E$ term derives from the geometrical energy-dependent de Broglie wavelength of the particle, i.e. $1/E = \pi/k^2$. By writing the cross section in this form the strongly energy dependent factors are factored explicitly, with a residual function of energy, $S(E)$, left. For non-resonant reactions, $S(E)$ is a smoothly varying function with energy, with a much smaller variance with respect to beam energy than the cross section. This makes it extremely useful in extrapolating results into astrophysical regions, as is shown in Figure 2.2(b).

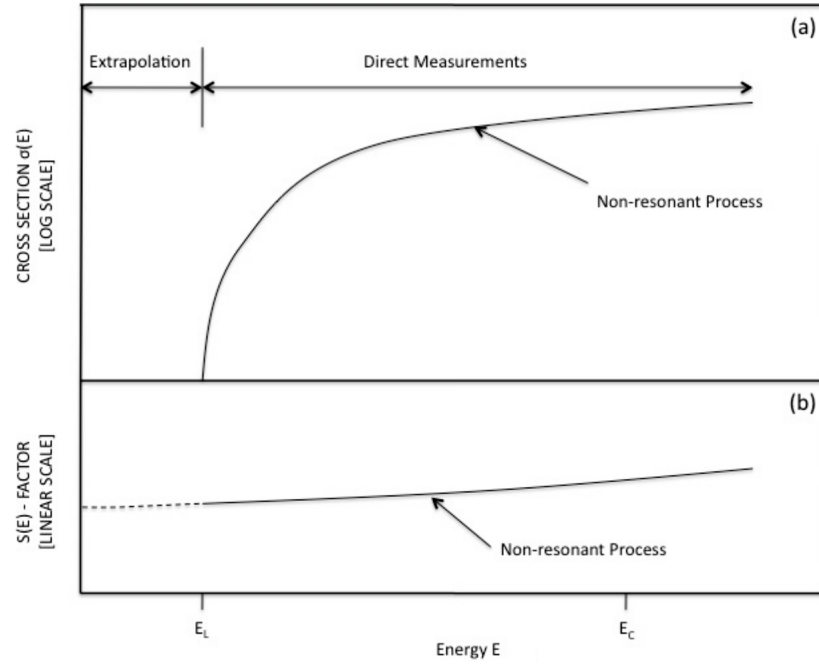


Figure 2.2: (a) Reaction cross section, $\sigma(E)$, as a function of the beam energy. (b) Astrophysical $S(E)$ -factor as a function of beam energy. The value E_L is the lowest beam energy cross sectional measurements can be made and the value E_C is the height of the combined coulombic and centrifugal barrier. This Figure is taken from [78] as an adaptation from Figure 4.3 of [79]

Substituting Equation 2.24 into the Equation 2.18, the reaction rate per particle pair can be re-written as:

$$r_{aX} = N_a N_X \left(\frac{8}{\pi\mu} \right)^{1/2} \frac{1}{(kT)^{3/2}} \int_0^\infty S(E) \cdot \exp\left(-\frac{E}{kT} - \frac{b}{E^{1/2}}\right) dE, \quad (2.25)$$

where the quantity b within the exponential term, which arises from the barrier penetrability, is defined as:

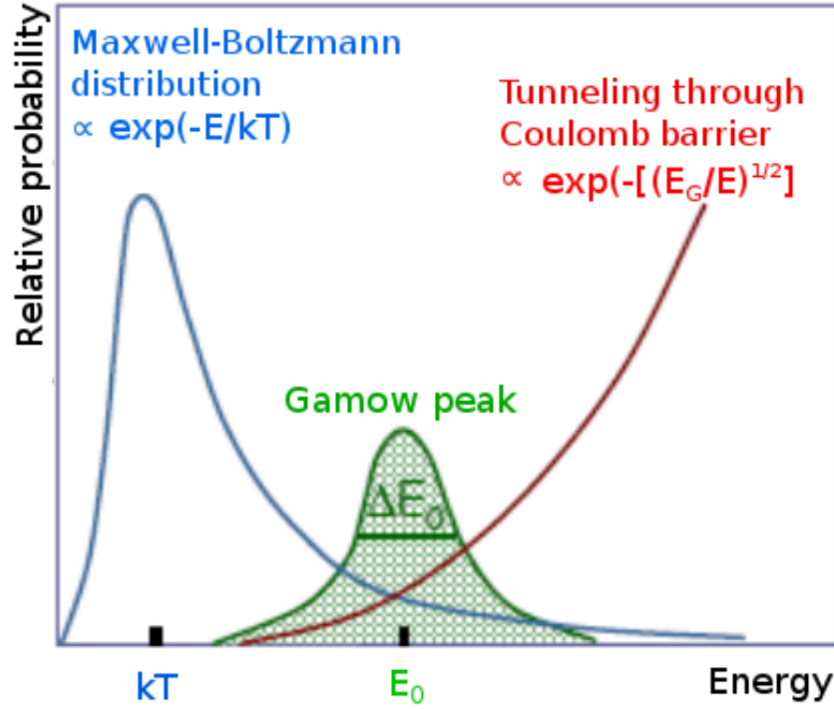


Figure 2.3: Diagram showing the Maxwell-Boltzmann distribution of energies and the tunnelling probability that feature within non-resonant nuclear reactions. Also shown is the convolution of these two terms that make up the Gamow window [80].

$$b = \frac{(2\mu)^{1/2} \pi e^2 Z_a Z_X}{\hbar} = \sqrt{E_G}, \quad (2.26)$$

where E_G is the Gamow energy. As a result, Equation 2.25 can be re-written as:

$$r_{aX} = N_a N_X \left(\frac{8}{\pi \mu} \right)^{1/2} \frac{1}{(kT)^{3/2}} \int_0^\infty S(E) \cdot \exp \left[-\frac{E}{kT} - \left(\frac{E_G}{E} \right)^{1/2} \right] dE. \quad (2.27)$$

For non-resonant reactions, $S(E)$ is a smooth function of beam energy. Therefore, the energy dependence of the integrand in the equation above is determined by the two exponential terms within the integral. These terms represent the Maxwellian distribution of energies and the energy dependent tunnelling probability. The product of which, leads to a peak of the integrand near an energy term, E_0 , known as the Gamow peak and is typically larger than kT . The width of this peak, ΔE_0 , is representative of the narrow energy window where nuclear reactions have a high probability of taking place, see Figure 2.3.

The factor $S(E)$ is approximately constant over the extent of the narrow Gamow window, allowing the reaction rate definition from Equation 2.27 to reduce to:

$$r_{aX} = N_a N_X \left(\frac{8}{\pi \mu} \right)^{1/2} \frac{1}{(kT)^{3/2}} \cdot S(E_0) \int_0^\infty \exp \left[-\frac{E}{kT} - \left(\frac{E_G}{E} \right)^{1/2} \right] dE. \quad (2.28)$$

Taking the first derivative of the integrand in Equation 2.28, one can find the energy E_0 to be:

$$E_0 = \left(\frac{bkT}{2} \right)^{2/3}. \quad (2.29)$$

If the integrand is approximated as a Gaussian function, the effective width of the Gamow energy window, or ΔE_0 , may be expressed as:

$$\Delta E_0 = \frac{4(E_0 kT)^{1/2}}{3^{1/2}}. \quad (2.30)$$

These two expressions can then be used within Equation 2.28 to produce a final analytical expression for non-resonant reaction rates of charged particles:

$$r_{aX} = N_a N_X \left(\frac{2}{\mu} \right)^{1/2} \cdot \frac{\Delta E_0 \cdot S(E_0)}{kT^{3/2}} \cdot \exp \left(-\frac{3E_0}{kT} \right). \quad (2.31)$$

If the astrophysical S-factor was always smooth and all stellar reactions were completed via non-resonant components, then the analytical formalism laid out throughout this section would form a complete picture for thermonuclear reactions. However, there exists resonances within many stellar reaction at effective stellar energies. These cause large spikes within the cross-sections of these reactions and strong variations within the astrophysical S-factor. An entirely different analytical formalism is required to encapsulate these phenomena.

2.3.2 Narrow-Resonance Reaction Rates

This section will discuss reactions where the astrophysical S-factor varies strongly with energy. In particular reactions where the resonances are narrow and isolated, such that the particle partial widths are approximately constant over the total resonance energy width, Γ .

Examining the energetics Equation 2.1 defined earlier, another reaction between the particles a and X can be considered. This time where a compound nucleus Z is formed within some excited state, before decaying into the exit channel particles Y and b , such as:



where Z^* represents the compound nucleus within an excited state of energy, E_x . Reactions occur through these resonances when the centre-of-mass energy of the entrance channel particles coincides with a stationary excited state within the compound nucleus.

The creation of a resonant state requires the conservation of angular momentum and parity. This means the angular momentum of the excited state within the compound nucleus, \vec{J}_{Z^*} , must be equal to the sum of the intrinsic angular momenta of the entrance channel particles, \vec{J}_a and \vec{J}_X , and the relative angular momentum between them, \vec{l} . This can be written formally as:

$$\vec{J}_{Z^*} = \vec{J}_a + \vec{J}_X + \vec{l}, \quad (2.33)$$

where the standard rules of vector addition apply. The conservation of parity requires that:

$$\pi(J_{Z^*}) = \pi(J_a) \cdot \pi(J_X) \cdot (-1)^l, \quad (2.34)$$

where $\pi(J_{Z^*})$ is the parity quantum number of the resonant excitation state within the compound nucleus, $\pi(J_a)$ and $\pi(J_X)$ are the parity quantum numbers for the entrance channel nuclei and the $(-1)^l$ value represents the parity due to the relative orbital angular momentum between the entrance channel particles.

All resonant states are naturally particle unbound, meaning they can be both formed by and decay back into the entrance channel particles with positive kinetic energy. These compound nucleus states can have significant lifetimes due to the high potential barrier against breakup. The likelihood of breakup occurring increases as the excitation energy increases because the width of the barrier potential decreases as the energy increases. The lifetimes of these high energy states is shorter as a result.

The energy dependent cross section for a single isolated resonance may be described by the Breit-Wigner formula. For the reaction described in Equation 2.32, this can be expressed as:

$$\sigma_{BW}(E) = \frac{\lambda^2}{4\pi} \cdot \frac{(2J+1)(1+\delta_{Xa})}{(2j_X+1)(2j_a+1)} \cdot \frac{\Gamma_1\Gamma_2}{(E_r-E)^2 + \Gamma^2/4}, \quad (2.35)$$

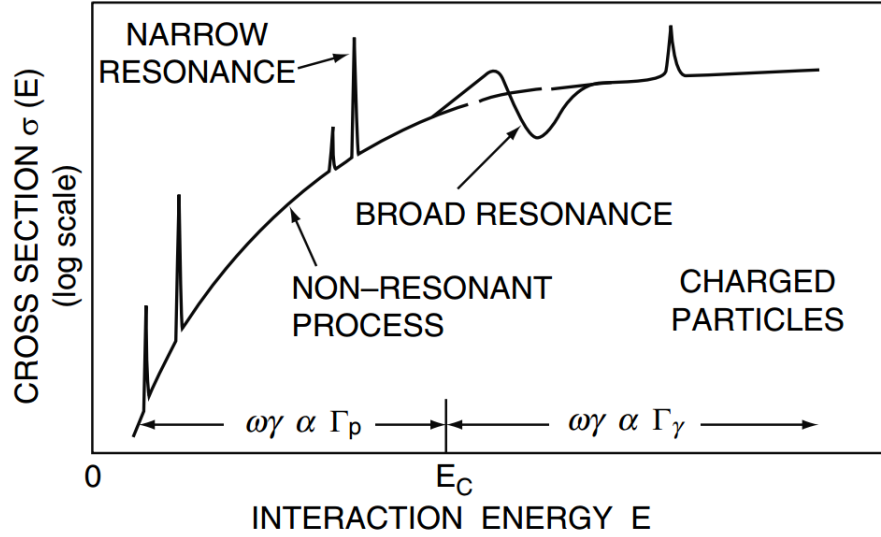


Figure 2.4: Schematic diagram showing the reaction cross section $\sigma(E)$ as a function of the interaction energy for both resonant and non-resonant processes. Adapted from [79].

where $\lambda = 2\pi\hbar\sqrt{2\mu E}$, j_a and j_X are the spins of the target and projectile, J and E_R are the spin and energy of the resonance, E is the centre-of-mass energy, Γ is the total width of the resonance, and Γ_1 and Γ_2 are the particle partial widths of “1” and “2”. These partial widths represent the formation/decay probability of the “1” and “2” channel respectively. The total width of the resonance is equal to the sum of all the reaction partial widths:

$$\Gamma = \sum_{i=1}^n \Gamma_n. \quad (2.36)$$

The Kronecker symbol, δ_{Xa} , has also been included for the case of identical entrance channel nuclei, which increases the cross section by a factor of 2. It follows from Equation 2.35 that, for a defined interaction energy, the cross section of a resonant reaction is larger than for a non-resonance reaction. This is displayed within Figure 2.4.

Equation 2.35 can be substituted into Equation 2.18 to obtain the stellar reaction rate for a narrow resonance, expressed as:

$$r_{aX} = N_a N_X \left(\frac{8}{\pi\mu} \right)^{1/2} \frac{1}{(kT)^{3/2}} \int_0^\infty \sigma_{BW}(E) \cdot E \cdot \exp\left(-\frac{E}{kT}\right) dE, \quad (2.37)$$

$$= \frac{N_a N_X \sqrt{2\pi\hbar^2\omega}}{(\mu kT)^{3/2}} \int_0^\infty \frac{\Gamma_a \Gamma_b}{(E - E_R)^2 + \Gamma^2/4} \exp\left(-\frac{E}{kT}\right) dE, \quad (2.38)$$

where $\omega = (2J+1)(1+\delta_{Xa})/[(2J_a+1)(2J_X+1)]$ and encapsulates the spin information of that resonance. For a very narrow resonance, the Maxwell-Boltzmann factor and the partial widths Γ_a and Γ_X can be approximated to a constant. These can be replaced by their respective values when $E = E_R$ and removed from within the integral from Equation 2.38, simplifying the expression as:

$$r_{aX} = \frac{N_a N_X \hbar^2 \sqrt{2\pi}}{(\mu kT)^{3/2}} \cdot \exp\left(-\frac{E}{kT}\right) \cdot 2\omega \frac{\Gamma_a \Gamma_X}{\Gamma} \int_0^\infty \frac{\Gamma/2}{(E - E_R)^2 + \Gamma^2/4} dE, \quad (2.39)$$

$$= N_a N_X \left(\frac{2\pi}{\mu kT}\right)^{3/2} \hbar^2 \cdot \exp\left(-\frac{E_R}{kT}\right) \cdot (\omega\gamma), \quad (2.40)$$

where $\omega\gamma = \omega\Gamma_a\Gamma_X/\Gamma$, also known as the resonance strength. Two important quantities can be extracted from Equation 2.40, the energy of the resonance (E_R) and its strength ($\omega\gamma$). When a reaction has several resonances, the total reaction rate is equal to the sum of their individual contributions, expressed as:

$$r_{aX} = N_a N_X \left(\frac{2\pi}{\mu kT}\right)^{3/2} \cdot \hbar^2 \cdot \sum_i \exp\left(-\frac{E_i}{kT}\right) \cdot (\omega\gamma)_i. \quad (2.41)$$

From examining 2.41 it is clear that to accurately determine the total contribution of resonances to the total reaction rate, the resonance energies and strengths of each resonance must be measured. In an ideal case, each resonance would be measured in a direct manner. However, in a lot of cases this is impossible due to experimental limitations. In these cases, measurements must be made using indirect techniques.

2.4 Direct Measurements of Resonances

In order to directly measure the resonance strengths, in the manner described by Equation 2.41, the cross section measurement must be made at the astrophysical energy of interest. These measurements use a beam of particle projectiles impinging onto a target in order to replicate the Gamow window of the stellar environment in question. A measurement of the total number of nuclear reactions that occurred throughout the experiment, $N_{reactions}$, and the total number of beam particles, N_{beam} , allows for the determination of the ‘‘yield’’ of the reaction to be made. The yield per incident particle is directly related to the reaction cross section and is defined as:

$$Y \equiv \frac{N_{\text{reactions}}}{N_{\text{beam}}}. \quad (2.42)$$

The yield is customarily plotted as a function of the bombarding energy, known as a “yield curve” or “excitation function”. The resonance strengths for each specific resonance energy, E_R can be calculated through:

$$\omega\gamma = \frac{2\epsilon Y}{\lambda^2} \cdot \frac{M_T}{M_P + M_T}, \quad (2.43)$$

where ϵ is the effective stopping power of the experimental target, λ is the De-Broglie wavelength within the centre-of-mass system, M_P and M_T are the masses of the projectile and target respectively.

2.5 Indirect Determination of Resonance Strengths

For a generalized proton radiative capture reaction of the form, $X(p, \gamma)Y$, the resonance strength is defined as:

$$\omega\gamma = \omega \frac{\Gamma_p \Gamma_\gamma}{\Gamma} = \frac{(2J+1)}{(2J_X+1)(2J_p+1)} \cdot \frac{\Gamma_p \Gamma_\gamma}{\Gamma}, \quad (2.44)$$

where Γ_p and Γ_γ are the partial widths for proton and γ decay respectively, J_X and J_p are the spins of particle “ X ” and the proton respectively and J depends on the spin of the resonant state. If a measurement of all these properties are made then a direct measurement is not required to determine the resonance strength. If just the spins are known then approximations can be made so only one partial width needs to be measured for the determination of the resonance strength. The astrophysical states of interest tend to be dominated by the weaker decay branch, which are harder to measure.

Assuming the resonant state of interest decays predominately via γ -emission, i.e. $\Gamma_p \ll \Gamma_\gamma$. Then the resonance strength is dominated by the proton partial width, Γ_p , as such the expression for the resonance strength is reduced to:

$$\omega\gamma = \omega \frac{\Gamma_p \Gamma_\gamma}{\Gamma_p + \Gamma_\gamma} \approx \omega \frac{\Gamma_\gamma \Gamma_p}{\Gamma_\gamma} = \omega \Gamma_p. \quad (2.45)$$

The proton partial width can be approximated through the expression:

$$\Gamma_p = C^2 \cdot S \cdot \Gamma_{sp}, \quad (2.46)$$

where C is the Clebsch-Gordan coefficient and S is the single particle spectroscopic factor. Together these two properties form the spectroscopic factor, this gives a measure of the wavefunction overlap between the initial state, $p + X$, and the final state, Y . Γ_{sp} is the single particle width and is given by:

$$\Gamma_{sp} = 2 \frac{\hbar^2}{mR^2} \cdot P_C \cdot \theta_{sp}^2, \quad (2.47)$$

where m is the mass of the particle, R is the radius of the nucleus ($R = 1.25A^{1/3}$ fm). P_C is the ‘‘penetration factor’’, which is defined as the probability of the particle penetrating the potential barrier that hinders the reaction and finally θ_{sp} is the dimensionless single-particle reduced width of the proton. The spectroscopic factor is quantitatively a value between 0 and 1. Experimentally, it is determined by the ratio of the experimental cross section and the theoretically calculated cross section.

The experimental differential cross section can be expressed with respect to the spectroscopic factor and theoretical differential cross section:

$$\left(\frac{d\sigma}{d\Omega} \right)_{\text{experimental}} = N \cdot C^2 S \cdot \left(\frac{2J+1}{2J_t+1} \right) \cdot \left(\frac{d\sigma}{d\Omega} \right)_{\text{theoretical}}, \quad (2.48)$$

where N is a normalization factor, J is the spin of the excited state in question and J_t is the transferred spin between the initial and final nuclei. The theoretical cross section can be calculated through eikonal models, examples of this are the Adiabatic Distorted Wave Approximation (ADWA) or the Distorted Wave Born Approximation (DWBA).

It is also possible for the resonant state to decay via particle emission instead of γ -decay. In this case $\Gamma_\gamma \ll \Gamma_p$ and the resonance strength is dominated by the γ -ray partial width, Γ_γ :

$$\omega\gamma = \omega \frac{\Gamma_\gamma \Gamma_p}{\Gamma_\gamma + \Gamma_p} \approx \omega \frac{\Gamma_\gamma \Gamma_p}{\Gamma_p} = \omega \Gamma_\gamma. \quad (2.49)$$

Unfortunately the direct measurement of these γ -ray partial widths is difficult. Typically they are of the order of 1 eV and are determined by the lifetimes of the resonant states. It is common for the astrophysical states of interest to be higher in excitation energy than the particle emission threshold. These states preferentially decay via particle emission and therefore measuring the γ -decay lifetimes of these states is

difficult. In these cases and in cases with unknown lifetimes, it is common to estimate the γ -ray partial width using the analogue bound states within the mirror nucleus. When using this technique a correction for the energy difference due to the Coulomb interaction is required.

2.5.1 Mirror Nuclei

Comparisons studies of mirror nuclei are important within nuclear astrophysics. Many properties within nuclei of astrophysical importance can be deduced through measurements made on the corresponding mirror nuclei. This is especially important for proton-rich nuclei of interest, which are difficult to measure due to experimental limitations. However, neutron-rich nuclei are more commonly accessible within experiment. Determining the properties of this mirror nuclei allows for the properties of the proton-rich nuclei to be inferred.

The charge-independent nature of the strong nuclear force leads to the isospin formalism. The neutron and proton can be treated as identical particles with isospin $T = 1/2$ and projections $T_z(n) = +1/2$ and $T_z(p) = -1/2$ respectively. For multi-nucleon systems, the individual projections of each nucleon combine to give a total isospin projection for the nucleus T_z , defined as:

$$T_z = \frac{N - Z}{2}, \quad (2.50)$$

where N is the number of neutrons and Z is the number of protons within the nucleus. The total isospin of the system, T_z , may take any integer value between $|N - Z|/2$ and $(N + Z)/2$. Isobaric nuclei with the same isospin T belong to a $2T + 1$ multiplet and with the same mass number, A , have near identical structures.

One of the best examples of these isobaric multiplet systems is a pair of “mirror” nuclei. These are nuclei with the same mass number, A , with the number of neutrons and protons interchanged. These systems would be perfectly identical without Coulomb effects and isospin-breaking nuclear effects. These lower the total binding energy of nuclear states in one member of the pair with respect to the other. The binding energy difference was first established by Wigner in 1957 [81] and is the result of the charge state difference through the isobaric multiplet and isospin quantum number.

This study resulted in the formation of the Isobaric Multiplet Mass Equation

(IMME):

$$\Delta BE(T, T_z) = a + bT_z + cT_z^2, \quad (2.51)$$

where, the coefficients a , b and c represent the isoscalar, isovector and isotensor Coulomb energies, respectively. However, this expression only represents the binding energy difference between ground states within the isobaric nuclei multiplet. It has been shown since this study that the IMME coefficients can also be used for the energy difference of the excited states of the isobaric multiplet nuclei [82]. Within these theoretical calculations, the Coulomb energy differences between excited states is a function of the state energy and angular momentum, after normalization of the ground states. For excited states within mirror nuclei this expression, known as the Mirror Energy Differences (MEDs), is given by:

$$MED_{J,T} = E_{J,T_z=-T}^* - E(Z < N)_{J,T_z=T}^* = -\Delta b_J, \quad (2.52)$$

where J is the total angular momentum of the excited state and Δb_J representing the change in coefficient b as a function of spin related to the ground state.

Within isospin triplets, the triplet energy displacement (TED) is given by:

$$TED_{J,T} = E_{J,T_z=-T}^* + E_{J,T_z=T}^* - 2E_{J,T_z=0}^* = 2\Delta c_J, \quad (2.53)$$

where Δc_J represents the change in coefficient c also as a function of the spin of the ground state.

2.6 Nuclear Shell Model

The nuclear shell model describes the nucleus with proton and neutrons arranged within well defined “shells”, comparable to the atomic shells of electrons around the nucleus. The quantised energy levels within the nucleus can be determined within this model by solving the three-dimensional time-independent Schrödinger Equation [83, 84].

$$E\Psi(r) = \left[-\frac{\hbar^2}{2m}\nabla^2 + V(r) \right] \Psi(r), \quad (2.54)$$

Where the wavefunction $\Psi(r)$ represents a particle moving through a mean field generated by the motion of the other nucleons. E is the energy eigenvalue, m is the mass

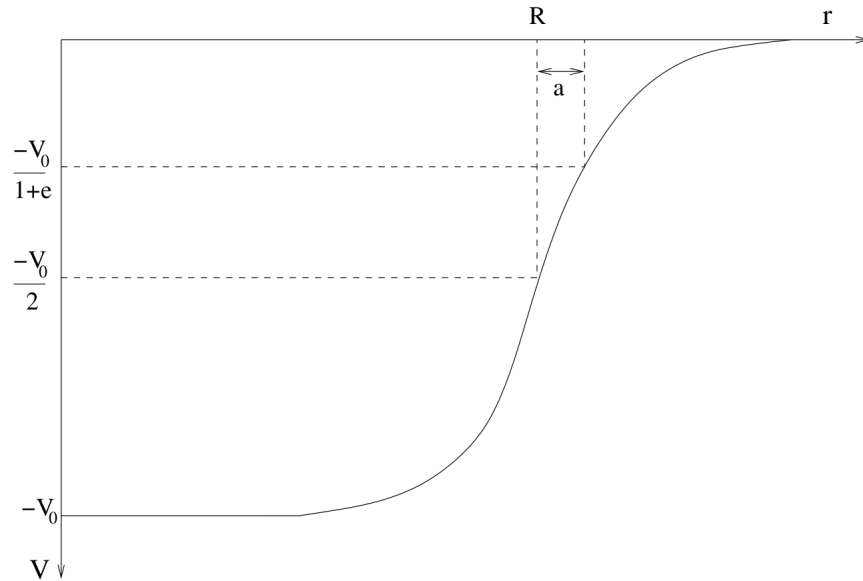


Figure 2.5: Schematic illustration of a Woods-Saxon potential. The relevant variable definitions are shown within the diagram.

of the nucleon and r is the distance of the nucleon from the centre of the potential. $V(r)$ is the key term within the Hamiltonian and can represent various potentials. The specific nature of the potential governs the nuclear interactions between the nucleons and therefore the resulting energy levels.

The simplest of these potentials, the Simple Harmonic Oscillator (S.H.O.), is relatively precise given the mathematical ease of the potential and that the asymptotic nature of this potential incorrectly increases with radius. Presently, the Woods-Saxon potential is commonly used [83, 85, 86], with the functional form of:

$$V(r) = \frac{-V_0}{1 + \exp[(r - R)/a]}, \quad (2.55)$$

where V_0 is the potential depth, a is the diffuseness of the nuclear surface and R is the mean nuclear radius of the form $R = r_0 A^{1/3}$ fm. This functional form is shown schematically in Figure 2.5. Typically V_0 is of the order 50 MeV and is matched to separation energies from experimental measurement, r_0 is generally of the order 1.25 fm and the diffuseness is of the order 0.65 fm. The solutions from this potential provides a major step towards experimental observations over the spherical harmonic oscillator potential, especially within the lowest shell closures [87].

The Woods-Saxon potential correctly predicts the observed magic numbers up to the $1f$ orbital, $A = 40$. In 1949, independent work by Mayer [88] and Haxel,

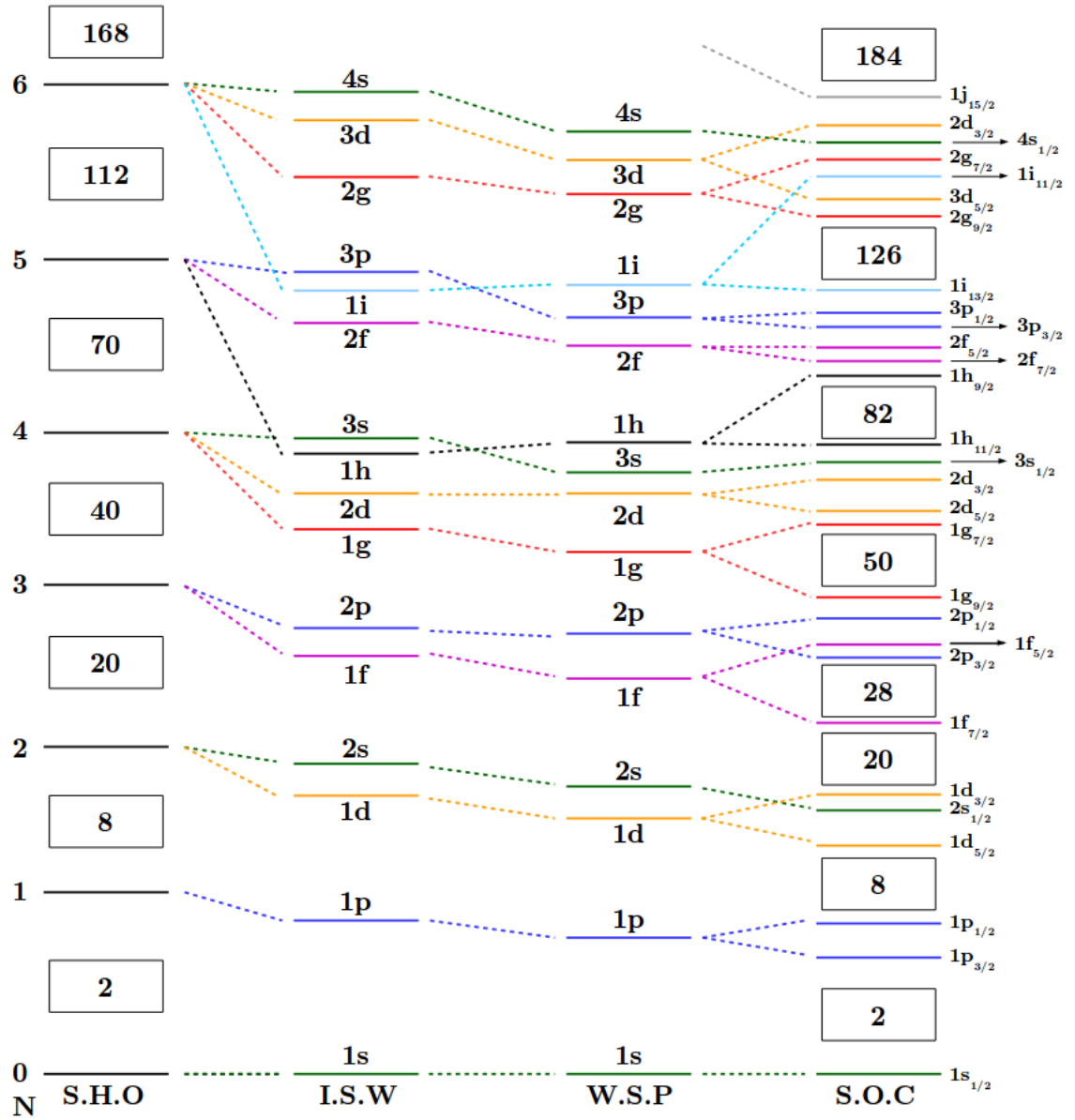


Figure 2.6: The calculated energy levels within the shell model from the Schrödinger Equation with various potentials. From left to right: Spherical Harmonic Oscillator (S.H.O.), Infinite Square Well (I.W.S.), Woods-Saxon Potential (W.S.P.) and the Woods-Saxon with Spin Orbit Coupling (S.O.C.). Magic numbers predicted by these potentials are shown within boxes. Figure adapted from [83]

Jensen and Suess [89] corrected this potential by introducing a separate spin-orbit coupling potential component. This spin-orbit term, $-V_{S.O.}(r) = \vec{l} \cdot \vec{s}$, accounts for the intrinsic spin (s) of an individual nucleon within the system relative to its orbital angular momentum (l). This also leads to a total angular momentum term, j , which is a combination of the orbital angular momentum magnitude, l , and the magnitude of the intrinsic spin, $s = \frac{1}{2}\hbar$. The intrinsic spin can either be in parallel to the orbital angular momentum, i.e. $j = l + \frac{1}{2}$ or anti-parallel, i.e. $j = l - \frac{1}{2}$, except when $l = 0$ where the only value of $j = \frac{1}{2}$. This leads to the change in the energy level splitting seen in Figure 2.6 between the Woods-Saxon potential alone and with the spin-orbit term. Converse to a similar phenomena observed in atomic physics, the parallel combination, $j = l + \frac{1}{2}$, produces lower energy eigenvalues than the anti-parallel pairing [90]. The difference between the energy split levels is proportional to $2l + 1$ [91].

2.7 Nucleon Transfer Reactions

Transfer reactions are those where one or more nucleons are transferred between the experimental target and beam nuclei. This family includes pick-up reactions, for example (p,d) and (d,t), and stripping reactions, such as (t,p) and (d,p). Unlike other reactions, such as fusion evaporation, there is no formation of a compound nucleus containing the nucleons of both the target and beam nuclei. They are direct reactions that occur at the peripheral of the target nuclei surface.

Of particular note to this work are single-nucleon transfer reactions, these reactions selectively populate shell-model states in the resultant nuclei. Therefore, they are well suited to studying single-particle states in nuclei [85, 92, 93]. These states can be theoretically interpreted within the shell model as the original core with a singular nucleon orbiting around it. The final nucleus from a reaction can then be described as the original nucleus plus an extra nucleon [94], for example within the (d,n) reaction, Equation 2.2 can be rewritten as:

$$X(d, n)Y = X(d, n)[X + p]. \quad (2.56)$$

The cross section for a reaction of this type is then the overlap of the incoming and outgoing wavefunctions, i.e. between X and $X + a$. Theoretical descriptions of the cross sections for a given state are given with the assumption that the final state

is a pure single particle state. Typically this pure description is not possible as the single particle strength is divided between a number of states within the final nucleus [95]. The ratio between the experimental and theoretical cross sections is defined as the spectroscopic factor [96]:

$$C^2S = \frac{\sigma_{\text{exp}}}{\sigma_{\text{the}}}, \quad (2.57)$$

where σ_{exp} is the experimentally measured cross section and σ_{the} is the theoretically calculated.

Cross sections within transfer reactions vary as a function of “theta” angle, known as the differential cross section or angular distribution. The wave nature of particles creates an interference pattern through the nuclear surface, producing maxima and minima. The specific pattern is like a fingerprint for the reaction, dependent on several factors including beam energy and polarisation, nuclear structure effects and the angular momentum transferred between the beam and target. By fitting the specific shape measured experimentally, the most likely l -transfer can be determined. Whilst the spin-orbit term is too small to infer from this method, if the original j is known then the most likely assignments can be found using the shell model.

2.8 Theoretical Analysis of Transfer Reactions

A number of methods to theoretically determine the cross section of a reaction exist. The simplest is the “Plane Wave Born Approximation (PWBA)”, which evolved into the “Distorted Wave Born Approximation (DWBA)” and then into the current most sophisticated model the “Adiabatic Distorted Wave Approximation”.

2.8.1 Plane Wave Born Approximation (PWBA)

Within this method, quantum mechanics is used to describe the motion of the incoming beam particle and outgoing ejectiles as one-dimensional planar wave. Using the mathematical form:

$$\psi(z) = Ae^{ikz}, \quad (2.58)$$

where ψ is a wave propagating in a direction, z , A is the amplitude of the wave and k is

the wave number. The target is treated as a spherically symmetric scattering potential, $V(r)$. If this potential is sufficiently weak then this can be treated as a perturbation problem.

The key component of this theory is the scattering amplitude between the entrance and exit channels. This is given by the transition matrix element or \mathcal{T} -matrix element, between the initial and final states [92, 97]. For a given reaction, $X(a, b)Y$, the entrance channel $X + a$ and exit channel $Y + b$ are denoted by α and β respectively. The transition element is given by:

$$\mathcal{T}_{\beta\alpha} \cong \langle \phi_\beta | V_\beta | \Psi_\alpha^+ \rangle, \quad (2.59)$$

where V_β is the scattering potential, ϕ_β is the final state wavefunction and Ψ_α^+ is the initial state wavefunction. The final differential cross section is proportional to the square modulus of the \mathcal{T} , i.e. $d\sigma/d\Omega \propto |\mathcal{T}_{\beta\alpha}|^2$. The PWBA model can successfully predict the shapes of angular distributions, but fails to reproduce experimentally derived cross sections. This is because reaction mechanisms such as inelastic scattering and absorption are not accounted for [85]. A full derivation of this approximation can be found in [98].

2.8.2 Distorted Wave Born Approximation (DWBA)

The ‘‘Distorted Wave Born Approximation’’ improves upon the PWBA model [99]. In this model, the incoming and outgoing waves are distorted waves, not planar. The spherical scattering potential within the PWBA is replaced with an optical potential, sometimes described as a ‘cloudy crystal ball potential’ [100]. This potential consists of a real and imaginary part and can account for elastic scatter, inelastic scatter or absorption. The real part of the potential, $V(r)$, is of a Woods-Saxon form and governs the scattering of incident waves. The imaginary part, $U(r)$, governs the absorption of incoming waves into any non-elastic channels. The potential also has a spin-orbit term, V_{SO} , and a Coulomb term, V_C . All of these terms represent a more physically realistic potential. Typically for single-nucleon transfer reactions the derivative of the Woods-Saxon potential, represents a surface reaction peaking near to the nuclear surface. All of the parameters within this potential are constrained with elastic scattering data from similar mass and energy regimes to the reaction of interest.

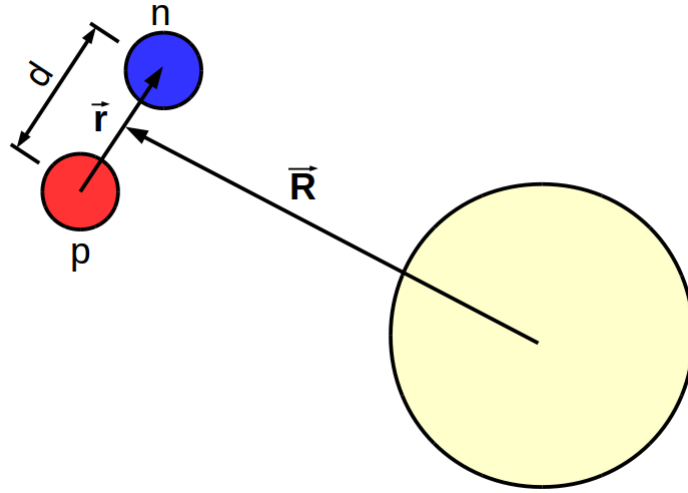


Figure 2.7: Schematic illustration of the three-body model of a reaction between a deuteron, d , and another nucleus, X . The vector \vec{R} representing the deuteron-nucleus distance and the vector \vec{r} is the distance between the nucleons within the deuteron.

The \mathcal{T} -element within the DWBA model [92], for a $X(d,p)Y$ reaction is given by:

$$\mathcal{T}_{\beta\alpha} = \langle \psi_p^- \phi_{n,nlj} | V_{np} | \psi_d^+ \rangle, \quad (2.60)$$

where the (+) and (−) superscripts represent the ingoing and outgoing wave boundary conditions. ψ_p^- represents the outgoing proton distorted wave and ψ_d^+ is the incoming deuteron distorted wave. The other term in the equation, $\phi_{n,nlj}$ [101], represents a “form factor” describing the transferred neutrons wavefunction.

Within this model the deuteron distorted wave function, determined by fitting to elastic scattering data, is given by:

$$\psi_d^+ = \phi_0(\vec{r})\chi_0(\vec{R}), \quad (2.61)$$

where $\phi_0(\vec{r})$ is the deuteron wavefunction and $\chi_0(\vec{R})$ describes the elastic deuteron scattering. In this form the vectors \vec{r} and \vec{R} are the relative coordinates of the neutron and proton and the distance between the deuteron and the target respectively. Whilst this model has invaluable in analysing direct reactions, spectroscopic factors and C^2S factors can still vary by up to a factor of 5 for (d,p) reactions [102].

2.8.3 Adiabatic Distorted Wave Approximation (ADWA)

Not accounted for within the DWBA model is the breakup effects of the deuteron, with a binding energy of 2.2 MeV [103]. It is a reasonable assumption that the breakup of the deuteron would have a significant contribution to the cross section. This breakup channel is a 3-body problem, not accounted for within the DWBA model. These effects are taken into account within the ADWA model developed by Johnson and Soper and represent a significant improvement for (d,p) reaction calculations [104].

The three-body nature of this interaction is simplified within the ADWA model as two two-body reactions. Achieved by considering the internal motion of the deuteron, i.e. the relative motion between neutron and proton, to be significantly slower than the relative centre of mass motion between deuteron and target. The proton and neutron are treated as “frozen” relative to each other. It is then possible to treat the effective interaction, $V_l(p, n)$ between the d system and the target, as two separate interactions, namely neutron-target and proton-target. These interactions, V_{pX} and V_{nX} respectively, are optical potentials fit to elastic scattering data at half the deuteron energy.

With the inclusion of two key assumptions the \mathcal{T} -matrix elements are evaluated similarly to the DWBA model. The first of such assumptions is that the matrix elements are only evaluated when the vector, \vec{R} , is within the range of proton-neutron interaction potential. Applying the “zero-range approximation”, i.e. $\vec{R} = 0$, results in only $\psi^+(p, n)$ components in which the proton and neutron are in a relative S-state contributing to the stripping matrix [105]. Finite-range effects are then re-corrected for by multiplying the final matrix element by a constant factor [106]. The second assumption is that if the spin-dependent terms within $V_l(p, n)$ are symmetric in the neutron and proton spin coordinates, and taking into account the symmetric initial state of the deuteron ($l = 0, s = 1$), then only triplet states, or $s = 1$, can contribute to $\psi^+(p, n)$. It is worth noting that aside from these two assumptions, the key difference between the DWBA and ADWA models is the interpretation in that the ADWA contains outgoing waves interpreted as breakup channel. Aside from this the numerical procedure between the two differs very little.

Chapter 3

Investigation of the $^{25}\text{Mg}(d,p)^{26}\text{Mg}$ Reaction

In this experiment, excited states within ^{26}Mg were populated via one-neutron transfer. A $197\ \mu\text{gcm}^{-2}$ thick deuterated polyethylene $(\text{CD}_2)_n$ target was bombarded with a $10\ \text{MeV}/A$ stable beam of ^{25}Mg , accelerated by the K-150 cyclotron at the Cyclotron Institute, Texas A&M University. The beam intensity impinging onto the target was up to 9.3×10^7 particles per second. The high efficiency silicon detector array, TIARA, was used to detect light ejectiles, particularly at intermediate and backwards angles, see Figure 3.1. This allowed the measurement of both energy and angle for emitted protons from the (d,p) reaction mechanism, from which the excitation energies and angular distributions were calculated, assuming two-body kinematics. Deuteron ejectiles elastically scattered at angles forwards of 90° were measured for cross section normalization measurements. The kinematics for the reactions of interest and the respective coverage of TIARA are shown in Figure 3.1.

Four segmented High Purity Germanium (HPGe) clover detectors from the HYPERION array surrounded the target to detect the gamma rays resulting from the de-excitation of populated states within the heavy residual nucleus. Beam-like reaction products were then separated using a combination of the MDM-2 magnetic spectrometer and Oxford focal-plane detector. Particle identification was achieved using a combination of energy loss and residual energy measurements. All three detection systems were combined to form triple coincidences on an event by event basis. A schematic diagram of the experimental setup at the Cyclotron Institute is shown in

Figure 3.2. The aim of this study was to determine spin-parities of resonant states within the $^{22}\text{Ne} + \alpha$ system, between the α -emission and n -emission thresholds within ^{26}Mg . These states would have significant γ -decay widths and would be important for the $^{22}\text{Ne}(\alpha, \gamma)^{26}\text{Mg}$ weak s -process poisoning reaction.

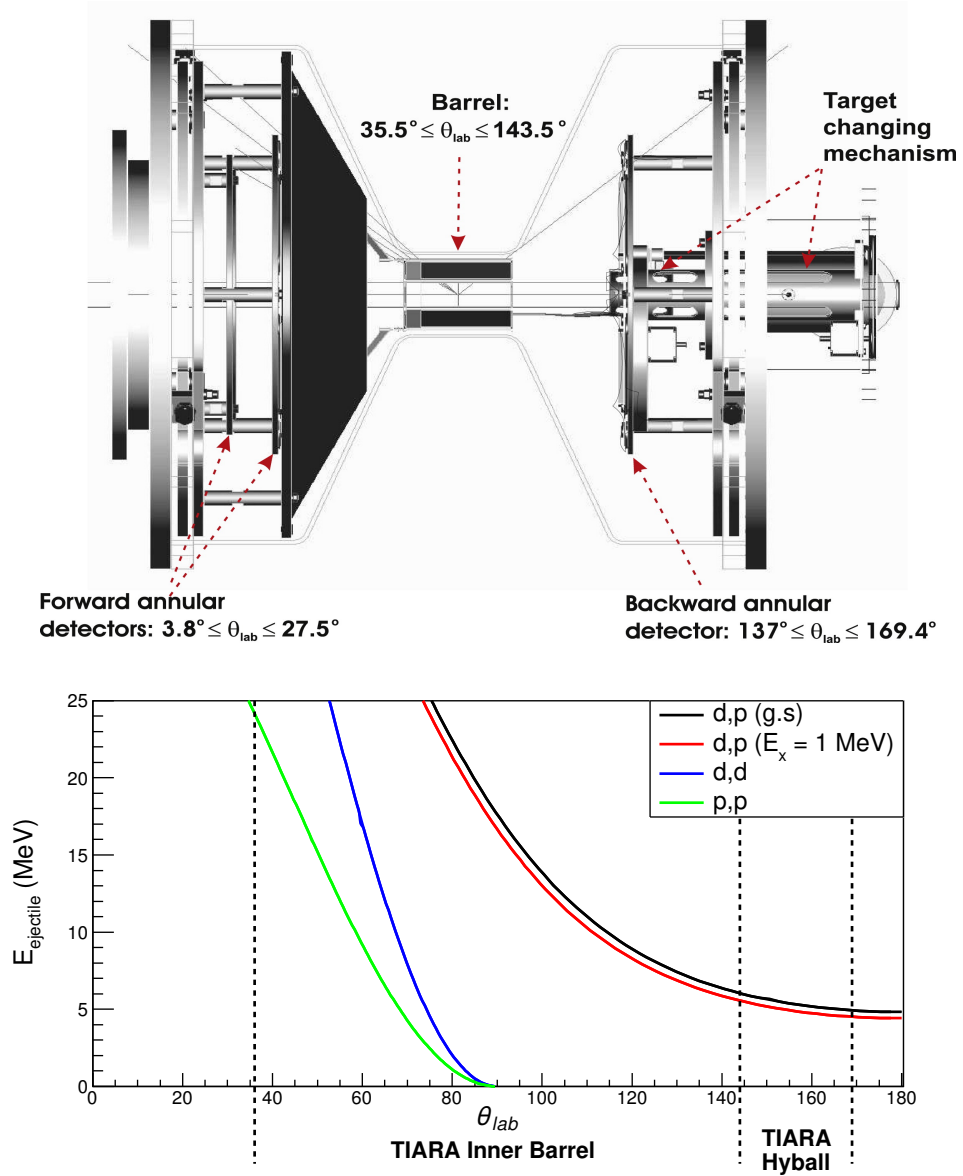


Figure 3.1: Upper: A schematic indication of the angular coverage of each individual component within the TIARA set-up. In the case of this work the forward annular detectors and target changing mechanisms was not in use [107]. Lower: Two-body kinematics calculations for light particles from the reactions of interest.

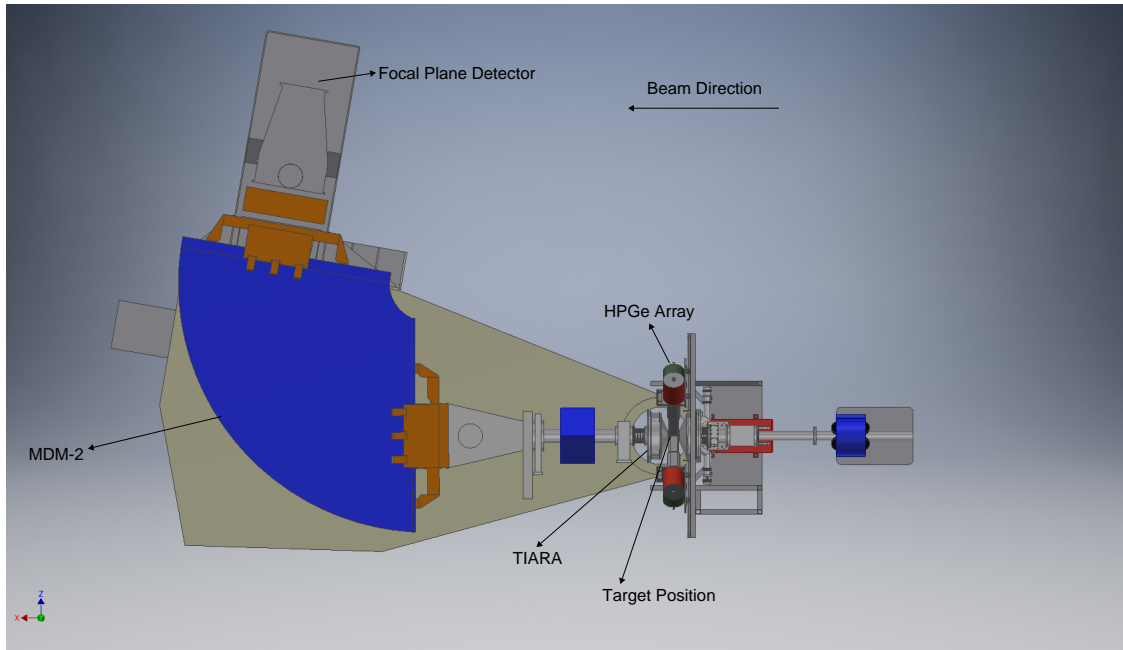


Figure 3.2: A schematic diagram of the detector set up. The Barrel and Hyball detectors constitute the TIARA silicon array. The ^{25}Mg beam passed through the centre of the Hyball array and impinged upon the CD_2 target, which was surrounded by the Barrel.

3.1 Previous Research

The study of this reaction can be traced back to research undertaken in the 1940's where E. Pollard and R. Humphreys reported the observation of three definitive groups of protons relating to the ground, first and second excited states within ^{26}Mg [108]. Excitation energies of 1.85 and 3.00 MeV were determined for the first and second excited states. A study by H. Allan and C. Wilkinson used a range of deuteron bombarding energies in an unsuccessful attempt to determine the Q -value of the ground state reaction [109, 110]. Work by J. Ambrosen in 1952 using 1.9 MeV deuterons extended this type of study to include three more excited states at 4.0, 4.41 and 4.91 MeV excitation energy [111].

A study by Endt *et al.* was the first to magnetically analyse the protons from this reaction with a 1.8 MeV deuteron beam. As a result observed excitations were extended up to 6.147 MeV, with a total of 5 new levels being observed for the first time [112]. Up to this point in history only the Q -value and excitation energies of this reaction was measurable. Then a study by Holt *et al.*, using a rotatable proportional counter set-up and 8 MeV deuterons, determined the first angular distribution measured of

this reaction and found significant $l = 0$ and $l = 2$ components for the first excited state and strong $l = 0$ components for 4 further excited states. Two more states with excitation above 7 MeV were also observed [113]. However, the intensity of the ground state was too small for them to create angular distributions and they quote absolute errors of $\pm 50\%$ of their measurements.

During the 1960's a number of $^{25}\text{Mg}(d,p)^{26}\text{Mg}$ reaction studies were performed over a range incident deuteron energies with the aim of determining angular cross sections and l -transfer determination. These are briefly reviewed in increasing deuteron energy, from 1.5 to 15 MeV, beginning with a study by Takano *et al.* which determined absolute angular distributions for the first and second excited states using 1.5-3.0 MeV deuterons, including at $\theta_{lab} = 0$ degrees [114]. Weinberg *et al.* impinged deuterons with energies between 3.0 and 5.2 MeV to create absolute angular distributions down to $\theta_{lab} = 15$ degrees, observing a number of $l = 0$ and $l = 2$ transfers [115]. Lutz *et al.* determined absolute angular cross sections for the ground state and the first three key excited states using a deuteron energy of 8 MeV [116]. Hinds *et al.* performed a high-resolution study using a 10 MeV deuteron beam. This populated excitations up to 7 MeV of energy in the ^{26}Mg system, then created relative angular distributions normalized on the absolute measurement of the 3.945 MeV state from the Holt *et al.* study [113, 117]. The final study in this quick review was the study by Cujec *et al.* which measured this absolute reaction cross section at four discrete angles between 10 and 40 degrees [118].

Two further studies were published in 1984 by Burlein *et al.* and Arciszewski *et al.* with deuteron energies of 12 and 13 MeV respectively. These both presented absolute angular distribution measurements of excited states up to 6.3 MeV and 8 MeV respectively. These distributions were compared to similar DWBA calculations allowing for l -transfer values and spectroscopic strengths to be determined.

The final relevant study is the recently published work by Hamill *et al.*, where the $^{25}\text{Mg}(d,p)^{26}\text{Mg}$ reaction was investigated with a deuteron energy of 8 MeV. This study focused specifically on the excited states relevant to the $^{25}\text{Al}(p,\gamma)^{26}\text{Si}$ mirror astrophysical reaction. Therefore, only excited states between 5.5 MeV and 6.5 MeV in the ^{26}Mg system were investigated in that work [119].

3.2 Beam Production & Acceleration

In the present work, the beam nuclei were produced by baking a magnesium compound within an oven. The heat of the oven vaporises the compound creating a gaseous form of Magnesium which passes into an ECRIS (Electron Cyclotron Resonance Ion Source). Within this ion source the atoms were ionised and accelerated using the electron cyclotron resonance phenomenon. This is where an electron situated within a uniform and static magnetic field will produce a Lorentz force such that electrons traverse through the source in a circular motion. The magnetic field B produces a centripetal force such that:

$$\frac{mv^2}{r} = Bqv, \quad (3.1)$$

where m is the electron mass, v is the velocity of the electrons in the source, q is the electron charge and r is circular radius. The angular frequency of this motion is defined as:

$$\omega = 2\pi f = \frac{v}{r} = \frac{eB}{m}. \quad (3.2)$$

As part of a planned Radioactive Ion Beam (RIB) upgrade, Texas A&M University have recently recommissioned their 88" K150 cyclotron. This cyclotron has a main-coil current of 2800 A and a bending factor of $K=140$. Isotopes are fed into the cyclotron and accelerated up to an energy of 55 MeV per nucleon. In the present work the beam nuclei were accelerated to a beam energy of 250 MeV or 10 MeV per nucleon. The nuclei traversed a 90° analysing magnet for isotopic selection before being directed into the experimental set-up. A layout of the laboratory is shown in Figure 3.3.

3.3 Detection Systems

3.3.1 The TIARA Array

The Transfer and Inelastic All-angle Reaction Array (TIARA) is a high efficiency, quasi- 4π silicon array designed specifically for transfer reactions with Radioactive Isotope Beams (RIBs). It has a compact geometry that allows for both high efficiency charged particle detection but also closely arranged High Purity Germanium (HPGe) detectors

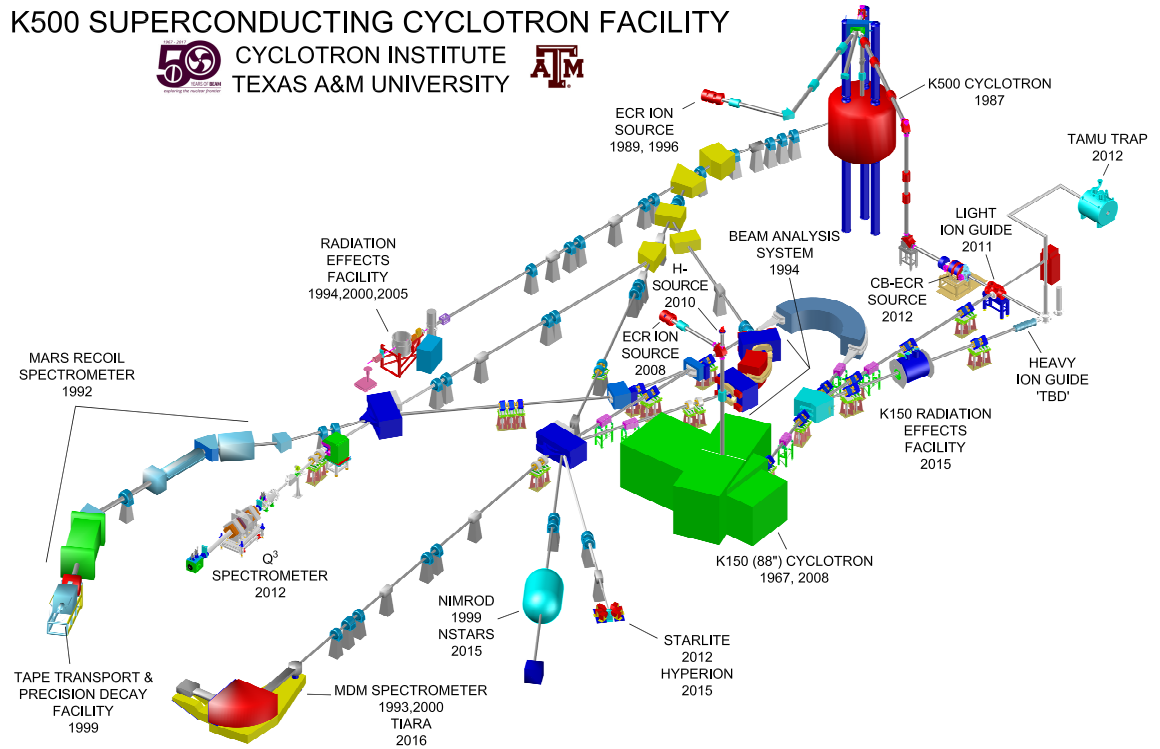


Figure 3.3: A 3D schematical layout of the experimental equipment and facilities available at the Cyclotron Institute. Shown the with the beam line pathways from the two cyclotrons to various experimental setups. TIARA was located in front of the MDM section.

for γ -ray detection. Due to the low intensity nature of these RIBs a high efficiency detector is required for good statistics collection. Silicon detectors are ideal for this as their intrinsic efficiency is almost 100% and so to create a high efficiency detectors a large solid angle coverage is required.

Transfer reaction experiments rely on constructing the angular distributions of proton ejectiles, to determine the spin and parity of populated states. This requires a large angular θ range to accurately map the l -transfer of the reaction. TIARA meets both of these requirements, with a coverage of close to 76% of 4π and an laboratory angular coverage in θ from 36° to 169° . The current configuration of TIARA consists of two silicon detector types the “Barrel” and the “Hyball”. Both of which are created by p^+ implantation on n-type silicon. Further information on Silicon detectors can be found in Section A.1.2.

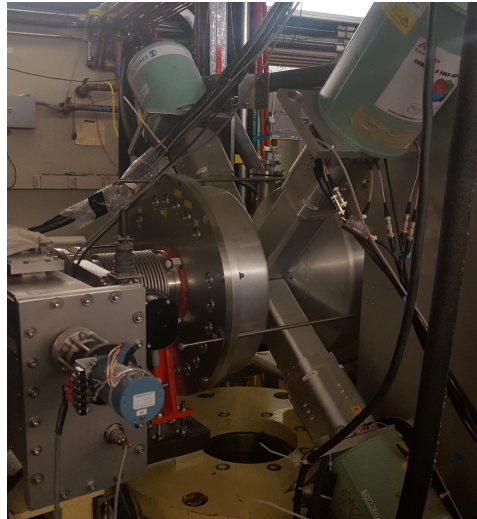


Figure 3.4: The TIARA set-up located at the Cyclotron Institute, Texas A&M. Shown here facing upstream.



(a) Barrel



(b) Hyball

Figure 3.5: (a) The octagonal Barrel of silicon detectors of TIARA. The experimental target is placed on an extended arm such that it is within the centre of this Barrel. (b) Hyball annular array with the 16 front facing annular rings visible. Taken from [107].

3.3.1.1 The Barrel

The Barrel consists of two parts, an inner resistive charge division Barrel and an outer non-resistive Barrel, as shown in Figure 3.5a. The Inner Barrel consists of 8 rectangular PSSSDs orientated in a concentric octagonal Barrel configuration centred around the target position and beam axis. This octagonal Barrel has a cross-section of 27.6 mm side length and 33.3 mm inner radius. Each PSSSD is divided further into 4 rectangular strips, position sensitive along the beam axis. These detectors are based on 6-inch wafer technology with an active area of 94.6 mm long and 22.5 mm wide. The detectors are 400 μm thick. Each strip has a pitch of 5.65 mm with an inter-strip gap of 100 μm . The Barrel has an angular coverage of 36° to 144° and each individual strip provides an azimuthal coverage of 9.5° . For 5.5 MeV α -particles a position resolution of 1.0 mm and an energy resolution of 140 keV at FWHM is nominal. Each strip has a resistance of 4 k Ω s and is connected to 2 offset connectors of 1 k Ω s each, one at each end. The Barrel has a shaping time of 1 μs and as such will be subjected to the non-linear dependence effects on the energy sum, or Ballistic Deficit, as discussed in Section A.1.2.3.

The Outer Barrel configuration is also of 8 rectangular silicon detectors in an octagonal layout. In the same manner as the Inner Barrel the Outer Barrel is segmented into 4 strips. However, the Outer Barrel pieces is not comprised of PSSSDs and is not resistive or position sensitive. The Outer Barrel detectors are 20% wider than the Inner Barrel detectors. They have an inner radius of 40 mm and a thickness of 700 μm . The Outer Barrel provides energy information about particles that penetrate or punch-through the Inner Barrel. Position information is not required from these detectors as this is obtained from the Inner Barrel.

3.3.1.2 The Hyball

The Hyball is a collection of 6 wedge shaped DSSSD detectors, as shown in Figure 3.5b. These are placed in an annular configuration positioned 150 mm upstream of the target position. The inner radii of this array is 28.11 mm and outer radii of 140 mm, altogether providing an angular coverage from the end of the Barrel up to 169° , there is however a small angular overlap between edge of the outer Hyball and Inner Barrel. Each wedge provides an azimuthal coverage of 55° , with a 5° gap in-between each wedge. These wedge are segmented into 16 target facing annular rings and 8

azimuthal back sectors. Each ring has an pitch of 5.3 mm and an individual angular range of 2° . The DSSSDs are $400\ \mu\text{m}$ thick with a nominal energy resolution of 50 keV FWHM, for 5.5 MeV α -particles.

3.3.2 The Oxford MDM-2 Magnetic Spectrometer

The Multipole-Dipole-Multipole spectrometer was coupled downstream to TIARA for particle identification. Measuring of energy loss, residual energy and particle position along the dispersive x-direction. The magnetic elements of this spectrometer have the following configuration: entrance sextupole and multipole, gradient field dipole and exit multipole [120]. The maximum entrance solid angle acceptance is 8 msr with a maximum mass-energy product through the 1.6 m radius dipole of 315 MeV amu. The spectrometer can accept a ratio of energies (E_{max}/E_{min}) of 1.31. It has a maximum measured energy resolution of $E/\Delta E$ of 3000.

The entire spectrometer can be rotated about the target position by 200° , from 150° to -50° . The dipole angle of deflection is 100° .

3.3.2.1 Ionisation Chamber

The Ionisation Chamber of the MDM-2 Spectrometer was used to measure the dispersion of reaction like particles along the x-direction and the energy loss by these particles through a volume of gas [121, 122]. From the Bethe-Bloch formula, the energy loss of charged particles is related to the atomic number of the particle squared and their mass. This energy loss information was used to identify different isotopes. For this experiment isobutane at a pressure of 29.5 Torr was used within the chamber. A mylar sheet $25\ \mu\text{m}$ thick forms the entrance window to the chamber and a $50\ \mu\text{m}$ thick mylar window forms the exit window.

There are several components within the Ionisation Chamber, these are: 4 resistive proportional counting wires, a cathode, 2 anode plates, a Frisch grid and a MICROMEAS plate. The resistive wires provide the number of particles passing through the ionisation chamber along with their x-position. The wires provide two signals, one from each end. By comparing the amplitudes of these signals the event position along the wire can be calculated. The reaction products pass through the Ionisation Chamber between the cathode and the Frisch grid with electron liberated from

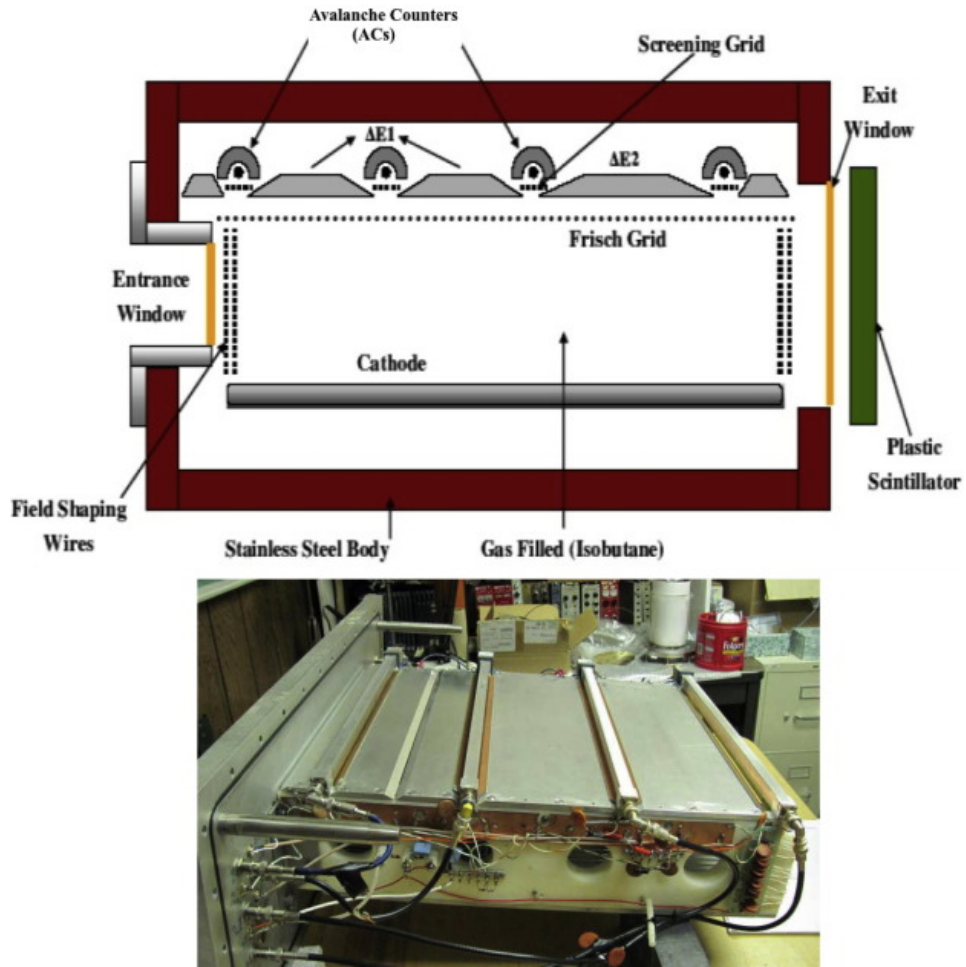


Figure 3.6: (Top) Schematic drawing of the Oxford Focal Plane detection system, the MICROMEAS were at the $\Delta E2$ position. (Bottom) Photo showing the Oxford detector across the same plane as the schematic above. Taken from [123].

the gas drifting toward one of the anode plate or the MICROMEAS plate [124]. The amplitude of these collected anode signals is directly proportional to the energy loss of the particle passing beneath them. The MICROMEAS (MICRO-MESH-Gaseous Structure) detectors act like two-stage parallel-plate avalanche chambers with two main regions. The first a 50-300 μm “amplification” region and a second “drift” region, with a size on the order of centimetres [125]. These two regions are separated by a thin electroformed micromesh. This plate is segmented into 4 rows in z and 7 columns in x , creating 28 separate MICROMEAS signals. The MICROMEAS not only allow for a more resolved energy loss measurement (factor 2-3 improvement over anode plates) of particles within the ionisation chamber but also a coarse positional measurement in both x and z .

3.3.2.2 Plastic Scintillator

Scintillation detectors convert the kinetic energy of an incident particle into detectable light. This can be collected, amplified and measured to provide a signal relative to the energy deposited within the detection material. These materials become excited as incident ionising radiation interact with the material and as it subsequently de-excites re-emits the energy as scintillation light. The best materials for this detector type have a high efficiency of this conversion over short time scales. In practise, it is a balance between light output, response times and radiation hardness [126].

The reaction products that pass through the ionisation chamber were stopped within a NE102A plastic scintillator, placed 42 mm downstream of the exit window [127]. This plastic scintillator is coupled with 2 photomultiplier tubes (PMT), 1 at either, which combined provide a residual energy reading for a $E-\Delta E$ correlation. Plastic scintillators have a quick response time but become radiation damaged over time, affecting the light output characteristics of the plastic.

3.3.3 Germanium Array

In this experiment, 4 high efficiency, segmented HPGe clovers from the HYPERION array was implemented around the TIARA target position [128]. Within each cryostat are four coaxial n-type germanium crystals within a four-leaf clover configuration. The faces of these crystals are 50 mm by 50 mm and the crystals have a depth of 80 mm. The front face of each clover is approximately 50 mm radially from the target position. The four clovers are arranged at 90° with respect to the beam axis, with approximate azimuthal angles of 45° , 135° , 225° and 315° . Each clover has 3 electronic segments on the outer contact signals aligned with the beam axis. The central segment is approximately aligned at 90° with the other segments either side, one upstream and one downstream [128]. This electronic segmentation allows for a coarse angular measurement to be made in order to Doppler correct the energy measurement from the inner contacts of the crystals [129]. The set-up of these clovers with respect to the TIARA array is shown in Figure 3.4

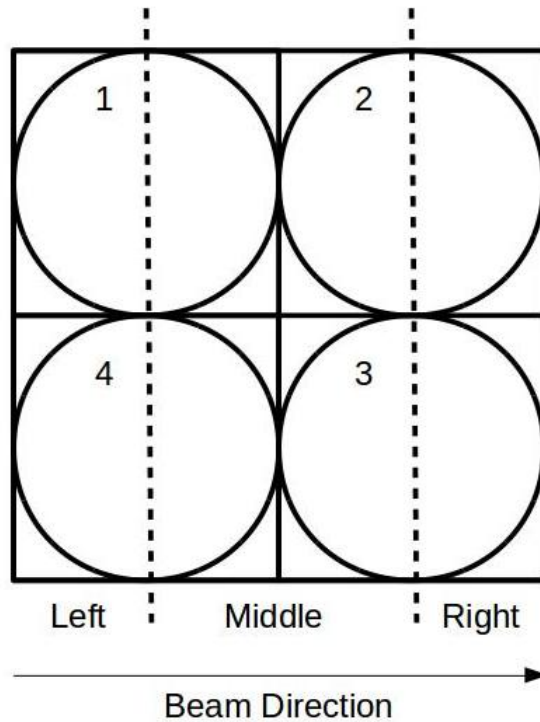


Figure 3.7: A schematic of the electronic and crystal segmentation of the HPGe clovers used. Here crystals are denoted by solid circles and labelled numerically, whilst, electronic segmentation is denoted by dashed lines and labelled positionally respective the beam axis and target position.

3.3.3.1 Add-back Scheme

The add-back scheme employed ensured that γ -ray events were only summed together if registered within the same HPGe clover. Scattering events from a neighbouring clover were not be reconstructed in this add-back scheme. The energy of the γ -ray events and angle of emission from the original radiative event was needed to employ this scheme, the core contacts were used for their better resolution and the segment contact for the highest energy event was used to determine the emission angle. Discussed further in Section A.2.3.

3.3.3.2 Doppler Effects

It is impossible to perfectly correct for Doppler shift due to the continuous nature of the correction with emission angle compared to the discretized nature of detectors measuring this angle. In this study, θ was defined using the mean of the angular range

covered by the segmentations of the HPGe clover. This mean value usage creates the observed Doppler broadening effect introducing with small errors in the correction based on the standard deviation of the emission angle of events around the assumed angle. In general, higher levels of segmentation increases the degree of accuracy within the Doppler correction.

3.3.4 Signal Processing & Data Acquisition System

The signals from the TIARA detectors were passed to GANIL custom made charge sensitive preamplifiers. These preamplifiers were mounted in close proximity to the chamber to minimise the capacitance and induced noise of the connecting cables. The HPGe clovers have in-built preamplifiers within their vacuum vessels. Post pre-amplification the TIARA and HPGe signals are passed to CAEN N568B spectroscopy amplifiers, where the pulse was shaped. These amplifiers produce a fast and a shaped slow signal. The fast signal of these amplifiers were passed to CAEN V895 constant fraction discriminators to generate the trigger. For this experiment the TIARA triggers were taken from the Hyball sector signals or the Inner Barrel. Signals from the MDM-2 Focal Plane Detector components were passed to charge sensitive preamplifiers then to programmable Mesytec MSCF-16 shaping amplifiers with in-built constant fraction discriminators, where the pulse is shaped and triggers created. These are controlled using a locally developed software package.

The OR signal of all the fast outputs were collected within a 4x4 Fan In Fan Out (FIFO) NIM module. Another FIFO collected a combination of the triggers to create a single master trigger signal. This master signal was passed to a gate generator, where it was stretched to 12 μ s length, before being passed to a Silena Acquisition Control (SAC) module. For this experiment, only the TIARA OR signals formed the master trigger. All of the OR signals were passed in various combinations directly to a gate generator and stretched, then passed to a CAEN V820 scalar module via a NIM-ECL translator. This allowed the rates of the various detectors to be monitored throughout the experiment. Several Time-Amplitude-Converters (TACs) were implemented in this experiment. The following start/stop trigger combinations were used: Silicon OR/beam-left PMT OR, Silicon OR/HPGe OR, Silicon OR/MICROME GAS OR.

The shaped outputs from the amplifiers were passed to CAEN V875 Analogue

to Digital Converters (ADCs), which digitised the pulse amplitude to an electronics channel number to be passed into the DAQ. All of the CAEN VME modules (the V895 CFDs and V785 ADCs) were controlled using a CAEN V288 VME controller module [107]. Their thresholds remotely set, as close to the noise as possible, using the software package MIDAS (Daresbury) [130]. MIDAS was used as the controlling mechanism for the DAQ, providing controls for all of the electronics described above through the various controllers. It was also used to provide some rudimentary online data analysis, providing online data on a channel-by-channel basis for all of the detection systems and of note providing data on the TACs set up throughout the experiment. Offline analysis was completed using the NPTOOL software package with a specific project set-up for this experimental campaign set-up [131].

3.4 Detector Calibrations

Presented within this section is the work completed to calibrate the detectors within TIARA. It should be noted that the Outer Barrel detectors were not used within this experimental campaign. As such, the terms Inner Barrel and Barrel will be used interchangeably for simplicity. Detector threshold issues ultimately prevented the Barrel from being used to extend the angular range of the (d, p) transfer reaction but the Barrel was critical for measuring the elastic scattering (intensity calibration) data.

3.4.1 Pulser Calibrations

Inherent non-linearities and offsets have previously been seen within electronic data acquisition systems, these occur within the pre-amplifiers and ADCs of the system. Small changes because of these features can still noticeably effect the energy output of the detectors within TIARA. To correct for these effects, a pulser calibration was completed. A pulser signal was fed into pre-fabricated “test” inputs on the pre-amplifiers to simulate a signal within each ring and sector of TIARA. A stepping voltage script was created for a remotely controlled pulse generator, creating pulses that covered the dynamic range of the ADCs used within this set-up. The amplification and digitisation of these voltage stepping pulses were used to create a “matchstick” spectrum for each channel. An example of this is shown within Figure 3.8.

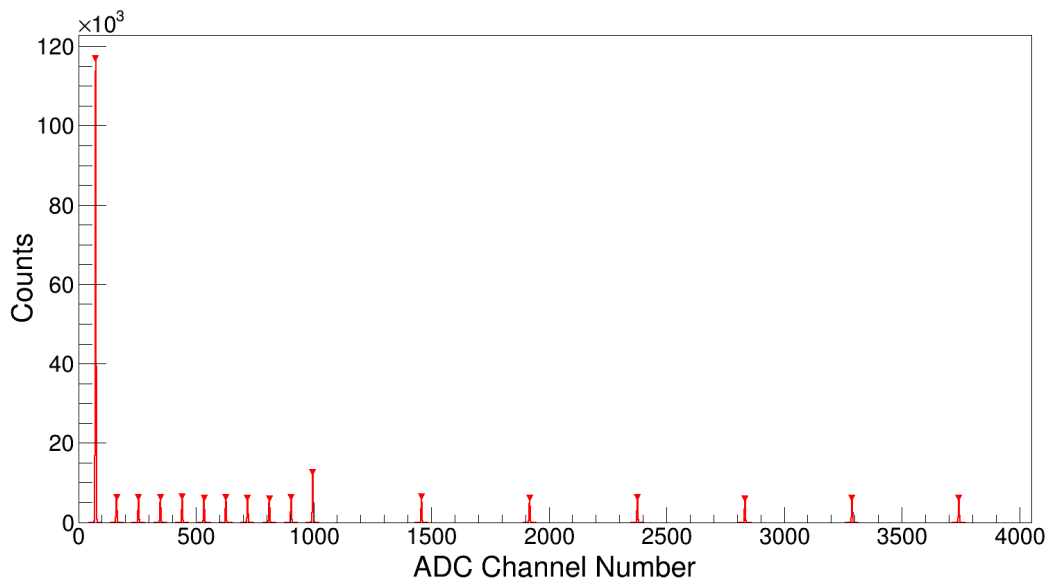


Figure 3.8: “Matchstick” spectrum for one of the Hyball rings. Each peak represents a different output voltage from the pulser. The first peak is from the electronic noise of the detector, whilst, the slightly larger peak in the first quarter of the spectrum is a marker voltage.

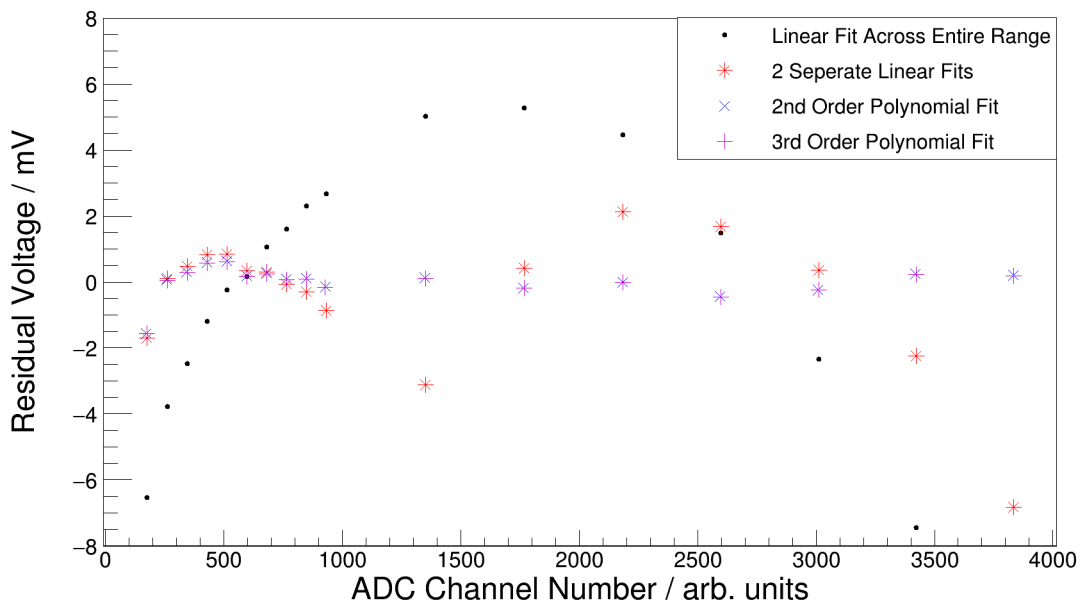


Figure 3.9: The pulser residual voltages calculated using the various functional form fitted. Residual voltage calculated as the difference between the output pulser voltage and the converted channel number through the functional form.

The response of the electronics chain was then determined by plotting the fitted

centroids of these peaks against the known input pulser amplitude voltages. The best functional form of this response was determined by a minimisation of the “residual voltage difference”, defined as the difference between the known input voltage from the pulse generator and the calculated voltage from this functional form, see Figure 3.9. It was determined that a second order polynomial functional form produced suitable corrections for the non-linearities and offsets within the electronic chain.

3.4.2 Charged Particle Energy Loss Corrections

The excitation energy of states within the recoil nucleus were calculated from the measured proton angle and energy, detected within the TIARA array. The energy required correcting for the energy losses within the CD_2 target and dead layer of the silicon detectors. These corrections were calculated using proton energy loss tables from SRIM. The analysis of elastically scattered deuterons was completed using deuteron SRIM energy loss tables.

The scale of the dead layer correction was determined using a triple-alpha source calibration, assuming negligible energy loss within the thin layer of material of the source. The matchstick calibration created an extra degree of freedom by mapping the charge measured within the detectors through the functional form determined by the matchsticks. The energy calibration functional form between this mapped charge and the emitted energy of the particle should be a linear first order polynomial with a zero value offset. Any non-zero offset co-efficient is assumed to be the result of an improper treatment of the dead layer energy loss correction. By varying the dead layer thickness, minimizing around this offset co-efficient, thicknesses of $0.3 \mu\text{m}$ and $0.61 \mu\text{m}$ were found for the Barrel and Hyball respectively. A nominal value of $1.95 \mu\text{m}$ was used for the target thickness from the manufacturers quoted thickness.

3.4.3 Hyball Calibration

The Hyball detector is calibrated on an individual ring-by-ring and sector-by-sector basis with a triple- α source, as described in Table 3.1, mounted at the target position of the chamber. The four most outer rings of each Hyball wedge was not illuminated by this source because of a significant angular overlap between the Barrel edges and outermost rings of the Hyball. As discussed in Section 3.3.4, the Hyball sector signals

define the master trigger. This meant that only pixels within the Hyball with good sector signals provide useful data for calibration.

Nuclide	E_α (MeV)
^{239}Pu	5.157
^{241}Am	5.486
^{244}Cm	5.805

Table 3.1: Nuclides contained within the triple- α source used to calibrate the TIARA detection systems. Shown with their dominant α -decay branch energies.

The raw data for each pixel was first linearised using the pulser calibration, as described in Section 3.4.1. The centroids of the triple- α peaks within this data were then fit against the known α particle energies using a first order polynomial, providing energy calibration coefficients. The result of this process is shown in Figure 3.10.

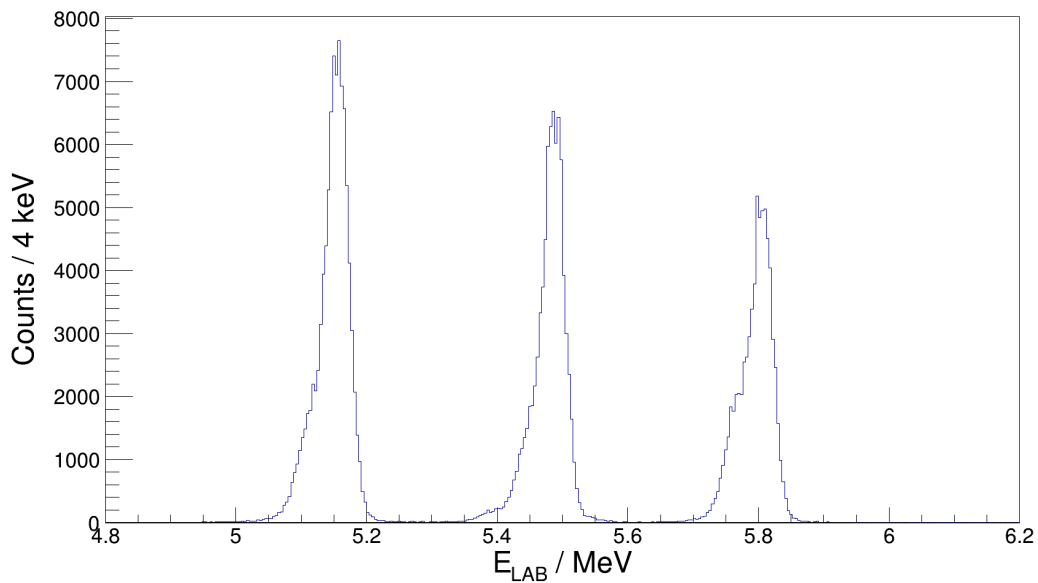


Figure 3.10: A combined calibrated energy spectrum for the Hyball detector, including dead layer corrections. The three alpha peaks of the combined Pu, Am and Cu source. The smaller branches of each isotopes decay are not resolved within many of the Hyball channels.

3.4.4 Barrel Calibration

The Barrel is a more complex silicon detector than the Hyball. Whilst the latter is a DSSSD type detector and can be calibrated in the simple manner discussed previously, the former is comprised of resistive strips meaning that the signal from an individual event is split into two and read from both ends of the strip. For the purposes of this study these signals will be denoted in relation to the target position, with one signal being the upstream (or “ U ”) end signal and the other being the downstream (or “ D ”). The elemental investigative tool is a simple plot of U against D such as that in Figure 3.11.

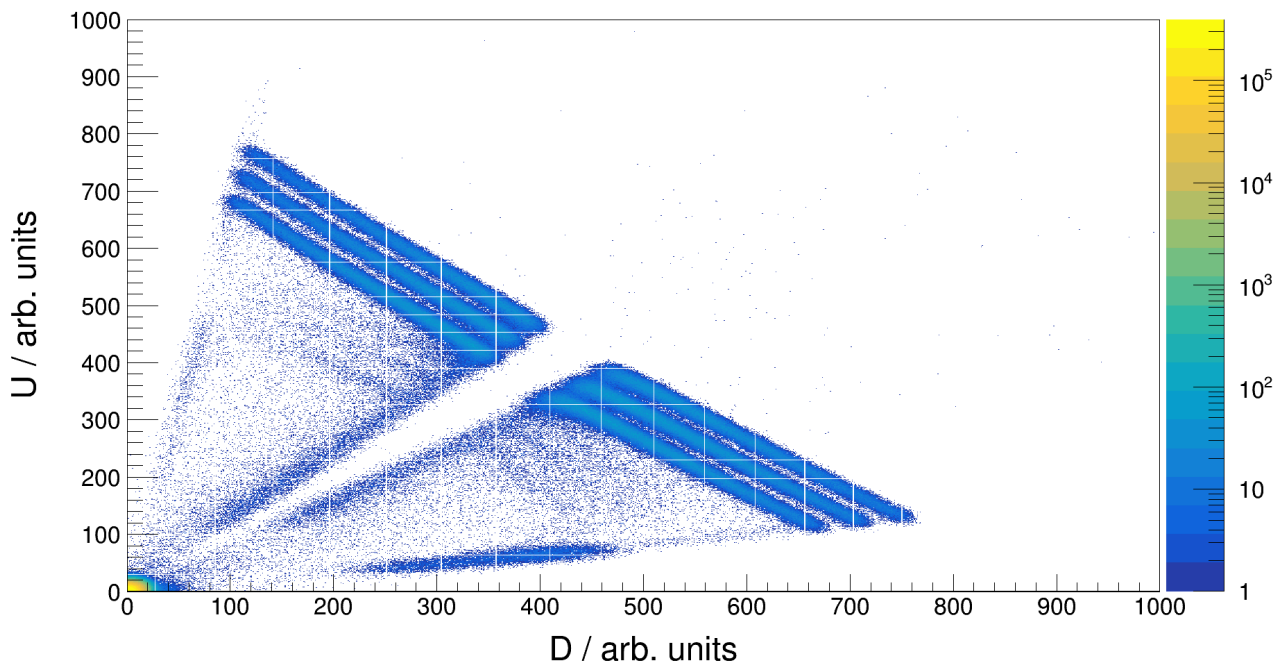


Figure 3.11: The upstream vs downstream signals for an example detector and strip combination within the Barrel of TIARA. This plot is the starting point for all Barrel calibration and analysis. The three characteristic decays from the triple- α source can be seen. The gap at approximately 45 degrees is the shadow of the double-sided source in the target position. The intensity along the lower side of the data corresponds to particles that hit conductor tracks on the detector mount and the very weak triplet of lines is due to cross talk.

The calibration of these strips is a two-step process. Firstly, a functional form for the position of events across the strips was found, then, the energy of the event can be calibrated from a combination of the two end signals. Both steps were completed using a triple- α source as described in Table 3.1.

3.4.4.1 Barrel Position Calibration

The position of the event upon the resistive strip, or P , is defined by a relative measure between the two split energy signals and can be calculated through the following relationship:

$$P = \frac{U - D}{U + D}. \quad (3.3)$$

It can be seen from this equation that the values of P are constrained within a range between $+1$ and -1 . Each of these values are representative of the extreme positional cases:

$$P = +1 \quad \because U \rightarrow 0 \quad \& \quad D \rightarrow E \quad \therefore U \ll D, \quad (3.4)$$

$$P = -1 \quad \because D \rightarrow 0 \quad \& \quad U \rightarrow E \quad \therefore D \ll U. \quad (3.5)$$

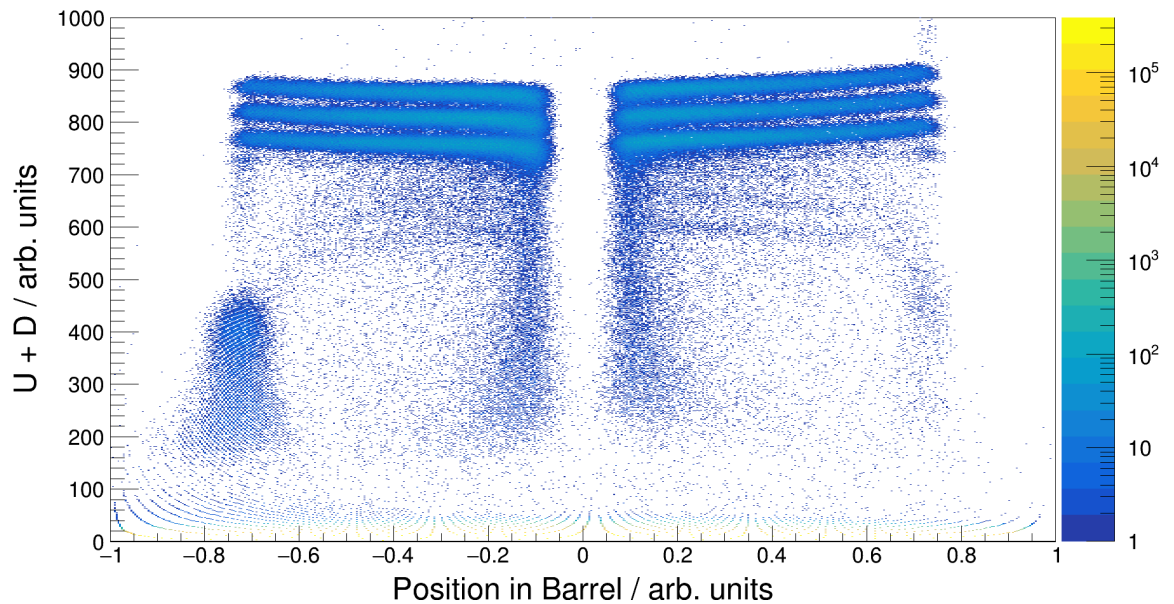


Figure 3.12: Plot depicting the relationship between a raw energy combination of the upstream and downstream signals and the raw position variables based on these signals, with pulser calibrations. The three approximately horizontal bands are representative of the triple- α calibration source.

In the realistic case, the positions will tend towards these values without ever reaching them. As events interact close to the end of the active area of the detector

strips the signal to the opposite end of the strip tends to zero. The electronics require a minimum signal at both end of the strips in order to define the event as “valid”. The effect leads to a small “dead region” where the degradation of the signal traversing the strip is such that it no longer meets this criterium. This degradation is caused by a combination of the read-out capacitors found at each of the strip as well as the capacitance of the strip itself.

With the pulser calibrations applied to each end of the resistive strips, plots of P as a function of the summed value of U and D for those working strips could be made. This type of plot is shown in Figure 3.12. For this step the electronic thresholds were disabled to minimise the electronically created dead zone at the allowance of extra electronic noise. From these plots, one dimensional projections across the y-axis of Figure 3.12 were created. The two projections corresponding to the maximum and minimum values of P are then fit to find the maximum and minimum realistic P values for each individual strip. Examples of these projections are shown in Figure 3.13.

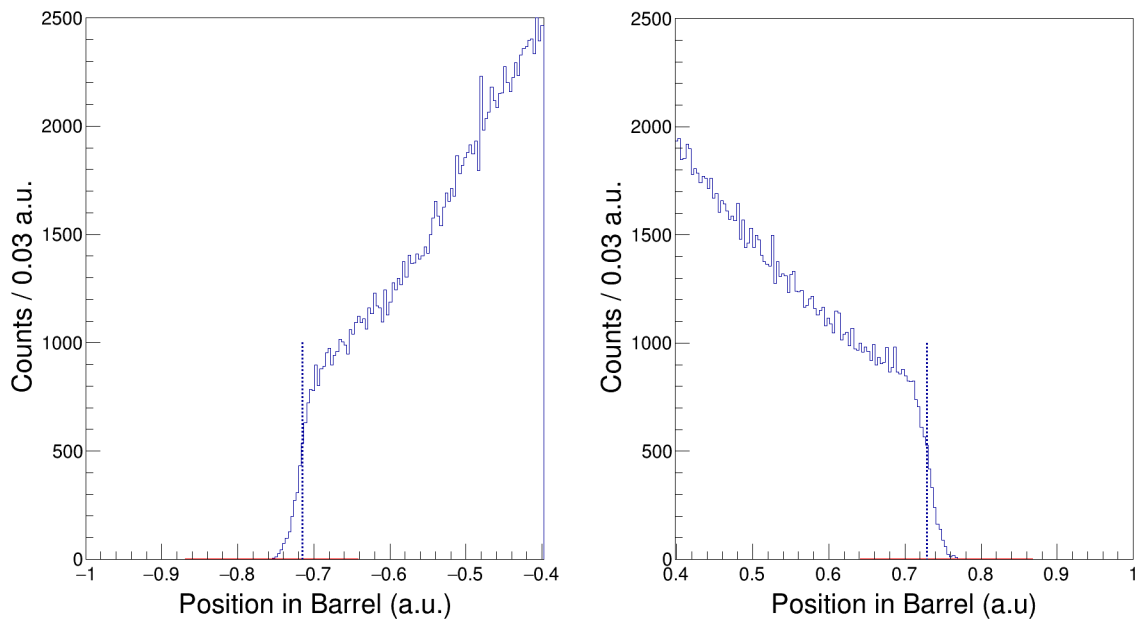


Figure 3.13: Projections of the downstream end (left) and upstream end (right). The individual modified Gauss error functions for each end are indicated in red with their inflection points denoted by the dashed vertical lines. Where the dashed line meets the x-axis is the value used to extract the position calibration parameters.

The strip end-point projections were fit with a modified Gauss error function, in the form of:

$$f(x) = \frac{a}{2} \left(\left(\frac{2}{\sqrt{\pi}} \right) \int_0^{(x-b)/c} e^{-t^2} dt \right) + \left| \frac{a}{2} \right|, \quad (3.6)$$

where b is the most important free parameter from the function as it represents the position along the x-axis corresponding to the inflection point of the slope or the realistic extreme value. While a represents the amplitude of the function, and c , represents the steepness of the curve. These free parameters are determined from the projection fit. The position calibration parameters input into data stream are defined by the following function:

$$j = \frac{b_U + b_D}{2}, \quad (3.7)$$

$$k = \frac{b_U - b_D}{2}, \quad (3.8)$$

where b_U and b_D are the b values associated with the upstream and downstream ends of each strip respectively. b_U is defined as the positive axis of P .

3.4.4.2 Barrel Energy Calibration

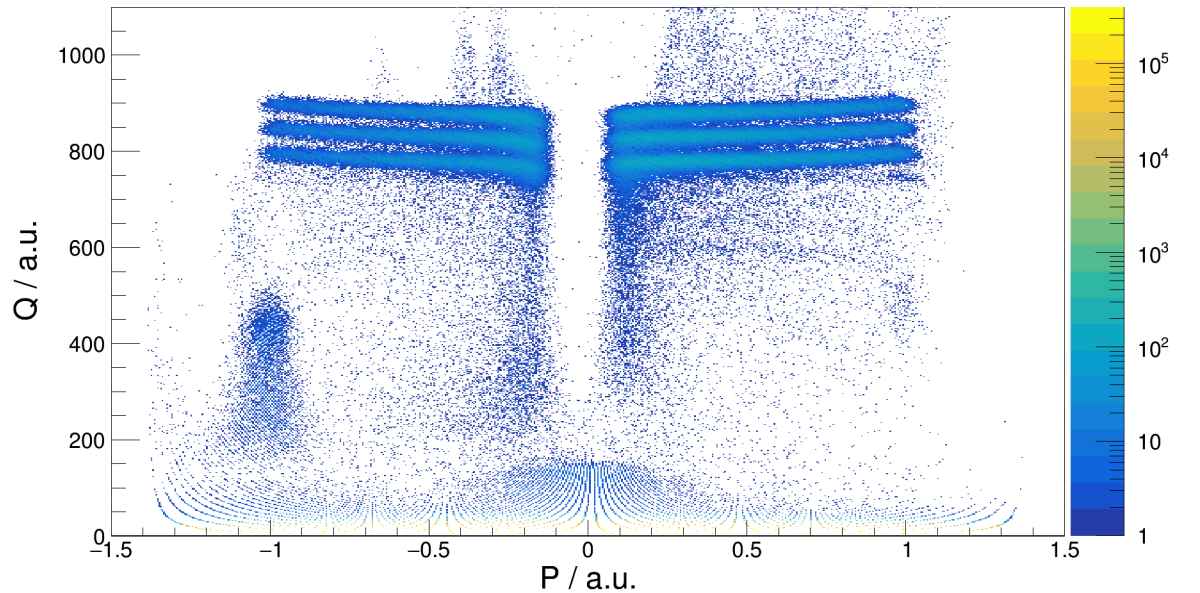


Figure 3.14: Charge vs position plot for a given strip within the Barrel of TIARA. Here the triple- α spectrum can be seen without energy calibrations.

A triple- α source was also used to illuminate the Barrel to calibrate the energy profile of collected charges. In the simplest picture, the detected energy of a given particle within the Barrel is a summation between the recorded upstream and downstream readouts, i.e. $Q = U + D$. This can be seen in Figure 3.14, with the position calibration from the previous step folded in and with U and D representing the signals after the pulser calibration was applied.

With the data in this form, i.e. parametrised in terms of P and Q , it is possible to create a calibration to convert the measured charge into an energy scale, $Q \rightarrow E_{Barrel}$. This was done by applying a first order polynomial function to each end of the strip separately before the summation:

$$E_{Barrel} = ((a \cdot U + b) + (c \cdot D + d)), \quad (3.9)$$

where, a and c represent the gains for the upstream and downstream readouts, b and d are the upstream and downstream offsets respectively.

By incorporating the relation between these readouts and the position of the hit, it was possible to derive expressions of the measured readouts at each strip end in terms of P and Q , i.e:

$$U = \frac{Q}{2}(1 + P), \quad (3.10)$$

$$D = \frac{Q}{2}(1 - P). \quad (3.11)$$

A substitution of these equations in Equation 3.9 provides an analytical expression for the measured energy in terms of P and Q matching that of Figure 3.14:

$$E_{Barrel} = \left(\frac{Q}{2}(P(a - c) + a + c) + b + d \right). \quad (3.12)$$

One-dimensional projections onto the Q axis of these plots for a series of small sub-ranges of constant width within the P axis were created. Each projection was then fitted for 3 centroid values that corresponded to the three main α decaying branches of the source. This provided three series of points describing the value of Q as a function of P . The three series were then simultaneously fitted with a re-arrangement of Equation 3.12:

$$Q = \frac{2(E_\alpha - b - d)}{P(a - c) + a + c}, \quad (3.13)$$

The values of a , b , c and d that best fit the data were then extracted. The resulting data can be seen in Figure 3.15.

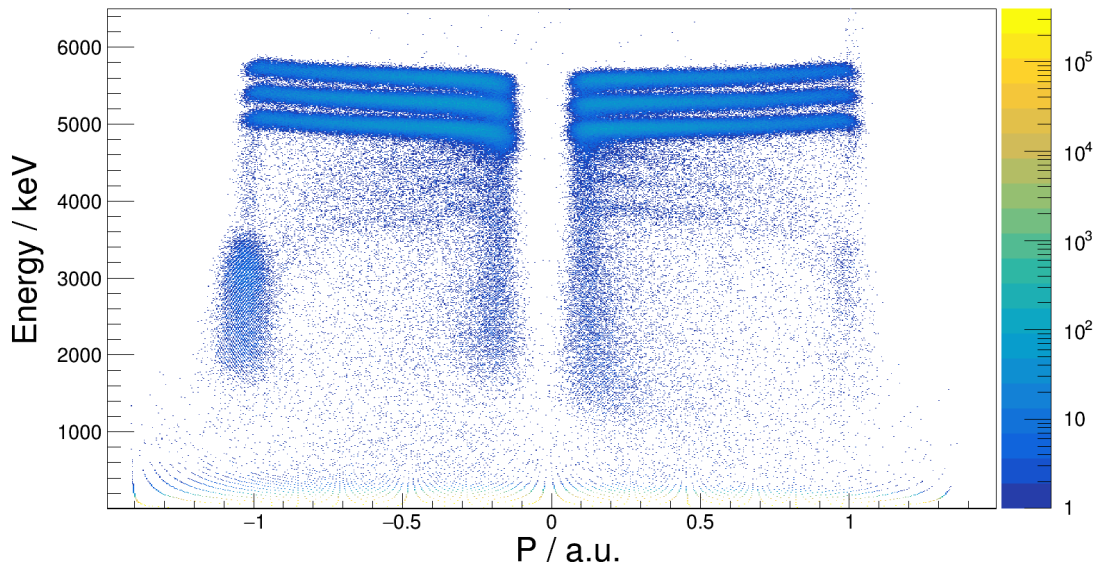


Figure 3.15: Energy vs position plot for a given strip within the Barrel of TIARA. Here the triple- α spectrum can be seen without ballistic deficit corrections.

A major correction within this calibration is needed to compensate for a phenomenon known as the “ballistic deficit”, which causes an underestimation of the actual energy of any particle incident within the Barrel. Figure 3.15 displays the nature of this phenomenon on the alpha energy signals. Where 3 straight horizontal lines of α energy with respect to Barrel position would be expected, 3 parabolic lines are observed with the largest ballistic deficit effect towards the centre of the Barrel strips. The cause of the ballistic deficit is the long charge collection time as the signals have to travel across the length of strip before reaching the read-out electronics. This leads to a large preamplifier rise time and a loss of signal amplitude during the shaping process of the amplifier. A further complication is the position dependence as seen in Figure 3.15, if there was no position dependence the effect would be a constant accounted for in a simple energy calibration. To correct for this ballistic deficit positional dependence, a second order polynomial function is multiplied to the simplistic energy summation case:

$$E_{Barrel} = ((a \cdot U + b) + (c \cdot D + d)) \cdot (1 - e(k^2 - P^2)), \quad (3.14)$$

where, e and k are coefficients related to the ballistic deficit corrections, the former being the ballistic deficit correction factor for the strip and the latter being the normalisation factor for this correction as described in Equation 3.8.

A substitution of the equations defining the upstream and downstream signals in terms of charge and position, Equations 3.10 and 3.11, into this analytical expression provides a form also parametrised in terms of P , and Q :

$$E_{Barrel} = \left(\frac{Q}{2}(P(a - c) + a + c) + b + d \right) \cdot (1 - e(k^2 - P^2)). \quad (3.15)$$

$$\therefore Q = \frac{2 \left(\frac{E_{\alpha}}{1 - e(k^2 - P^2)} - b - d \right)}{P(a - c) + a + c}, \quad (3.16)$$

The same fitting procedure is then performed with the 2 ballistic deficit variables also added to the best fit. The results of incorporating the ballistic deficit corrections are represented in Figures 3.16 and 3.17.

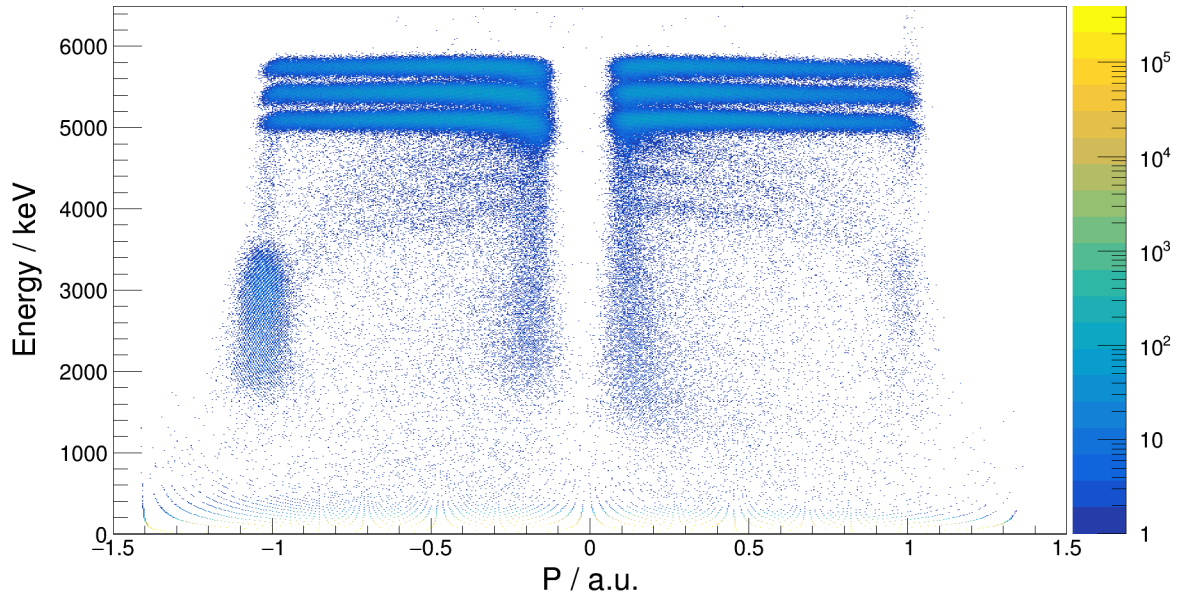


Figure 3.16: Energy vs position plot for a given strip within the Barrel of TIARA. Here the triple- α spectrum can be seen with ballistic deficit corrections. Strip 1 of Barrel segment 2 is used here as an example.

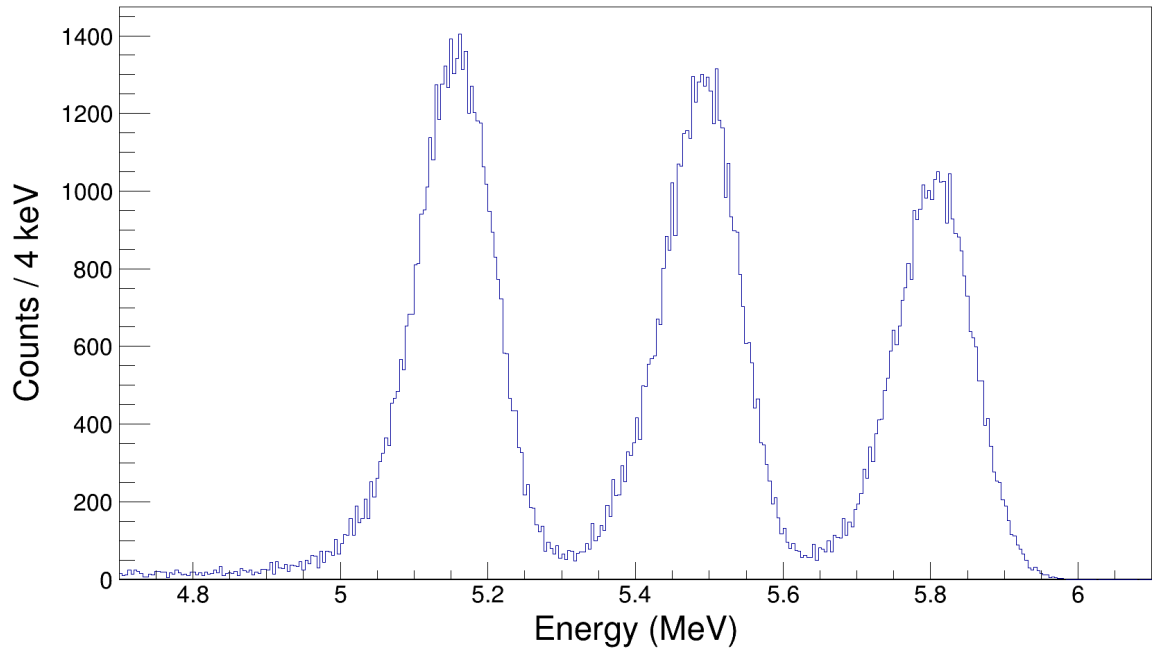


Figure 3.17: Final energy spectrum of the combined Barrel signals that include the energy calibrations and all corrections. The three alpha peaks are shown at their correct energies.

3.4.5 Germanium Calibrations

The germanium detectors within this experimental set-up were calibrated with a combination of ^{152}Eu and ^{60}Co sources, placed individually at the target position. These sources provide several well-known peaks across a wide energy range of the spectrum. 7 known peaks from the ^{152}Eu spectrum and the 2 dominant peaks from the ^{60}Co spectra provide a 9 point energy calibration. The ADC channel number centroids were determined by a combined function of a Gaussian distribution and second-order polynomial. The polynomial accounts for the background in the spectra.

The calibration coefficients for each of the 4 crystal contacts in each clover were determined by fitting known γ -ray energy vs ADC channel plots. The polynomial order was determined by checking the residuals from the calibration function and energy of the peaks within the spectra.

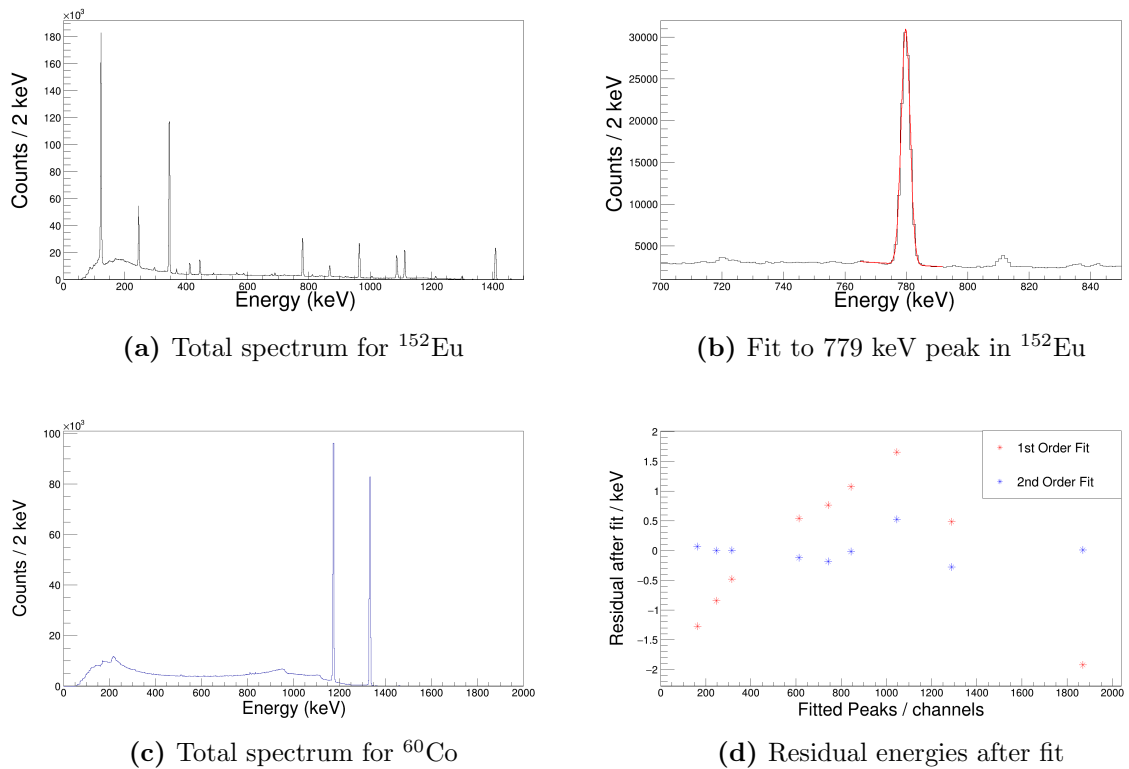


Figure 3.18: Calibration of the HPGe clovers. a) is the total spectrum of a ^{152}Eu source. b) a zoom of the 779 keV peak from the ^{152}Eu decay, fitted with a Gaussian and flat background function for determining the photopeak energy resolution. c) is the total spectrum of a ^{60}Co source. d) the residual energies of the ^{152}Eu and ^{60}Co peaks after different calibration fits.

3.4.6 Focal Plane Calibrations

3.4.6.1 Avalanche Wire Calibrations

As described in Section 3.3.2.1 the energy signal deposited in each wire is split between readouts at each end of the wire. These two readouts are first gain-matched using an alpha source within the focal plane chamber. Then the position calibration of the resistive wires was performed online before the experiment began. A ^{25}Mg beam of the experimental beam energy was focused through the TIARA array with no target installed and a narrow mask at the entrance to the MDM-2 spectrometer. The mask was to ensure only narrowly focused beam particles enter the spectrometer. The field strength of the MDM-2 dipole magnet was configured such that the beam traversed through the spectrometer perpendicular to the focal plane.

A “magnetic sweep” was then performed across the length of the focal plane. The

centre of each MICROMEAS column was used as a central reference point to which the magnetic field was varied to. It was determined the reference point was reached when the online spectra indicated no events in neighbouring columns. The magnetic field settings for each reference point was noted.

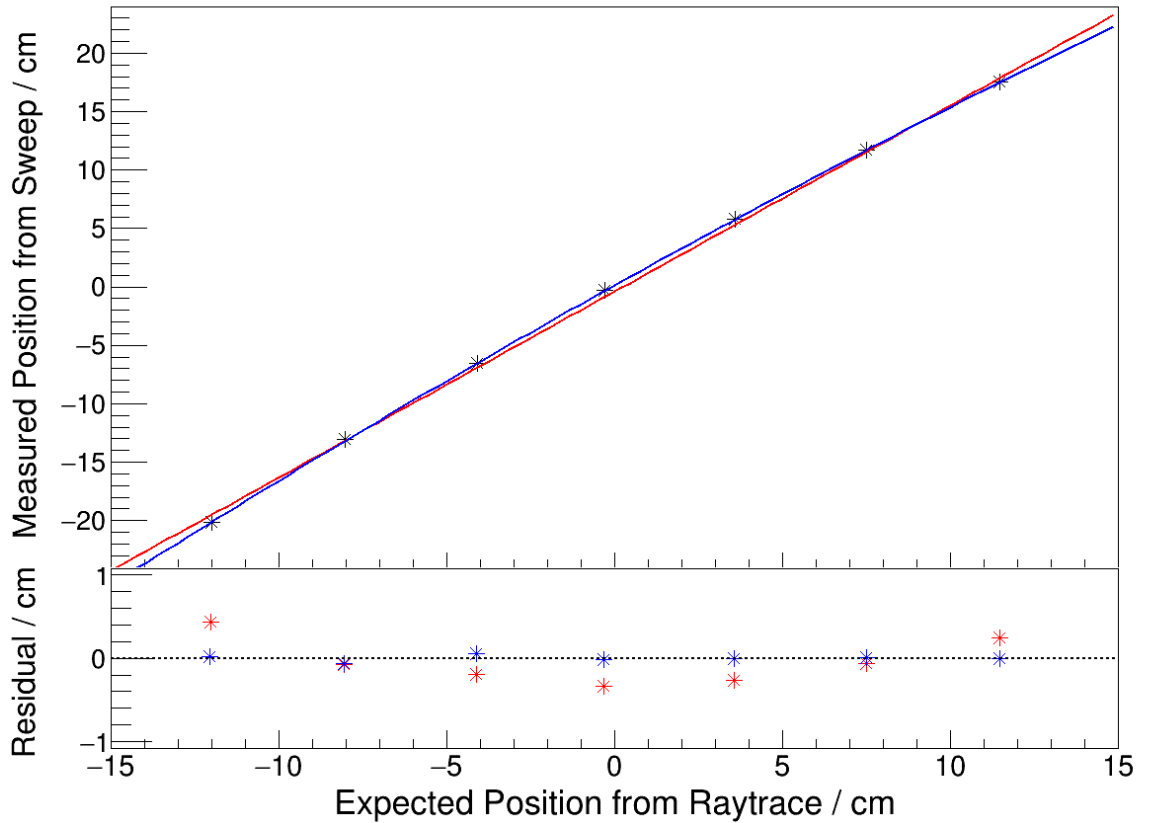


Figure 3.19: Above is the functional form between the measured position on a wire in positional units and a calculated position determined by RAYTRACE. The position residuals between the calculated by RAYTRACE and the functional form of the calibration. It can be clearly seen that the position resolution is best met by a second order polynomial fit.

The dipole field settings of the MDM-2 were used as an input into the RAYTRACE simulation software for the MDM-2 and Oxford focal-plane detector. This simulation provides an absolute position across each of the four wires, taking into account the entrance angle of the beam into the Oxford detector. These simulated absolute positions were then related to the measured position on the wire, defined by a relative measure of the charges collected at each end of the wire:

$$x_{rel} = l_{wire} * \frac{Q_L}{Q_L + Q_R}, \quad (3.17)$$

where x_{rel} is the position on the wire in an uncalibrated centimetres scale, l_{wire} is the length of the wire in centimetres, Q_L is the charge measured at one end of the wire and Q_R is the charge measured at the other end of the wire. A second order polynomial was then determined to be the best functional form of this relationship from the standard deviation between the resulting measured positional fits and those expected from the simulation. The functional form and residual plots are displayed in Figure 3.19.

3.4.6.2 MICROMEAS Energy Calibrations

The MICROMEAS energy calibration was completed simultaneously with the resistive wire position calibration. Each column of the MICROMEAS was individually centred upon during this experimental process, providing approximately uniform energy loss data across the respective column. The experimental data was then compared to a simulation of the Oxford detector environment, using identical experimental conditions, within the LISE++ framework. These simulations provided an absolute energy loss value of the narrow focussed beam for each component of the Oxford detector. By comparing the raw channel data for each row/column of the MICROMEAS with this simulation, a calibration of this detector suite was built on a pixel-by-pixel basis.

3.4.6.3 Plastic Scintillator

For this experiment, the plastic scintillator of the Oxford focal plane detector was used uncalibrated. Whilst a similar procedure to the MICROMEAS energy calibration could have been used to provide an energy calibration. The LISE++ simulation does not model the second-order effects that are observed within plastic scintillators to the degree required. Effects such as reflection, absorption and the relationship between light output and energy could not be taken into account. However, the raw ADC channel numbers provide resolution enough to perform particle identification with.

3.5 Particle Identification

Identifying the various nuclear species at the focal plane of the Oxford detector was a key part of this analysis. By separating the focal plane data linked to ^{26}Mg , it can be ensured that the silicon data analysed is only from the reaction of interest, $^{25}\text{Mg}(d,p)^{26}\text{Mg}$. This prevents other open reaction channels from being analysed. The

following sections outlines how the various detectors within the Oxford detector are used in this particle identification analysis.

3.5.1 Si-FPD TAC Data

The Si-FPD TAC signal represented the time between an event within the plastic scintillator of the Oxford detector and the delayed signal of an event within the silicon detectors. The data from this TAC can be seen in Figure 3.20, which shows a statistical time-window peak of real coincidences between the silicon detectors and plastic scintillator. The oscillations either side of the statistical peak within this figure are random coincidences between silicon and focal plane events produced by a beam bunch, separated in time by a multiple of the RF period. This condition removed a significant background from fusion evaporation events. Only events within this central TAC window were considered within the particle identification process and this was a software condition implemented in all further analysis.

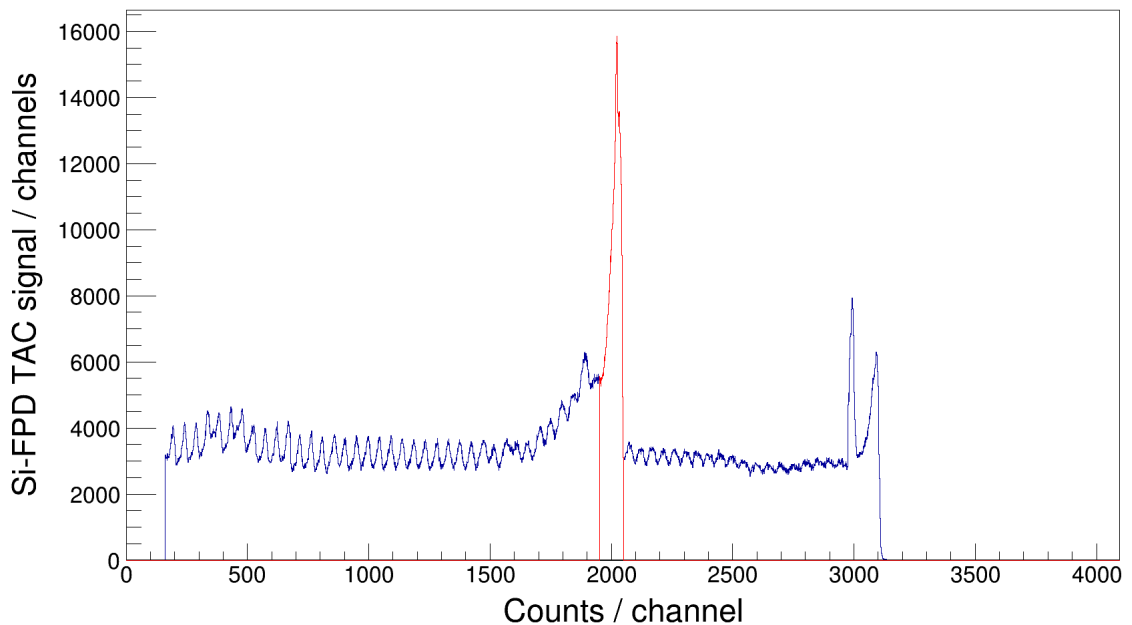


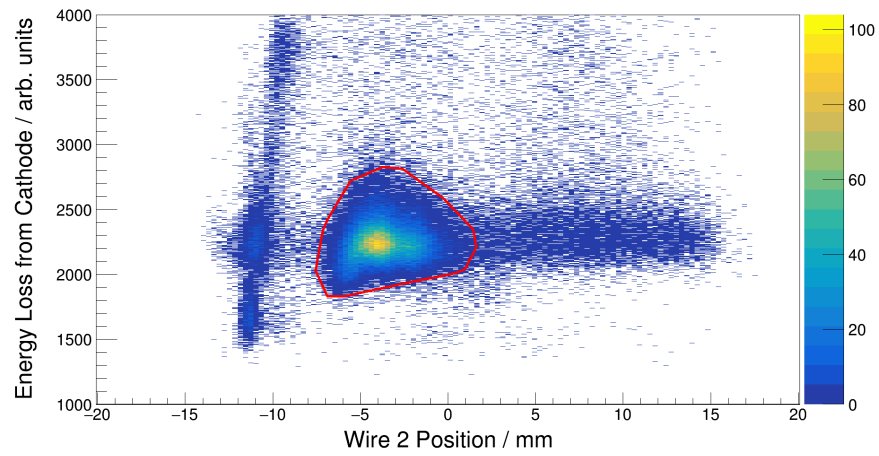
Figure 3.20: The Si-FPD TAC signal data obtained from the $^{25}\text{Mg}(d,p)^{26}\text{Mg}$ experiment. The region outlined in red is region of time related to the (d,p) reaction products used for this analysis. The undulations within this data is a result of the cyclotron RF.

3.5.2 Oxford-2 Data

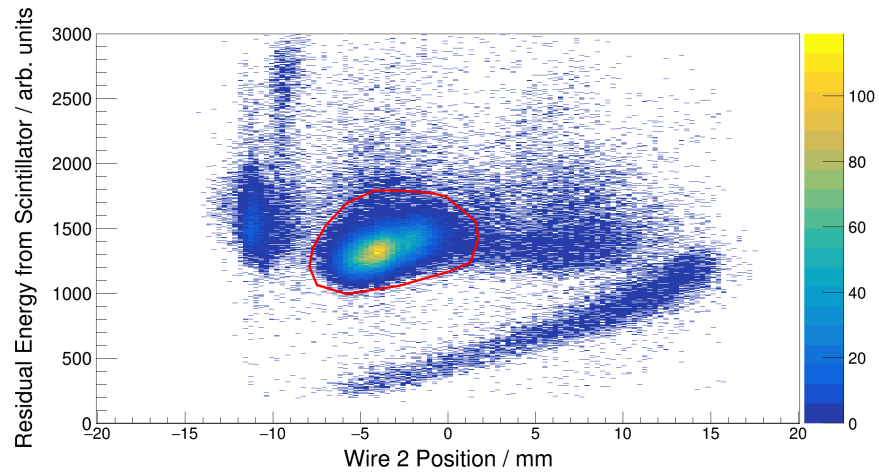
The Oxford detector is further used to identify (d,p) reaction products within the TIARA silicon detectors. Combined data from the proportional wire detectors, cathode detector and plastic scintillator stopping detector was used to identify ^{26}Si reactant products. As this work focused on the proton information within the Hyball detectors, a software gate of an event within the Hyball was applied to the following analysis. This also reduced background focal plane data as the likelihood of a coincidence between these detection systems from scattered beam-like products is relatively smaller than the Barrel.

The positional data from the proportional wires of the Oxford-2 detector can be used as an analogue for the $B\rho$ of the particles that have traversed the MDM magnetic spectrometer. The second of the four wires within the Oxford detector is the closest to the focal plane within the ionisation chamber and provides the clearest $B\rho$ separation. The energy loss and residual energy of these particles are then measured within the cathode and plastic scintillator respectively. As different nuclear species are likely to have different $B\rho$ values and will deposit energy within the ionisation chamber according to the Bethe-Block formula these are powerful tools for differentiating the beam-like nuclear species from TIARA.

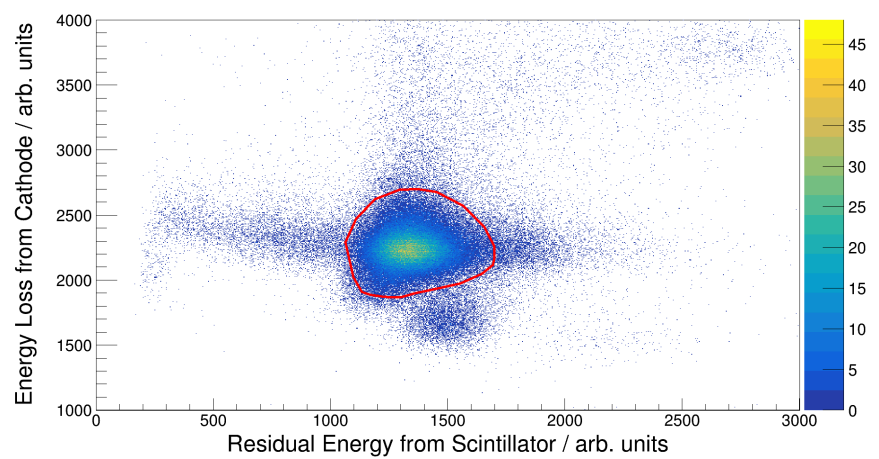
Figure 3.21 represents the 2-dimensional software cuts representing ^{26}Mg ions within the Oxford-2 detector. To begin an assumption that the majority of events within these plots was linked to the reactant products from the (d,p) reaction was made, presuming that the TAC software gate discussed earlier filtered a substantial number of non-interest events. This assumption was then tested against the 2-dimensional “kinematic” plot from TIARA, consisting of target-like particle theta angle vs corresponding laboratory energy. This plot displayed characteristic kinematic shape expected from a (d,p) transfer reaction, when these focal plane software cuts were applied confirming that these loci corresponded to ^{26}Mg .



(a) Energy Loss vs Wire 2 Position



(b) Residual Energy vs Wire 2 Position



(c) Residual Energy vs Energy Loss

Figure 3.21: Various data combinations from the detectors within the Oxford-2 focal plane detector. The red polygons display the software gates that were used to identify ^{27}Si ions.

3.6 Beam Spot Corrections

Initially it was assumed that the target was perfectly central within TIARA with respect to the beam axis, i.e. that the target was in the middle of the Barrel. Also that the beam spot was at the geometric centre of the target. Tests of these assumptions were completed using the experimental data of both the transfer reaction of interest $^{25}\text{Mg}(d,p)^{26}\text{Mg}$ and the deuteron elastic scattering by-product of this experiment $^{25}\text{Mg}(d,d)^{25}\text{Mg}$. Using primarily data for the Hyball for the former, and data from the Barrel for the latter.

These data sets have very well defined target-like particles relationships between their kinetic energy angle of emission. Within the transfer reaction channel, protons emitted from a specific state within ^{26}Mg follow specific kinematic relationships between energy and angle. With an ideal geometrically central beam spot, all of the events within a specific ring of the Hyball would have the same lab-frame angle and identical kinetic energy. Within the elastic channel, events detected with a specific kinetic energy should have identical reconstructed angles of emission. Specifically, they would be found at the same z -coordinate along the length of the Barrel for each individual strip. Deviations away from these two relationships would suggest that the initial assumption of a geometrically centred target was invalid.

A chi-squared minimisation routine was developed to find the values that best described the beam spot position upon the target, relative to the TIARA detectors. Two sets of values were extracted assuming a geometrically central beam spot. One for the z -coordinate values for a specific small energy window within the Barrel. The second being the proton energies from transfer reaction peaks extracted from a given Hyball ring. Simulated values of the same conditions, using assumed beam spot coordinates, were created for each test case and the two sets of values compared against each other.

A chi-squared value for each test case was calculated representing how the quantities extracted from the data compare to a simulated data set. A single chi-squared value was created from the sum of the two chi-squared values. This process was repeated using different starting assumptions until a minimum value of the combined chi-squared value was found, i.e. the values that best represented the experimental data. Within this experiment the beam spot position was determined to be

$(x, y, z) = (+1.22, +2.59, +4.21)$ mm. It should be noted that previous experiments during this campaign found evidence of a beam angle with respect to the TIARA detectors, this study also found evidence of this feature. This was included in the chi-squared minimisation routine described above and the beam vector was determined to be $\vec{v} = (v_x, v_y, v_z) = (0.009, -0.001, 0.999)$. Figure 3.22 represents the Barrel data of these tests with and without the minimised beam spot position.

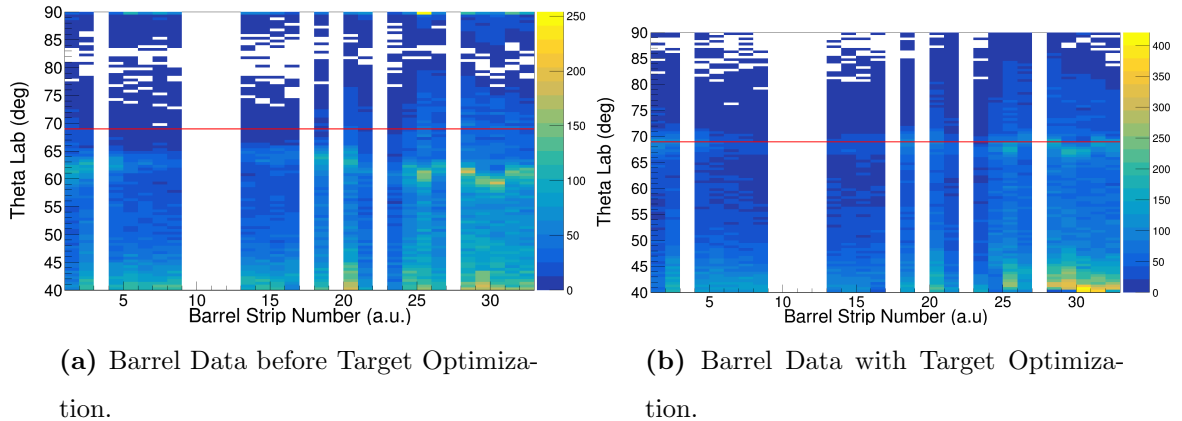


Figure 3.22: The effects of optimizing the beam position upon the target. This minimization uses the elastically scattered deuterons from the target with a specific energy gating, optimized to the expected theta value from kinematic calculations.

3.7 Constructing Particle Excitation Spectra

The most important information within this study is the excitation energy spectrum for events associated with the $^{25}\text{Mg}(d,p)^{26}\text{Mg}$ reaction. Applying the corrections previously discussed and the software gates from the focal plane data it is possible to create this excitation spectrum. Figure 3.23 displays the results of the corrections and ^{26}Mg particle identification cuts and as such the final events used in the excitation spectrum. The first sub-figure in Figure 3.23 displays the total data from the experiment with the beam spot minimisation corrections used and ensuring the only events considered are those with TIARA multiplicity equal to 1. The second sub-figure displays the same data after the application of the TAC signal gate, ensuring a coincidence event between TIARA and the detectors in the Oxford-2. The final sub-figure is with the Oxford-2 data software cuts also applied such that only events associated with a ^{26}Mg ion are included.

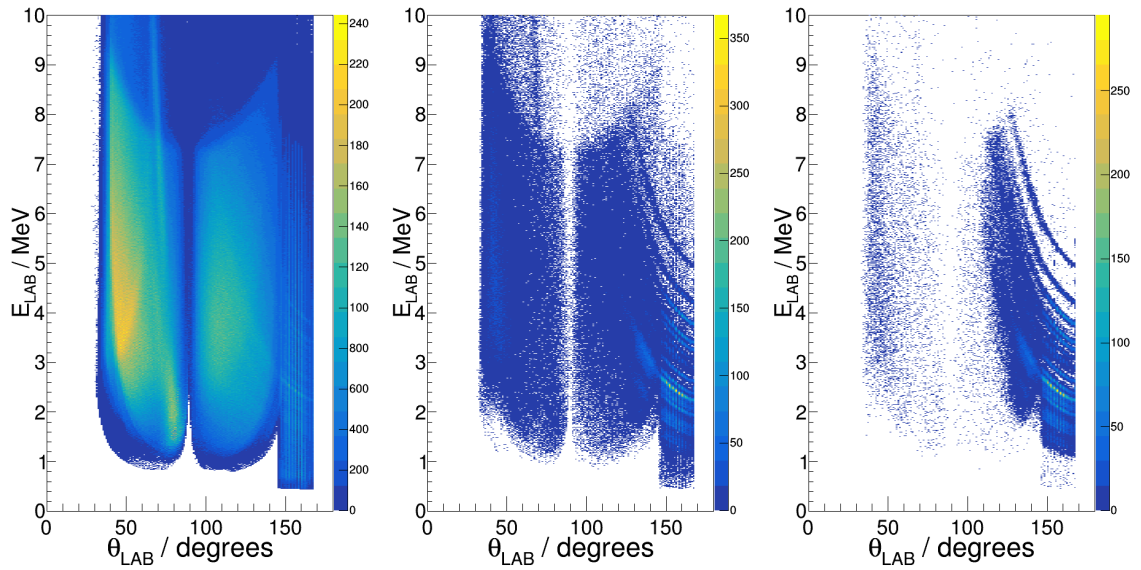


Figure 3.23: Left hand figure: The kinematic plot from the total TIARA data after applying the beam spot corrections. Middle figure: The same plot after applying the software gate based upon the TAC signal. Right hand figure: Final kinematic plot only considering data that is software gated upon ^{26}Mg particles within the Oxford-2 detectors.

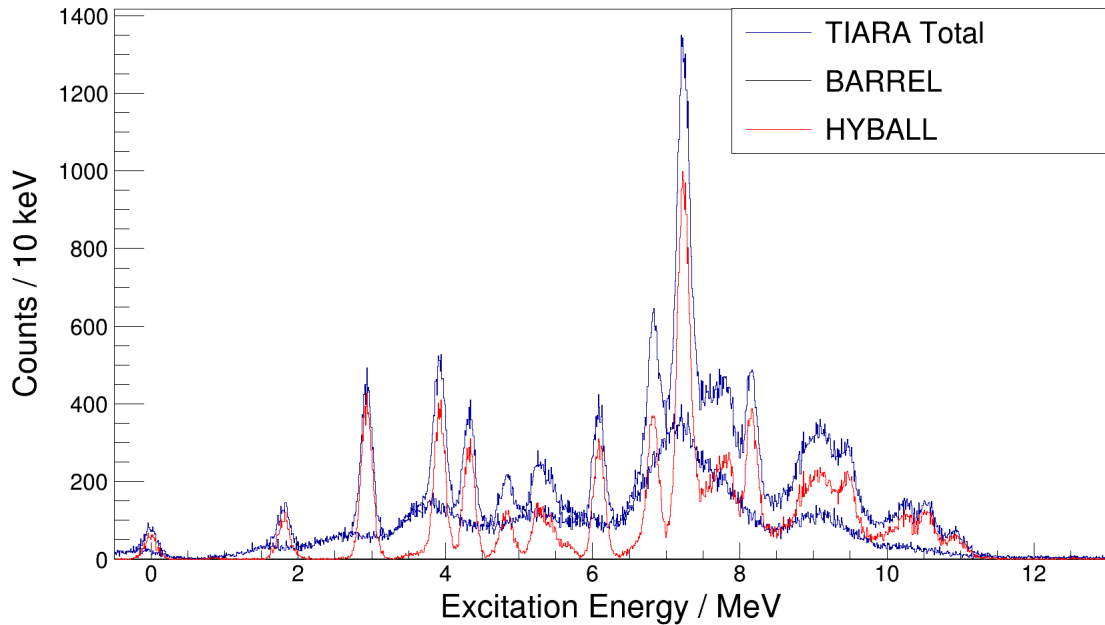


Figure 3.24: Excitation spectrum obtained from the $^{25}\text{Mg}(d,p)^{26}\text{Mg}$ reaction events observed in the TIARA detectors. The individual contributions from the Hyball and Barrel are also within the spectrum. It can be seen that the Hyball has both superior resolution and statistics. From this point on the Hyball is the only detection system used in further analysis for this study.

The proton energy and angular information from the TIARA array were combined on an event-by-event basis to recreate the excitation energies of the ^{26}Mg ions. Figure 3.24 shows the final excitation spectrum alongside the individual contributions from the two detectors within TIARA. The peaks within this spectrum are related to strong single-particle states within the final ^{26}Mg nucleus. As can be seen the Hyball has much improved energy resolution compared to that seen in the Barrel. As a result the spectroscopy work for this study has been completed using Hyball information only. This ensured as many states as possible were resolved and analysed.

Performing this study in inverse kinematics has the consequence of a poorer resolution with respect to the studies of this reaction performed in normal kinematics, such as performed by Lutz *et al.* [132], Burlein *et al.* [133] and Arciszewski *et al.* [134]. However, the major benefit of inverse kinematics is the reduction of the emitted proton background from reactions between a deuteron beam with various impurities within a target. Especially in the case of magnesium, which must be backed with another material to prevent oxidation.

3.8 Determining State Population and Decay

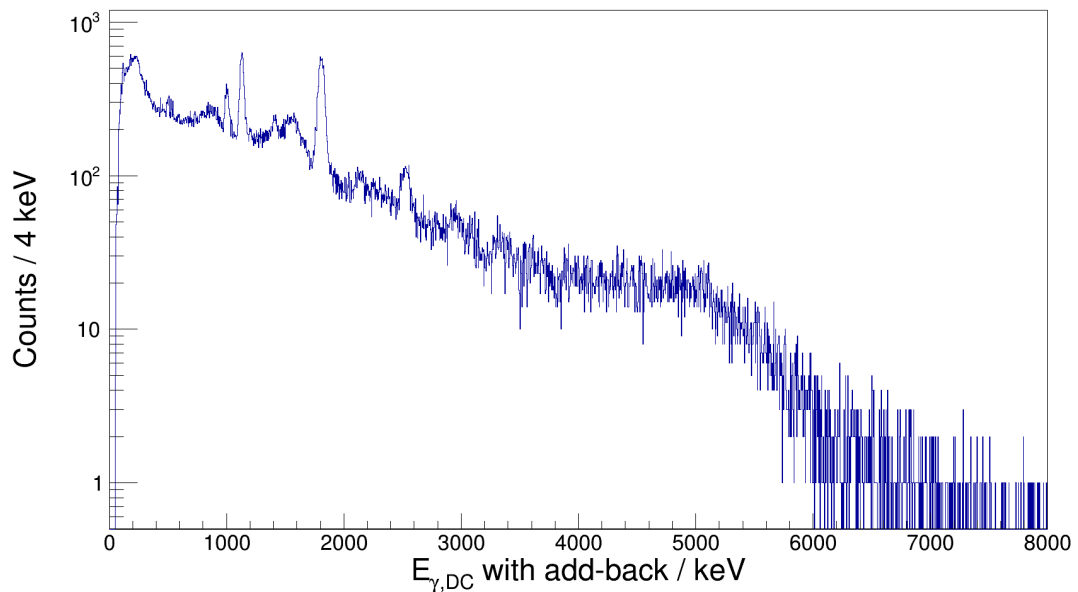


Figure 3.25: Energy calibrated γ -ray spectrum for $^{25}\text{Mg}(d,p)^{26}\text{Mg}$. Includes Doppler corrections and using add-back scheme.

In order to differentiate between unresolved states from the proton spectrum, particle- γ coincidence information was used in order to determine which states were populated. The increased resolution of the HPGe detectors within this set-up was helpful for the clearing up of ambiguities in state population within the proton excitation spectrum. Importantly, this method allows the use of characteristic decays from ambiguous states to be used, whilst two states may have similar excitation energies they may have very different γ -ray decay pathways so this is a powerful tool. Figure 3.25 shows the total energy calibrated γ -ray spectrum linked to ^{26}Mg ions, including applied Doppler corrections and using the add-back scheme previously discussed. The spectrum clearly contains a number of γ -ray peaks linked to de-excitations within ^{26}Mg . These include strong peaks at ~ 1003 keV, ~ 1129 keV and ~ 1808 keV corresponding to the successive decays from the third excited state through the second excited state and the first excited state to the ground state respectively.

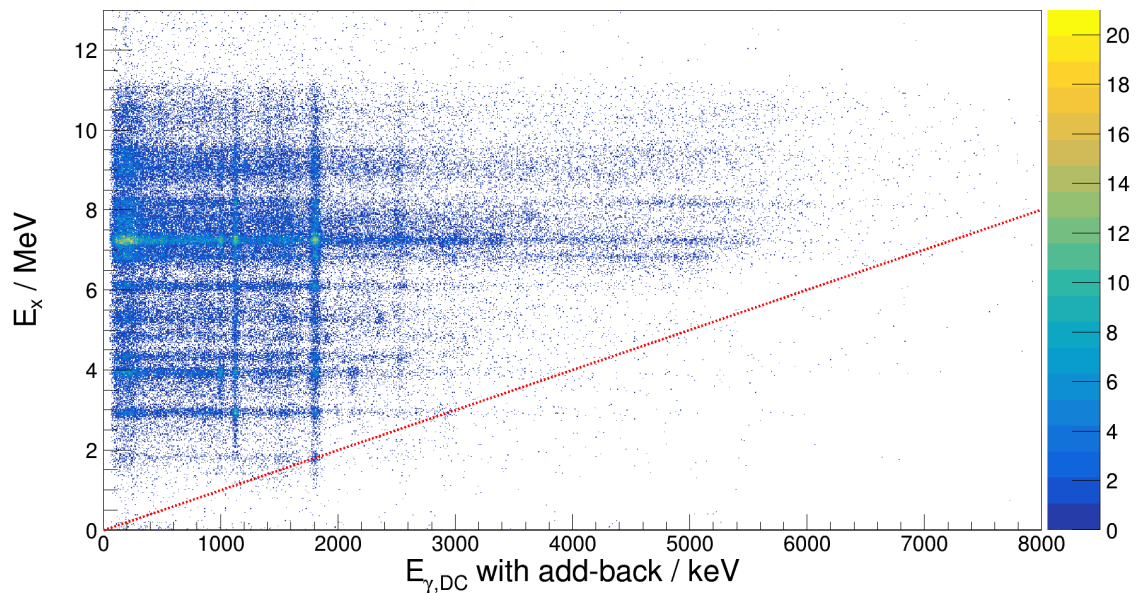


Figure 3.26: Excitation energy of ^{26}Mg as a function of coincident γ -ray events. The red dashed line has the function $E_\gamma = E_x$ and corresponds to the maximum γ -ray energy possible from a given state. The horizontal bands are related to the structure observed within the proton spectrum and the vertical lines within correspond to major photopeaks from the HPGe. The figure highlights the large range of states at different excitation energies that decay via the first 2^+ state at 1.809 MeV.

Used in conjunction with the particle data it was possible to investigate γ -ray

spectra not only gated on ^{26}Mg ions but specific excitations of ^{26}Mg . This allowed the analysis of the specific characteristic decays of individual excitations without any background from other excitations. Figure 3.26 shows the γ -ray spectrum in Figure 3.25 as a function of the excitation energy determined by the TIARA detectors. Horizontal bands within this plot correspond to the excitation structure as observed from the protons in Figure 3.24 and contain the γ -ray decay information related.

The following sections will describe the analysis of these bands individually to identify the states within each band. It should be noted, that the even-even nature of ^{26}Mg and limited statistics within the proton spectrum push this technique to the limit. Most of the higher excitations within ^{26}Mg decay either first or second excited state in a single high energy γ -ray step, which is hard to observe without good levels of statistics.

3.8.1 $1.6 < E_x < 2.1$

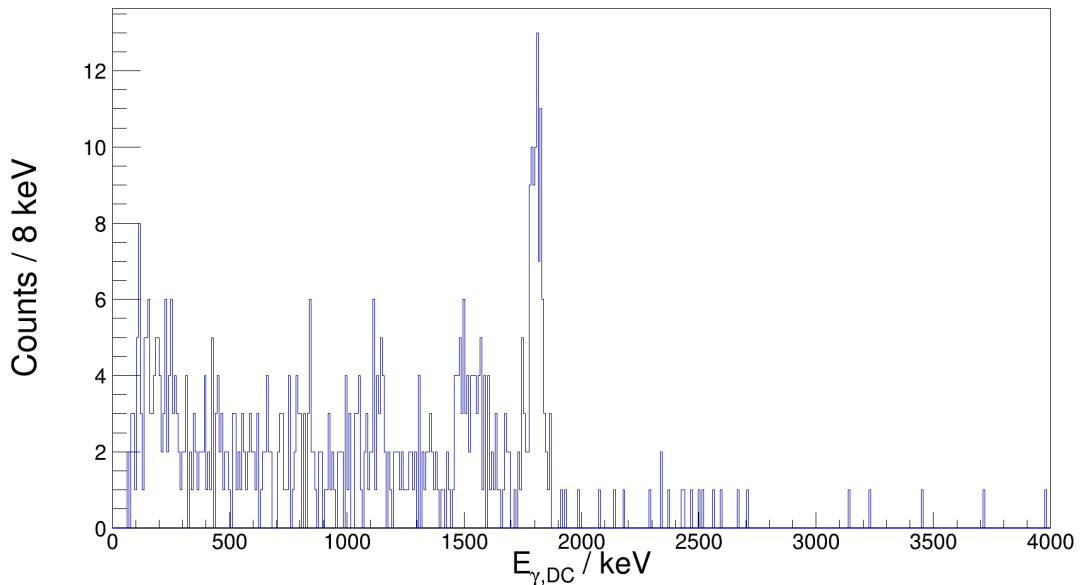


Figure 3.27: Coincident γ -ray energy spectrum for ^{26}Mg events with excitation energy between $1.6 < E_x < 2.1$ MeV. The diffuse peak centred slightly above 1500 keV is the Compton edge of the 1.808 MeV γ -ray transition to the ground state. This feature is enhanced compared to the rest of the continuum because they represent the back-scattered Compton events which escape the detectors and have minimal probability of being captured by the add-back procedure.

The first horizontal band considered from Figure 3.26 was the region of $E_x = 1.6 - 2.1$ MeV. The first band within a method like this is typically linked to the first excited state within the nucleus of interest. Within ^{26}Mg there is only one possible state within this excitation energy region. This the 1.808 MeV, 2^+ state, this has been observed in all historical $^{25}\text{Mg}(d,p)^{26}\text{Mg}$ studies [116, 133, 134]. As the first excited state within ^{26}Mg this state decays with a 100% branch to the ground state.

Even with the limited statistics, the excitation energy gated γ -ray energy spectrum within this region clearly contains the one peak. Figure 3.27 shows this spectrum and the extracted centroid of the visible peak was determined as 1.807 (3) MeV. This is in good agreement with the literature values of 1.80868 MeV from NNDC (4) [103] and 1.8092 (10) MeV, given by a γ -ray spectroscopy study after population by fusion evaporation [135]. With the first peak in the proton spectrum is well isolated from all other peaks, it was possible to perform a confidence test of this method by comparing the centroid of the γ -decay with that within the excitation spectrum. The fitted peak centroid from the protons was determined as 1.808 (10) MeV is in good agreement with the extracted γ -ray centroid implying great agreement between the two spectrum and as such giving confidence to this state population determination technique.

The unique properties of the first excited state's singular exclusive decay pathway allowed for the γ -ray efficiency at the 1.808 MeV energy to be determined directly from the experimental data and independent of source measurements. The number of events measured in coincidence with the γ -ray decay, or N_{coinc} is equal to:

$$N_{\text{coinc}} = N_{\text{sing}} \cdot \epsilon_{\gamma=1.808}, \quad (3.18)$$

where N_{sing} is the number of events populating the first excited state without a γ -ray coincidence and $\epsilon_{\gamma=1.808}$ is the efficiency of the 1.808 MeV γ -ray decay. This can be re-arranged for the efficiency as:

$$\epsilon_{\gamma=1.808} = \frac{N_{\text{coinc}}}{N_{\text{sing}}}. \quad (3.19)$$

In this study, the number of events in singles and coincidence was measured by integrating over the first excitation peak in the proton spectrum with and without the γ -ray coincidence condition. The efficiency is then determined as the ratio between these values, which for this study was found to be 4.6 (5)%. The most interesting

feature of this process is that by scaling the γ -ray coincidence proton spectrum, an inference of which excitation states decay through the first excited state can be found. Figure 3.28 shows the 1.808 MeV γ -ray efficiency scaled proton spectrum and it clearly shows that the majority excitations observed exhibit γ -ray coincidences with the first excited state. It should be noted that a portion of these coincidences for higher energy excitations can be with compton-scatter events of γ rays with energy higher than 1.808 MeV.

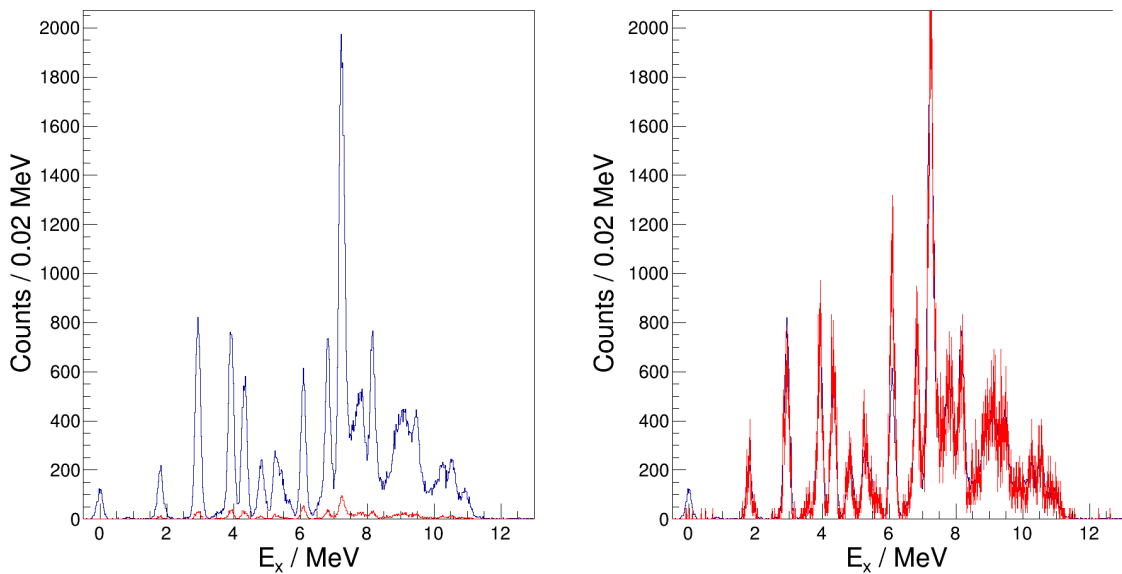


Figure 3.28: Left: Plot of singles and 1.808 MeV photopeak γ -ray coincidence proton spectra. Right: Plot of singles proton spectrum and 1.808 MeV photopeak γ -ray coincidence proton spectrum scaled by the determined relative efficiency of the 1.808 MeV photopeak.

3.8.2 $2.6 < E_x < 3.2$

This region is known to contain two excited states within ^{26}Mg . One is the second excited state of ^{26}Mg measured at 2.938 MeV and the second has been measured from a γ -ray spectroscopy performed by Bhattacharjee *et al.* and measured to have an energy of 3.082 (2) MeV [135]. The proton structure within this region is symmetric around the centroid 2.9321 (9) MeV which points more towards the 2.938 MeV state. The error on this value is likely an underestimate of the true error from the recreation of excitation energy from measured protons and purely comes from the peak fitting procedure. This state has been populated in all historical studies and is typically observed with more

strength than the first excited state, both are assigned as 2^+ spin-parities [116, 133, 134]. There is no indication from the proton spectrum that the 3.082 state is populated.

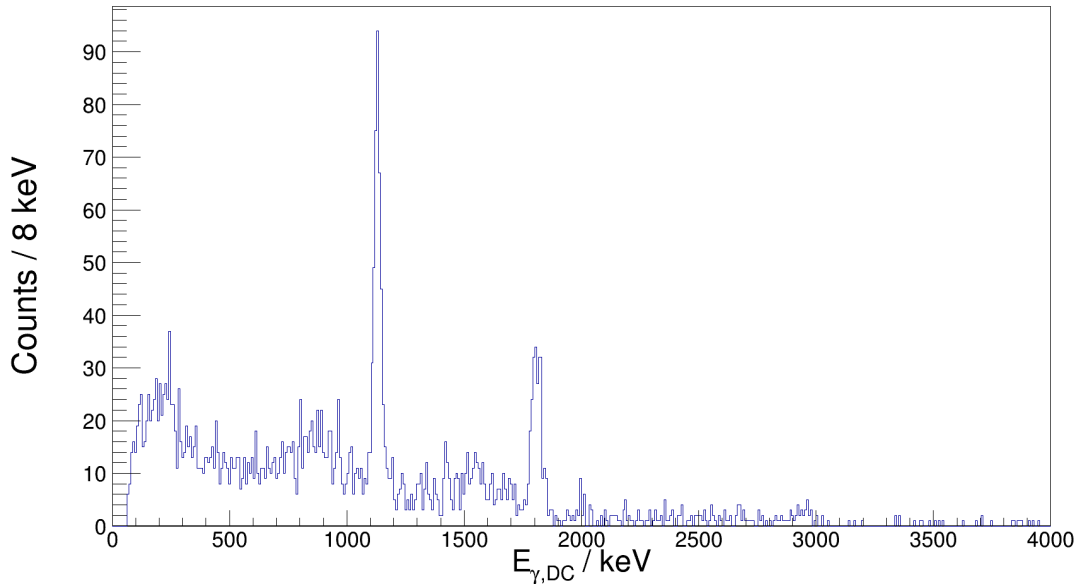


Figure 3.29: Coincident γ -ray energy spectrum for ^{26}Mg events with excitation energy between $2.6 < E_x < 3.2$ MeV.

Figure 3.29 displays the excitation energy band gated γ -ray spectrum for this region. There are three possible γ -ray decays from the two states within this region. Firstly, if the 3.082 state was populated, the 1.274 (2) MeV decay to the first excited state should have been observed within Figure 3.29 and so we can conclude that there was no population here. It is noted that the two further states between 3.0 and 4.0 MeV from the study by Bhattacharjee *et al.* are also unlikely to be observed within this study and so will not be discussed further. The dominant peak within Figure 3.29 is found at 1.131 (9) MeV which is in good agreement with the literature value for the second to first excited state decay of 1.12961 (4) MeV. This state also features a weaker decay straight to the ground state with an energy of 2.93815 (5) MeV, this is also observed within this study with a peak energy of 2.94 (2). The third clear peak within this spectrum is the 1.808 MeV peak decay from the first excited state to the ground, this is observed due to the population of the first excited state via the 1.129 MeV γ -ray decay. The combination of proton and γ -ray data leads to the conclusion that the only state populated within this region is the 2.938 MeV state.

3.8.3 $3.3 < E_x < 4.15$

There are four excited states known within this region, but as mentioned within the previous section there are two of these only observed within a γ -ray spectroscopy study and so will not be considered. The two states remaining are the 3.58856 (9), 0^+ state, and the 3.94157 (4), 3^+ state. Both of these have been observed in previous (d,p) measurements made by Burlein *et al.* [133] and Arciszewski *et al.* [134] whilst only the 3.941 MeV was observed by Lutz *et al.* [132], whose study was much more limited in scope. The 3.588 state is expected to be a much weaker population branch than the 3.941 MeV and this is corroborated by the proton excitation spectrum, where a clear peak with an asymmetric tail on the lower energy edge can be observed. The weak population of the 3.588 MeV state and poor resolution of the inverse kinematic method means that the shape of this state is not fit well using a Gaussian form. Instead the 3.941 MeV is fit with a Gaussian form with a tightly bound second-order polynomial describing the 3.588 state was used.

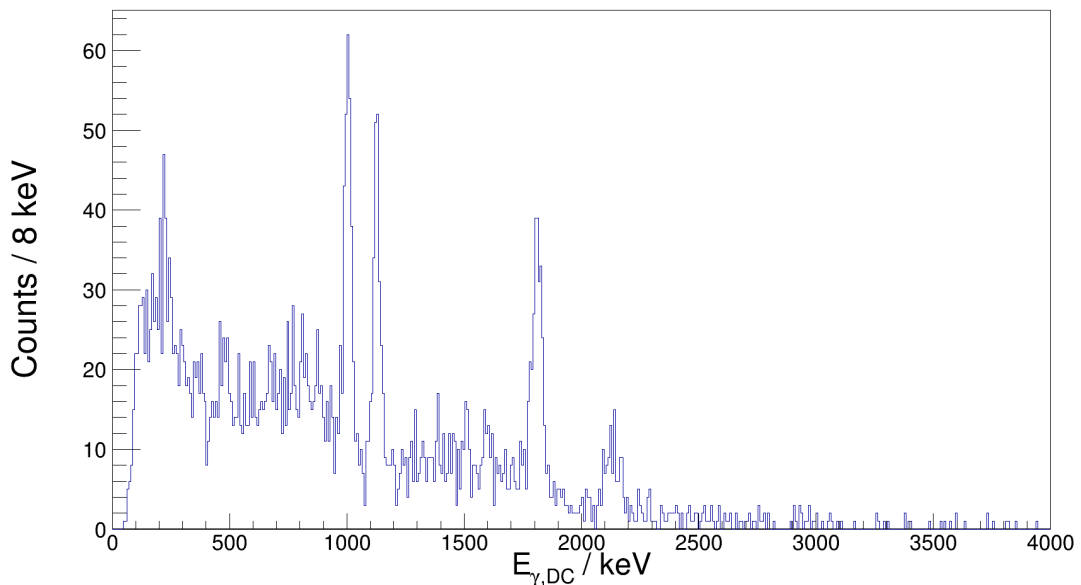


Figure 3.30: Coincident γ -ray energy spectrum for ^{26}Mg events with excitation energy between $3.3 < E_x < 4.15$ MeV.

Figure 3.30 shows the γ -ray coincident data for this energy band. There are four clear peaks observed within the spectrum, from the well-populated 3.941 MeV state these are 2 known decay pathways, a 1.00325 (4) MeV decay to the second excited state

at 2.938 MeV and a 2.13271 (4) decay to the first excited state at 1.808 MeV. These are both observed with peak energies of 1.004 (2) and 2.129 (6) MeV respectively. This confirms the population of the 3.941 MeV state. The other two γ -ray peaks observed in this energy coincidence are the subsequent decays from the second and first excited states as previously discussed. The 1.77974 (8) MeV decay from the 3.588 MeV state is not observed clearly within this plot and most likely contributes to the low energy tail of the 1.808 MeV decay.

3.8.4 $4.15 < E_x < 4.55$

This excitation region contains a well-known triplet of excitations with energies of 4.31889 (5), 4.33252 (5) and 4.35009 (4) MeV. Previous (d,p) studies have been unable to resolve this triplet with the resolution of the particle detectors used within these studies and had no γ -ray detection to support in the assignment [133, 134]. The proton spectrum in this energy region does not help for this study. The resolution covers a wide enough energy space that any of the triplet states could be populated and unresolvable. The γ -ray decay information would ideally provide clarity.

Figure 3.31 shows the γ -ray information for this excitation energy slice. Similar to the proton excitation spectrum, these states exhibit similar energy γ -ray decay pathways through the first and second excited states. However, the clear difference between the states is the branching ratios between these decays. The 4318 MeV, 4^+ state decays almost completely via a 2.51001 (5) MeV γ -ray transition to the first excited state, bypassing the second excited state. The 4.332 MeV state is dominated by a 2.52369 (6) MeV to the first excited state but also exhibits a small branch through the second excited state with an energy of 1.39428 (7) MeV and $I_\gamma = 19.3\%$. Finally, the 4.350 MeV state has almost equal branching ratio between decays to the first and second excited state with energies of 2.54118 (6) and 1.41172 (4) MeV respectively.

Within the spectrum from this study the subsequent decays from the first and second excited states can be observed again. There appears two more peaks with centroids of 1.418 (9) MeV and 2.532 (8) MeV. Both of these centroids are in partial agreement with the decays from the 4.350 MeV state and therefore imply this is the dominant state within this triplet. The branching ratios also support this hypothesis, as the 4.332 MeV state exhibits a 1.394 MeV decay with an I_γ of only 19.3%, which

is not observed. This is also reflected in the intensity of the 1.129 MeV peak between the second and first excited states, which is populated by both lower energy transitions from the 4.332 and 4.350 MeV states, but only with significant intensity through the 4.350 MeV. It should be noted with the resolutions involved it is incorrect to rule out the population of the 4.332 MeV state but it is clear that the 4.350 dominates the excitation spectrum observed and as such will be treated within this study as a single state going forward.

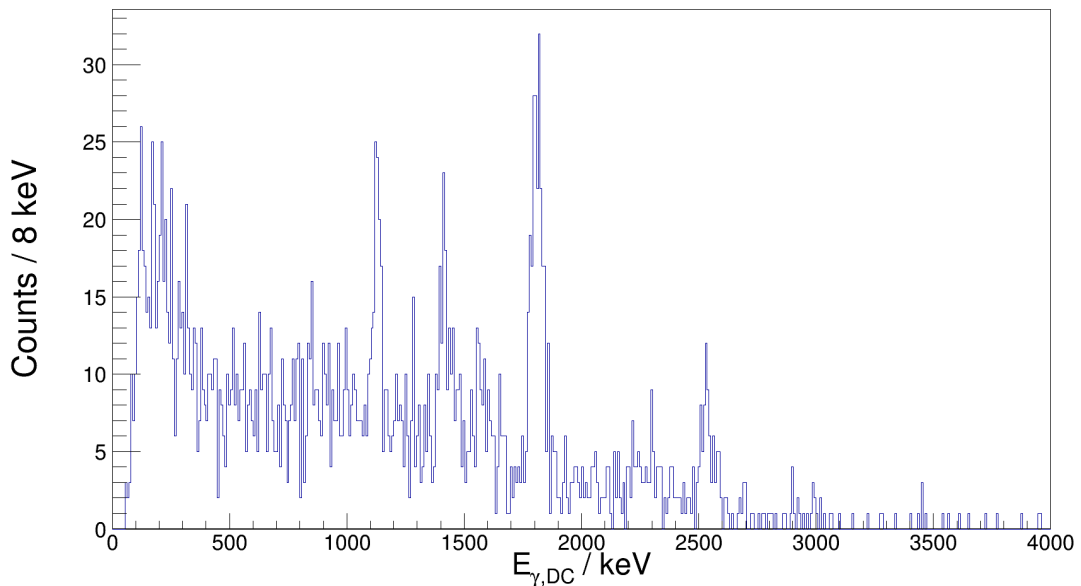


Figure 3.31: Coincident γ -ray energy spectrum for ^{26}Mg events with excitation energy between $4.15 < E_x < 4.55$ MeV.

3.8.5 $4.6 < E_x < 5.1$

There are three known excited states within this excitation energy region all of which have been observed previously in this reaction [133, 134]. Both of the earlier studies point towards a weakly populated 4.972.30 (13) MeV, 0^+ state alongside two excitations at 4.83513 (5) MeV, 2^+ , and 4.90144 (7) MeV, 4^+ , which should be populated with a relatively similar strength. The excitation energy spectrum from this study has a single peak centred around ~ 4.86 MeV. Fitting this feature as a single state using a Gaussian form produces a relatively good fit but has a standard deviation approximately ~ 50 keV larger than that of the nearby peaks at 3.941 and 4.350 MeV. This would suggest this feature does not correspond to a single state. Unfortunately, the resolution is too

poor to resolve this further.

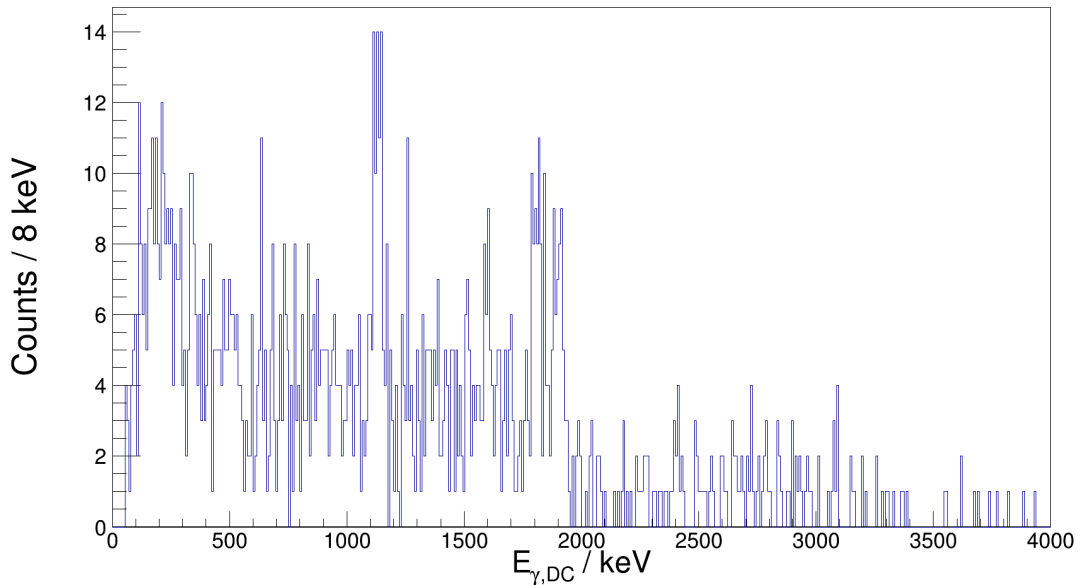


Figure 3.32: Coincident γ -ray energy spectrum for ^{26}Mg events with excitation energy between $4.6 < E_x < 5.1$ MeV.

Figure 3.32 shows the corresponding γ -ray information for this energy region. It is clear that this is a statistically poor spectrum which corresponds to the low statistic population observed from the excitation spectrum. There is no strong evidence from this figure that the 2.033 MeV decay from the 4.972 MeV which supports the previous weak population determinations. There is a poorly defined peak which provides evidence for the population of the 4.835 MeV state. The centroid of this peak at 1.900 (5) MeV is in good agreement with the dominant decay of 1.89672 (5) MeV decay to the second excited state. This would also explain the apparent 1.129 and 1.808 MeV peaks observed as the subsequent decays from the second excited state. The third state within this region of 4.901 MeV is dominated by a 3.092 (2) MeV decay to the first excited state [103]. Whilst the efficiency at this energy would be expected to be low, it is clear that there is a small peak corresponding at ~ 3.090 MeV of energy. It is therefore fair to summarize this energy band as including the population of both the 4.835 and 4.901 MeV states as previously seen in historical studies. It would be expected that these would have a near equal share of the events within the excitation energy spectrum.

3.8.6 $5.1 < E_x < 5.85$

The previous (d,p) studies by Burlein *et al.* [133] and Arciszewski *et al.* [134] identify four states of interest for this excitation energy band. These have energies of 5.29174 (6), 5.47605 (7), 5.711.2 (8) and 5.71591 (8) and J^π assignments of 2^+ , 4^+ , $(1^+, 2^+)$ and 4^+ respectively. Another state has been observed in other reaction studies that populate states in ^{26}Mg at an energy of 5.69108 (19) and with a J^π assignment of (1^+) . The triplet of states, 5.691, 5.711 and 5.715 MeV, have been previously unresolvable within (d,p) studies and in fact both Burlein *et al.* and Arciszewski *et al.* do not claim to have observed the reported 5.691 MeV state [133, 134]. There has also been speculation about an otherwise unobserved negative parity state (possibly the 5.711 MeV state) within this region due to the need of an $l = 3$ contribution to describe the differential cross sections of this triplet. However, these studies do point to the 5.715 MeV state being predominately populated by this reaction. In this study, the excitation energy region is best fit by using three Gaussian forms. This would imply the population of the 5.291, 5.476 and 5.711/5.715 MeV states.

Figure 3.33 displays the coincident γ rays for this excitation band. The proton statistics in this region is poor considering the assumption of 3 states being populated and this is reflected by the limited information observed in Figure 3.33. The decays from the first (1.808 MeV) and second states (1.129 MeV) are clearly visible within this spectrum. There is also a peak centred at 2.352 (5) MeV, which is in good agreement with the 2.353 MeV γ -ray decay from the 5.476 MeV state to the second excited state. The 5.476 MeV state decays via four γ -ray transitions with energies: 0.6405 (3), 1.15723 (6), 1.53449 (15) and 3.6674(5) MeV and intensities measured as: 10 (6), 100 (4), 51 (4) and 25 (2)% respectively. There is a small peak near to ~ 0.640 MeV but no clear evidence of any of the other energies. It is possible that the 1.157 MeV decay forms part of the upper edge of the 1.129 MeV peak and so is unresolvable, whilst the 1.534 MeV could be underneath the Compton continuum of the 1.808 MeV decay. This could also be the result of poor statistics given the branching ratio sharing of these four decays. A similar situation exists for the 5.715 MeV decay pathways, where the dominant 1.36554 (20) and 1.7740 (9) MeV are not observed in the current study. The 5.711 MeV state only has one observed transition to the 3.588 MeV, 0^+ state through a 2.122 MeV γ -ray transition which was not observed. This is expected considering the

poor proton statistics and low photopeak efficiency of the transition.

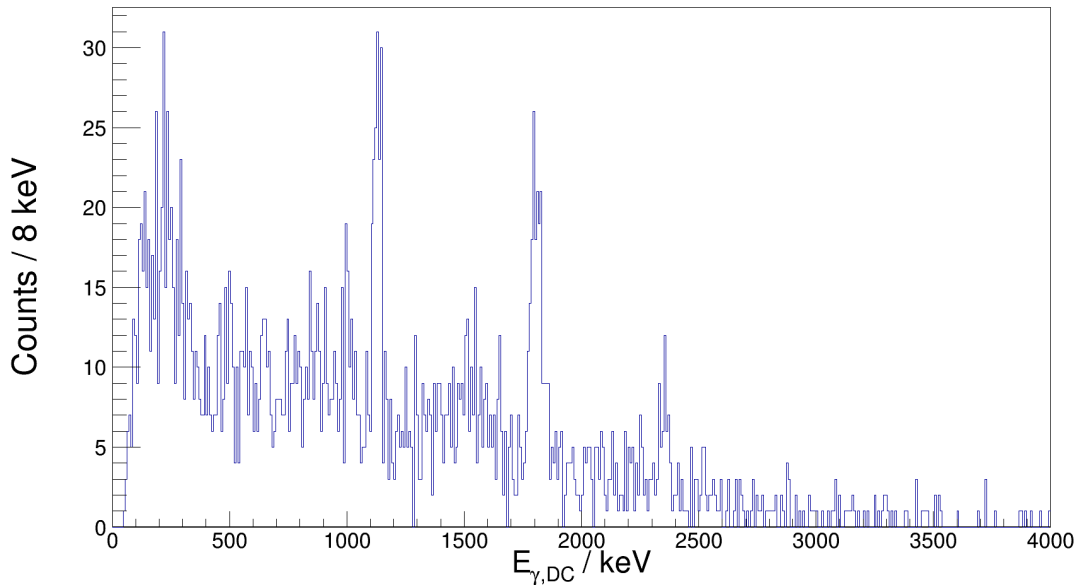


Figure 3.33: Coincident γ -ray energy spectrum for ^{26}Mg events with excitation energy between $5.1 < E_x < 5.85$ MeV.

3.8.7 $5.9 < E_x < 6.3$

Only two states are known within this excitation energy band, namely a 3^+ state with an energy of 6.12547 (5) MeV and a 0^+ state at 6.2562(14) MeV. In a previous study, it has been observed that the 6.125 MeV state dominates the spectroscopic strength in this region with the 6.256 being treated as a high energy tail contribution [133]. The excitation energy spectrum supports this conclusion with there being one clear feature that is well fit using a Gaussian form with comparable width to other isolated peaks within the spectrum.

Figure 3.34 displays the excitation energy gate γ -ray spectrum for this excitation energy feature. The 6.256 MeV state primarily decay to the first excited state (and the subsequent decay from this state is observed) via a 4.4471 MeV γ -ray decay which is not observed within this study. The efficiency would be extremely small for a photopeak at this energy and so this would not rule out the population entirely, however, there also exists a lower energy 0.5651 (13) MeV decay to the 5.691 MeV state which is also not observed. Whilst the intensity of this decay pathway is smaller by an order of magnitude this would be compensated for by the differences in photopeak efficiency for

this energy and is observed by the γ -ray spectroscopy study performed by Bhattacharjee *et al.* without observation.

In terms of 6.125 MeV state's γ -ray decay, the dominant decay pathway is to the 4.350 MeV state via a 1.77531 (6) MeV γ -ray. This is not resolved within this study from the 1.808 MeV decay from the first excited state to the ground, but this feature within Figure 3.34 is best explained by two peaks centred at 1.810 (6) and 1.776 (6) MeV. There is also evidence of a peak at 2.550 (15) MeV energy which is in good agreement with the subsequent 2.541 MeV decay from the 4.350 MeV state. The 1.411 MeV decay from this state is not observed above the Compton background from the 1.779 and 1.808 MeV γ -ray decays. The observed 1.129 MeV decay from the second excited state in this region can be explained by the cumulative population of the second excited state by a collection of the smaller γ -ray branches from the 6.125 MeV state, which are not observed directly.

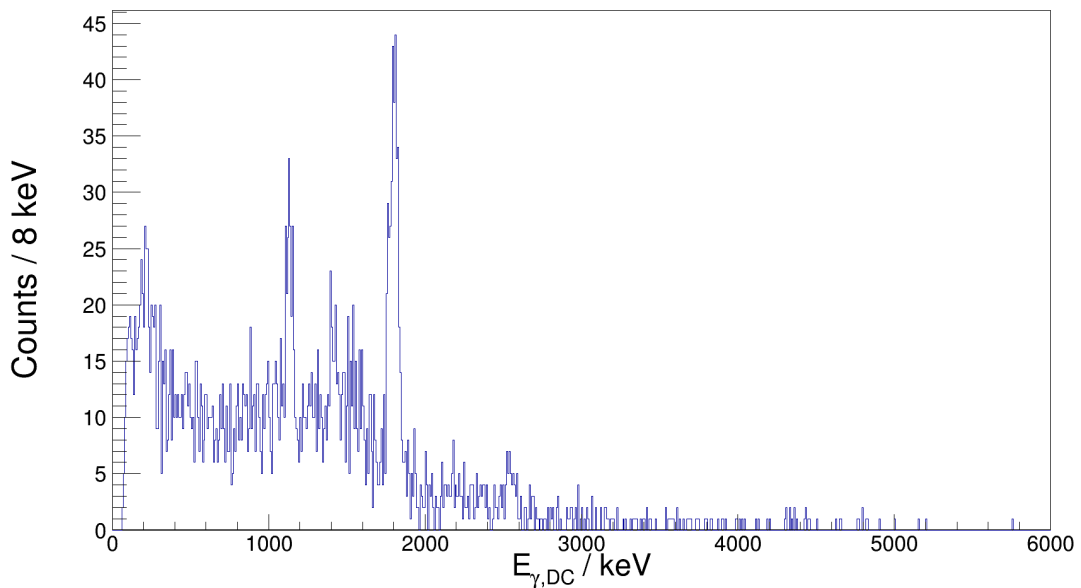


Figure 3.34: Coincident γ -ray energy spectrum for ^{26}Mg events with excitation energy between $5.9 < E_x < 6.3$ MeV.

3.8.8 $6.4 < E_x < 7.0$

Four states with excitation energy between 6.4 and 7.0 MeV have been observed in previous studies of the $^{25}\text{Mg}(d,p)^{26}\text{Mg}$ reaction, at 6.62294(14), 6.74513 (15), 6.87642 (5) and 6.9783 (8) MeV [117, 134]. Most of the spectroscopic strength has been ob-

served in the 6.745 and 6.876 MeV states with the other two states only being weakly populated in comparison. The excitation spectrum from this study does not have the same resolution as the previous studies and as result this region appears to be one peak with a low energy tail that points towards at least two separate state population. Fits of this singular “peak” produce a standard deviation value ~ 80 keV wider than the fit for the 6.125 MeV state, as the proton laboratory energies are similar for these energies the excitation spectrum implies at least three states observed. The 6.978 MeV would be observed between the two major features at ~ 6.8 and ~ 7.25 MeV and as such is not resolvable from the proton information. This implies that the states observed are the 6.622, 6.745 and 6.876 MeV states.

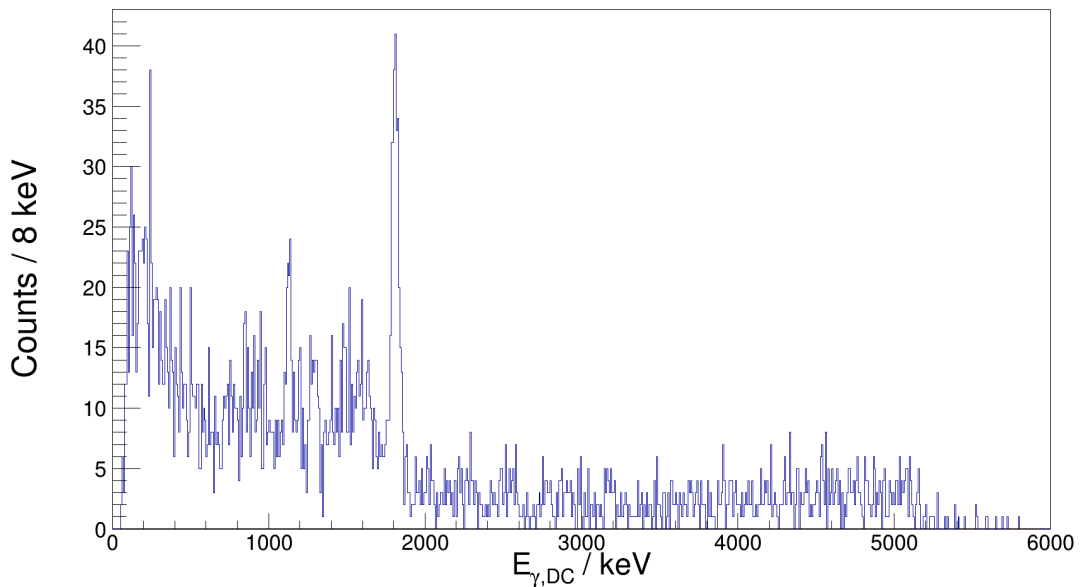


Figure 3.35: Coincident γ -ray energy spectrum for ^{26}Mg events with excitation energy between $6.4 < E_x < 7.0$ MeV.

States at these excitation energies exhibit γ -ray transitions to either the ground, first or second state, therefore, the γ rays are likely to have an energy above 4 MeV. The photopeak efficiency of this set-up at these energies mean they are very unlikely to be observed and that state assignment will be made on circumstantial evidence from subsequent state decays. Figure 3.35 shows the γ -ray information in coincident with the excitation energy band. The clear photopeaks at 1.128 (3) and 1.811 (3) MeV are in good agreement with the transitions between the second and first excited states, and first and ground states respectively. There is a possible photopeak with a

centroid of 5.153 (3) MeV, however, the error on this is most likely an underestimate considering the energy calibration is based on ^{152}Eu and ^{60}Co sources with a maximum energy of 1.408 MeV and so will not be well constrained at these much larger energies. Therefore this photopeak could be related to the 5.092 MeV decay from the 6.876 MeV state, as this state predominately decays into the first and second states, the confirmed population of this state would explain the 1.129 and 1.808 MeV decays also observed. Whilst there are no clear direct transitions from the 6.745 MeV state observed within this spectrum, the previously seen spectroscopic strength dominance of the 6.876 and the high energy decays from the 6.745 does not rule out the population of the 6.745 MeV state with no observable photopeaks within this study. No photopeaks previously observed from the 6.622 MeV decay within this study either, but the excitation energy spectrum implies very minimal population of this state making it unlikely for transitions to be observable with the limited γ -ray efficiency.

3.8.9 $7.0 < E_x < 7.45$

The excitation energy spectrum contains the most populated feature of the overall plot and which dominates this excitation space. When fit with a singular peak, this feature exhibits a centroid of 7.233 (9) keV which is in good agreement with a previously observed triplet containing the states: 7.24649 (17), 7.26140 (4) and 7.28282 (6) MeV [134]. This feature is not well fit by a singular Gaussian peak, appearing asymmetric on the higher energy edge, suggesting one of the lower excited states has the greater population than the higher. Previous studies have also observed the population of a 7.34886 (6) MeV state which is likely to be populated within this study but is unresolvable from the protons here. States at 7.0619 (2) and 7.09968 (13) MeV excitation energy have been populated through other reaction mechanisms and β -decay studies. There evidence within the Arciszewski et al. (d,p) reaction for the population of the 7.099 MeV state, but this was previously attributed as a background peak. There is a slight increase observed at the low energy tail of this triplet feature which could be evidence for this state within study, but more statistics would be required for a definitive statement.

The excitation energy gated γ -ray energy spectrum corresponding to this excitation energy band is shown in Figure 3.36. The clearest peaks within this spectrum

are the decays from the first, second and third excited states at 1.808, 1.129 and 1.003 MeV. The high energy Comptons observed would give evidence to a high energy γ -ray decay with significant intensity such as the 5.452 MeV decay from the 7.261 MeV state. There is some evidence of the 1.411 MeV decay from the the 4.350 MeV state which is supported by a broad feature at ~ 2.5 MeV. This state would be populated by transitions from the 7.246 MeV state, one of the triplet states, but there is limited evidence of the 2.411 or 2.896 MeV main transition energies from this state. There is limited evidence for any other photopeaks with the limited statistics within this energy region. The circumstantial evidence from the subsequent decays does not help very much in the identification of state population as these states decay into the same states and with states possibly contributing it is difficult to pick these apart through intensity arguments.

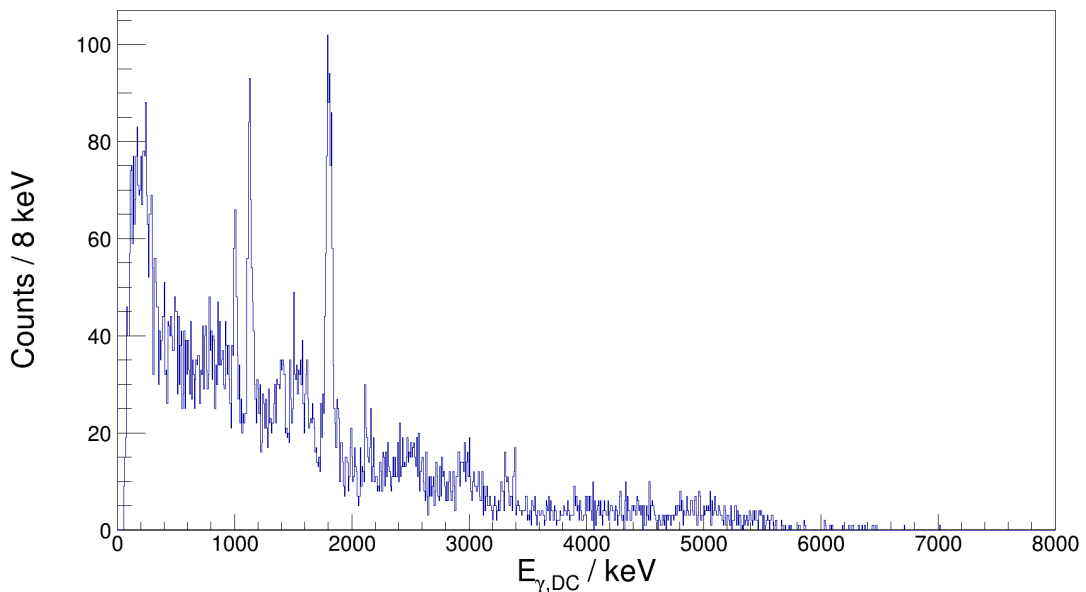


Figure 3.36: Coincident γ -ray energy spectrum for ^{26}Mg events with excitation energy between $7.0 < E_x < 7.45$ MeV.

3.8.10 $7.45 < E_x < 8.0$

This is the final excitation energy region with states previously observed through the (d,p) reaction mechanism in the study by Arciszewski *et al.*. Seven states were previously reported within this region by Arciszewski *et al.* with five of these between 7.67 and 7.82 MeV, overlapping each other with the resolution provided by a normal

kinematics experiment [134]. A similar conclusion could be drawn from the excitation spectrum in this study because there is one feature covering approximately this entire region with no clear resolved states. It is clear that there is a slight increase in events close to 7.8 MeV of excitation but none of the previously reported states can be excluded by the evidence within the spectrum.

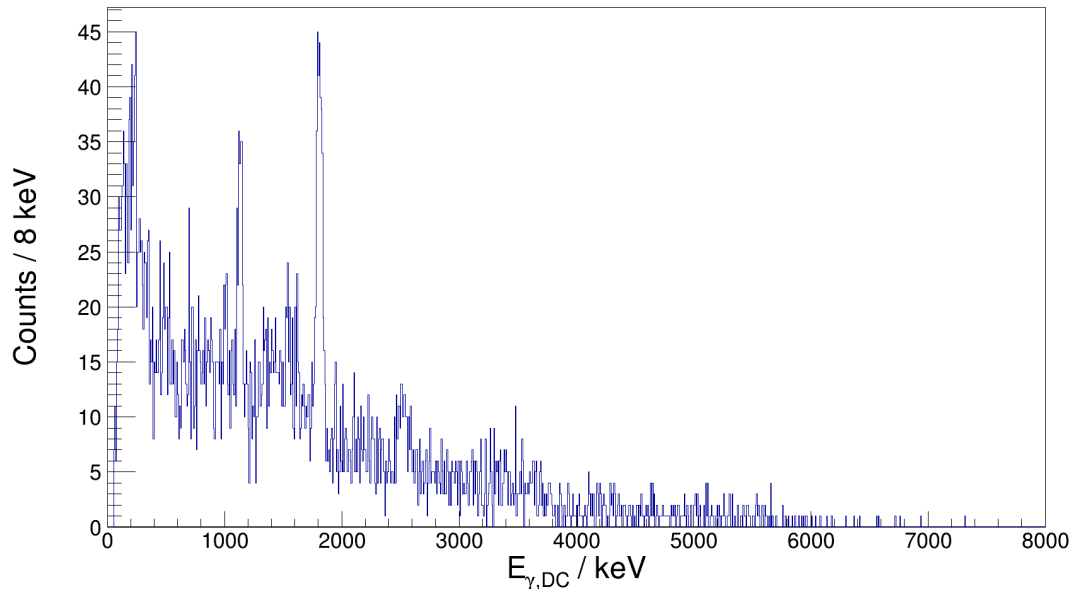


Figure 3.37: Coincident γ -ray energy spectrum for ^{26}Mg events with excitation energy between $7.5 < E_x < 8.0$ MeV.

The γ -ray data gated on this excitation band, see Figure 3.37, also supports the low population of a number of states within this region, which in combination explain the excitation spectrum feature. There is no clear photopeak observation of any direct γ -ray transitions from states within this region suggesting no one state dominates the population within this peak, in fact the γ -ray data provides little help in resolving this excitation feature. As seen in other coincident spectra, the decays from the first, second and third excitations are evident, but unfortunately many of the states within this region eventually decay through these lower levels and so intensity arguments are of little help. There is a broad peak centred at 2.523 (9) MeV which could be evidence for the secondary population of the 4.332 MeV state, assuming this is a singular resolved peak. The simplest explanation for this peak would be a significant population of the 7.8178 (7) MeV state which has been observed to predominately decay to the 4.332 MeV state whilst not significantly contributing to other γ -rays observed. The only

decay path for this state is a 6.0087 MeV transition (not observed) to the first excited state, the subsequent decay from this first excited state to the ground state is clearly observed here.

3.8.11 $8.0 < E_x < 8.4$

This is the first excitation band with no previously reported states populated through the $^{25}\text{Mg}(d,p)^{26}\text{Mg}$ reaction. It should be noted that whilst Arciszewski *et al.* did not report any states in this region, the proton spectrum published from their study does have two further peaks without state assignments which could be excitations within this region instead of being part of the background reactions within that study [134]. This study exhibits a singular peak-like feature within this region with a centroid of 8.161 (3) MeV which if assumed to be a single state would imply population of a previously reported 8.18493 (15) MeV state. However, the standard deviation value of a singular peak assumption fit is ~ 15 keV larger than that of the well-known triplet at 7.2 MeV, which could imply more than one unresolvable state.

Figure 3.38 shows the excitation energy gate γ -ray spectrum for this band. Only two clear photopeaks are observed which are in good agreement with the subsequent decays through the second and first excited states. The ratios of the 1.129 and 1.808 MeV within this spectrum is similar to the spectrum gated upon the second excitation state, see Figure 3.29, which would imply that this region predominately populates the 2.938 MeV state directly. In comparison to the second excitation gated spectrum there is an excess of counts within the 1.808 MeV decay peak implying a second decay path either directly to the first excited state or through states that bypass the second excited state to the first. The fraction $N_{\gamma=1.808}/N_{\gamma=1.129}$ for the second excited state band was determined as 0.62 (2) whilst the same fraction for this excitation is determined as 1.28 (3) implying that the first excited state is populated twice the population of the second excited state. This evidence does not support the population of the 8.184 MeV state which has known I_γ intensities of 28 (4) and 100 (4) for decays into the second and first excited states respectively, which would equate to a ratio of 4:1 population of the first excited state with respect to the second. This corroborates the possible two excitation possibility discussed from the excitation spectrum. Two other states within this region are known to populate the second excited state, these

are the 8.034 (2) MeV and 8.25058 (16) MeV states. Two other states of note here are the 8.052 (7) and 8.22731 (MeV) state which decay primarily to the first excited state or direct to the ground state. The lack of Compton scattering events with energy larger than 7 MeV, within Figure 3.38, would not support the population of the 8.227 MeV state which exhibits an 8.225 MeV transition directly to the ground state.

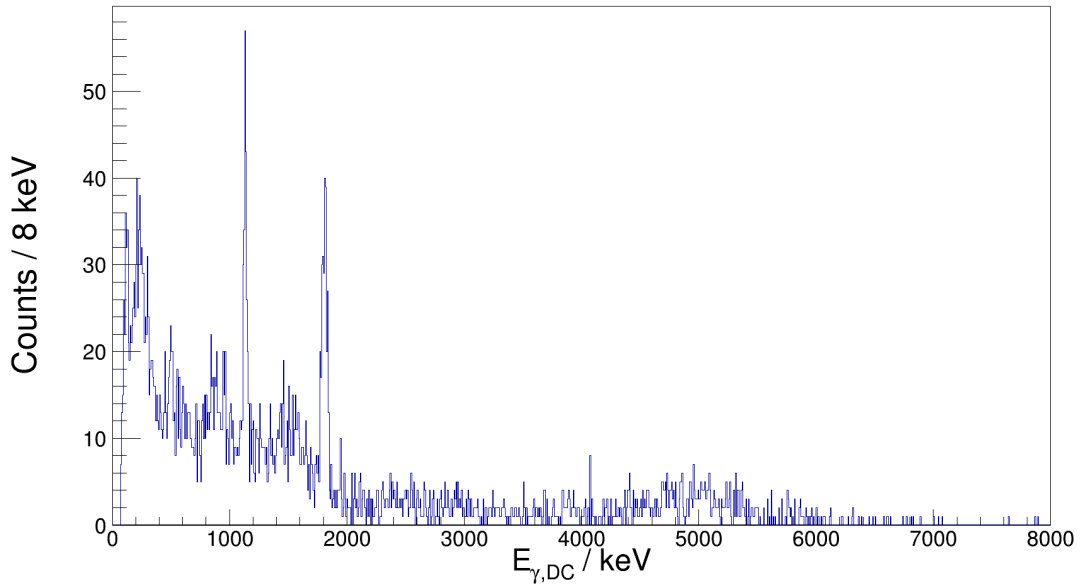


Figure 3.38: Coincident γ -ray energy spectrum for ^{26}Mg events with excitation energy between $8.0 < E_x < 8.4$ MeV.

3.8.12 $8.5 < E_x < 9.7$

The level density within this excitation energy region significantly affects the resolving power of this study within this band. The first observation to note is that the excitation spectrum does not return close to background within this band, implying reasonable spectroscopic strength across the entire band with no individual resolution of states. It is also clear that the majority of the population is observed within the small energy band $8.8 < E_x < 9.6$. With no guidance from previous (d,p) studies in normal kinematics and the high level density it is hard to make any conclusions about individual state within this region based on the observed protons.

A similar picture exists within the coincident γ -ray spectrum for this region, shown in Figure 3.39. The majority of states within this region exhibit large energy transition ($E_{\gamma} > 3$ MeV) where the efficiency of the HPGe detectors within this

study is minimal. As a result there is minimal direct transition energy evidence. As previously discussed it is a relatively common feature for states within ^{26}Mg to decay via the first, second or third excited states, which is also observed within this region. Also observed within this region is the 1.41 and 2.54 MeV transitions from the 4.350 MeV state. This could be circumstantial evidence for the 9.574 MeV state which has an observed strong transition to the 4.35 MeV state.

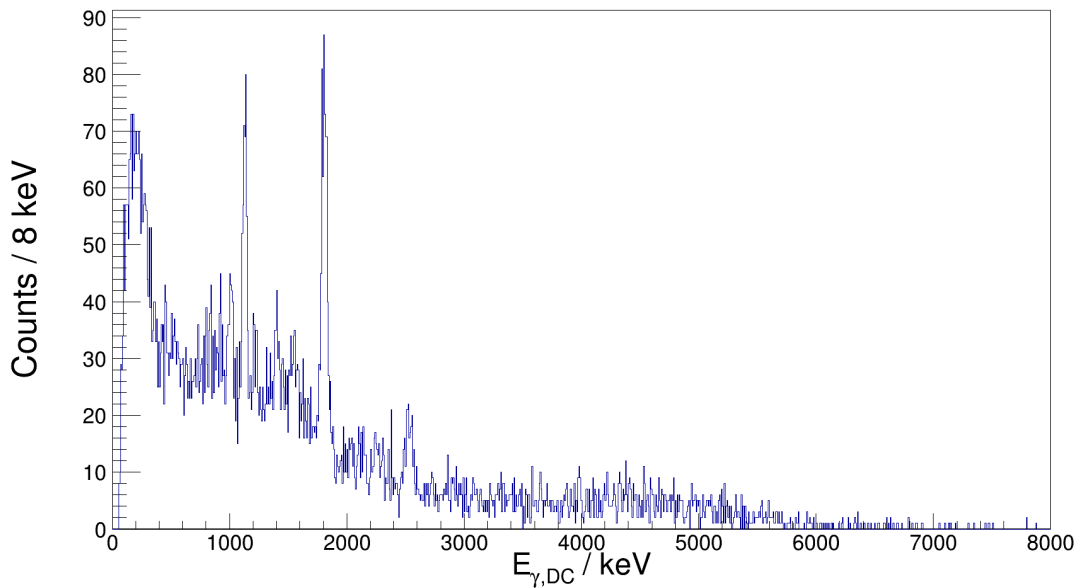


Figure 3.39: Coincident γ -ray energy spectrum for ^{26}Mg events with excitation energy between $8.5 < E_x < 9.7$ MeV.

3.8.13 $9.9 < E_x < 11.5$

The final energy band can be described in a similar way as the previous energy band. There is a clear feature that suggests a number of states populated but are not resolved within this study. Considering the state population appears to end here, it is possible to say something about the final peak-like feature centred at ~ 10.9 MeV by constraining the Gaussian form using the trailing edge of the edge and assuming that there is no small population within this tail. A Gaussian form centred on 10.952 (10) MeV which is in partial agreement with a previously reported 10.949 MeV, 1^- state. Figure 3.40 shows the coincident γ -ray spectrum for this excitation energy band. There are no observed direct transitions from states within band but circumstantial evidence for the population for states that decay into the first, second and 4.350 MeV states. Within

this excitation band there are many states without previously observed γ -ray decays, another complication within the assignment of the broad feature within this band.

It is of note that the overall goal of this experiment was to populate states above the neutron separation threshold, $S_n = 11.093$ MeV, that could be important resonances states for the $^{22}\text{Ne}(\alpha, n)^{25}\text{Mg}$ astrophysical reaction. The experimental beam energy was selected to be 10 MeV/ mu such that states above this energy could be populated and there is no evidence that the detection systems used within this study had any physical or electrical threshold preventing the observation of these states. It is therefore important to note that it would appear that there is no evidence for states above this region with a strong spectroscopic strength or with large γ -ray partial width. It is possible, due to the gating upon ^{26}Mg ions within the Oxford focal plane detector, that states above this threshold were populated but decay via neutron emission before the focal plane and so would not be included within this analysis.

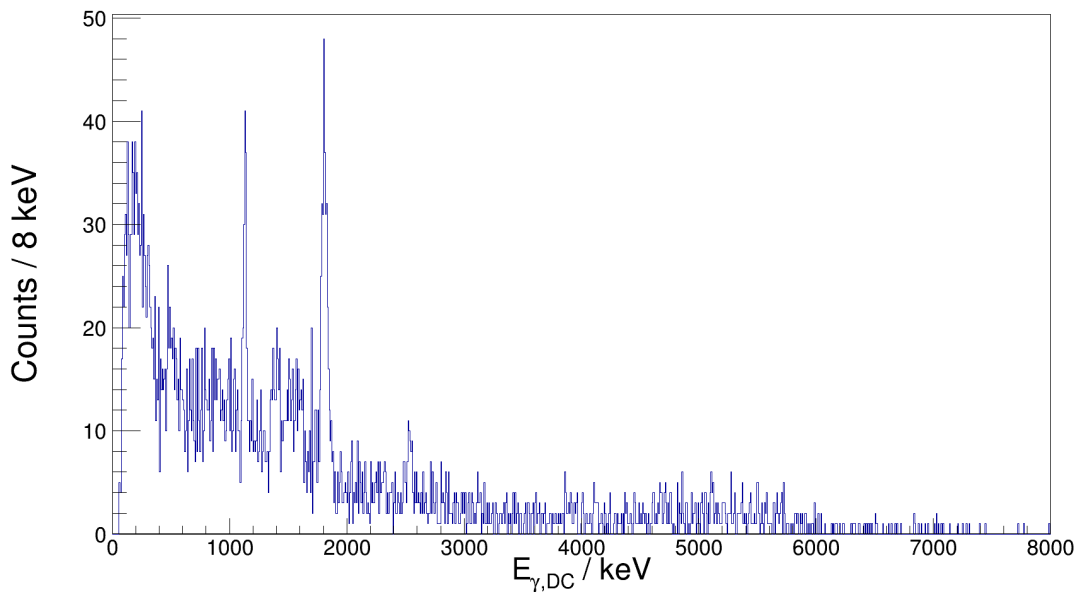


Figure 3.40: Coincident γ -ray energy spectrum for ^{26}Mg events with excitation energy between $9.9 < E_x < 11.3$ MeV.

3.8.14 State Population Summary

The previous subsections detailed the state population identifications made using the combined TIARA particle and HPGe γ -ray information from this study. Table 3.2 presents the summarised state population from this study based on clear direct γ -ray

transitions from the state.

$E_{x,i} / \text{MeV}$	J^π	E_γ / MeV	$E_{x,f} / \text{MeV}$
1.809	2^+	1.809	0.0
2.938	2^+	1.129	1.809
		2.938	0.0
3.941	3^+	1.003	2.938
		2.132	1.809
4.350	3^+	1.411	2.938
		2.541	1.809
4.835	2^+	1.896	2.938
5.291	2^+	2.353	2.938
5.715	4^+	1.365	4.350
6.125	3^+	1.775	4.835

Table 3.2: Table summarising the states populated within this experiment. Only states with clear direct transitions from the excited state observed are presented. States without clear γ -ray information were excluded from this table.

3.9 Constructing Proton Angular Distributions

For a given excited state, the variation in the differential cross section with angle (either in the laboratory or centre-of-mass frame) is known as the angular distribution. The shape of these distributions is determined by the shell-model orbital which the transferred neutron is transferred into the final nucleus. It is possible to infer the l -value or total transferred angular momentum of this transfer by comparing the angular distribution from the data to those from theoretical calculations performed using a specific shell-model orbital. In this study the theoretical distributions were calculated using the TWOFNR ADWA reaction code.

The experimental differential cross section was determined by quantifying the number of counts within a given excitation energy peak within a constrained solid angular range. This is defined by the following equation:

$$\frac{d\sigma}{d\Omega} = \frac{N_{det}}{\epsilon \cdot I \cdot t \cdot d\Omega}, \quad (3.20)$$

where N_{det} is the number of counts within the excitation energy peak, ϵ is the total detection efficiency, I is the number of incoming beam particles, t is the number of target scattering particles and $d\Omega$ is the solid angular range considered for the peak. The solid angular range is between the angles θ_{min} and θ_{max} is defined as $2\pi(\cos(\theta_{min}) - \cos(\theta_{max}))$. The total efficiency is the product of various characteristic efficiencies of this set-up. There are three efficiencies considered for the composition of the total detection efficiency, these are: the geometric efficiency (ϵ_g), the live time (ϵ_{lt}) and the intrinsic detection efficiency of the detection material which in the case of Silicon detectors is approximately unity. Therefore, Equation 3.20 can be rewritten as:

$$\frac{d\sigma}{d\Omega} = \frac{N}{\epsilon_g \cdot \epsilon_{lt} \cdot I \cdot t \cdot d\Omega}. \quad (3.21)$$

At this point it is useful to define two new terms, $d\Omega'$ and C . The term $d\Omega'$ is the product of ϵ_g and $d\Omega$ and accounts for where the geometric solid angle annulus defined in $d\Omega$ is reduced by non-functioning detectors within that annulus, i.e. the geometric efficiency, ϵ_g . C is a normalization factor relating the number of counts within a excitation peak to its differential cross section and is defined as the product of $\epsilon_{lt} \cdot I \cdot t$. Therefore, C summarizes the electronic live time and the experimental luminosity.

3.9.1 Beam Normalisation

The process of beam normalisation encapsulates the beam and target ion information from an experiment, in which, the beam current could not be directly measured. This process requires a well known differential cross section from another observed reaction process to be compared to data. In the present work, the elastic scattering differential cross section was calculated and then compared to measured deuterons detected within the Barrel detectors. This allows for the beam normalisation factor, C , to be determined using Equation 3.20 rearranged for C where $d\sigma/d\Omega$ is now a calculable variable, see Equation 3.22. C is therefore independent of the reaction type being studied, as it is the definition of the beam and target information from the experiment which applies to all reaction mechanisms ongoing.

$$C = \frac{N_{det}}{\epsilon_g \cdot d\Omega \cdot d\sigma/d\Omega} = \frac{N_{det}}{d\Omega' \cdot d\sigma/d\Omega}. \quad (3.22)$$

It was not possible within this set-up to measure the elastic scattering reaction in its totality, so the value of C is determined within a selection of small laboratory energy defined integrals, or slices. It was also important to select energy slices that avoid the deuteron punch-through threshold, above this threshold no deuterons would be observed and near to this the probability of the determined N_{det} being a misrepresentation increases. Figure 3.41 displays the chosen energy slices used for determining N_{det} for the $^{25}\text{Mg}(d,d)^{25}\text{Mg}$ elastic scattering data. Projections of θ_{LAB} across these energy slices were created showing the elastic scattering events atop a large background. These events were then fit using an asymmetric Gaussian atop an exponential background, N_{det} was determined as the integral of the asymmetric Gaussian function.

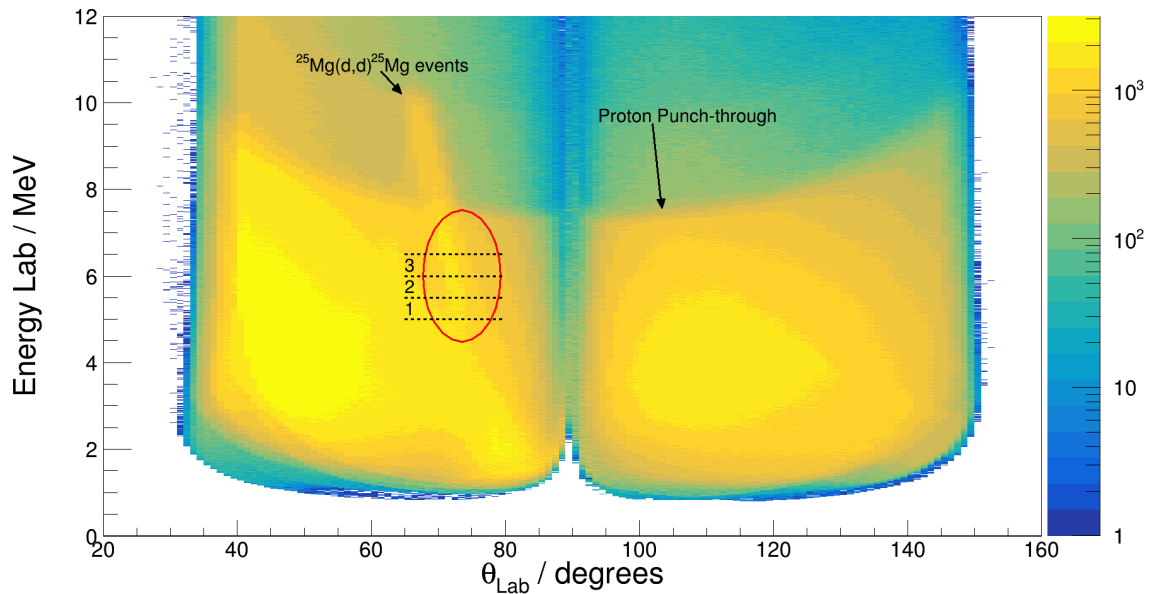


Figure 3.41: Plot of E_{LAB} vs θ_{LAB} used for determining the cross section of the $^{25}\text{Mg}(d,d)^{25}\text{Mg}$ scattering reaction. The region indicating the scattering events are highlighted as well as the energy projections used for the calculation of the beam normalisation factor, C .

The values $d\Omega'$ and $d\sigma/d\Omega$ are defined within an angular range determined by the energy slice being examined. The observed laboratory energy of the deuteron has a well defined relationship to the emission angle from the reaction centre. Therefore the angular range of the slice is determined by the laboratory energies at the extreme

values of the slice. The value of $d\Omega'$ is defined by the product of the solid angle annulus, defined by the angular range of the energy slice, and the geometric efficiency of the Barrel detectors. In this study, the geometric efficiency was determined through high statistics Geant4 simulations with a deuteron source, placed at the minimised target position as described in Section 3.6, decaying isotropically within the centre-of-mass frame of the reaction. The key output of this simulation was the detection efficiency of deuterons as a function of the centre-of-mass emission angle. The average detection efficiency within a given energy slice was then extracted and combined with the solid angle annulus to define the efficiency corrected solid angle, $d\Omega'$ for each energy slice. Table 3.3 summarises all of the relevant values for the determination of $d\Omega'$.

Slice	$\theta_{CM,min}$	$\theta_{CM,max}$	$d\Omega / \text{sr}$	ϵ_g	$\Delta\epsilon_g$	$d\Omega' / \text{sr}$	$\Delta d\Omega' / \text{sr}$
1	31.1	32.8	0.0775	0.589	0.058	0.0456	3.9×10^{-3}
2	32.8	34.3	0.0772	0.592	0.057	0.0457	3.8×10^{-3}
3	34.3	35.8	0.0771	0.589	0.059	0.0455	3.9×10^{-3}

Table 3.3: Table outlining relevant values in determining the solid angle corrected for non-contributing regions of the annulus, due to non-functioning detectors or space between neighbouring detectors.

The differential cross section for the $^{25}\text{Mg}(d,d)^{25}\text{Mg}$ reaction is composed of scattering through Coulomb and nuclear processes, which are calculated separately. LISE++ was used to determine the Rutherford scattering differential cross section, or the Coulomb process, as a function of centre-of-mass emission angle. The FRESCO reaction code was used to determine the nuclear process component of the scattering differential cross section as a fraction of the Rutherford differential cross section [136]. The product of these two processes describes the total differential cross section of this elastic scattering channel. The value of $d\sigma/d\Omega$ was then determined by the average value of this functional form within the angular range defined by the energy slice. Figure 3.42 summarises the total and individual differential cross sections of the $^{25}\text{Mg}(d,d)^{25}\text{Mg}$ reaction channel.

Using Equation 3.22 and the values presented in Table 3.4 the values of C were calculated within each investigated slice. The final value of C used within this analysis was determined using the average of the three investigated slices, yielding a final value of

$C = 22592 \pm 1340$. As previously discussed the value of C is equal to the product of the number of scattering centres within the target, the beam flux upon the target and the total experimental live time. With C determined it is possible to quantify the average incoming beam flux over the experiment. Given that a CD_2 target with a thickness of $197 \mu\text{gcm}^{-2}$ was used and that the experimental run-time was ~ 310547 seconds, it is estimated that average incoming beam flux was 4.91 particles per second. This is assuming a negligible dead-time, which given TIARA was designed for experimental luminosities of 1×10^9 pps is reasonable.

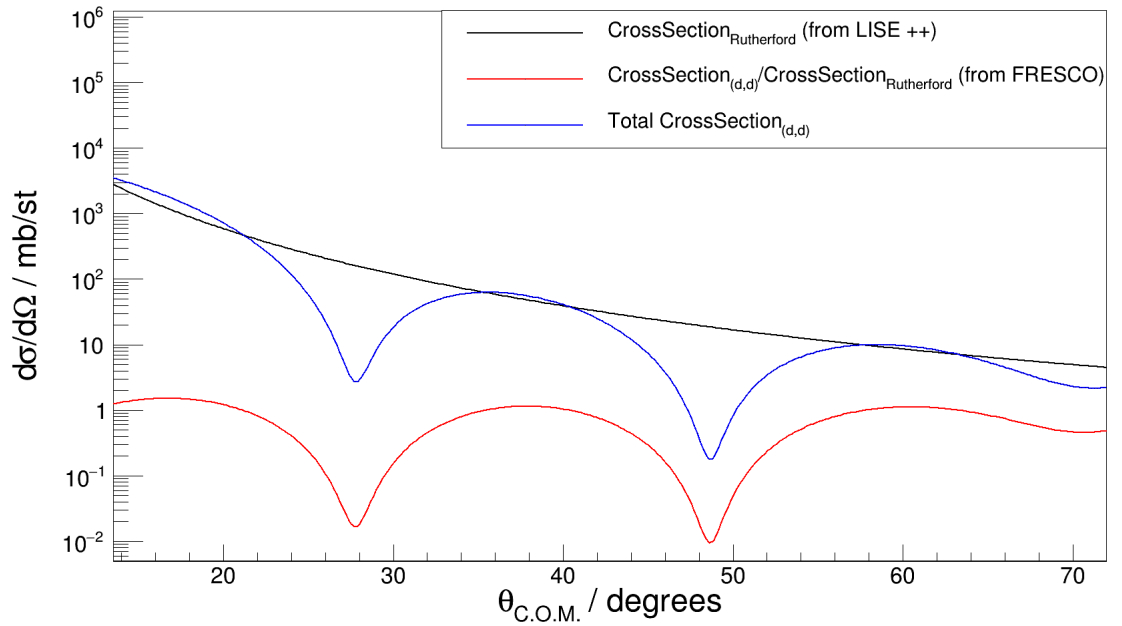


Figure 3.42: Figure displaying the total differential cross section for the $^{25}\text{Mg}(d,d)^{25}\text{Mg}$ scattering reaction and the individual components as calculated from FRESCO and LISE++.

Slice	N_{det}	ΔN_{det}	$d\Omega' / \text{sr}$	$\Delta d\Omega' / \text{sr}$	$d\sigma/d\Omega / \text{mb/sr}$	$\Delta d\sigma/d\Omega / \text{mb/sr}$
1	41999	205	0.0456	3.9×10^{-3}	42.0	4.2
2	55892	236	0.0457	3.8×10^{-3}	56.3	4.3
3	68178	261	0.0455	3.9×10^{-3}	62.2	4.5

Table 3.4: Table outlining the values used to determine C , or the normalisation factor, and the final extracted values.

3.9.2 Calculating $d\Omega'$

The construction of angular distributions depends upon defining distinct angular sub-ranges within the total observed angular ranges, within which the differential cross section is independently calculated as per Equation 3.20. These angular ranges are contribute to the differential cross section by defining the solid angle coverage through their extreme values. The product of this solid angle and the geometric efficiency provides a determined $d\Omega'$.

The only detection system used within this study for construction of angular distributions was the Hyball detector, with the Barrel being used only for the normalisation as discussed previously. The Hyball is physically divided into 16 annular rings, which in theory could be used to simply define separate angular ranges using various combinations of neighbouring rings. In practise, the outermost 6 rings are geometrically shadowed by the upstream edges of the Barrel detector, therefore only the inner 10 rings are illuminated by target reactions. This would still provide a maximum of 10 angular ranges within the Hyball which could be used for angular distribution construction. Within this study the Hyball data was split into 7 angular regions, such that the remaining extreme edges of the Hyball were avoided in order to avoid any unforeseen detector “edge effects”. In the case of a perfectly central target position with respect to the Hyball, this would simply be defined by the ring shape of the Hyball as discussed, discounting the first, ninth and tenth rings. In the current case with an non-central target, these same rings were in general avoided for the same reasons.

In a similar methodology to the process of the beam normalisation, the geometric efficiencies associated with these defined angular regions were determined through high statistics Geant4 simulations of the $^{25}\text{Mg}(d,p)^{26}\text{Mg}$. Within this simulation, protons were emitted isotropically within the centre-of-mass frame with any non-functioning channels disabled and with the inclusion of the minimised beam position and vector. Figure 3.43 represents the determined geometric efficiency from these simulations as a function of the laboratory angle for the ground state excitation of ^{26}Mg . The overall geometric efficiency for a given angular range was then determined as the average efficiency value over that range. These were then multiplied by the solid angle of that range in order to determine values of $d\Omega'$ associated with each range. This process was repeated for each observed excitation within this study to account for the changing

observed proton emission kinematic energy/angle function.

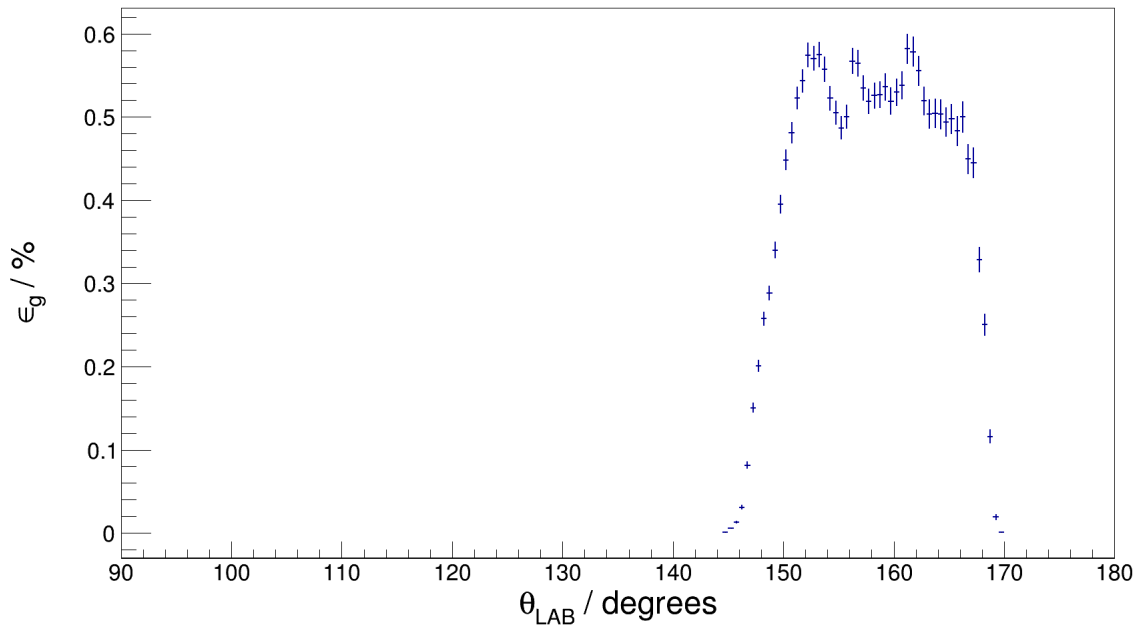


Figure 3.43: Plot of the geometric efficiency as a function of laboratory angle for the Hyball as determined through high statistic Geant4 simulations. The shape of this plot, within the confines of the Hyball angular range, is determined by the various faulty channels within this study. Where the efficiency tends to zero defines the extreme angles wherein the Hyball is illuminated by protons from the target position, either due to the edge of the detector or the shadowing by the Barrel detectors.

3.9.3 Calculating N_{det}

The number of detected counts (N_{det}) is determined by fitting the various states observed within the excitation energy spectrum. For each angular range, the excitation energy spectrum for ^{26}Mg events was gated upon the seven distinct angular ranges within the Hyball as described previously, therefore producing seven variants of this spectrum. Within each of these angle gated spectra the various states were fitted and integrated over in order to determine the number of detected counts within each angular range. Two examples of these angular gated spectra are shown in Figure 3.44

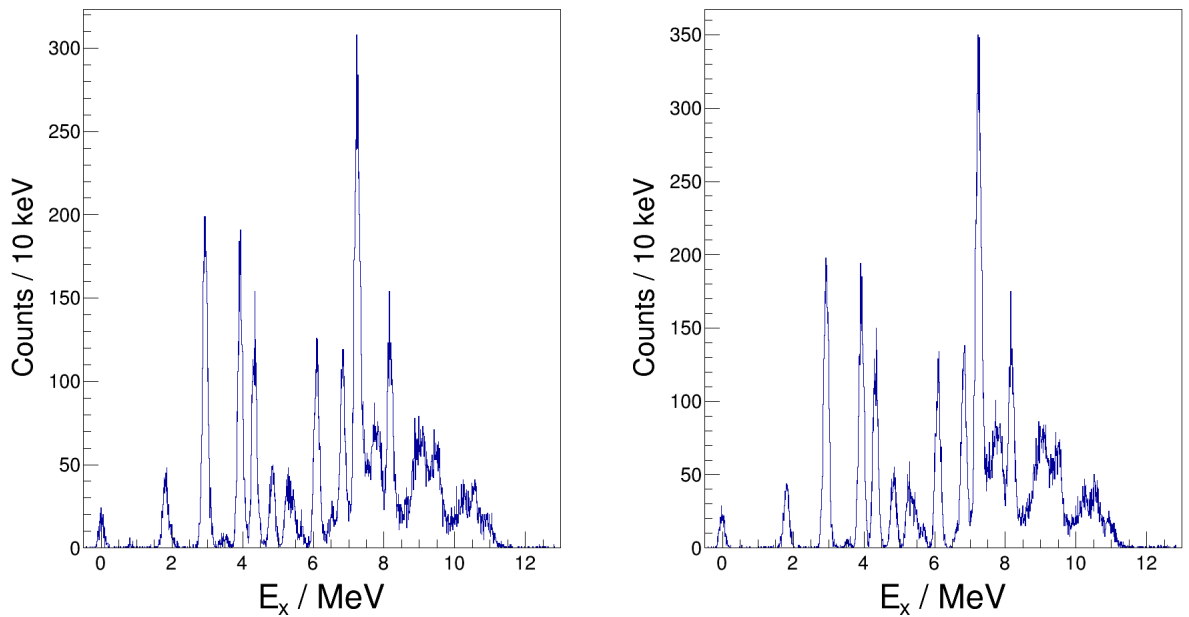


Figure 3.44: ^{26}Mg excitation energy spectrum from two separate angular ranges within the Hyball detector. The fitting of the various peaks within these spectra, allowed for the various N_{det} values to be extracted and differential cross section values to be determined.

Each excitation peak observed was fit using a Gaussian function and where multiple states were not fully resolved, these were fit simultaneously ensuring the width of the peaks were kept the same. As the excitation energy increased the allowed width of these Gaussian function were increased to match the proportionality between excitation energy and resolution. Where possible the widths of states in a cluster were tied to a nearby “resolved” state. The fit parameters of these Gaussian functions then allowed for the number of counts within the peak to be calculated.

3.9.4 Angular Distributions

This subsection will discuss the angular distributions extracted for the excited states within this study. These are analysed by comparisons to theoretical angular distributions using relevant l -transfer values. Within this study these theoretical angular distributions were calculated using the TWOFNR ADWA reaction code [137]. This is a three-body method that incorporates deuteron breakup and proven to be a good description of transfer reaction, it was discussed in more detail in Section 2.8.3. The Koning-Delaroche global optical model[138, 139] was used for the nucleon-target optical

potential and the Reid SC np interaction was used to describe the deuteron wavefunction. A central real Woods-Saxon potential with a radius $r = 1.25$ fm, a spin-orbit term $V_{SO} = 6$ MeV and a diffuseness parameter $a_0 = 0.65$ fm was used, with the same geometry in the central interaction. The results are compared to historical studies where appropriate.

3.9.4.1 $E_x = 0$ MeV

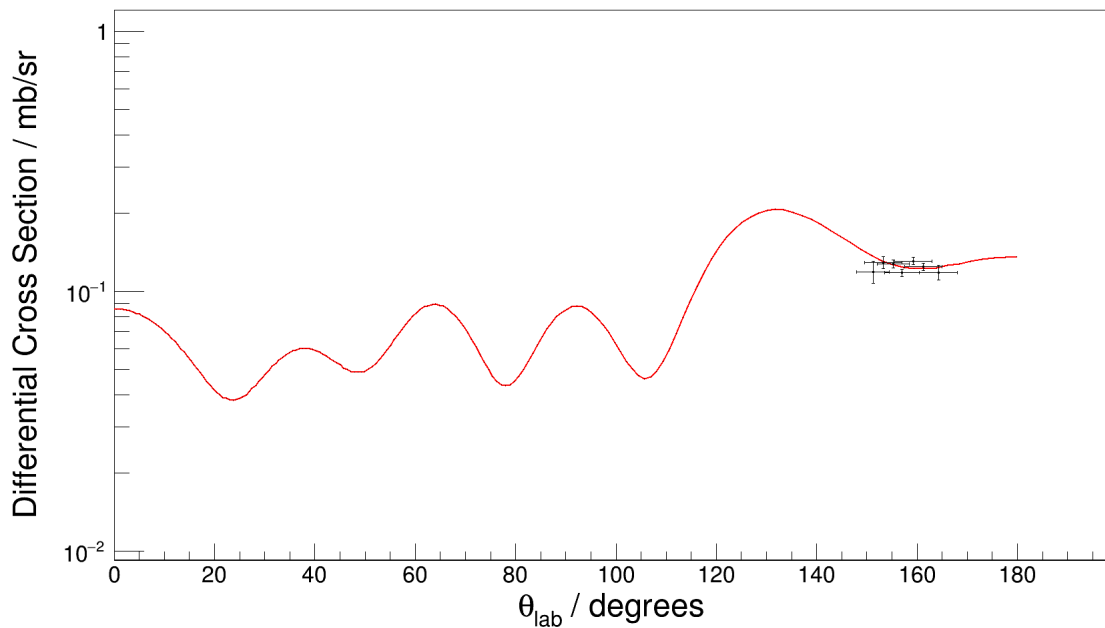


Figure 3.45: Angular distribution for the ground state. The red curve, produced by the TWOFNR reaction code, shows the theoretical angular distributions corresponding to the $l = 2$ transfer into the $0d_{\frac{5}{2}}$.

Naturally the first angular distribution determined from this study is for the population of the ^{26}Mg ground state. This state has a spin-parity of 0^+ as is commonplace with even-even nuclei, as such the single particle transfer interpretation of this is the transfer of a neutron into the $0d_{\frac{5}{2}}$ shell model orbital carrying two units of angular momentum, or $l = 2$. Figure 3.45 shows the differential cross section as a function of the laboratory angle. The ground state is a relatively simple case study within ^{26}Mg with only one possible l -value for the description of the transfer and being a well known final spin parity such that the l -value is known. As can be seen within Figure 3.45, there is good agreement between the differential cross section extracted for the seven angular ranges

defined for the Hyball and the theoretical curve.

3.9.4.2 $E_x = 1.808$ MeV

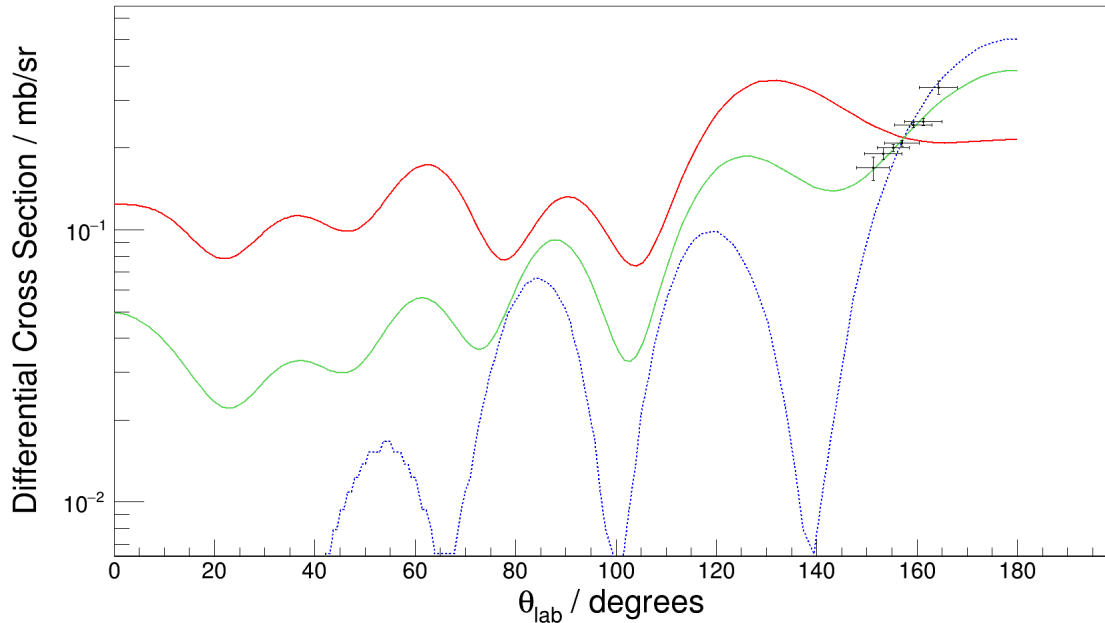


Figure 3.46: Angular distribution for the state at $E_x = 1.808$ MeV. The blue and red curves, produced by the TWOFNR reaction code, shows the theoretical angular distributions corresponding to the $l = 0$ and $l = 2$ respectively. The green curve represents a minimised combination of the two differing l -values transfer curves.

The second angular distribution to be determined was for the first excited state of ^{26}Mg with a literature energy of 1.808 MeV. This state has an assigned spin-parity of 2^+ , as the initial spin-parity within ^{25}Mg is $5/2^+$ it is possible for the this transfer to carry either 0 and/or 2 units of angular momentum, or l -value. In the case of $l = 2$ transferred units, the interpretation of the j angular momentum transfer is typically through the magnetic sub-orbitals of the shell-model orbital used. Within ^{26}Mg , $l = 2$ transfers are interpreted using either the $0d_{5/2}$ or the $0d_{3/2}$ shell-model orbitals. The angles in which protons are observed within this study restricts the assignment between differing d-wave orbitals as they typically present the same angular distribution shape over the Hyball laboratory angles but with differing extracted spectroscopic factors. As a result, only one of these orbitals is chosen for the interpretation of the angular distribution.

For this first excited state, historical studies have shown an admixture of both $l = 0$ and $l = 2$ angular momentum transfer with the d -wave contribution dominating the spectroscopic strength [132–134]. There is some discrepancy between Burlein *et al.* and Arciszewski *et al.* on the choice of d -wave components but this will be discussed as part of the spectroscopic factor discussion in the next session. Figure 3.46 shows the angular distribution constructed within this study alongside the theoretical angular distributions corresponding to $l = 0$ transfer into the $1s_{\frac{1}{2}}$, $l = 2$ transfer into the $0d_{\frac{5}{2}}$ orbital and a minimised combination of the two l -transfer values, shown in blue, red and green respectively. It can be seen that there is good agreement between the data from this study and the admixture of the two l -transfer values, except for the largest angular data point.

3.9.4.3 $E_x = 2.938$ MeV

The third angular distribution determined was for the second excited state within ^{26}Mg with a literature energy of 2.938 MeV. This state has a previously assigned spin-parity of 2^+ and has an observed stronger population than the ground and first excited states. While Lutz *et al.* did not publish the used d -wave orbital choice, both Burlein *et al.* and Arciszewski *et al.* interpreted this state as a pure $l = 0$ transfer into the $1s_{\frac{1}{2}}$ shell-model orbital, with a negligible to non-existent d -wave contribution [132–134].

The angular distribution for this state from this study is shown in Figure 3.47 alongside the theoretical angular distributions corresponding to $l = 0$ transfer into the $1s_{\frac{1}{2}}$, $l = 2$ transfer into the $0d_{\frac{5}{2}}$ orbital and a minimised combination of the two l -transfer values, shown in blue, red and green respectively. It is clear that the s -wave transfer dominates the spectroscopic strength of this state, with minimal difference to the data fit with the inclusion of an $l = 2$ component. The angles covered by this study are not as sensitive to the $l = 2$ component as to the $l = 0$ component, with the $l = 2$ component peaking at much lower laboratory angles than those covered by the Hyball detector. If the Barrel data had provided better resolution excitation data, this may have been useful to determine whether this minor d -wave component was physical or a manifestation of the minimisation within the error margin of the observed Hyball angular distribution. The evidence presented is in agreement with the previous assessments of this state deriving from a pure s -wave transfer.

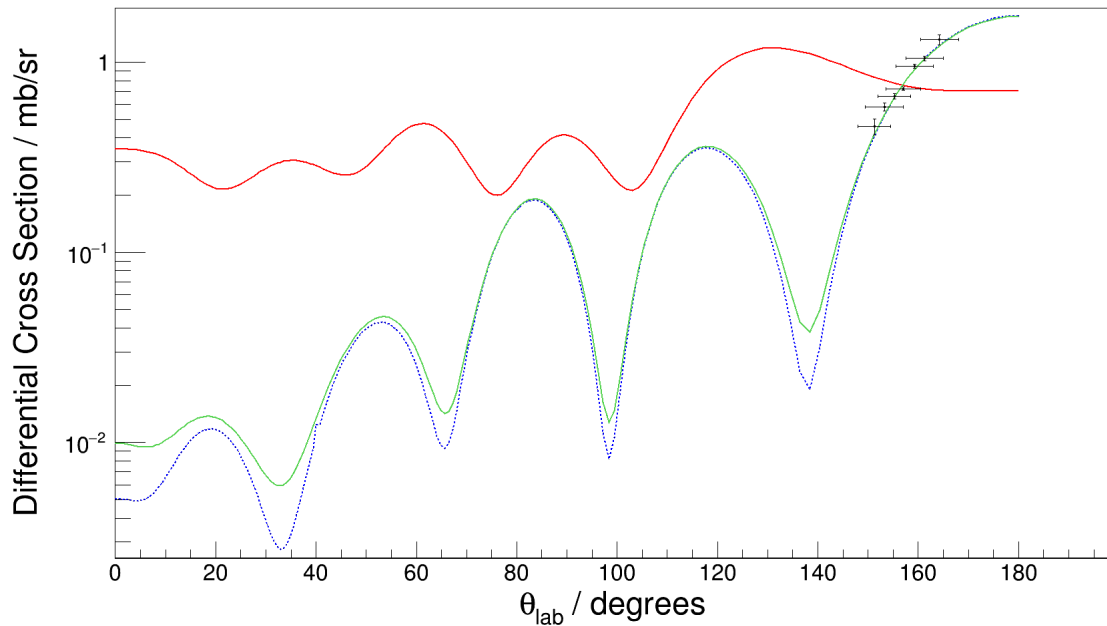


Figure 3.47: Angular distribution for the state at $E_x = 2.938$ MeV. The blue and red curves, produced by the TWOFNR reaction code, shows the theoretical angular distributions corresponding to the $l = 0$ and $l = 2$ respectively. The green curve represents a minimised combination of the two differing l -values transfer curves.

The fourth angular distribution constructed was for the first observed 0^+ excited state within ^{26}Mg with an excitation energy of 3.588 MeV. This has been observed to be very weakly populated within historical $^{25}\text{Mg}(d,p)^{26}\text{Mg}$ studies and within this study. As this is a 0^+ state, the only l -transfer value possible is 2 units and with a j -transfer of 2.5 units, it must be interpreted as a single neutron transfer into the $0d_{\frac{5}{2}}$ shell-model orbital. Figure 3.48 shows the determined angular distribution alongside the theoretical distribution with an $l = 2$ angular momentum transfer. There is relatively good agreement between these distributions, especially considering the low statistics for this excitations.

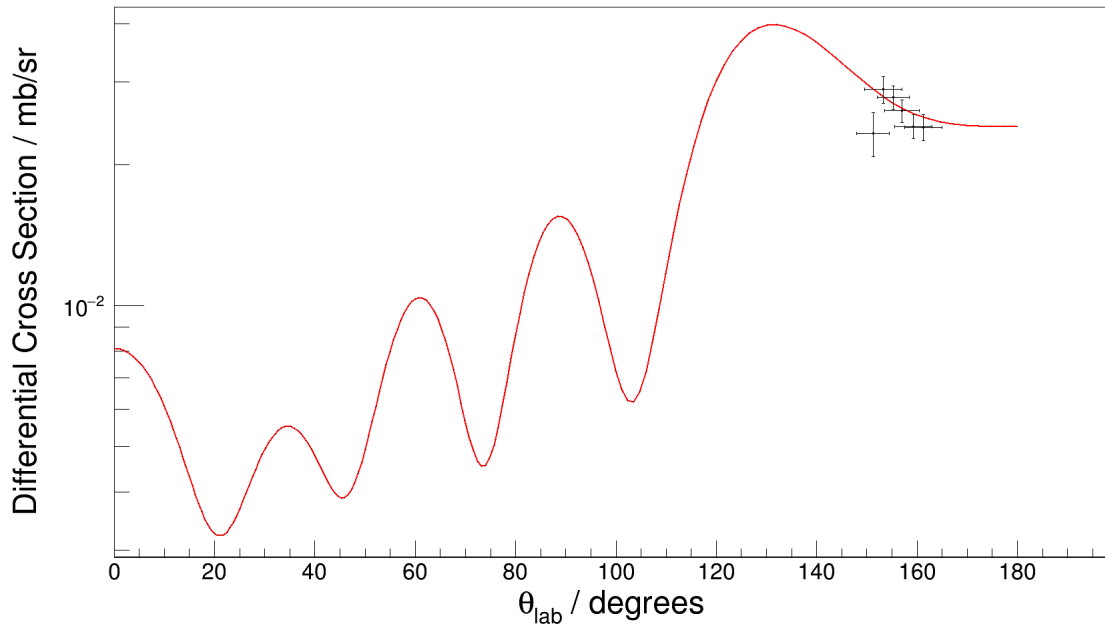
3.9.4.4 $E_x = 3.588$ MeV

Figure 3.48: Angular distribution for the state at $E_x = 3.588$ MeV. The red curve, produced by the TWOFNR reaction code, shows the theoretical angular distributions corresponding to the $l = 2$ transfer.

3.9.4.5 $E_x = 3.941$ MeV

The fifth angular distribution to be constructed was for the excitation with a literature energy of 3.941 MeV. This has previously been assigned as the first 3^+ spin-parity state within ^{26}Mg . The interpretation of this spin-parity combination identical to that of a 2^+ assignment, where both $l = 0$ and $l = 2$ transfers are possible and typically a combination of both is used to describe the angular distribution. Both historical studies by Burlein *et al.* and Arciszewski *et al.* have interpreted this state with transfers into the $1s_{\frac{1}{2}}$ and $0d_{\frac{3}{2}}$ shell model orbitals, with $l = 0$ and $l = 2$ units of transferred angular momentum respectively.

The angular distribution for this state from this study is shown in Figure 3.49 alongside the theoretical angular distributions corresponding to $l = 0$ transfer into the $1s_{\frac{1}{2}}$, $l = 2$ transfer into the $0d_{\frac{3}{2}}$ orbital and a minimised combination of the two l -transfer values, shown in blue, red and green respectively. There is good agreement between the angular distribution from this study and that produced by a theoretical

admixture of $l = 0$ and $l = 2$ units of angular momentum. However, it is noted that it would appear the spectroscopic strength is dominated by the s -wave component of this transfer at the observed angles.

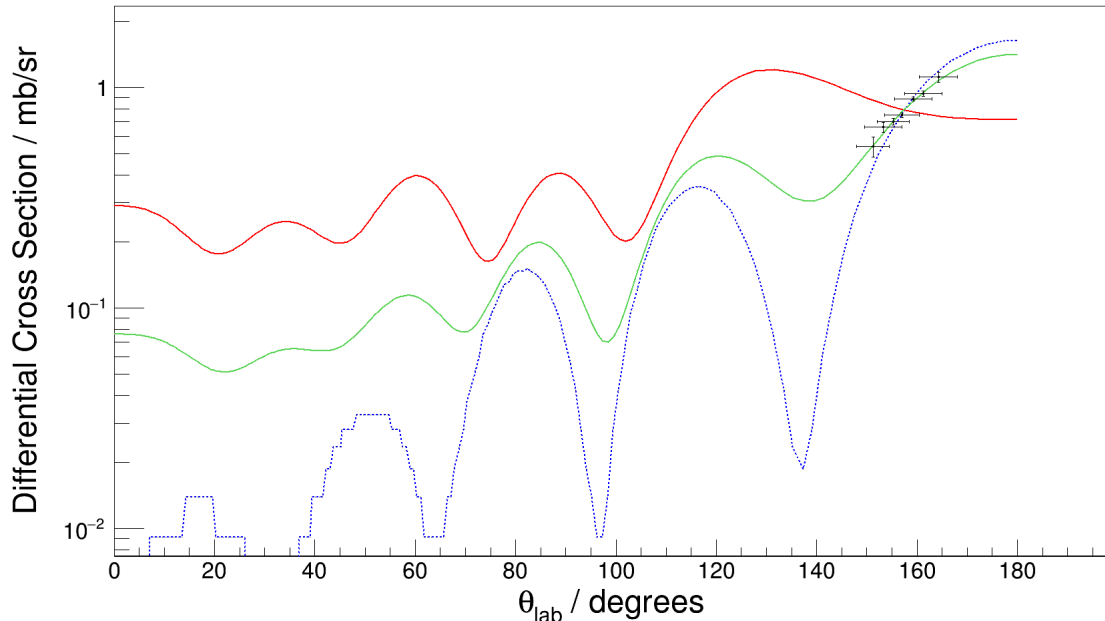


Figure 3.49: Angular distribution for the state at $E_x = 3.941$ MeV. The blue and red curves, produced by the TWOFNR reaction code, shows the theoretical angular distributions corresponding to the $l = 0$ and $l = 2$ respectively. The green curve represents a minimised combination of the two differing l -values transfer curves.

3.9.4.6 $E_x = 4.350$ MeV

The angular distribution constructed here is for the region previously observed to contain a triplet of states but within this study is being interpreted as a singular state with an excitation energy of 4.350 MeV and an assigned spin-parity of 3^+ . Previous studies have not been able to resolve between this triplet and as such construct an angular distribution based on a combined population of the entire triplet [133]. Whilst this study has shown evidence that this triplet is dominated by population into the 4.350 MeV, the analysis of this state is applicable for the entire triplet if there is unseen contributions from the other two states and is therefore directly comparable to previous studies [133, 134]. The other two states within this triplet have spin-parity assignments of 2^+ and 4^+ and therefore the entire region can be aptly described with $l = 0$ and $l = 2$ transfer values in a similar manner to the singular 3^+ , 4.350 MeV state.

Previous studies have interpreted this region using a combination of s -wave transfer into the $1s_{\frac{1}{2}}$ and d -wave transfer into the $0d_{\frac{5}{2}}$ shell-model orbitals.

The angular distribution for this state from this study is shown in Figure 3.50 alongside the theoretical angular distributions corresponding to $l = 0$ transfer into the $1s_{\frac{1}{2}}$, $l = 2$ transfer into the $0d_{\frac{3}{2}}$ orbital and a minimised combination of the two l -transfer values, shown in blue, red and green respectively. There is good agreement between the angular distribution from this study and that produced by a theoretical admixture of $l = 0$ and $l = 2$ units of angular momentum. It is also clear that the s -wave dominates the transfer strength of the observed angles, but as mentioned previously, the parameters of this study means there is limited sensitivity to the d -wave component of the transfer.

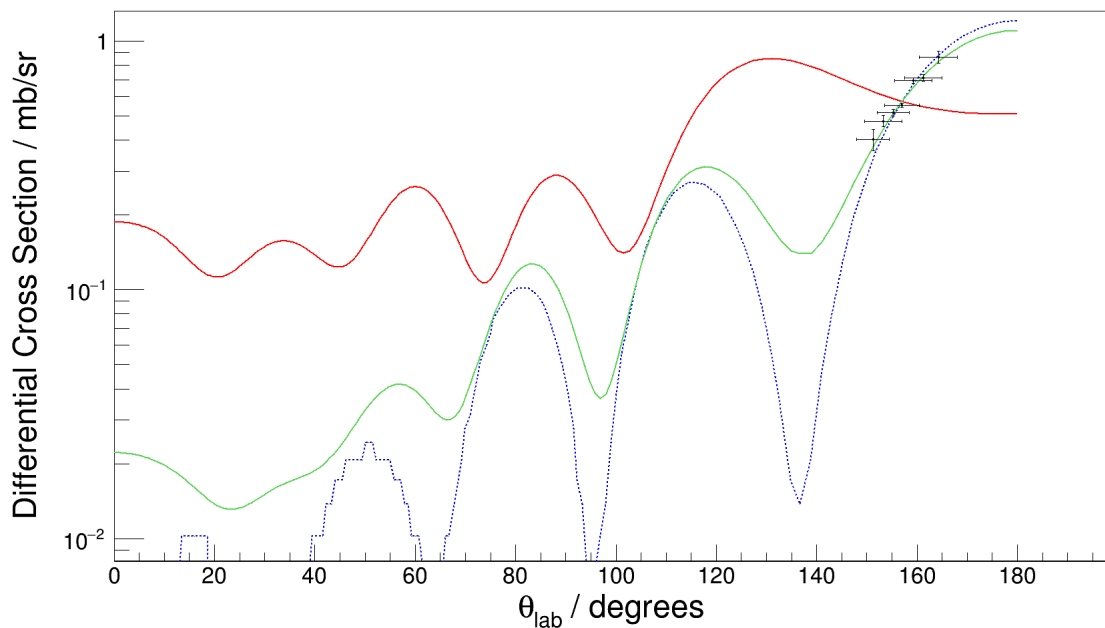


Figure 3.50: Angular distribution for the state at $E_x = 4.350$ MeV. The blue and red curves, produced by the TWOFNR reaction code, shows the theoretical angular distributions corresponding to the $l = 0$ and $l = 2$ respectively. The green curve represents a minimised combination of the two differing l -values transfer curves.

3.9.4.7 $E_x = 5.291$ MeV

The next angular distribution constructed was the lowest energy component of an unresolved combination of three states between 5 and 6 MeV excitation energy. This component has an excitation energy of 5.291 MeV and an assigned spin-parity of 2^+ .

Both Burlein *et al.* and Arciszewski *et al.* interpreted this state as a pure $l = 2$ transfer into the $0d_{\frac{5}{2}}$ shell-model orbital, with no reported s -wave contribution [133, 134].

The angular distribution for this state from this study is shown in Figure 3.51 alongside the theoretical angular distributions corresponding to $l = 0$ transfer into the $1s_{\frac{1}{2}}$ and $l = 2$ transfer into the $0d_{\frac{3}{2}}$ orbital, shown in blue and red respectively. As can be seen the data is in good agreement with a pure $l = 2$ transfer into the $0d_{\frac{5}{2}}$ shell-model orbital. No mixture of the two l -transfer values is plotted because the minimised mixture overlaps with the pure $l = 2$ component.

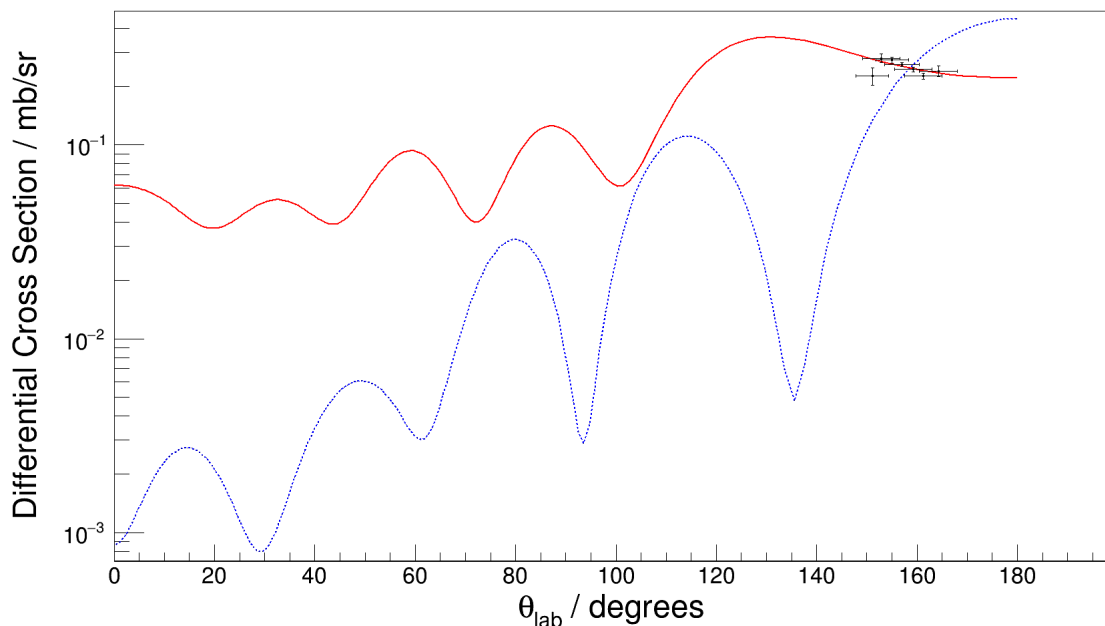


Figure 3.51: Angular distribution for the state at $E_x = 5.291$ MeV. The blue and red curves, produced by the TWOFNR reaction code, shows the theoretical angular distributions corresponding to the $l = 0$ and $l = 2$ respectively.

3.9.4.8 $E_x = 5.476$ MeV

The next angular distribution constructed was the second energy component of an unresolved combination of three states between 5 and 6 MeV excitation energy. This component has an excitation energy of 5.476 MeV and an assigned spin-parity of 4^+ . This state can only be populated through a pure $l = 2$ units of transferred angular momentum. Both Burlein *et al.* and Arciszewski *et al.* interpreted this state as a pure $l = 2$ transfer but disagree on the shell-model orbital used to describe the j -transfer

value. Burlein *et al.* interpret this using a single neutron transfer into the $0d_{\frac{3}{2}}$ whilst Arciszewski *et al.* used a single neutron transfer into the $0d_{\frac{5}{2}}$ shell-model orbital [133, 134]. This study cannot distinguish between these orbitals and as such both orbitals were explored within this study.

Figure 3.52 shows the determined angular distribution alongside the theoretical distribution with an $l = 2$ angular momentum transfer into the $0d_{\frac{5}{2}}$. The $0d_{\frac{3}{2}}$ orbital was also explored but is not plotted within Figure 3.52 because it is indistinguishable from the $0d_{\frac{5}{2}}$ over the angles covered by the Hyball. It can be seen there is relatively good agreement between these distributions except for the lowest angular range reviewed.

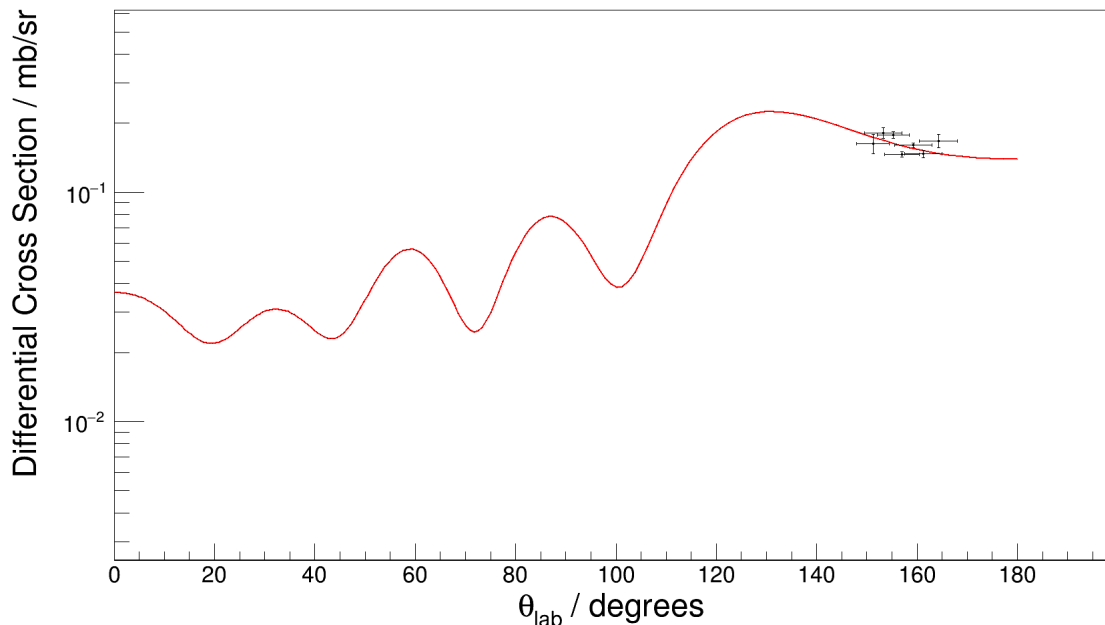


Figure 3.52: Angular distribution for the state at $E_x = 5.476$ MeV. The red curve, produced by the TWOFNR reaction code, shows the theoretical angular distributions corresponding to the $l = 2$ transfer.

3.9.4.9 $E_x = 5.715$ MeV

The next angular distribution constructed was the second energy component of an unresolved combination of three states between 5 and 6 MeV excitation energy. This component has an excitation energy of 5.715 MeV and an assigned spin-parity of 4^+ . This state can only be populated through a pure $l = 2$ units of transferred angular momentum. Both Burlein *et al.* and Arciszewski *et al.* interpreted this state as a pure

$l = 2$ transfer but disagree on the shell-model orbital used to describe the j -transfer value. Burlein *et al.* interpret this using a single neutron transfer into the $0d_{3/2}$ whilst Arciszewski *et al.* used a single neutron transfer into the $0d_{5/2}$ shell-model orbital [133, 134]. This study cannot distinguish between these orbitals and as such both orbitals were explored within this study. It is worth noting that previous studies also required an $l = 3$ component to completely describe the angular distributions observed which was attributed to an underlying unresolved negative parity state. This is of importance as recent neutron capture experiments have determined another state within this region with a 1^+ spin-parity. This state was previously the prime candidate for this unresolved negative parity state and as such the observed $l = 3$ component has not been explained.

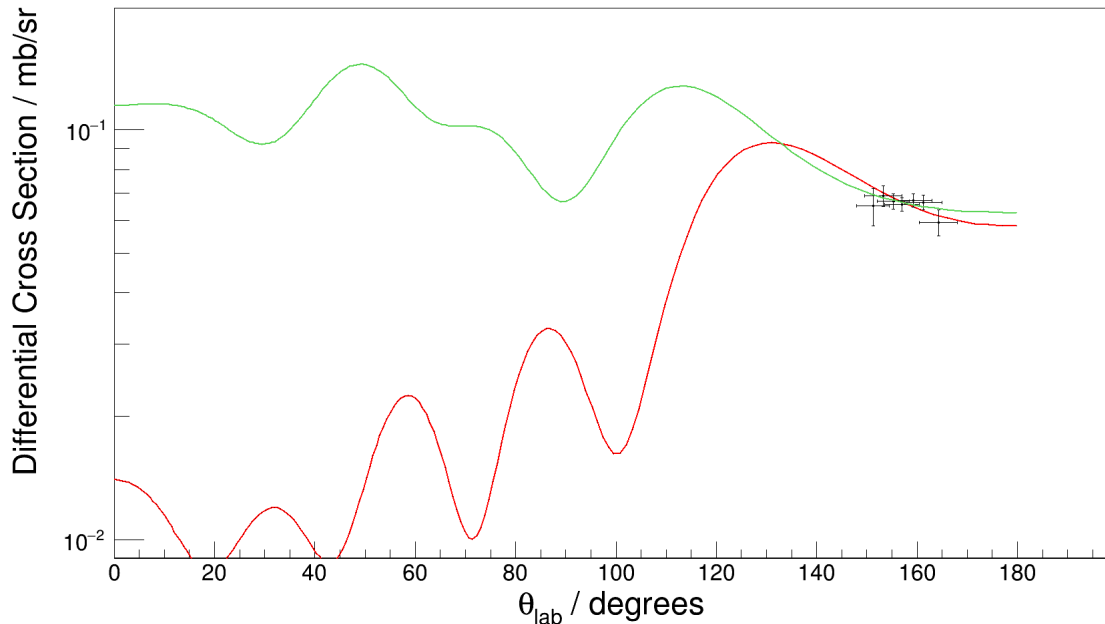


Figure 3.53: Angular distribution for the state at $E_x = 5.715$ MeV. The red curve, produced by the TWOFNR reaction code, shows the theoretical angular distributions corresponding to the $l = 2$ transfer. The green curve displays a minimised combination from $l = 2$ and $l = 3$ transfers, as previously observed in Burlein *et al.* and Arciszewski *et al.* [133, 134].

Figure 3.53 shows the calculated angular distribution alongside the theoretical distribution with an $l = 2$ angular momentum transfer into the $0d_{5/2}$. The $0d_{3/2}$ orbital was also explored but is not plotted within Figure 3.52 because it is indistinguishable from the $0d_{5/2}$ over the angles covered by the Hyball. Also plotted is a minimised combination between $l = 2$ and $l = 3$ angular distributions as explored within previous

studies of this reaction. The combined angular distribution arguably provides a better fit of the extracted angular distribution from this study. However, as discussed the angles within this study are not sensitive to the $l = 2$ transfer strength and this is also true of the $l = 3$ transfer strength which peaks at even smaller angles. Therefore whilst this study does not confirm the $l = 3$ transfer observation seen in previous studies it does not rule it out either and the question around this region remains.

3.9.4.10 $E_x = 6.125$ MeV

The next angular distribution constructed here is the state with an excitation energy of 6.125 MeV and an assigned spin-parity of 3^+ . This state is the mirror counterpart to a resonant state within ^{26}Si for the $^{25}\text{Al}(p,\gamma)^{26}\text{Si}$ astrophysical reaction. Previous studies have interpreted this region using a combination of s -wave transfer into the $1s_{\frac{1}{2}}$ and d -wave transfer into the $0d_{\frac{3}{2}}$ shell-model orbitals [133, 134].

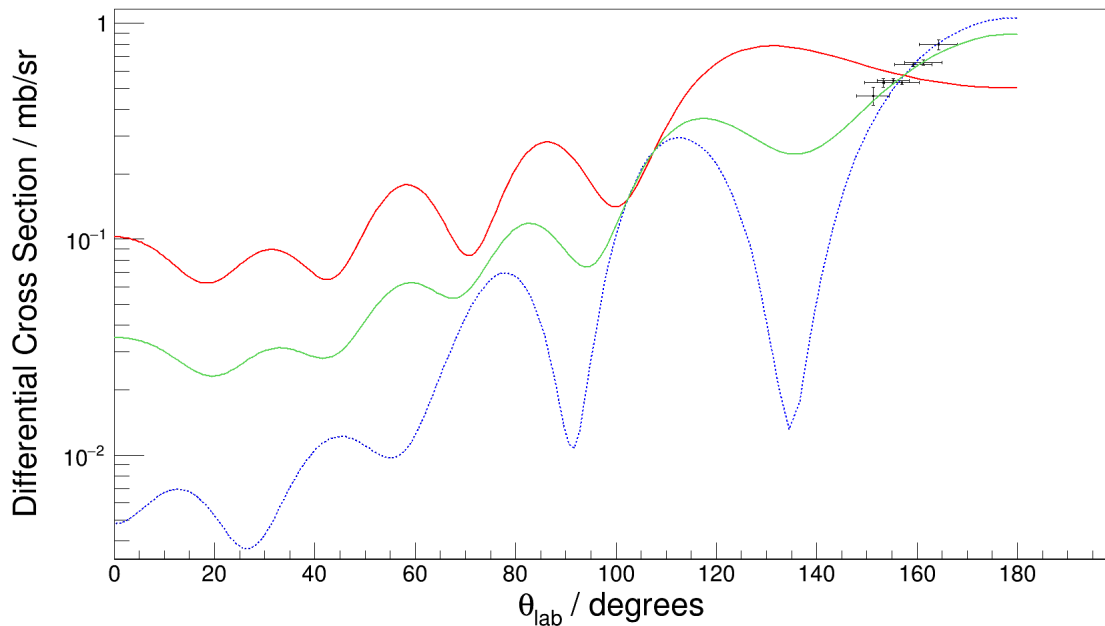


Figure 3.54: Angular distribution for the state at $E_x = 6.125$ MeV. The blue and red curves, produced by the TWOFNR reaction code, shows the theoretical angular distributions corresponding to the $l = 0$ and $l = 2$ respectively. The green curve represents a minimised combination of the two differing l -values transfer curves.

The angular distribution for this state from this study is shown in Figure 3.54 alongside the theoretical angular distributions corresponding to $l = 0$ transfer into the

$1s_{\frac{1}{2}}$, $l = 2$ transfer into the $0d_{\frac{3}{2}}$ orbital and a minimised combination of the two l -transfer values, shown in blue, red and green respectively. There is good agreement between the angular distribution from this study and that produced by a theoretical admixture of $l = 0$ and $l = 2$ units of angular momentum. There is evidence from the minimised combination of the two l -transfer values that each orbital provides a relatively equal contribution to the overall spectroscopic strength. It is also clear that a pure $l = 0$ transfer provides a relatively good fit for the data as well and data at lower angles would be necessary to constrain the d -wave strength for this state.

3.9.4.11 $E_x = 10.949$ MeV

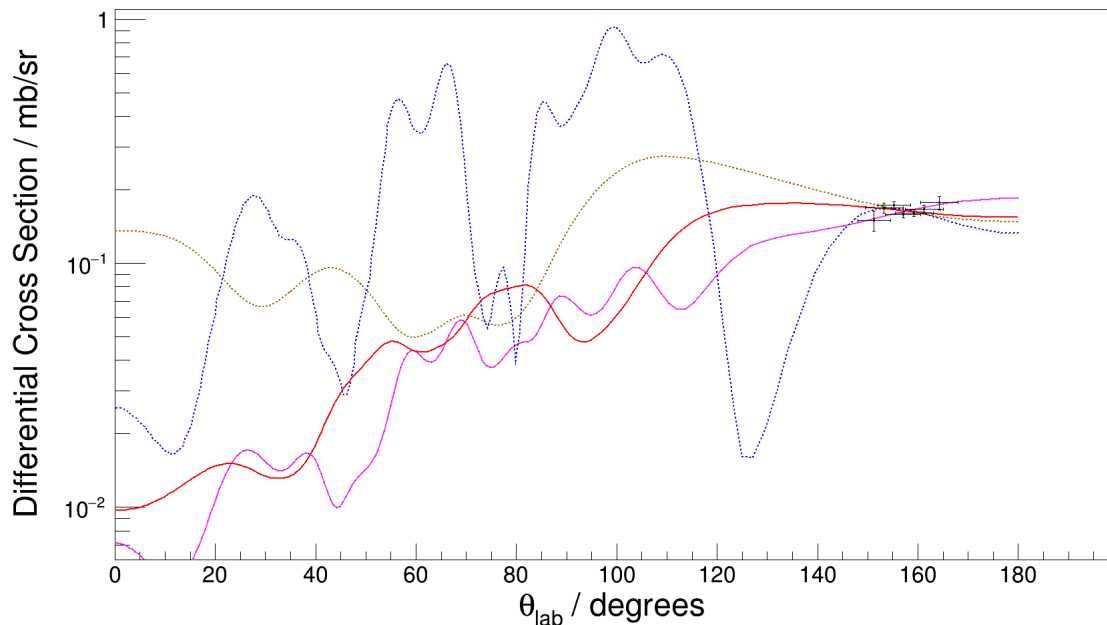


Figure 3.55: Angular distribution for the state at $E_x = 10.949$ MeV. The blue and red curves, produced by the TWOFNR reaction code, shows the theoretical angular distributions corresponding to the $l = 0$ and $l = 2$ respectively. The pink and brown curves, produced by the TWOFNR reaction code, shows the theoretical angular distributions corresponding to the $l = 1$ and $l = 3$ respectively. It can be seen that this angular distribution is best represented by an $l = 1$ transfer.

The final angular distribution constructed was for the only state resolvable above the α -particle separation threshold within ^{26}Mg and therefore of importance for the $^{22}\text{Ne}(\alpha, \gamma)^{26}\text{Mg}$ astrophysical reaction. This state is was measured to have an excitation energy of 10.952 (10) MeV which would correspond well with the known 10.949

MeV, 1^- state. A 1^- state within this reaction could be populated by either an $l = 1$ or $l = 3$ angular momentum transfer. Due to the high density of states at this excitation energy it was sensible to compare the angular distribution extracted against all possible l -transfer values.

Figure 3.55 shows the angular distribution analysis of this state in comparison to theoretical angular distributions. The various coloured lines represent the possible l -transfer values: blue representing $l = 0$ into $1s_{\frac{1}{2}}$; pink representing $l = 1$ into $1p_{\frac{3}{2}}$; red representing $l = 2$ into $0d_{\frac{3}{2}}$ and brown representing $l = 3$ into $0f_{\frac{7}{2}}$. It is clear that $l = 1$ provides the best representation of the extracted differential cross section and there is good evidence that the analysed state is indeed the 10.949 MeV, 1^- state.

3.10 Spectroscopic Factors

The spectroscopic factor is a dimensionless quantity and is a measure of the single-particle nature of a given state. It is typically defined as the fraction of the theoretical prediction of the reaction cross section and the experimentally determined cross section, both using a single-particle description. In this study, the spectroscopic study was defined as described by Equation 2.57. The angular distributions can be used to infer the l -transfer required for the population of a given state as discussed within the previous section. Furthermore, the spectroscopic factor can be determined by a comparison between the experimental data and the theoretical angular distributions. The numerical factor which scales the TWOFNR calculated theoretical distribution to best fit the experiment angular distribution is defined as the spectroscopic factor within this study.

This quantity was determined for each of the excitations described in Section 3.9.4. Where applicable these were compared against values obtained from previous studies by Lutz *et al.*, Burlein *et al.* and Arciszewski *et al.* [132–134]. Shell-model calculations of states within ^{26}Mg have been recently performed [140] using the NuShellX code [141] with a modified WBP-M interaction known as WBC [142] within the $sd-pf$ Hamiltonian for negative parity states, this modification reduces the shell gap between sd and fp shells in line with experiments around the $N = 20$ shell gap. For positive parity states calculations were performed using the USDA Hamiltonian within the sd shell-model space [143].

Table 3.5 summarises the combined spectroscopic factors from previous studies, shell-model calculations and those extracted from this study. It is worth noting that the Burlein *et al.* and Arciszewski *et al.* studies used the same theoretical inputs in their respective studies and as such the discrepancies arise entirely from differences in the experimental differential cross section measured in each study. It is clear from Table 3.5 that there is serious disagreement across historical studies for the spectroscopic strength of the ground state. Whilst the studies by Lutz *et al.* and Burlein *et al.* are in relatively good agreement with each other whilst the Arciszewski *et al.* is in relative agreement with the present study as well as shell-model calculations performed as part of this work. Using the shell-model as guide it is fair to suggest that the work by Lutz *et al.* and Burlein *et al.* underestimated the strength of this state. The other 0^+ state observed with an excitation energy of 3.588 MeV and was interpreted as a single neutron within the $0d_{\frac{5}{2}}$ orbital in the same manner as the ground state. The study performed by Burlein *et al.*, whilst providing no error margin on their extracted spectroscopic strength is in relatively good agreement with the shell-model predictions. These calculations also suggest that the extracted spectroscopic strength from this study is an overestimate, however, as previously noted this present study is not sensitive to the d -wave spectroscopic strength due to the angular ranges observed.

There were 3 observed 2^+ states within this study, the first of which was the first excited state at excitation energy of 1.808 MeV. Of note is the discrepancy between d -wave orbital choices for this state between the Burlein *et al.* and Arciszewski *et al.* studies. Shell-model calculations suggest that the $0d_{\frac{3}{2}}$ contribution to the spectroscopic strength of this state is minimal compared to that of the $0d_{\frac{5}{2}}$ orbital, there is good agreement for the $0d_{\frac{3}{2}}$ orbital strength between the Burlein *et al.* study, shell-model calculations and this study. The second excited state has previously been reported to have no d -wave contribution in all previous studies except that performed by Lutz *et al.*, shell-model calculations are in good agreement with this hypothesis with a minimal d -wave contribution and is observed by this study. The final 2^+ state observed was the 5.291 MeV state and is described as a pure d -wave transfer reaction, this has been confirmed by all previous studies. The d -wave contribution has an observed discrepancy with the shell-model suggesting that the Arciszewski *et al.* and current work overestimating this strength.

There is relatively good agreement between the respective s -wave contributions

for all of the observed 3^+ states within this study those previously performed, excluding the measured s -wave contribution of the 3.941 MeV state determined by Lutz *et al.*, which similarly appears to overestimate the d -wave contribution for this state. No additional information about the triplet near ~ 4.3 MeV is gained from the determined spectroscopic strengths summarised here. Comparison to the shell-model calculations for the 4.350 MeV 3^+ state suggest an overestimated d -wave contribution from this study, this could either arise due to the lack of the d -wave sensitivity or the population of unresolved state within this triplet with a strong d -wave contribution. The shell-model strongly suggest this is an overestimated d -wave contribution even in the case of an underlying state considering its predictions for the other two triplet states are of the order ~ 0.05 each.

Two 4^+ spin-parity states were observed within this study, forming an unresolved cluster of states between 5 and 6 MeV. The current and previous studies appear to overestimate the strength of the first of these states ($E_x = 5.474$ MeV) when compared to shell-model calculations. This is also reflected in the second of the two 4^+ states with excitation energy of 5.716 MeV. As previously discussed, the angular distributions of this state have needed an $l = 3$ transfer component in order to explain the shape of the angular distribution. It is therefore possible that the extracted strengths of the 5.716 MeV state entirely underestimate the contribution of this underlying negative parity state theorized in the region. It is interesting to note that the shell-model does not predict any negative parity states within this energy region, with the best candidate being a 1^- state predicted at an excitation energy of 6.298 MeV. Finally, the observed 1^- state with excitation energy of 10.949 MeV is determined with twice the spectroscopic strength as that predicted by shell-model calculations for the p -wave component. It does however agree with the minimally observed f -wave contribution which is predicted to be negligible.

The main source of statistical uncertainty within the spectroscopic factors derives from the beam normalisation procedure used within this study to create absolute differential cross sections. The resolution in both energy and position within the Barrel leads to a significant overlap between the angular ranges used for this determination. The beam spot size and non-centralized position and vector also add to the extracted normalisation factors, as well as contributing to the angular uncertainty in the angular distribution construction. Whilst this is not quantified within this study, a percentage

uncertainty of 20% should encompass these values from a purely statistical objective.

E_x MeV	J^+	nlj_{th}	C^2S [132] Lutz ¹	C^2S [133] Burlein	C^2S [134] Arciszewski	C^2S SM ²	C^2S Present Work ³
0.0	0_0^+	$0d_{\frac{5}{2}}$	1.8	1.85	2.81 (30)	2.48	2.91 (58)
1.808	2_0^+	$1s_{\frac{1}{2}}$	0.018	0.036	0.032 (10)	0.034	0.071 (14)
		$0d_{\frac{3}{2}}$	0.44 ¹	-	0.702 (70)	0.01	0.426 (85)
		$0d_{\frac{5}{2}}$	-	0.33	-	0.335	0.368 (73)
2.938	2_1^+	$1s_{\frac{1}{2}}$	0.15	0.388	0.674 (60)	0.441	0.405 (81)
		$0d_{\frac{5}{2}}$	0.32 ¹	0.0	-	0.086	0.044 (9)
3.588	0_1^+	$0d_{\frac{5}{2}}$	-	0.22	0.31 (3)	0.247	0.39 (8)
3.941	3_0^+	$1s_{\frac{1}{2}}$	0.097	0.25	0.283 (29)	0.213	0.207 (41)
		$0d_{\frac{3}{2}}$	0.43 ¹	0.1314	0.157 (71)	0.297	0.497 (99)
4.350	3_1^+	$1s_{\frac{1}{2}}$	-	0.254	-	0.118	0.173 (35)
		$0d_{\frac{5}{2}}$	-	0.268	-	0.061	0.171 (34)
5.291	2_4^+	$1s_{\frac{1}{2}}$	-	0.0	-	0.0	
		$0d_{\frac{3}{2}}$	-	0.42	0.658 (60)	0.436	0.69 (13)
5.474	4_2^+	$0d_{\frac{3}{2}}$	-	-	0.239 (28)	0.106	0.226 (45)
		$0d_{\frac{5}{2}}$	-	0.1278	-	0.088	0.187 (37)
5.716	4_3^+	$0d_{\frac{3}{2}}$	-	-	0.062 (22)	0.004	0.142 (28)
		$0d_{\frac{5}{2}}$	-	0.0622	-	0.046	0.302 (60)
		$0f_{\frac{7}{2}}$	-	0.0911	-		
6.125	3_2^+	$1s_{\frac{1}{2}}$	-	0.1214	0.106 (12)	0.125	0.142 (28)
		$0d_{\frac{3}{2}}$	-	0.2057	0.60 (14)	0.264	0.302 (60)
10.949	$1_{(9)}^-$	$1p_{\frac{3}{2}}$	-	-	-	0.152	0.31 (62)

¹ The shell-model orbitals used in this study were not published, therefore the determined value was placed in first row relating to the l -transfer value.

² SM - Shell-model calculations using USDA Hamiltonian within the sd shell-model space for positive parity states [143] and for the negative parity states, a WBP-M Hamiltonian including a $sd - pf$ Hamiltonian[142]. All performed in NuShellX by Prof. W. N. Catford [140].

³ Where more than one value for a single l -transfer value, only one was used for comparison to the relevant study between Burlein *et al.* or Arciszewski *et al.*.

Table 3.5: Spectroscopic factors obtained for all previously discussed excitations from the $^{25}\text{Mg}(d,p)^{26}\text{Mg}$ reaction in Section 3.9.4. Also, shown is related spectroscopic factors determined in historical studies and from shell-model calculations.

3.10.1 *d*-wave Sensitivity

A source of systematic uncertainty of note within this experimental effort was the constraints placed on *d*-wave components within transfer to positive parity state within ^{26}Mg . This limited angular range of the Hyball detectors used to construct angular distributions does not cover the laboratory angles where the *d*-wave components of this reaction “peak” providing a reasonable observed cross section to constrain against. To highlight and explore this systematic the angular distribution of the 3.941 MeV, 3^+ state was deliberately manipulated. This state was determined to have a significantly shared *s*-wave and *d*-wave contributions to its spectroscopic strength ($C^2S_{l=0} = 0.207$ & $C^2S_{l=2} = 0.497$), and considering the *s*-wave was well constrained by the angular range of the Hyball detector, made an ideal candidate for this exploration.

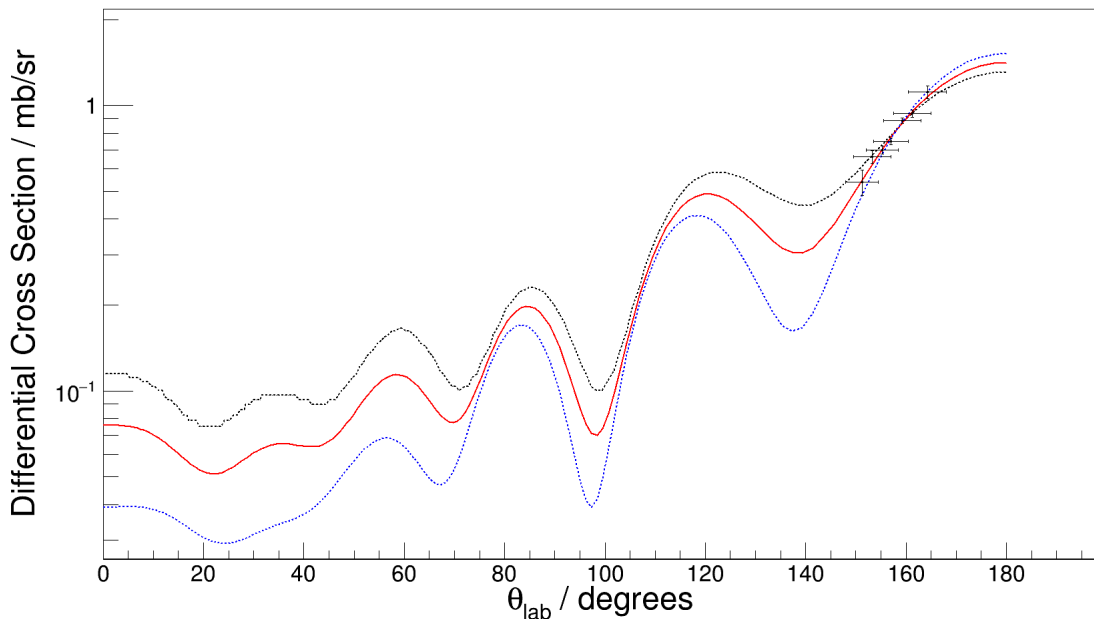


Figure 3.56: Effects of *d*-wave manipulation on the overall minimised theoretical angular distribution for the 3.941, 3^+ state. The solid red line depicts the original minimised admixture of the *s*-wave and *d*-wave contributions. The dashed black and blue lines representing the new minimisations whilst fixing the *d*-wave contributions by increasing/decreasing its original value by 50%.

For this investigation, the *d*-wave contribution was deliberately increased and decreased by 50% of its originally minimised value, and the *s*-wave contribution re-minimised over to provide a new best fit of the angular distribution. Figure 3.56

displays the plot of the original minimised angular theoretical angular distribution, alongside these manipulated fits compared to the data extracted for the 3.941 MeV state. This figure displays that despite a 50% change in the d -wave contribution a new minimised fit could be found that relatively well described the observed angular distribution for this state.

$C^2 S_{l=0}$	$C^2 S_{l=2}$	Comments
0.173	0.745	d -wave components $\cdot 1.5$
0.207	0.4969	Original Normalisation parameters
0.240	0.249	d -wave components $\cdot 0.5$

Table 3.6: Effects on the determined l -transfer value spectroscopic contributions when specifically increasing/decreasing the d -wave component by 50%.

Not only does the angular distribution still relatively well describe the data within this manipulation, but Table 3.6 shows the re-minimised spectroscopic strengths of the s -wave contribution to the state with the manipulated d -wave component. It shows that there is a maximum of 20% change in the newly minimised s -wave component, highlighting how the angular distribution constraints are dominated by the s -wave fit. This 20% change is within generally agreed systematic uncertainties of these AWBA theoretical calculations, typically on the order of 20%.

3.10.2 Relation to $^{25}\text{Al}(p,\gamma)^{26}\text{Si}$ proton spectroscopic factors

Whilst not the primary goal of this study, the analysis of the 6.125 MeV, 3^+ state within this present study of the $^{25}\text{Mg}(d,p)^{26}\text{Mg}$ reaction is related to an indirect measurement of a resonant state within the $^{25}\text{Al}(p,\gamma)^{26}\text{Si}$ astrophysical reaction. This reaction contributes to the stellar nucleosynthesis within nova environments and is thought to be dominated by resonant capture into low-lying 1^+ and 3^+ states above the proton separation threshold at 5.5178 MeV. This reaction could remove the ^{26g}Al flux by increasing the reaction rate of the chain $^{25}\text{Al}(p,\gamma)^{26}\text{Si}(\beta\nu)^{26m}\text{Al}(\beta\nu)^{26}\text{Mg}$. Whilst major experimental effort has been put into understanding this reaction through particle transfer and γ -ray spectroscopy studies, there is still considerable uncertainty on the rate. Table 3.7 shows a summary of the experimental measurements for this particular

state and it is clear that there is relatively good agreement across all studies.

E_x MeV	J^+	l	C^2S [133] Burlein ¹	C^2S [134] Arciszewski	C^2S [119] Hamill	C^2S SM ²	C^2S Present Work
6.125	3 ⁺	0	0.121	0.106 (13)	0.11 (2)	0.125	0.142
		2	0.206	0.60 (14)	0.27 (6)	0.264	0.302

¹ No uncertainties published.

² SM - Shell-model calculations using USDA Hamiltonian within the sd shell-model space for positive parity states [143] and for the negative parity states, a WBP-M Hamiltonian including a $sd - pf$ Hamiltonian [142]. All performed in NuShellX by Prof. W. N. Catford [140].

Table 3.7: Summary of previously measured spectroscopic factors of note for this mirror reaction.

Considering that ^{26}Mg and ^{26}Si are mirror nuclei, the neutron spectroscopic factors from the $^{25}\text{Mg}(d,p)^{26}\text{Mg}$ reaction are theoretically identical to the proton spectroscopic factors from the corresponding mirror analogue states within the $^{25}\text{Al}(p,\gamma)^{26}\text{Si}$ reaction. Therefore the neutron spectroscopic factor for the 6.125 MeV state within this study should be identical to the proton spectroscopic factor for the $^{25}\text{Al}(p,\gamma)^{26}\text{Si}$ into the mirror analogue 3⁺ state with 5.929 MeV excitation energy. In the $^{25}\text{Al} + p$ system this has a resonance energy of 415.2 keV taking $S_p = 5.5138$ (5) MeV [144]. It should be noted that there is still considerable uncertainty in the true excitation of this mirror state with some studies observing this excitation at 5.914 MeV and therefore a resonance energy of 400.2 keV [145, 146].

This proton spectroscopic factor can then be used to calculate the proton partial width of the state using Equation 2.46, which requires the single-particle width of the state to be calculated, this was performed using proton penetrabilities determined using an analytical code based on the methodology developed by Barnett *et al.* [147] and formalism discussed by Clayton [148]. Within this study θ_{sp} is taken from Ref. [149] and the values used for this reaction are 0.55, 0.7, 0.36 and 0.35 for the l -values 0, 1, 2 and 3 respectively. Considering that within the astrophysical reaction the resonant captured proton can carry either 0 or 2 units of transferred angular momentum, or $l = 0$ or $l = 2$, there are therefore two single particle widths for this reaction matching the two spectroscopic factors extracted from the (d,p) reaction. The single-particle

width of a state is defined in Equation 2.47. Multiplying this analytically determined single-particle width by the determined C^2S factor provides an estimation of the proton partial width, Γ_p .

Study	E_x / MeV	E_r^1 / MeV	Γ_p / eV	Γ_γ / eV	$\omega\gamma$ / eV
Present Study	5.914	0.4002 ²	3.32	0.047 ⁴	2.6×10^{-2}
	5.929	0.4152 ³	4.75	0.067 ⁴	3.8×10^{-2}
Parpottas <i>et al.</i> [145]	5.912	394	1.68	0.033	1.9×10^{-2}
Peplowski <i>et al.</i> [150]	5.914 (4)	0.396	2.9(10)	0.092	5.2×10^{-25}
Hamil <i>et al.</i> [119]	5.9294 (8)	0.4154 (8)	2.6 ⁶	6	6
Bennett <i>et al.</i> [151]	5.9294 (8)	0.4154 (8)	2.9 ⁷	0.04	2.3×10^{-2}

¹ Based on $S_p = 5.5138$ (5) MeV [144]

² $S_p = 5.5138$ (5) MeV [144] - E_x determined by [145, 150].

³ $S_p = 5.5138$ (5) MeV [144] - E_x determined by [119, 151].

⁴ Calculated using the partial width ratio, Γ_p/Γ_γ , published by Bennett *et al.* [151].

⁵ No published value. Calculated by author based on published partial widths.

⁶ Values adopted by this paper were taken from Ref. [151].

⁷ Value adopted from [150].

Table 3.8: Comparison between the reaction strength variables between that determined within this study and those published by previous investigations.

Typically, where the Γ_γ is not known it can be determined by estimating the total width of the state using the known lifetime of the state, $\Gamma = \tau/\hbar$ and deducting a determined proton partial width. In this present case, the lifetime of the resonant state in the $^{25}\text{Al} + p$ system is unknown but the lifetime of the mirror state in ^{26}Mg is known to be 20 fs. In previous studies of this the $^{25}\text{Al} + p$ system, this mirror state lifetime has been adopted for γ -ray width, Γ_γ for the resonant state, as a result $\Gamma_\gamma = 20 \text{ ms} / \hbar = 0.033 \text{ eV}$. The study performed by Bennett *et al.* determined the ratio between the proton and γ -ray partial widths, or $\Gamma_p/\Gamma_\gamma = 0.014(4)$ and using a previously determined $\Gamma_p = 2.9 \text{ eV}$ estimated the γ -ray partial width to be 0.04 eV which is in agreement with that estimated from mirror symmetry arguments [151]. This study presents Γ_γ using the same method as the Bennett *et al.* using their determined width ratio with the determined Γ_p from this study. The summary of these determined partial widths,

the resonance strength based on this work and comparisons to a selection of previous studies is shown in Table 3.8. For completeness this has been done for both current excitation values.

Chapter 4

Investigation of the $^{26m}\text{Al}(p,\gamma)^{27}\text{Si}$ Reaction through a Novel Isospin Analogue Reaction

Whilst the $^{26g}\text{Al}(p,\gamma)^{27}\text{Si}$ has been thoroughly studied over the last three decades, the role of the low-excitation isomeric state within ^{26}Al within stellar environments is poorly understood. The work presents a novel method in determining the resonance strengths of key states for the $^{26m}\text{Al} + p$ system using a surrogate $^{26}\text{Si}(d,p)^{27}\text{Si}$, performed at the National Superconducting Cyclotron Laboratory. This experiment was performed with a radioactive ^{26}Si beam and 9.1 mgcm^{-2} thick CD_2 target with relevant γ -ray decay data and beam-like reaction nuclei measured within the GRETINA HPGe array and S800 spectrograph respectively. The following chapter outlines the historical research surrounding this system, describes the experimental details of the current work and presents the data analysis and results from this recent study. Finally, the resonance strengths of key states within this system were determined and the effect on the resonance reaction rate was evaluated and compared to previous indirect studies and theoretical predictions.

4.1 Previous Research

In general, the nucleosynthesis of a given isotope within a stellar environment is dominated by the creation/destruction of its ground state. Internal decay lifetimes

of excited states are typically much smaller than the probabilities of particle decay or reaction mechanisms upon them. However, some states within these isotopes can have a large enough lifetime to participate in other processes, these are known as isomeric states. For the stellar nucleosynthesis of ^{26}Al there exists a 0^+ isomer with $E_x = 228.31(3)$ keV and $t_{1/2} = 6.3$ s above the 5^+ ground state with $t_{1/2} = 7.2 \times 10^5$ yr. Examination of the reactions involved in the creation and destruction of the ground and isomeric states is required to understand the galactic abundances linked to this isotope. For example ^{27}Al and ^{26}Mg observations in presolar grains or the ^{26}Al flux throughout the galactic plane.

The creation mechanism of the ground and isomeric states within stellar environments depends on the temperature of that environment. In AGB stars and classical nova environments, where the stellar temperature is less than 0.3 GK, both ^{26g}Al and ^{26m}Al are produced with approximately equal rates through the reaction chain $^{24}\text{Mg}(p,\gamma)^{25}\text{Al}(\beta^+,\nu_e)^{25}\text{Mg}(p,\gamma)$. However, within Oxygen-Neon novae and Core Collapse Supernovae, temperatures can exceed 0.3 GK and the $^{25}\text{Al}(p,\gamma)^{26}\text{Si}$ is a significant competitive reaction to the β^+ -decay of ^{25}Al , breaking the previous reaction chain. In environments such as explosive hydrogen burning events, the creation of ^{26}Al completely bypasses the ground state and the isomeric state would become the main component. In terms of nucleosynthesis calculations, the treatment of these states is also temperature dependent. At temperatures above 0.4 GK it is possible for these states to communicate via thermal excitations through higher energy excitations. As such, these two states can not be treated as individual nuclei within reaction network calculations.

The destruction of ^{26}Al will be dominated by the $^{26g}\text{Al}(p,\gamma)^{27}\text{Si}$ and $^{26m}\text{Al}(p,\gamma)^{27}\text{Si}$ reactions within AGB stars and classical novae, where the peak temperature reach ~ 0.14 GK and $\sim 0.2 - 0.4$ GK respectively. The Gamow window for the $^{26m}\text{Al}(p,\gamma)^{27}\text{Si}$ reaction for these environments would cover a range $\sim 100 < E_R < 500$ keV. The last three decades has seen extensive research into the ^{27}Si resonant states (above the proton threshold) expected to dominate the $^{26g}\text{Al}(p,\gamma)^{27}\text{Si}$ reaction rate [152–161]. To compensate for limited experimental information, previous network calculations have based their rates of the $^{26m}\text{Al}(p,\gamma)^{27}\text{Si}$ reaction on the $^{26g}\text{Al} + p$ resonances and Hauser-Feshbach calculations [162]. A post-processing study by Iliadis *et al* [163] calculated that the uncertainties from this process can affect the synthesized ^{26}Mg isotopic abundances in nova environments by up to a factor of 14, highlighting that this technique

may be inappropriate below 0.4 GK.

The destruction of ^{26m}Al will be dominated by the (p, γ) reaction into resonant states within ^{27}Si above the $^{26m}\text{Al} + p$ threshold energy of 7691.3(1) keV [75]. One of the first efforts to study the isomeric reaction specifically, was the observation of possible proton decaying excited states within ^{27}Si through $^{27}\text{Al}(^3\text{He}, t)$ and $^{28}\text{Si}(^3\text{He}, \alpha)$ reactions [164]. This study by Deibel *et al.* identified a dominant $^{26m}\text{Al} + p$ resonance at $E_r = 445(4)$ keV ($^{27}\text{Si } E_x = 8136(4)$ keV) at the top end of the Gamow window for AGB stars and classical novae [164]. Unfortunately, experimental limitations, including a detection energy cut-off threshold, prevented the observations of any resonances below $E_r < 445$ keV, i.e. the majority of the Gamow window. The proton decay angular correlations could only determine the minimum angular momentum transfer, l_{min} , between ^{27}Si and metastable states within ^{26}Al . As this study determined an $l_{min} = 0$ for the 445 keV resonance considerable uncertainty still exists in the spin-parity assignment of this resonant state ($J^\pi \geq 1/2^+$) [164].

A γ -ray spectroscopy study of ^{27}Si was performed at Argonne National Laboratory with the aim of identifying resonant states within the $^{26m}\text{Al} + p$ system, through the $^{12}\text{C} + ^{16}\text{O}$ fusion evaporation reaction [165, 166]. The angular resolution of GAMMA-SPHERE enabled the measurement of γ -ray angular correlation decays to determine the spin assignments of observed states. State parities were assigned through state matchings to the mirror system, ^{27}Al . Relevant states within both ^{27}Al and ^{27}Si for the $^{26m}\text{Al} + p$ system above the respective proton and neutron thresholds and are within the continuum. Whilst the mirror matching for this $A = 27, T = 1/2$ pair is robust for bound states, matching within the continuum is more challenging [165, 166]. This study affirmed the $J = 1/2$ assignment for the $E_r = 447.4(6)$ keV state as reported by Deibel *et al.* [164]. Newly observed resonant states with resonance energies $E_r < 445$ keV were also reported, including a $J = 5/2^+$, a $J = 3/2^+$ and two $J = 3/2^-$ states at resonance energies $E_r = 146.3(3), 217.8(7), 378.3(30)$ and $492.2(4)$ keV respectively. This study proposed, contrary to Deibel *et al.*, that the newly observed $5/2^+$, 146 keV resonance would dominate the $^{26m}\text{Al}(p, \gamma)^{27}\text{Si}$ reaction.

The parity assignments from the Lotay *et al* study have been updated through a study by Parikh *et al* using angular distributions of the $^{28}\text{Si}(^3\text{He}, \alpha)^{27}\text{Si}$ [167]. The 218 and 378 keV resonances were reassigned from this study as $3/2^-$ and $3/2^+$ respectively. It was suggested that the 218 keV would dominate this reaction instead of the 378 keV

resonance. A more recent study of the β -delayed proton-decay of ^{27}P questioned the 218 keV state negative parity assignment, despite it not being observed [168].

The last experiment of note was the first to utilise an isomeric beam of ^{26m}Al directly. A $^{26m}\text{Al}(d,p)$ transfer reaction was performed to extract neutron spectroscopic factors [169], for the $^{26m}\text{Al} + p$ analog states in ^{27}Al . The population of low spin excited states in ^{27}Al could be linked back to states in ^{27}Si . Unfortunately, no important states were observed. Instead upper limits were set on the spectroscopic factors for the 146 and 378 keV resonances, which have a moderate contribution in stellar environments up to $T < 0.2$ GK. The main challenge using isomeric radioactive beams is removing contamination from the ground state component. To that end this study [169] used a background subtraction based on the results of the independent study of the ground state component, $^{26g}\text{Al}(d,p)$ by Pain *et al* [159]. This method has considerable uncertainties in the extraction of spectroscopic factors and relies upon matching mirror assignments across the $^{27}\text{Si} - ^{27}\text{Al}$ system. Presently these are not robust within this resonance energy region as previously mentioned.

The presented work investigates the $^{26m}\text{Al} + p$ resonances through a novel approach. ^{26m}Al forms part of a 0^+ isobaric triplet with ^{26}Si and ^{26}Mg . As such it is possible to use the neutron transfer upon ^{26}Si , through a $^{26}\text{Si}(d,p)^{27}\text{Si}$ reaction as a surrogate reaction for the $^{26m}\text{Al}(p,\gamma)^{27}\text{Si}$. This experimental method has been used in spectroscopic factor studies before, for example, within $^{26}\text{Al}(d,n)$ and $^{30}\text{P}(d,n)$ studies [160, 170]. The benefit of a surrogate reaction mechanism over using a direct isomeric radioactive beam, is the removal of any background contaminants linked to the ground state of ^{26}Al . Which has a very different spin-parity in the initial system and is not a counterpart to the surrogate. Additionally, the associated Clebsh-Gordon coefficients between the surrogate and astrophysical reaction are such that the neutron spectroscopic factors are a factor of two larger than the proton capture system. Therefore, these states are more likely to be observed through this mechanism. Also tighter stringent upper limits can be placed on unobserved resonant states because the upper limits for the proton capture system are half that of the neutron transfer.

4.2 ²⁶Si Beam Production & Acceleration

At NSCL, exotic isotope beams are created in a fast projectile in-flight fragmentation process at intermediate energies. In this method, a heavy-ion non-radioactive primary beam is ionized within an ion source and accelerated to relativistic velocities. This stable beam is then impinged upon a thin production target, typically Beryllium. Nuclear reactions are induced between beam and target, producing a variety of different nuclei species or fragments, typically with fewer nucleons leading to the name “fragmentation” [171]. To create a secondary radioactive beam these fragments need to be filtered/separated by their mass and charge, selecting the nuclei of interest with as few contaminants as possible. This secondary beam is then transported to an experimental area for further processing.

4.2.1 Primary Beam Production

Rare isotopic beams at NSCL begin with the creation of ionized stable primary beams within the Coupled Cyclotron Facility (CCF). This facility consists of two ion sources and two cyclotrons. The two ion sources available at NSCL are the Superconducting Source for Ions (SuSI) and the Advanced Room TEMperature Ion Source (ARTEMIS). Primarily these sources require a stable material in a gaseous state either directly injected, if the base state of the material is gaseous in nature, or via a vaporising oven in the case of a solid material. The ion source relies on electron cyclotron resonance heating to ionize the atoms. In this experiment, the ARTEMIS ion source was used in order to extract ³⁶Ar ions in the 7+ charge state.

The two cyclotrons within this facility are coupled together with a transport beam line, hence the Coupled Cyclotron Facility. After extraction from the ion source, the ionized stable isotope beam is injected into a K500 cyclotron. In this first cyclotron the ions are accelerated up to an intermediate energy of 13.06 MeV/ μ . The ions are then injected into the K1200 cyclotron, the second of the two cyclotrons, in which the ions are fully stripped (using a carbon foil) into their final charge state and accelerated up to the final beam energy for the primary beam. The beam extracted from the K1200 is transported to the A1900 fragment separator, where it is impinged onto a production target, creating a secondary cocktail beam of isotopes. A schematic overview of the facility up to the A1900 is provided in Figure 4.1. ³⁶Ar was used as the primary beam

in this study, in the 18^+ charge state and with a beam energy of $150 \text{ MeV}/\mu$.

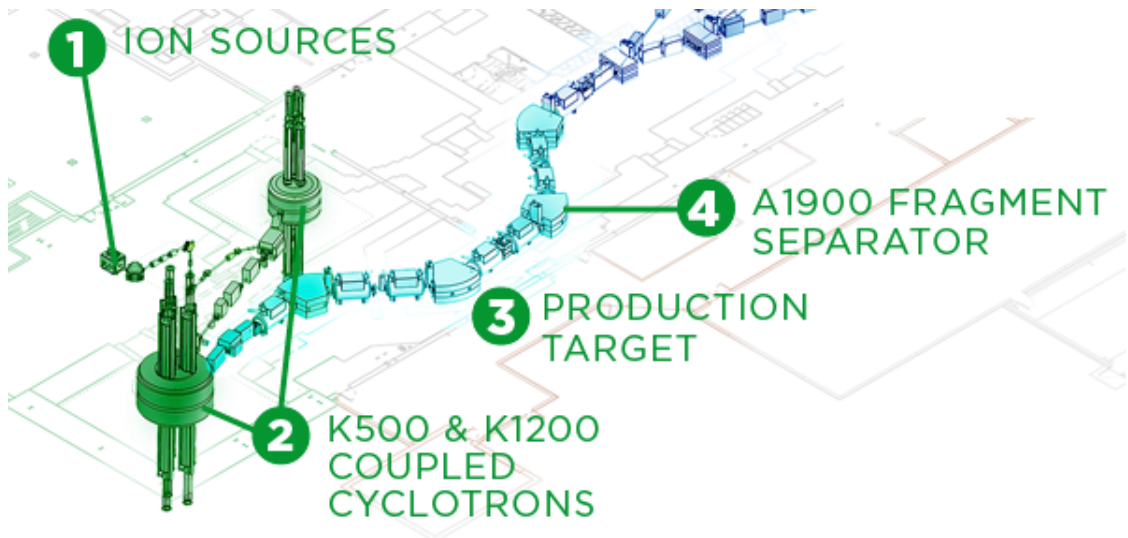


Figure 4.1: The coupled-cyclotron fragmentation facility at NSCL [172].

4.2.2 A1900 & Secondary Beam Production

The primary beam created and accelerated within the Coupled Cyclotron Facility is the most intense beam throughout the experimental facility. A production target is placed at the entrance to the A1900 Fragment Separator, this is typically Beryllium due to the materials high melting point, high number density of atoms and good thermal conductivity. The A1900 selects specific isotopes from the cocktail of fragmentation products after the target reaction. Within this fragment separator are four 45° bending dipole magnets and eight quadrupole triplet magnets for beam focusing [173]. In between each pair of triplet quadrupole is an image plane, within which is a pair of variable width slits. The four dipole magnets are the main control for ion separation, based on the magnetic rigidity of the ions being transported through the separator. Each species will have a specific magnetic rigidity given by:

$$B\rho = \frac{mv}{q} \propto \frac{Av}{z}, \quad (4.1)$$

where B is the magnetic field strength within the dipole, ρ is the gyroscopic radius of the dipole magnets curvature. The other components are all related to the specific ions, m , v and q are their mass, velocity and charge. The fragmentation process, typically creates ions with similar velocities, meaning that the separation relies on the mass to

charge ratio of the ions. Using dipoles to select the specific $B\rho$ of the isotope of interest, the ions are separated out in the dispersive direction of the beam. Coupled with narrow slits at the intermediate image locations, that block ions not bent through the centre of the beam line (i.e. of different $B\rho$ values), the secondary beam is cleaned up. Isotope are also separated within the A1900 using an aluminium wedge at the intermediate image point. The relationship between energy deposition and Z^2 produces a spread in velocities within the beam ions. This relationship is governed by the Bethe formula:

$$\frac{dE}{dx} = \frac{4\pi e^4 Z^2}{m_0 v^2} n_{\text{abs}} z_{\text{abs}} \left(\ln \frac{2m_0 v^2}{I} - \ln \left(1 - \frac{v^2}{c^2} \right) - \frac{v^2}{c^2} \right), \quad (4.2)$$

where e is the electron charge, m_0 is the rest mass of an electron, Z and v are the proton number and velocity of the particle travelling through the wedge. n_{abs} is the number density of the wedge, z_{abs} is the atomic number of the wedge and I is the average ionization potential of the absorber wedge. This velocity dispersion alters the magnetic rigidity of the ions traversing the A1900, increasing the dispersive power of the second set of A1900 dipoles. For this experiment, an aluminium wedge with a thickness of 300 mgcm^{-2} was employed and the slits of the A1900 were set to restrict the momentum spread of the beam to between $dp/p = 1\% - 2\%$.

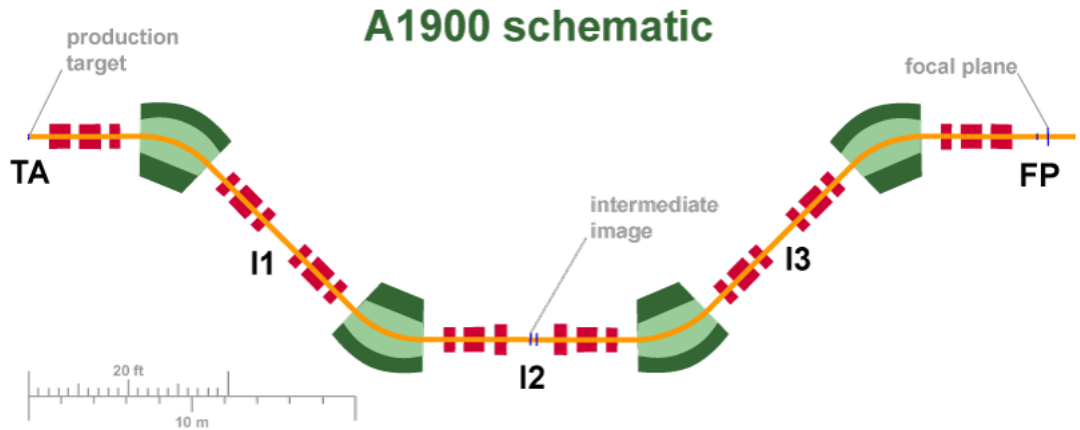


Figure 4.2: Schematic of the A1900 Fragment Separator. The four 45° dipole magnets are shown in green and the 8 triplet quadrupole magnets are shown in red. A 2 gcm^{-2} ^9Be target was placed at “TA” and a 300 mgcm^{-2} Al wedge was placed at the intermediate image point, “I2” [174].

The focal plane at the end of the A1900 fragment separator hosts a number of detectors used for beam diagnostics and identification. Of critical importance to this

work is the extended focal plane scintillator, “xfp”. Used in coincidence with the object scintillator of the S800 the components of the transmitted beam can be identified.

4.3 Detection Systems

This section describes the various detection systems used within this experiment. This will be broken down into the two separate systems in the experiment, the S800 spectrograph and the GRETINA Germanium array.

4.3.1 The S800 Spectrograph

The S800 spectrograph can be divided into two sections, an analysing beam line and the spectrograph section, see Figure 4.3. The analysing beam line section begins with the “object” scintillator, as described in Section 4.2.2, and contains a succession of superconducting magnets that focus and steer the beam down towards the spectrograph. The spectrograph is comprised of two superconducting dipole bending magnets that direct the beam and/or reaction products into the suite of detectors situated at the focal plane [175].

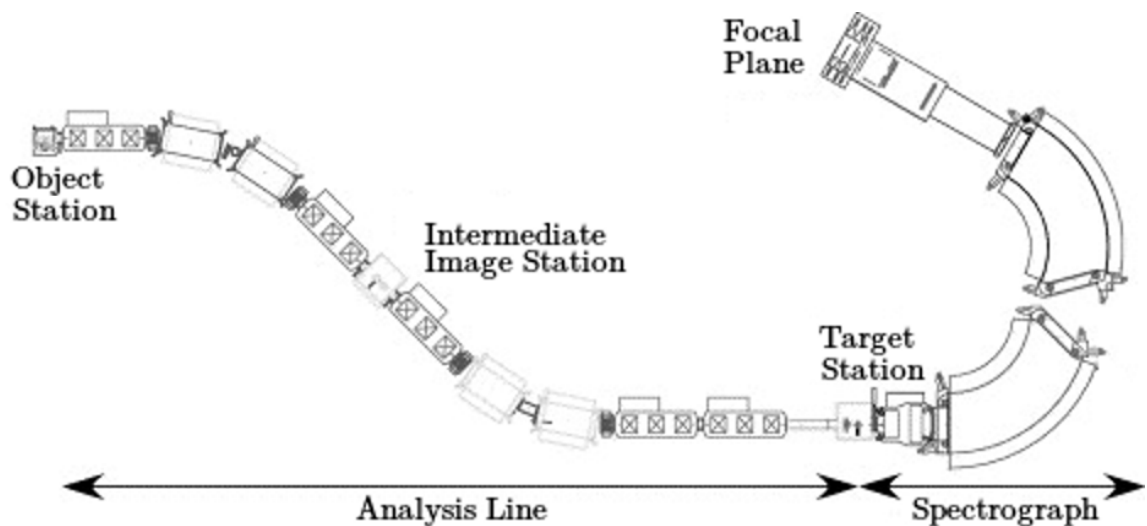


Figure 4.3: Figure showing the layout of the S800 Spectrograph, as discussed in detail above. Adapted from [175]

The S800 can be either operated dispersion-matching mode or in focus mode, a monochromatic mode is in development at the time of writing. In dispersion matching

mode both sections of the S800 (analysis line + spectrograph) are achromatic, such that the momentum is dispersed at the target but is cancelled at the focal plane. Practically, this limits the momentum acceptance to a $\pm 0.25\%$ for a 2" wide target. This mode provides the maximum energy resolution for this set-up but minimum acceptance. This research was completed with the S800 in Focused Mode. In this mode only, the analysis line of the S800 is achromatic, such that the beam is focused at the target position but the momentum spread is not cancelled through the spectrograph. This allows for a larger momentum acceptance window, $\pm 2\%$ constricted by the momentum acceptance of the A1900, but results in the fragment coordinates at the focal plane being linked to their momentum at the target position. Figure 4.4 provides a sketch of the particle trajectories within the dispersive direction as they traverse the spectrograph.

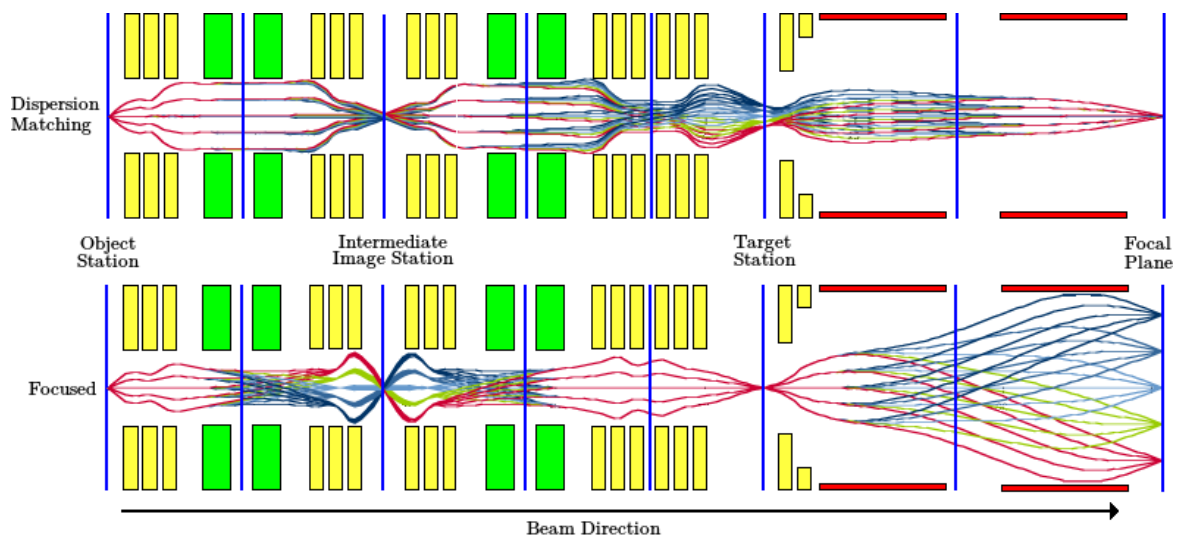


Figure 4.4: A sketch displaying the particle trajectories within the dispersive direction as they traverse through the S800 spectrograph. The difference between the 2 modes can be clearly seen. The magnetic beam line components are shown by the rectangles: yellow for quadrupoles, green for beam line dipole and red for the large S800 dipole magnets.

4.3.2 S800 Focal Plane Particle Detectors

After the two dipole magnets of the S800, the components of the secondary beam were identified using a suite of focal plane detectors. This suite determines the trajectory, position, energy loss and time-of-flight information on a particle by particle basis. The following detectors are all housed at the focal plane: two Cathode Readout Drift Chambers (CRDCs), a 16-fold segmented Ionization Chamber (IC), a number of plastic

scintillators and a CsI(Na) Hodoscope [175]. Their layout is shown in Figure 4.5. This experiment did not utilize the Hodoscope, which is primarily used for charge state identification, as such this detector will not be discussed in detail.

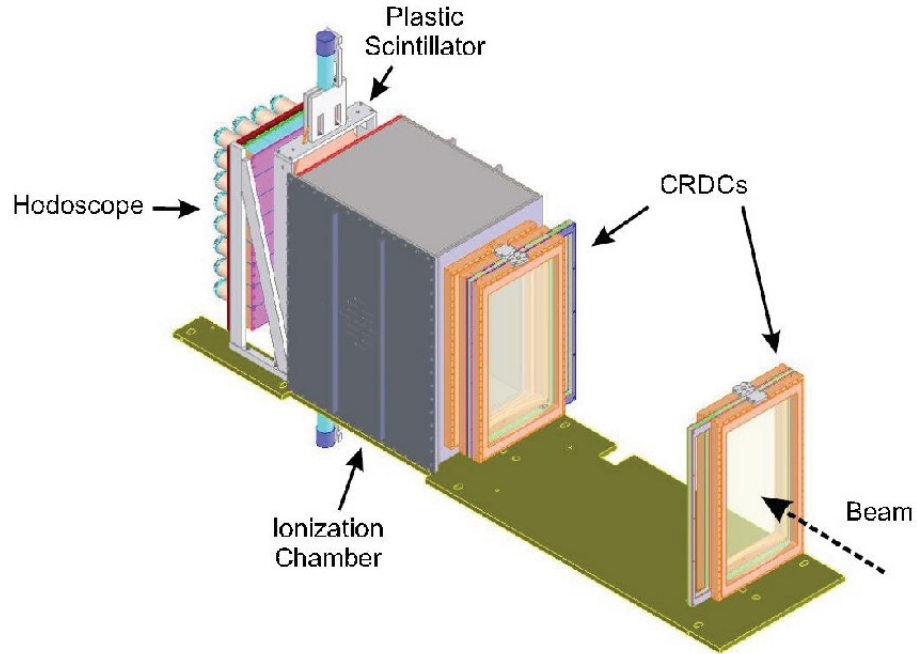


Figure 4.5: A basic schematic of the S800 focal plane detector set-up. Of note, the Hodoscope was not used in this current study.

4.3.2.1 Cathode Readout Drift Chambers

The CRDCs measure the x - y positions of beam-like particles after the S800 dipole magnets. With this information the angle in which a given particle traverses the focal plane can be reconstructed. This set-up incorporates two of these detectors separated by a gap of 1073 mm along the beam axis. Each individual CRDC has an active area of 30 cm x 59 cm with an active depth of 1.5 cm. The momentum of the particles is dispersed across the 59 cm axis with a positional resolution of ~ 0.5 mm in each direction.

Each CRDC is filled with a gas mixture of 80% of CF_4 (carbon tetrafluoride) and 20% C_4H_{10} (isobutane), a pressure of 50 Torr was maintained within these chambers. Projectiles passing through the chamber ionize the gas, the resultant free electrons drift toward and are collected upon an anode wire, held at a constant voltage. A negative bias voltage is applied through the chamber in the y direction to aid this drift.

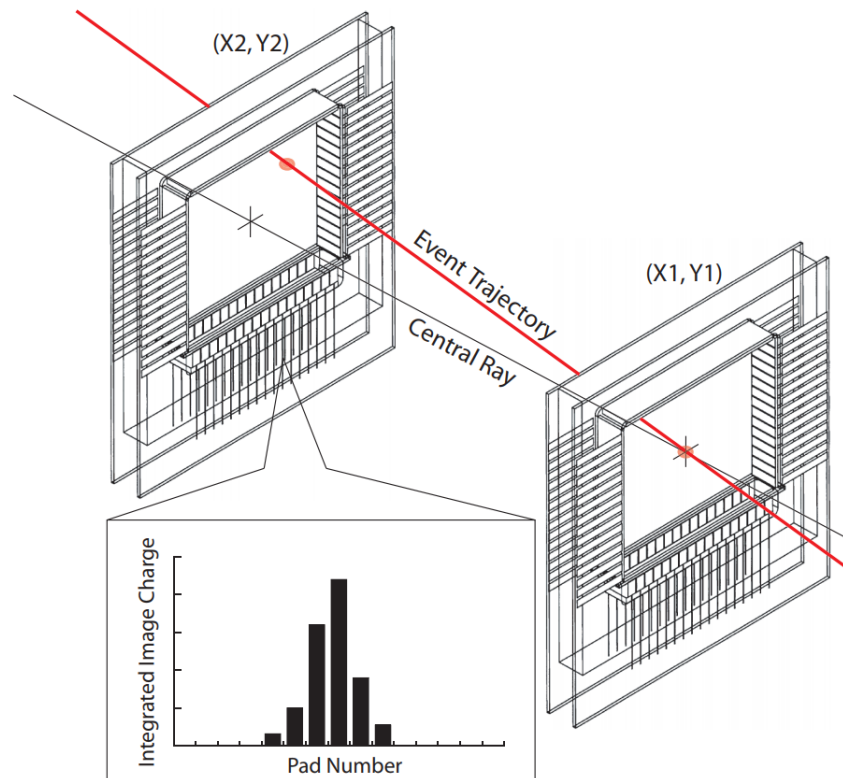


Figure 4.6: Sketch depicting the layout of the CRDC detectors and how the measured positions can be used to determine the particle trajectories. CRDC image originally from [176] and subsequently modified and taken from [177].

The cathode within each CRDC is divided into 224, 2.54 mm pads. As the electrons drift toward the anode, a distribution of charges are induced within the cathode pads. A fit of these induced charges using a Gaussian distribution provides the x -position, defined by the centroid of the Gaussian, see Figure 4.6.

The y -position of the projectiles within the CRDCs is determined by measuring the drift time of the electrons from the projectile position and the anode. The drift time is defined by the time difference between the anode signal time and the event stop signal from the projectile passing into the E1 scintillator.

The dispersive and non-dispersive coordinates of each beam particle at the focal plane are measured by the first CRDC, which is stationed at the optical focus of the S800. These coordinates are designated as x_{fp} and y_{fp} respectively. The second CRDC measures the coordinates of the beam particles after the focal plane. The difference between the positions at each CRDC determines the dispersive and non-dispersive vectors relative to a central trajectory through the S800 focal plane. These vectors are

designated as a_{fp} and b_{fp} respectively.

4.3.2.2 The Ionization Chamber

Immediately downstream of the CRDCs is an ionization chamber for energy loss measurements. The chamber of the detector is filled with a P10 gas mixture, composed of 90% Argon and 10% Methane, which was held at a pressure of 140 Torr. The active area of the ionization chamber is approximately 30 cm x 60 cm in size. This IC is divided into 16 1-inch sections providing a chamber depth of 16-inches in total. Within each section is a cathode-anode pair, created using aluminized mylar foils. The gas is ionized by traversing particles, with released electrons collected upon the anode and the positive ions collected on the cathode. The charge collected upon the anode-cathode pair is proportional to the number of electron-ion pairs created, which is in turn proportional to the energy loss within the gas. This energy loss is related to the square of the particles charge, and as such is used for determining their atomic number, Z .

4.3.2.3 Plastic Scintillators

The S800 utilizes three thin plastic scintillators in order to measure the time-of-flight of particles through the spectrograph on an event by event basis. The first of these scintillators is located at the extended focal plane of the A1900, as discussed in Section 4.2.2. The second scintillator is at the object station before the target position, whilst the third is stationed after the ionization chamber and before the hodoscope. This final scintillator is known as the “E1” scintillator and is used as the trigger signal for the S800 & GRETINA detection systems. The E1 has a large area of 30 cm × 59 cm, and is 5 mm thick. The photomultiplier tubes located at the top and bottom of the detector provide energy, time and position information of traversing beam projectiles.

Beam particles passing through these scintillators cause the emission of light which is collected within the photomultiplier tubes. The light emission within this plastic has a very fast decay time providing an excellent time resolution, down to the order of 100 ps, however, does not provide high energy resolutions. Combining the timing signals of the object and E1 scintillators, the time-of-flight through the spectrograph can be calculated. Combining the timing signals from the extended focal plane (“x_{fp}”) and E1 allows the measurement of the time-of-flight throughout the entire

system. Linking both allows for the incoming particles to be identified and tagged upon. A combination of the former time-of-flight and the energy measurements of the ionization chamber allows the identification of the outgoing particles after target reactions.

4.3.2.4 Trajectory Reconstruction

The CRDC detectors of the S800 allow for the position and momentum vectors of particles at the focal plane to be extracted. However, these same vectors are of greater interest at the target position. These target position vectors can be reconstructed on an event-by-event basis using a ray tracing procedure that computes the target position coordinates based on those at the focal plane.

Information from the S800 magnetic fields are input into an analytical calculation within the code COSY INFINITY [178]. This code creates an inverted matrix or inverse map to transform the focal plane beam parameters.

$$(dta, yta, ata, bta) = \mathbf{S}^{-1}(xfp, yfp, afp, bfp), \quad (4.3)$$

where

$$\mathbf{S}^{-1} = \begin{pmatrix} (dta|xfp) & (dta|yfp) & (dta|afp) & (dta|bfp) \\ (yta|xfp) & (yta|yfp) & (yta|afp) & (yta|bfp) \\ (ata|xfp) & (ata|yfp) & (ata|afp) & (ata|bfp) \\ (bta|xfp) & (bta|yfp) & (bta|afp) & (bta|bfp) \end{pmatrix}. \quad (4.4)$$

Within these matrices the parameters ending with “*fp*” relate to the coordinates/vectors at the focal plane and those parameters ending with “*ta*” refer to the target position. *x* and *a* relate to the position and angle within the dispersive plane, whilst *y* and *b* are similarly within the non-dispersive plane. The energy of the particle at the target position is also calculated, represented in form by “*dta*”. The beam position within the dispersive plane at the target cannot be calculated and assumed to be zero.

The assumption that $x_{ta} = 0$ means that the final resolution within the dispersive direction after the ray tracing procedure was found by folding the finite beam spot size with the size from the reconstruction. The latter of which is dependent on the detector

resolution and the order the calculation is performed to. The tracing procedure fits the measured magnetic fields through the S800 dipoles and related magnets with Enge functions of the form:

$$E(z) = \frac{1}{1 + \exp[P(z)]}, \quad (4.5)$$

where z is the direction of a reference path of the beam and $P(z)$ is a fifth order polynomial chosen such that the error in the mapping is comparable to the errors within the focal plane detectors of the S800.

4.3.3 Gamma-Ray Detection - GRETINA

GRETINA is the first phase in the development of the next generation HPGe detector arrays. The Gamma-Ray Energy Tracking In-beam Nuclear Array (GRETINA) is the first part of the Gamma-Ray Energy Tracking Array (GRETA) project, a full 4π solid angle array. At the time of this experiment GRETINA was composed of 10 detector modules, also known as “quads”. Each module is composed of four HPGe crystals, each crystal shaped to one of two irregular hexagonal designs. Each quad a composition is of two “type A” geometries and two “type B” geometries. Each individual crystal has a 36-fold segmentation, with 6 slices through the depth of the crystal and 6 regions across the face of the crystal, that perpetrate through the depth of the crystal. The slice boundaries through the depth of the crystal are located at 8 mm, 22 mm, 38 mm, 56 mm and 76 mm from the crystal face, with the crystals having an approximate depth of 90 mm and a face diameter of 80 mm [179–181].

The purpose designed frame and modular design of GRETINA allows the modules to be placed in a custom configuration that maximizes the efficiency of the array, on an experiment-by-experiment basis. Whilst GRETA will eventually be composed of 30 modules, GRETINA has a maximum capacity of 22 modules. The possible detector positions within the NSCL set-up are: 4 positions at 58° , 8 positions at 90° , 5 positions at 122° and 5 positions at 148° relative to the beam direction. The 10 modules used within this experiment were set up such that the 58° positions were filled with the 6 remaining modules placed at 90° .

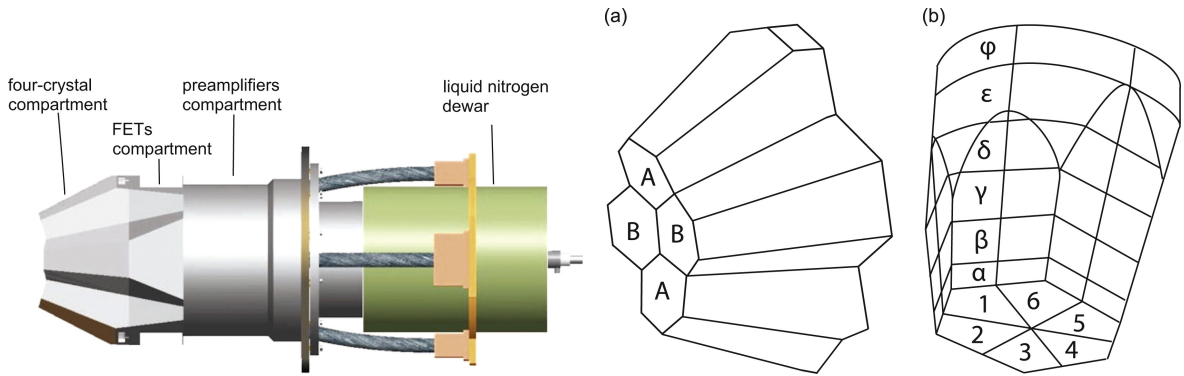


Figure 4.7: From left to right. An illustration of the component layout within a given module. A schematic of the different hexagonal crystal designs within a given quad. Lastly, a sketch of the segmentation within a given crystal, showing the 6 segmented regions upon the face of the crystal and the 6 layers of segmentation through the crystal, labelled α to ϕ [179]

GRETINA, and in particular GRETA, represents a significant advancement with respect to other modern 4π γ -ray detection set-ups. One important development is the signal decomposition within the DAQ firmware. This allows the positions of γ -ray interactions to be reconstructed with sub-segment resolution. The digitized signal pulses within each crystal provide information on the cylindrical co-ordinates of the interaction. The rise time of the real charge signal, measured within the segment containing the interaction point and the central-contact signal, is related to the radial distance from the central electrode of the interaction, providing “ r ”. From the shape and amplitude of the image signal, a superposition of the $< 0.5 \mu s$ signals in interaction neighbouring segments, the depth and polar angle can be determined, “ z ” and “ θ ”. These combined signals are fit against a linear combination of simulated detector responses, known as basis signals, to determine the interaction position to an average position resolution of < 2 mm. These basis signals are a simulated detector response to a unit charge at non-uniform grid spacings, with an average grid spacing of 1 mm, taking into account realistic charge carrier mobilities and electronic circuit effects [182].

Another important development is the capability to perform γ -ray tracking, the reconstruction of a photon’s path within the array in the case of a multiple scattering event. Firstly, simple geometrical criteria (for example, angular separation) are used to define the likelihood that multiple interaction points are from a single γ -ray. Next, scattering sequences for all possible combinations of interaction points within

these clusters are evaluated using the Compton scattering formula. Each is denoted a Figure-of-Merit (FM) based on the deviations between the measured angle between the interaction points and the expected angle from the scattering formula using the deposited energies. Theoretically, events with full deposition and events with “perfect” position and energy resolutions (and so “perfect” reconstruction) would have a FM of zero. Practically, both energy and position measurements of the interactions have a non-zero resolution and so can not be “perfectly” reconstructed and all reconstructions will have a non-zero FM. However, for all partial absorption events and incorrect reconstructions, the value of FM would be large. Lastly, all clusterings and angle fittings can be iteratively evaluated, an FM threshold can then be placed, eliminating events with only partial deposition, increasing the peak-to-total ratio. For this experiment, the γ -ray tracking capability was not used, due to concerns in the efficiency measurement.

4.3.3.1 Doppler-Correction Considerations

The resolution of Doppler-corrected energies is dependent upon the resolution of three parameters within Equation A.17: the intrinsic energy resolution of germanium ($\Delta E_{\gamma,lab}$), the uncertainty in the velocity of the emitting nuclei ($\Delta\beta$), and the uncertainty in the γ -ray emission angle ($\Delta\theta$). The angle uncertainty is a result of the uncertainties in the γ -ray emission point and the γ -ray interaction point within the array. The signal decomposition minimises the former, however, the latter has a large contribution due to the large beam spot needed within the dispersion matching technique of the S800. This large beam spot introduces ambiguity at non-90° emission angles as the interaction point could be related to any point within the beam spot.

4.3.4 Electronics

The S800 data acquisition consisted of analogue electronics based on a event-by-event readout scheme. The S800 trigger was provided by the thin focal-plane scintillator, which in this experiment required only single particle events. This trigger then initiated readout from both ADC and TDC modules into a VME framework. A time-stamp was then assigned to each event using a GRETINA clock source. This acquisition system provided a number of scaler module readouts necessary for measuring total beam incidences within the S800.

The GRETINA data acquisition is built around a custom digital system, utilizing digital pipelines within the architecture. In this system, individual triggers from all channels are stored locally and only readout when a global trigger signal is received, the S800 in this experiment. Computing resources for GRETINA are capable of processing 30,000 γ rays per second, if running as a sole system. These detection systems have independent data acquisitions combined through a simple time-stamp comparison in the analysis software. Simultaneously the S800 master trigger was fed into the GRETINA system to provide the validation trigger for particle- γ recording.

4.4 Detector Calibrations

4.4.1 CRDC Calibrations

As discussed in Sections 4.3.2.1 and 4.3.2.4, the S800 utilizes a pair of Cathode Readout Drift Chambers to determine (x,y) positions of particles traversing the focal plane. Using raytracing the positions and vectors of these particles at the target position can be reconstructed. To complete this procedure the signals from the CRDCs need to be translated into (x,y) spatial positions, in mm. This was completed by remotely inserting a tungsten mask with a well determined pattern of holes and slits directly upstream of each CRDC. Particles detected in the masked CRDC have passed through these drilled holes or slits and leave an impression of this pattern in the data.

The impression data was then fit with a first-order polynomial relating these hole positions to the relevant output from the CRDC. In the x -direction the centroid channel number is mapped and in the y -direction the drift time of the electrons released is mapped.

$$x_{1,2}(mm) = a_{1,2}(mm/pad) \cdot x_{1,2}(pad) + b_{1,2}(mm), \quad (4.6)$$

$$y_{1,2}(mm) = c_{1,2}(mm/ns) \cdot y_{1,2}(ns) + d_{1,2}(mm). \quad (4.7)$$

The functional form of Equation 4.6 is predetermined by the geometrical arrangement of the cathode pads within the CRDCs. The slope of this polynomial ($a_{1,2}$) is fixed by the width of each cathode pad, measured at 2.54 mm/pad. The constant ($b_{1,2}$) determined such the vertical sequence of holes to the left of the “L” shaped sequence

of holes are centred at 0 mm, see Figure 4.9. Typically equal to a negative shift by half the total number of cathode pads in the CRDC multiplied by the width of an individual pad. The data input for the x -position calibration is based on a Gaussian fit of the charge deposited across the cathode pads on an event-by-event basis. This was described and illustrated in Section 4.3.2.1 and Figure 4.6. For these Gaussian fits to be effective and accurate, the response of all cathode pads must be as uniform as possible. To achieve this uniformity, each of the CRDCs are gain-matched using experimental data. An arbitrary channel was chosen to match all other cathode pads against, in this case channel 166 was chosen. Finally, a range of isotopes with varying Z values was used to validate the calibration for any isotope traversing the focal plane. The results of this gain matching process can be seen in Figure 4.8.

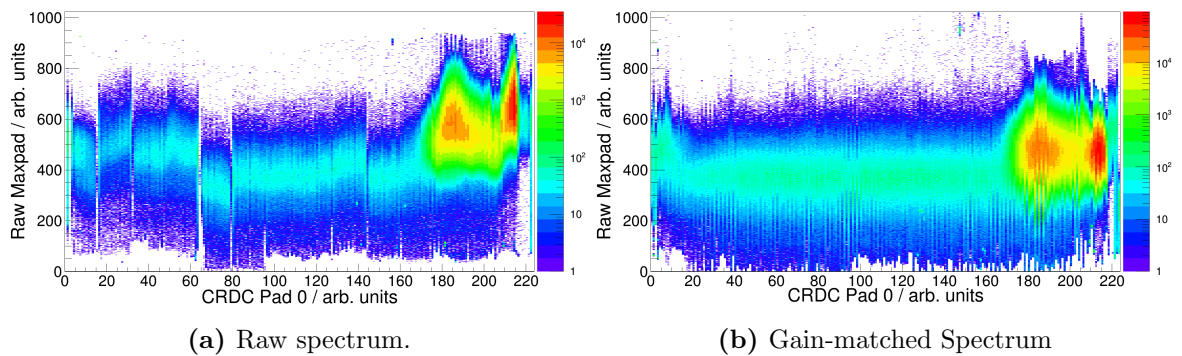


Figure 4.8: Calibration of the CRDCs. The 224 channels are gain matched relative to a chosen channel using the beam products on-line. The discrepancy in the centroids across the pads is due to the varying isotopes having different positional spread patterns through the CRDC.

In the y -direction the functional form as defined in Equation 4.7 derives from a linear relationship between the drift time of the electrons released in the gas to the y -position within the CRDC. This relationship is determined using a sequence of tungsten holes across the y -axis, such that the horizontal beam of the “L” shaped hole sequence is aligned with 0 mm, see Figure 4.9. The drift time is dependent on the temperature, pressure and changes in gas composition within the CRDCs, as such multiple mask runs were taken throughout the experiment and the positional changes were interpolated. The results of this positional calibration procedure are shown in Figure 4.9.

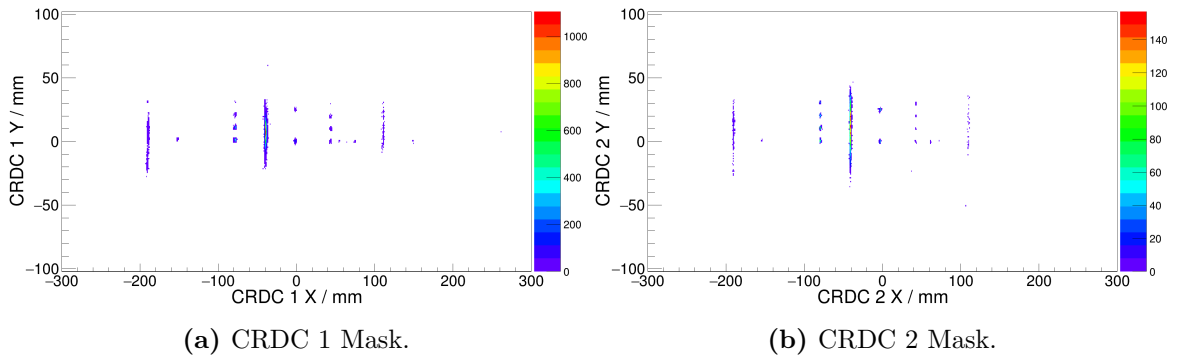


Figure 4.9: Position calibrated mask data for both CRDCs. The positions of the slits and holes can be seen in the data and are used to form the calibration as described above.

4.4.2 Ion Chamber Calibrations

There are sixteen pads in the ion chamber, as discussed in Section 4.3.2.2, are aligned along the beam-axis. The energy loss variable used was determined by the average energy loss within each pad of the chamber on an event-by-event basis. To prevent one channel dominating the average energy loss, the channels must be gain matched. This was achieved using the energy losses from a minimum of two nuclear species in each channel. The energy loss peaks of these species were fit with a Gaussian function. The centroids were fit with a linear function to scale each channel relative to one reference channel. In this case, Pad 0 was chosen as the reference channel. The results of this process are shown in Figure 4.10.

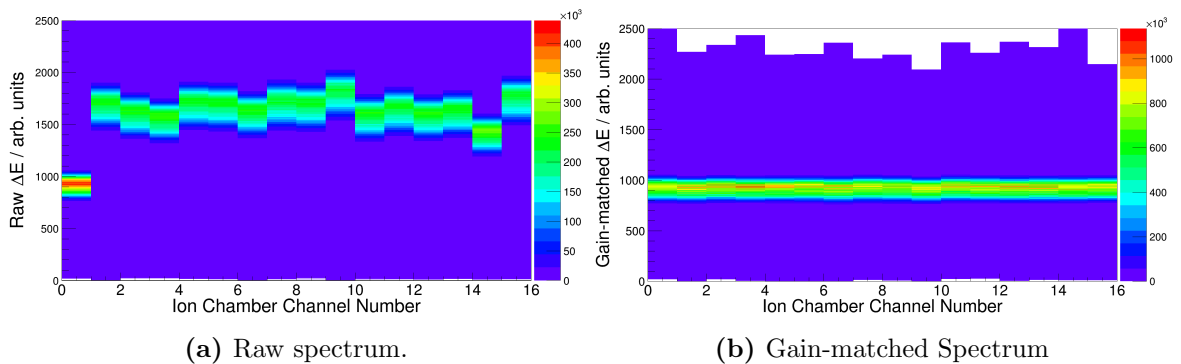


Figure 4.10: Calibration of the Ion Chamber. The 16 channels are gain matched relative to a chosen channel using the beam products on-line.

4.4.3 GRETINA Calibrations

GRETINA is maintained in a calibrated state and is delivered to every experiment as such. Source measurements were taken at the beginning and end of the experiment in order to certify this state. Data was taken for three γ -ray sources placed at the target position of GRETINA. The spectra of these sources and information from natural radioactive isotopes were fit with Lorentzian peaks on top a linear background. The centroid of this Lorentzian fit provided an observed γ -ray energy to compare against reference energies. The reference energies used in this calibration check are listed in Table 4.1. The result of this procedure is seen in Figure 4.11.

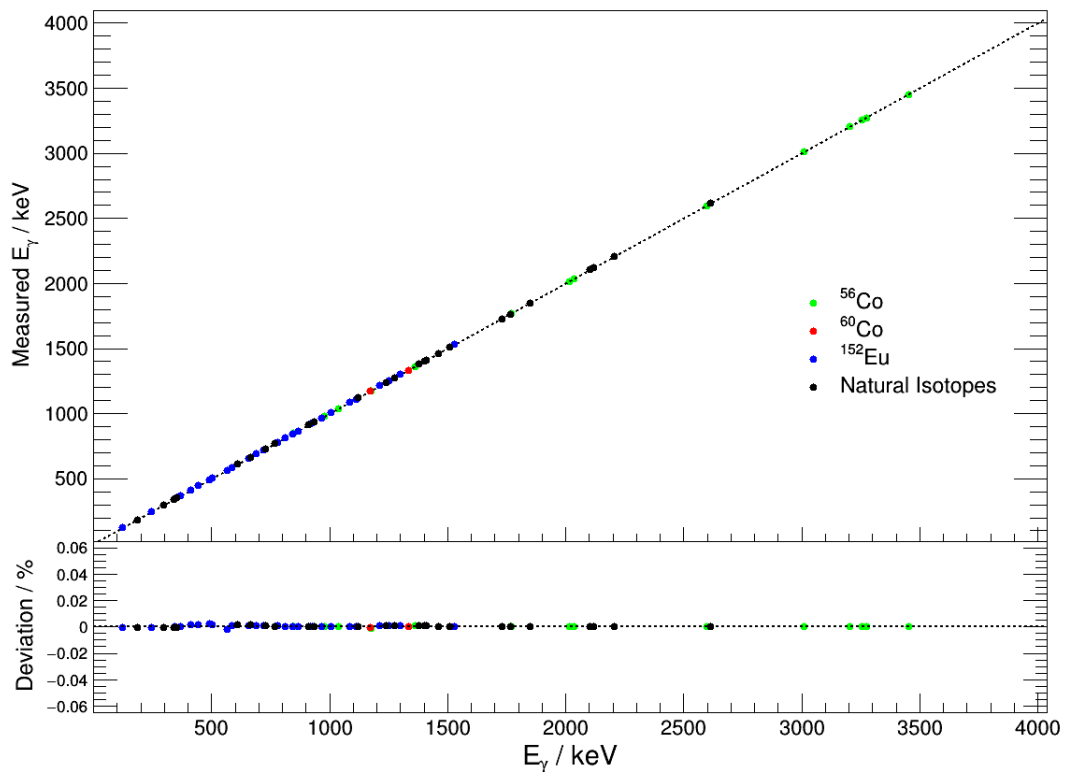


Figure 4.11: Proof of GRETINA energy calibration through a comparison of measured and known γ -ray energies. This was completed using the radioactive sources ^{56}Co , ^{60}Co , ^{152}Eu and a number of naturally occurring radioactive isotopes.

Nuclide	E_γ transitions used for calibration (keV)				
^{56}Co	846.77	977.37	1037.84	1175.10	1238.28
	1360.21	1771.35	2015.18	2034.75	2598.46
	3009.59	3201.96	3253.41	3272.99	3451.15
^{60}Co	1173.23	1332.50			
^{152}Eu	121.78	244.69	295.93	344.28	367.79
	411.12	443.96	488.68	503.47	566.44
	586.26	656.49	688.67	719.35	778.90
	810.45	841.57	867.38	919.34	926.31
	964.06	1005.27	1085.84	1112.08	1212.95
	1249.94	1299.14	1408.01	1528.10	
$^{22}\text{Na}^*$	1274.53				
$^{40}\text{K}^*$	1460.8				
$^{232}\text{Th}^*$	338.32	727.33	911.20	2103.51**	2614.51
$^{235}\text{U}^*$	185.72				
$^{238}\text{U}^*$	295.22	351.93	609.32	665.45	768.36
	934.06	1120.29	1238.12	1377.34	1401.51
	1407.99	1509.21	1729.59	1764.49	1847.65
	2118.51	2204.06			

* Naturally occurring radioactive isotopes.

** Single escape peak.

Table 4.1: Reference energies and isotopes within the energy calibration verification process.

4.4.4 Time of Flight Corrections

The time-of-flight measurements between the xfp and obj scintillators, and the E1 scintillator analysed the velocity of given particles traversing the experimental set-up. Since the S800 was tuned to a constant magnetic rigidity linked to recoils of interest ($B\rho$) and there was a known flight path length through the system (L), this velocity can be linked to the mass-charge ratio of the particles.

$$B_\rho = \gamma \frac{mv}{q} \rightarrow \frac{1}{v} = C \cdot \frac{m}{q} = \frac{\Delta T_{\text{scint}}}{L}, \quad (4.8)$$

where C is a constant and ΔT_{scint} is the time-of-flight of individual particles.

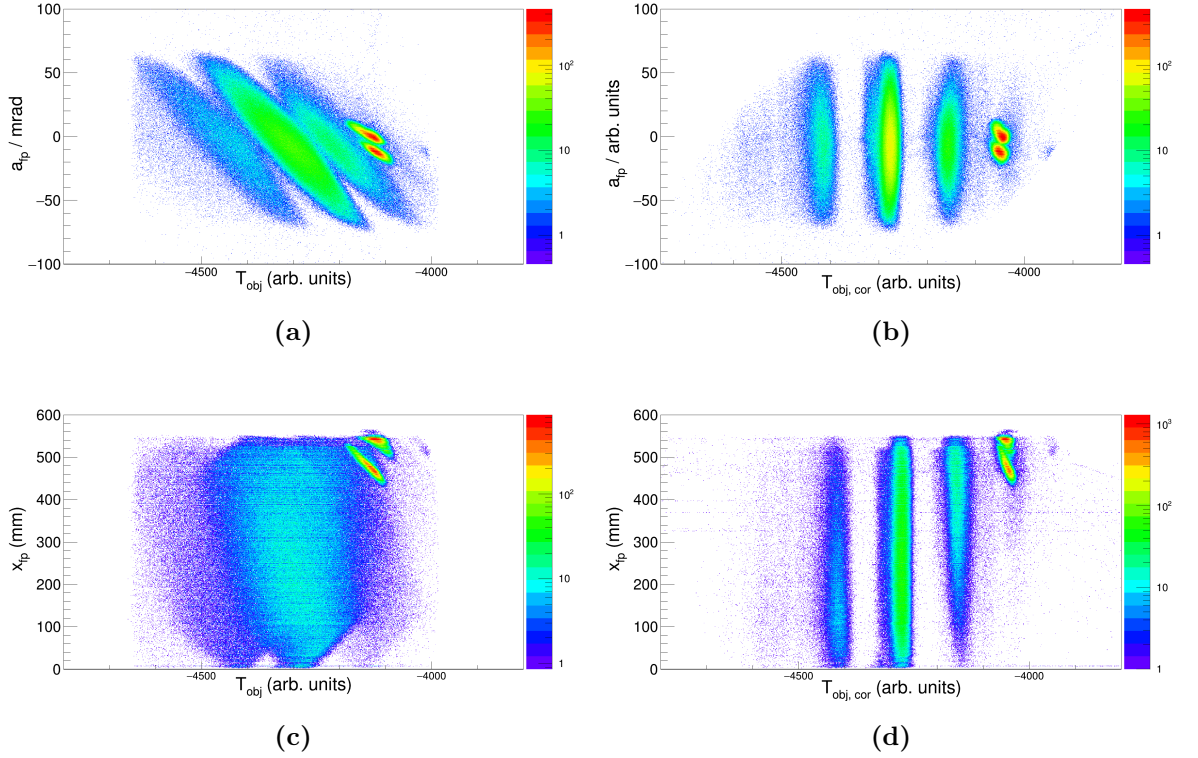


Figure 4.12: (a) afp angle in the dispersive direction vs time-of-flight parameter obj. (b) afp angle in the dispersive direction vs the corrected time-of-flight parameter obj. (c) x position in the focal plane of the S800 vs time-of-flight parameter obj. (d) x position in the focal plane of the S800 vs the corrected time-of-flight parameter obj.

The most effective implementation of the time-of-flight measurement takes into account the trajectory of the particles. There was a correlation between the time-of-flight through the spectrograph and trajectory of the particles within the dispersive plane. By correcting the linear dependence between the dispersive angle and the dispersive position the identification of different species within the beam can be improved. This correction takes the form:

$$T_{\text{scint, corr}} = T_{\text{scint}} + m a_{fp} + n_{fp}, \quad (4.9)$$

where a_{fp} is the dispersive angle and x_{fp} is the position at the focal plane. m and n are correctional constants to be determined. Figure 4.12 shows this correction in place

for the time-of-flight parameter from the object scintillator, but this is also done for the extended plane scintillator and the cyclotron RF signal.

4.4.5 Doppler Correction

Because the detected γ rays within GRETINA were emitted by a fragmented beam travelling at approximately 25% the speed of light, Doppler broadening and shift corrections were needed. These corrections are described in more detail in Section A.2.4. These corrections were performed on an event-by-event basis using the sub-segment γ -ray interaction position from GRETINA and the reaction recoil trajectory information recreated by the S800. The average velocity of the emitting particles was also needed to correct these Doppler effects. To determine this, the value of β was varied between 24.5% and 28.5% the speed of light and a γ -ray from ^{27}Si was fit with a Gaussian distribution. The optimized beta value was determined with the associated minimum FWHM value of the Gaussian distributions. Figure 4.13 shows this β minimization and the optimum beta value was found to be 0.264c. This value is reasonable given the $B\rho$ setting of the S800 and LISE++ reaction calculations.

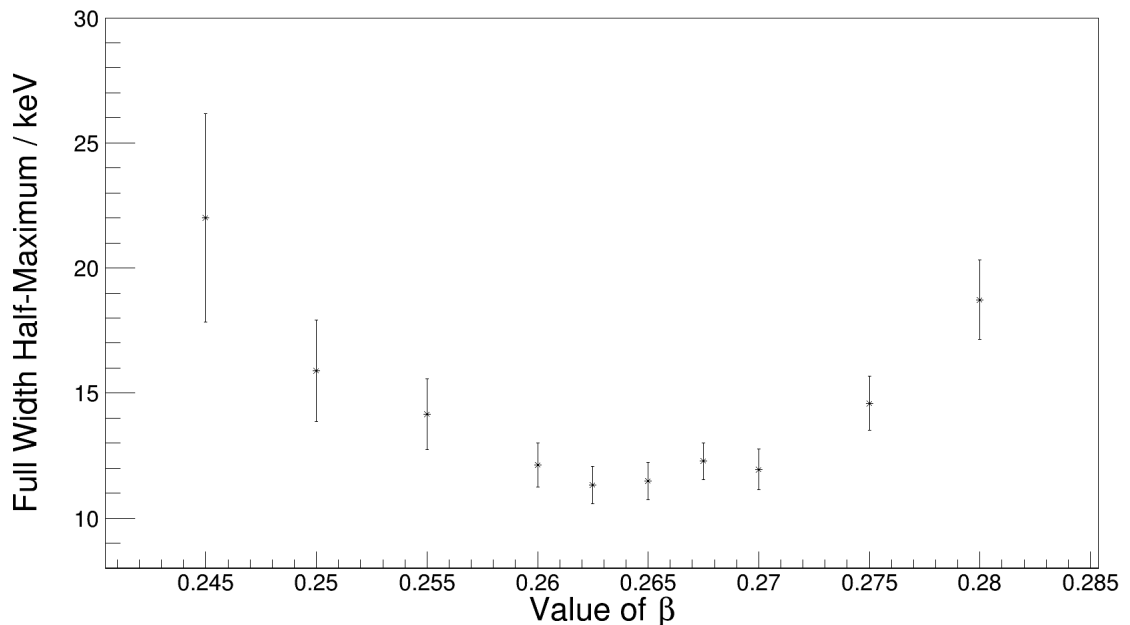


Figure 4.13: The FWHM of the 2866.1 keV peak in ^{27}Si versus the β value input into the Doppler correction. The optimum value of β is found where the FWHM is at a minimum, within this example that value is found to be 0.264c.

4.4.6 Target Placement Correction

The Doppler corrected energy is directly proportional to the scattering angle, or $\cos(\theta)$. The assumed scattering angle observed within GRETINA is dependant on the assumed target position with respect to the centre of this forward focused array. A shift of the assumed target position in the negative Z direction, or upstream from the target, has the effect of decreasing the scattering angle and subsequently increasing the Doppler corrected energy. Similarly, an increase within the Z direction increases the apparent scattering angle and so decreases the Doppler corrected energy. Figure 4.14 shows the effect of this assumed target positioning.

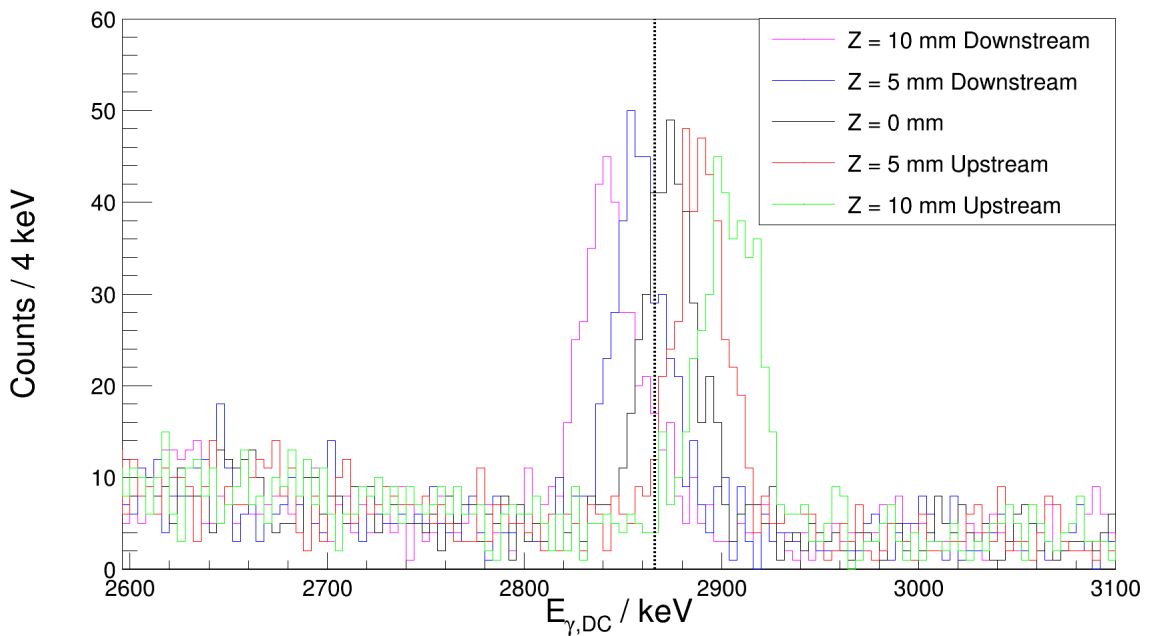


Figure 4.14: Effect of target placement with respect to the centre of the GRETINA array on Doppler corrected gamma-rays. Example using ^{27}Si 2866 keV decay.

To determine the optimum assumed position for the target, this value was varied within the analysis software through a range of $-5 \text{ mm} < Z < 5 \text{ mm}$ in steps of 0.5 mm. The Doppler corrected peaks were fit with a Lorentzian fit upon a linear background to determine the energy and width of the peak and compared to a known energy. The optimum position for the target z-position was determined where the energies matched to be 2 mm downstream. Figure 4.15 shows the corrected gamma-ray spectrum for the 2866 keV Doppler corrected decay within ^{27}Si as a function of phi. This highlights the combined beta and target position corrections together.

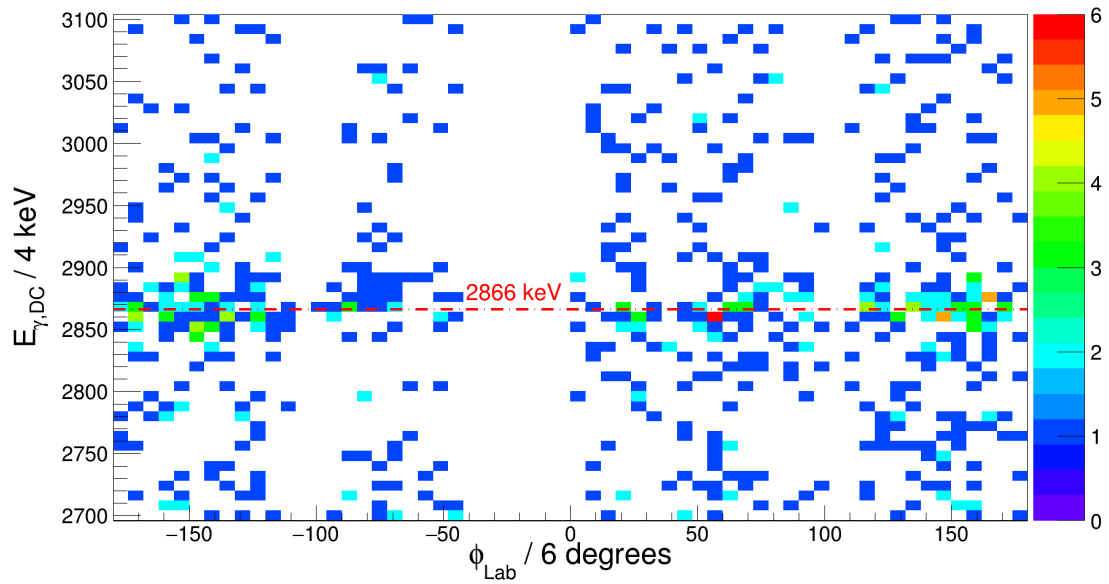


Figure 4.15: Target holder position corrected and Doppler minimized spectrum focused on the 2866 keV gamma-ray, as a function of lab phi angle.

4.5 ^{27}Si Particle and State Identification

4.5.1 ^{27}Si Particle Identification

After detector calibrations and corrections, a key part of the analysis was selecting the reaction species of interest within the S800 focal plane. This allowed only data corresponding to ^{27}Si nuclei populated through the (d, p) reaction to be considered within further analysis. This prevented any nuclei populated through other reaction channels to be considered, such as fusion evaporation or inelastic scattering.

The first step in this process was to identify the incoming beam fragments delivered to the target station. The primary beam of ^{36}Ar was delivered onto a ^9Be target at the entrance to the A1900. The resultant secondary cocktail beam after separation can be seen in Figure 4.16. The time-of-flight differences between the extended focal plane of the A1900 and the at object station of the S800, to the focal plane of the S800 can distinguish between the various cocktail ions. This particle identification plot separates the ions with respect to their beam energy and can be used to determine the relative composition between the ions. This secondary beam was composed of $\sim 60\%$ ^{26}Si and $\sim 40\%$ ^{25}Al particles. Software gates were used in the analysis to focus on

events related to the ^{26}Si secondary beam ions.

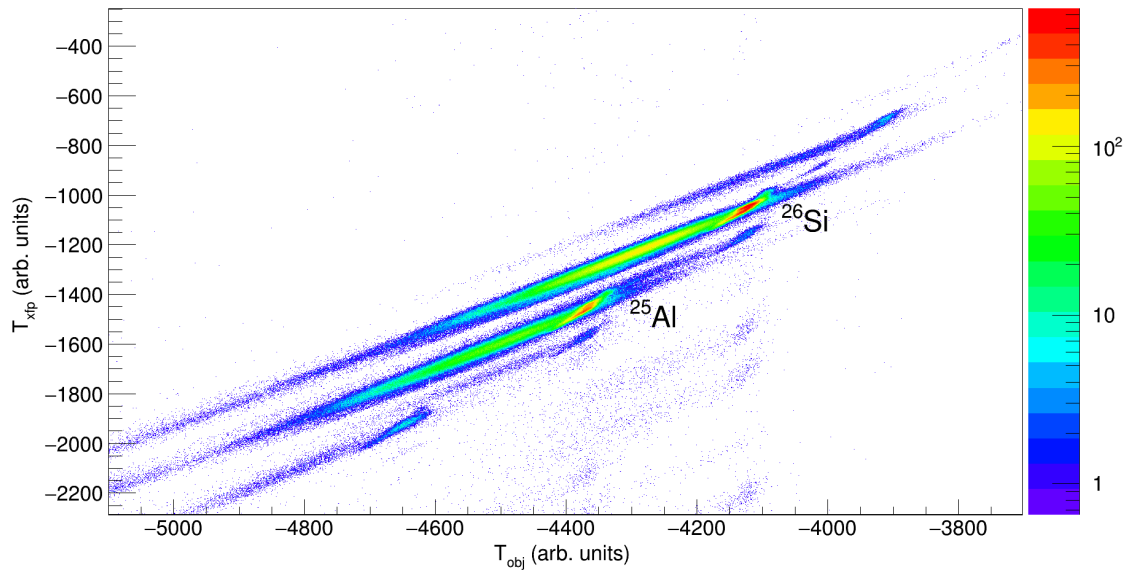


Figure 4.16: The secondary beam composition after purification through the A1900 fragment separator. Each individual component within the beam can be distinguished by the time-of-flight differences between A1900 extended focal plane scintillator (xfp) and the S800 object scintillator (obj) and the E1 scintillator at the end of the S800. The beam is composed of almost equal parts ^{26}Si and ^{25}Al , as well as some other smaller components.

Using the secondary beam software gates, the S800 focal plane data was used to identify the reaction products produced at the S800 target station. In general, many species of reaction products with the same A/Q and Z , but different recoil angles, will enter the S800 focal plane detectors. Correcting for dispersive effects using the CRDCs it was possible to identify the reaction products using the time-of-flight between the S800 object scintillator and focal plane, T_{obj} , and the energy deposited within the ionisation chamber. These provided a separation based on the A/Q and Z of the ion respectively. The results of this analysis can be seen with Figure 4.17. This provided a second software gate to ensure subsequent analysis only referred to the ^{27}Si ions produced by $^{26}\text{Si}(d,p)$ transfer.

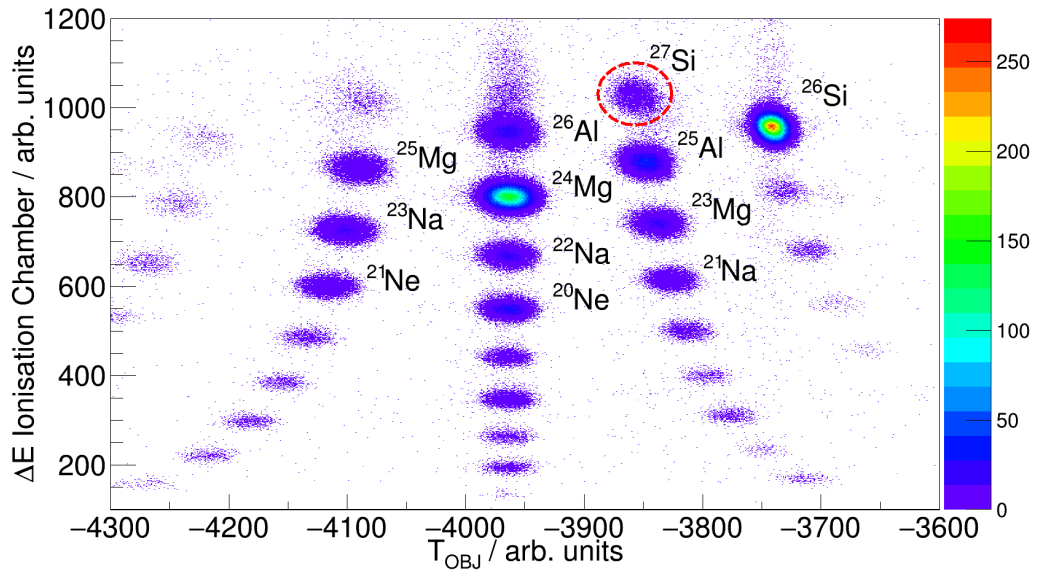


Figure 4.17: Secondary beam reaction products using the ^{26}Si software gate. ΔE separates the isotopes at the focal plane based on their Z^2 whilst the time-of-flight from the S800 object scintillator to the S800 E1 scintillator separates the isotopes by their A/Z . Elements are therefore separated in the vertical axis, with isotopic chains following slanted lines from left to right in decreasing neutron number. Moving along the vertical columns changes the locus by one neutron and one proton. The unreacted beam component is the dominant locus within this plot, with the isotope of interest ^{27}Si located one locus left on the Si elemental slant.

4.5.2 ^{27}Si State Identification

In this work, a γ -ray add back spectrum gated on ^{27}Si ions at the S800 focal plane was obtained, displayed in Figure 4.18. This spectrum gives no information about the ordering of the levels observed, and the limited statistics for a $\gamma - \gamma$ matrix provided little information. ^{27}Si has a well documented level scheme and decay structure and no new levels are assigned from this work. Information from previous studies was used to determine the state population from the γ -ray singles spectrum. Figure 4.19 displays the observed state population and subsequent decays observed or analysed in this work.

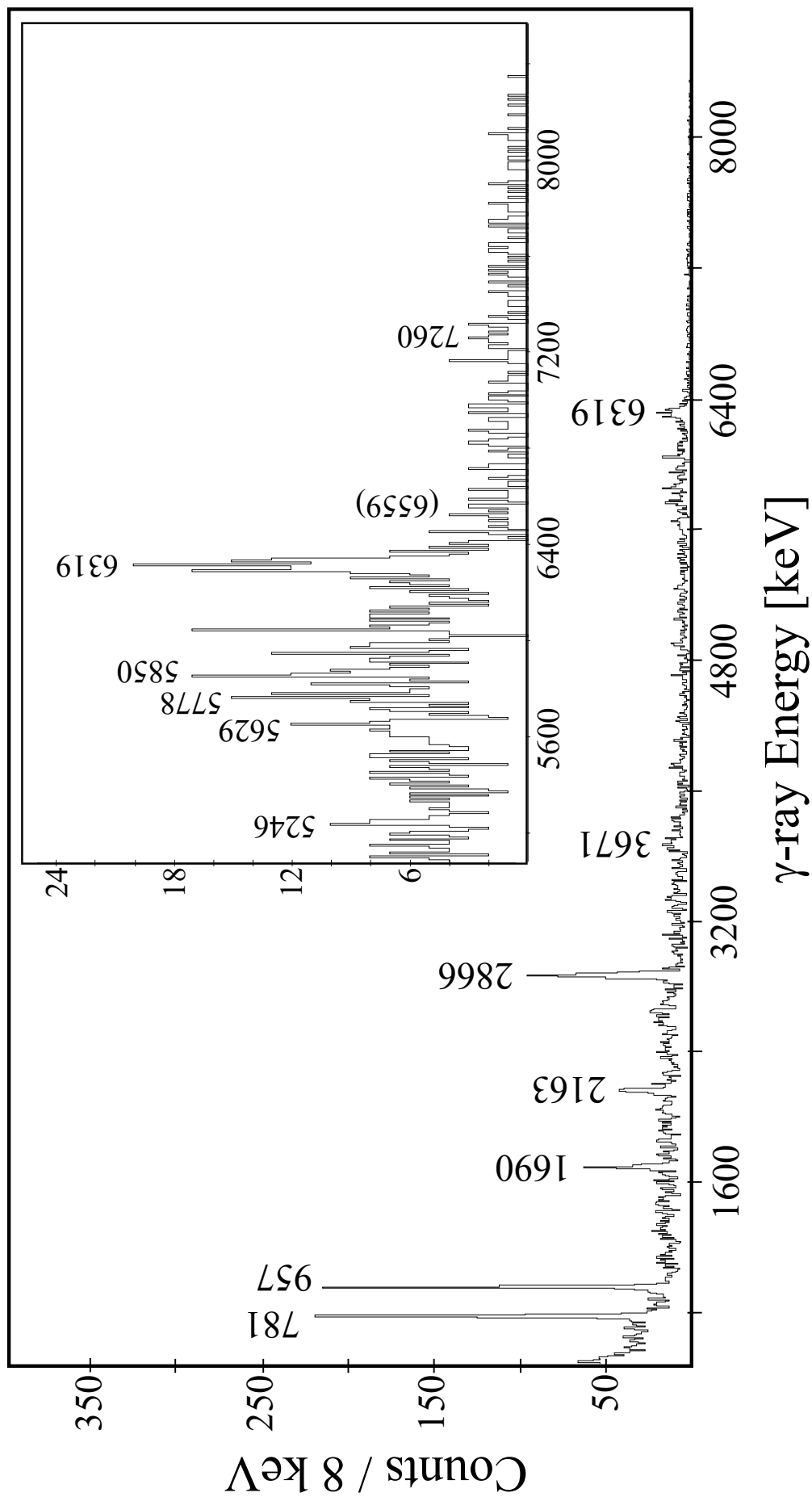


Figure 4.18: Doppler-reconstructed γ -ray spectrum in coincidence with ^{27}Si recoils. (Inset) Expanded energy region of interest for nuclear astrophysics.

4.5.3 Reaction Mechanism Determination

Due to the presence of carbon atoms within the deuterated polyethylene target there was the possibility of populating states within ^{27}Si via $^{26}\text{Si}(^{12}\text{C},^{11}\text{C})^{27}\text{Si}$. To explore this possible source of background within the ^{27}Si PID gate, an 13 (1) mgcm^{-2} non-deuterated polyethylene, CH_2 was installed at the target position of GRETINA. In a similar manner to the CD_2 target data analysis, the time-of-flight difference between the extended focal plane scintillator and the object scintillator was used to identify the incoming beam species. Gating on the ^{26}Si beam species an outgoing beam species PID plot was created, seen in Figure 4.20.

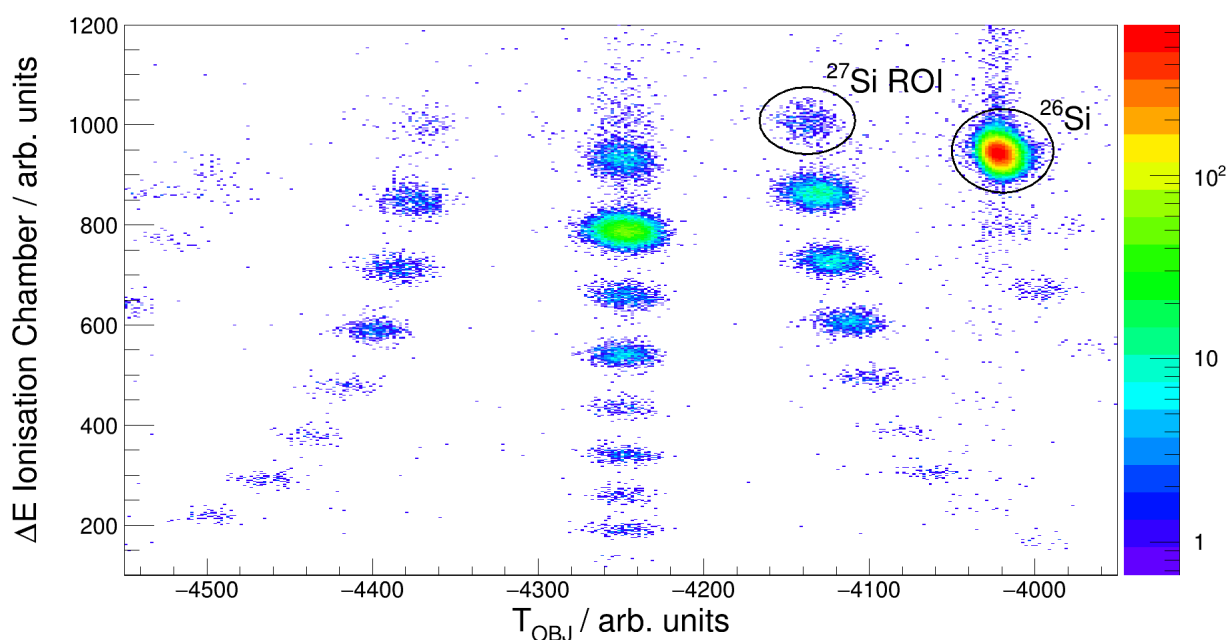


Figure 4.20: Particle identification using CH_2 target.

A particles gate was then placed around the possible outgoing ^{27}Si ions and the γ -ray information from GRETINA analysed. The γ -ray singles spectrum from this particle gate is shown in Figure 4.21. This is the summary of 12 hours worth of beam-on data. As can be seen within the spectrum there is no evidence of strong excitation population. No clear photopeaks are observed at 781 or 957 keV, the strongest lines from the CD_2 data. Therefore background from this reaction was deemed to be negligible.

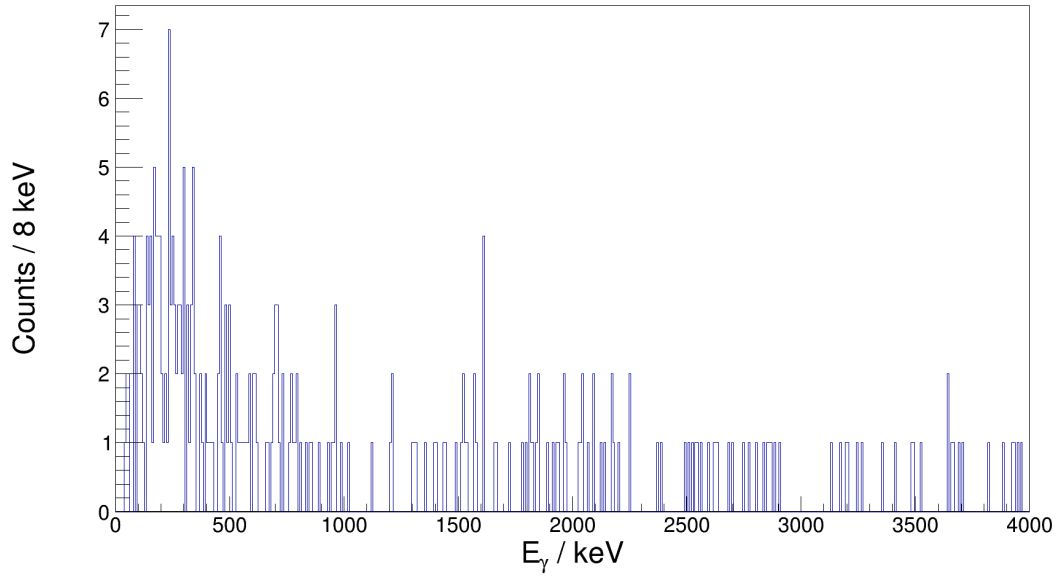


Figure 4.21: γ -ray information gated on the CH_2 ^{27}Si ROI.

4.6 Determining Cross Section

Transfer reaction cross sections are determined through the following equation:

$$\sigma_{(d,p)} = \frac{(N_R/t)}{(N_B/t)(N_T/A)}, \quad (4.10)$$

where N_R is the number of recoils created by the reaction, N_B is the number of incident beam particles involved, N_T is the number of target atoms, t is the time the beam is incident on the target and A is the target area illuminated by the beam. For this study, recoil- γ coincidence data was used to determine the number of recoils for a given recoil excitation. This was determined by the number of γ rays associated with the excitation, accounting for the branching ratios associated with the γ -ray and the efficiencies of detecting the γ -ray and recoil particles. Defined as:

$$N_R = \frac{N_\gamma}{(\epsilon_{S800} \cdot \epsilon_\gamma \cdot B_\gamma)}, \quad (4.11)$$

where N_γ is the number of detected γ rays associated with a given state gated upon the ^{27}Si recoils within the S800, ϵ_{S800} is the efficiency of detecting the ^{27}Si recoils, ϵ_γ is the detection efficiency of the γ rays as a function of its energy and B_γ is a correction for the branching ratio from the excitation through the observed γ -ray transition. The

cross section was then determined by the product of information from GRETINA and S800, and so Equation 4.10 can be defined as:

$$\sigma = \frac{N_\gamma}{(\epsilon_{S800} \cdot \epsilon_\gamma \cdot B_\gamma)} \cdot \frac{1}{N_B \cdot (N_T/A)}. \quad (4.12)$$

This section summaries the various analyses used to determine these quantities.

4.6.1 Determining N_R

The total number of ^{27}Si recoil particles created in the reaction was determined from the S800 focal plane detection systems. The γ -ray information from GRETINA then enabled the determination of the excitation specific information of these recoils to be inferred. As previously stated, the number of S800 particle gated γ rays observed in GRETINA is related by:

$$N_R = \frac{N_\gamma}{(\epsilon_{S800} \cdot \epsilon_\gamma \cdot B_\gamma)}. \quad (4.13)$$

The two efficiency factors related to the GRETINA γ -ray and S800 recoil detection are dealt with in separate subsections 4.6.1.1 and 4.6.1.2.

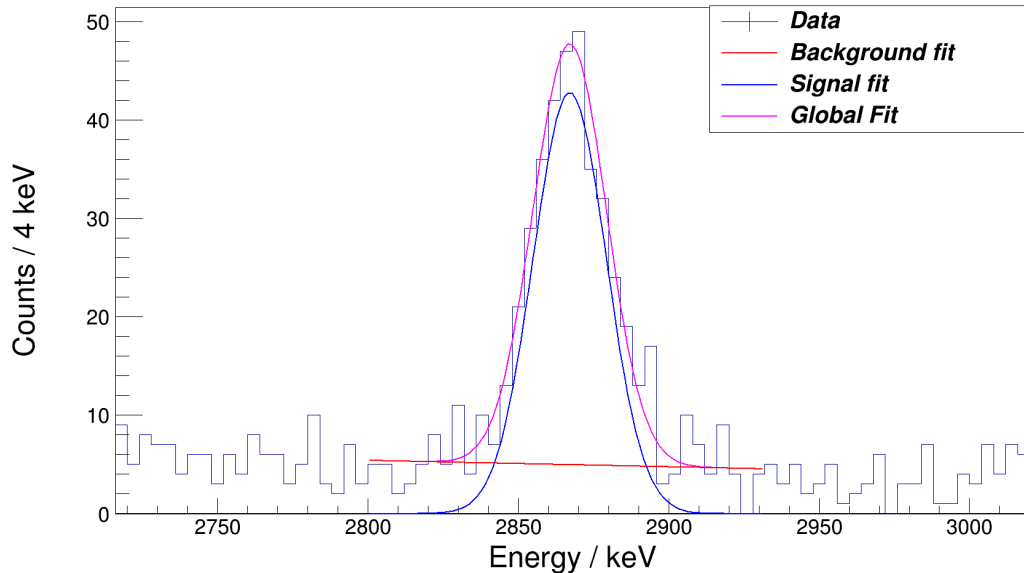


Figure 4.22: Example fit of the 2.866 MeV decay for the determination of N_γ . The integral of a Gaussian function upon a linear background was used in this example.

E_x (MeV)	E_γ (MeV)	N_γ	I_γ	ϵ_γ	N_R
0.781	0.781	315.5 (20)	100 ¹	8.71	3621 (225)
0.957	0.957	213.2 (19)	100 ¹	8.01	2836 (261)
2.163	2.163	99.3 (11)	100 ¹	4.85	2048 (217)
2.647	1.690	62.0 (12)	100 ¹	5.76	1399 (485)
	2.647	13.2 (4.0)	26 ¹	5.76	1577 (266)
2.866	2.866	309.9 (18)	100 ¹	3.89	8354 (510)
4.289	4.289	25.2 (12)	100 ¹	3.43	1784 (640)
	3.330	23.1 (9.0)	79 ¹	3.43	1631 (857)
5.850	5.850	42.0 (6.5)	75 ³	1.93	2903 (691)
	4.892	14.0 (3.7)	25 ³	2.35	2381 (1020)
6.027	5.246	12.6 (3.8)	100 ²	2.18	805 (144)
6.319	6.320	151.8 (12)	100 ²	1.76	13210 (1072)
	4.165	31.0 (5.6)	18 ²	2.78	9465 (1700)
	3.670	50.0 (7.1)	30 ²	3.13	8147 (1293)
6.559	6.559	19.7 (4.4)	34 ²	1.68	7126 (1647)
	5.778	62.3 (7.9)	100 ²	1.96	6596 (830)
6.586	5.630	19.0 (4.4)	100 ³	2.01	943 (217)
7.262	7.262	<11.0 (3.3)	100 ³	1.47	<748 (226)
7.838	6.879	<11.0 (3.3)	100 ¹	1.56	<784 (236)
7.909	7.127	<3.0 (1.7)	100 ¹	1.50	<200 (116)
8.070	7.112	<2.0 (1.4)	100 ¹	1.52	<132 (94)
8.140	7.180	<3.0 (1.7)	100 ¹	1.49	<201 (116)
8.184	7.402	<1.0 (1.0)	100 ¹	1.43	<699 (70)

^a Taken from the NNDC [103].

^b Assumed from mirror nuclei ²⁷Al structure.

^c Assumed intensity.

Table 4.2: Summary of the measured number of recoil ²⁷Si ions with a given excitation energy, determined using γ -ray information from GRETINA.

The number of γ rays, N_γ , associated with a given excitation was determined by fitting the various γ -ray photopeaks, displayed in Figure 4.18, with a Gaussian

function combined with an appropriate background function. An example of this fit can be seen in Figure 4.22. Figures 4.18 and 4.22 show that no γ -ray decays from excited states above the proton separation threshold were observed. However, it was possible to place stringent upper limits on states between $100 \text{ keV} < E_r < 500 \text{ keV}$ for the $^{26m}\text{Al} + p$ system. This was achieved by fitting appropriate γ -ray energy region linked to the decay from known resonant states. These fittings were constrained in width by fixing the width to the observed 7.262 MeV γ -ray transition and in height using the excess counts within the fit space.

The branching ratios used were taken from the NNDC [103] where available. For excitations above 5 MeV there is limited evaluated I_γ information, in these cases the information has been inferred using the evaluated mirror excitations within ^{27}Al . In the circumstances where both of these data sources were unavailable the intensity is assumed to be representative of 100% of the excitation's decay pathway. A summary of the extracted information can be seen in Table 4.2. The uncertainty in the number of recoils was determined by a addition in quadrature of the fitting error, uncertainty in the efficiencies and branching ratio uncertainty.

4.6.1.1 Determining γ -ray Efficiencies

Decaying ions travelling at relativistic energies complicates the determination of the γ -ray efficiency. At such energies the effect of the Lorentz boost is to push γ -ray emission angles to more forward angles. Stationary sources cannot be used to recreate the efficiencies under these conditions and in-beam tests are an expensive method for determination on an experiment-by-experiment basis.

The absolute efficiency of the GRETINA array was determined using a Geant4 simulation package, UCGretina [183]. Developed at Ursinus College, this package contains the complete geometry of the array, fully segmented detectors with cryostats, the mounting hemispheres, aluminium beam pipe, target material, the S800 geometry and components and the capability to include in-beam experimental parameters. The energy and position of interactions within the GRETINA geometry are determined on an event-by-event basis, such that it can be analysed in an identical manner to experimental data.

The in-beam reaction is modelled as a single step into an excitation before emitting a γ -ray with an energy equal to the excitation energy. γ rays are emitted isotrop-

ically in the rest frame before the Lorentz boost is applied based on the experimental details. This simulation package has been proven in multiple experiments to replicate efficiency calculations from stationary source data. Shortly after the completion of this study, an in-beam study was completed by Dirk Weissnar to study the efficiency of GRETINA at energies above radioactive decay source energies [184]. The simulation was still accurate at these energies whilst extrapolated stationary source data over-estimated efficiencies. As a result this reaction was simulated in γ -ray energy steps of 100 keV in a range of $0.2 < E < 8.5$ MeV to provide a detailed efficiency curve with energy. The resulting efficiency curve can be seen in Figure 4.23.

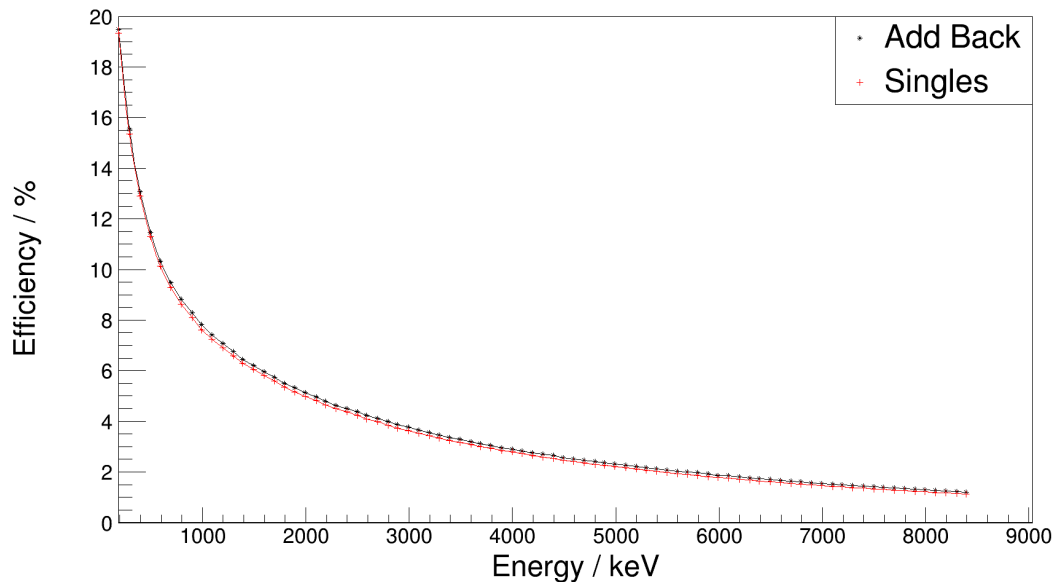


Figure 4.23: Simulated efficiency curves for both single and add-back data. These were used in the determination of the number of recoil particles from their γ -ray decays.

4.6.1.2 Determining S800 Efficiencies

The number of reactant products was determined by the number of γ -ray decays observed within GRETINA. These observed decays were determined using a software gate on ^{27}Si ions observed within the S800 focal plane. Whilst the magnetic spectrograph has a large angular and momentum acceptance, the transmission percentage of the ions of interest is an important factor. Figure 4.24 displays the positional peak of ^{27}Si ions within the second CRDC. The X position is inversely proportional to the momentum of the ion. It can be seen that the centroid of the peak is firmly within the

positional range of the detector. Assuming the momentum distribution of the ions is symmetric, one would expect that there would be an equivalent number of ions on both sides of the centroid. An integration from either side of the peak determined that there was 2% less ^{27}Si ions within the low momentum tail (high CRDC X position) than the high momentum tail (low CRDC X position). Previous experiments have shown that the momentum distribution is typically asymmetric towards the lower momentum end [185]. As such, it was estimated that the actual transmission rate of the S800 was 95%, this value is also typical from previous S800 experiments.

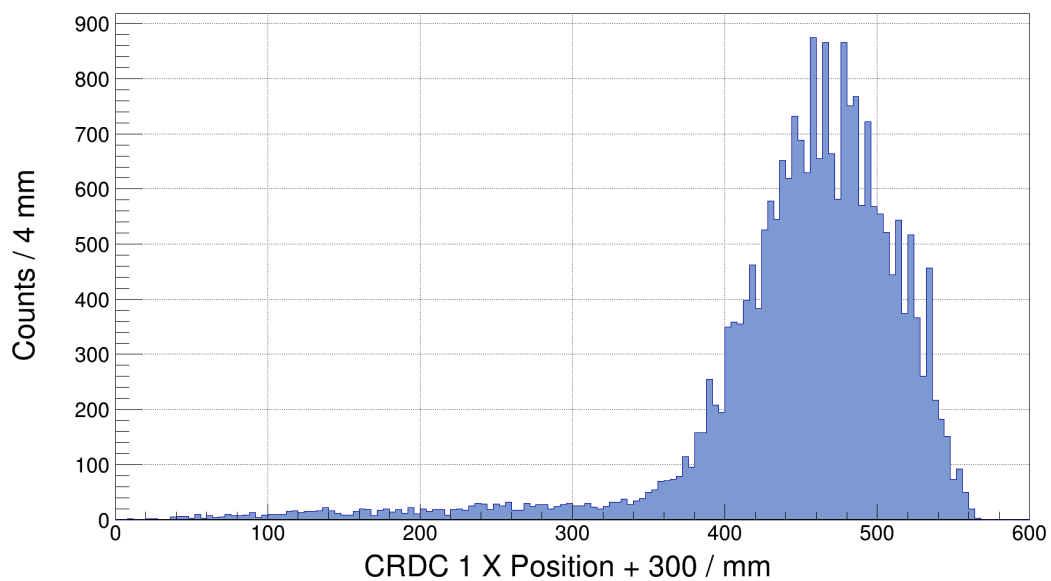


Figure 4.24: CRDC 1 X position of ^{27}Si ions determined by the focal plane detectors of the S800. This distribution was used to estimate the transmission percentage through to the focal plane of the S800.

4.6.2 Determining N_B

Quantifying the number of incident beam particles that impinged upon the target during the course of the experiment is critical to the calculation of the cross section. In this study, the total number of beam particles was monitored using the thin plastic scintillators throughout the beam line. A set of scalar modules was connected to the output of these scintillators to record the number of events during each run. The analysis of these scalar outputs provided an estimation of the number of ^{26}Si ions incident on target.

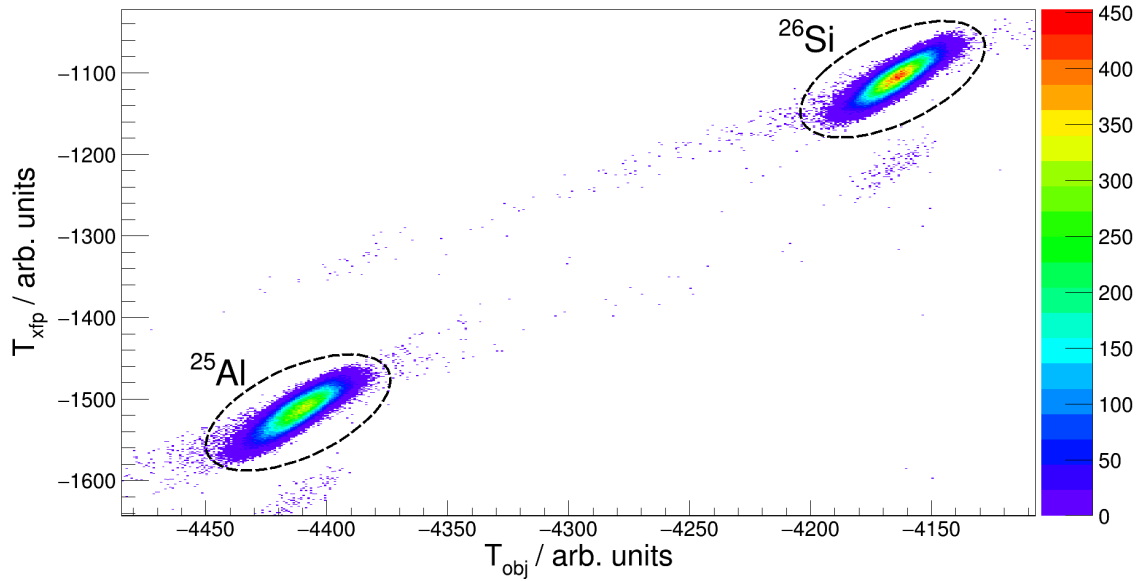


Figure 4.25: PID plot from a mass calibration run carried out periodically during the experiment. By integrating these isotopic groups a determination of the composition was made.

Key to the analysis of these scalars was a number of calibration runs taken periodically throughout the experiment. During these runs the focus of the S800 was tuned to allow all of the beam-like products into the focal plane, with an attenuated beam to prevent significant dead time. These calibration runs allowed a beam composition measurement to be made by a time-of-flight comparison on an event-by-event basis. The main contaminant within this experiment was determined to be ^{25}Al and was clearly separated by the analysis line of the S800, as can be seen in an calibration run example in Figure 4.25.

Mass Run No.	$N(^{26}\text{Si})$	$\%(^{26}\text{Si})$	$N(^{25}\text{Al})$	$\%(^{25}\text{Al})$	$\%\text{Other}$
1	11474 (107)	52.85	9452 (97)	43.53	3.62
2	43129 (208)	63.96	21450 (146)	31.81	4.22
3	25020 (158)	62.83	13232 (115)	33.23	3.94
4	217505 (466)	49.99	205280 (453)	47.19	2.82
5	67823 (260)	60.12	41108 (202)	36.44	3.45
6	175078 (418)	63.15	92069 (303)	33.21	3.65

Table 4.3: Information determined from mass calibration runs.

Table 4.3 displays the information extracted from the mass measurement runs. The variation in composition throughout the experiment stems from various optic fluctuations and tuning efforts on the production target within the A1900. Interpolating between these mass measurement runs allowed for the estimation of the number of ^{26}Si ions. Using the object scintillator, which is upstream from the target, the total number of ions traversing the analysis line was on a run-by-run basis. The mass measurement interpolation was then applied to the resultant scalar values producing the total number of ^{26}Si ions throughout the experiment. The total number of ^{26}Si ions throughout the experiment was determined to be $6.8 (13) \times 10^9$. The main source of uncertainty derives from the changes in composition run-to-run basis and estimated up to 20%.

4.6.3 Determining N_T/A

The reaction target used within this study was composed of deuterated polyethylene $(\text{CD}_2)_2$, commonly known as CD_2 . The number of deuterium atoms over the target area, N_T/A , is a necessary component to determine the cross section of the reaction and is quantified by the thickness of the target. The thickness of the target was determined to be 9.1 mgcm^{-2} through α -particle stopping measurements made by the NSCL group led by Remco Zegers. Equation 4.14 quantifies the relationship between the target thickness and the number of target atoms.

$$\frac{N_T}{A} = \frac{t_{TAR} \cdot N_A \cdot N_{((\text{CD}_2)_2)} \cdot \text{at}\%(D)}{M_{((\text{CD}_2)_2)}}, \quad (4.14)$$

where t_{TAR} is the target thickness in mgcm^{-2} , N_A is the Avogadro constant, $N_{((\text{CD}_2)_2)}$ is the number of atoms in a single unit of the compound, $\text{at}\%(D)$ is the atomic percentage of deuterium in the compound and $M_{((\text{CD}_2)_2)}$ is the molar mass of a compound unit. Table 4.4 displays the individual quantities within Equation 4.14.

t_{TAR} (g/cm^{-2})	$N_{((\text{CD}_2)_2)}$	$\text{at}\%(D)$	$M_{((\text{CD}_2)_2)}$ (g/mol)	$\frac{N_T}{A}$ ($\text{atoms}/\text{cm}^{-2}$)
$9.1 (8) \times 10^{-3}$	6	4/6	32.05	$6.8 (6) \times 10^{20}$

Table 4.4: Quantities used to determine the deuterium density within the target for cross section calculation.

4.6.4 Summary of measured cross sections

E_x (MeV)	E_γ (MeV)	N_R	σ (mb)
0.781	0.781	3621 (225)	0.78 (17)
0.957	0.957	2836 (261)	0.61 (14)
2.163	2.163	2048 (217)	0.44 (10)
2.647	1.690	1399 (485)	0.30 (8)
	2.647	1577 (266)	0.34 (13)
2.866	2.866	8354 (510)	1.8 (4)
4.289	4.289	1784 (640)	0.38 (20)
	3.330	1631 (857)	0.35 (16)
5.850	5.850	2903 (691)	0.62 (20)
	4.892	2381 (1020)	0.51 (25)
6.027	5.246	805 (144)	0.17 (6)
6.319	6.320	13210 (1072)	2.85 (65)
	4.165	9465 (1700)	2.04 (57)
	3.670	8147 (1293)	1.76 (47)
6.559	6.559	7126 (1647)	1.54 (48)
	5.778	6596 (830)	1.42 (35)
6.586	5.630	943 (217)	0.20 (6)
7.262	7.262	748 (226)	0.008 (6)
7.838	6.879	<784 (236)	<0.17 (6)
7.909	7.127	<200 (116)	<0.04 (2)
8.070	7.112	<132 (94)	<0.01 (1)
8.140	7.180	<268 (134)	<0.06 (3)
8.184	7.402	<70 (35)	<0.02 (1)

Table 4.5: Summary of the measured cross sections of recoil ^{27}Si ions with a given excitation energy, determined using γ -ray information from GRETINA.

Table 4.5 summarises the final cross sections determined using Equation 4.12 and all of the information discussed in the previous sections. The uncertainty in the cross section is determined by an addition in quadrature of the uncertainty in the number of

^{26}Si ions, number of deuteron atoms in the target and the uncertainty in the number of ^{27}Si , the latter of which is dominated by the fitting uncertainty. The cross section uncertainty is then either dominated by the number of ^{26}Si ions in the beam which was calculated to be up to 20% or by the fitting uncertainty in the γ rays.

4.7 Determining Spectroscopic Factors

The dimensionless spectroscopic factor, as defined in Equation 2.57, is a representation of the single particle nature description of a given excited state. This factor was discussed in more detail in Section 2.7. In this study, the spectroscopic factor is the factor relating the total cross section described in the previous section with the total cross section determined from the TWOFNR ADWA reaction code [137]. This is a three-body method that incorporates deuteron breakup and proven to be a good description of transfer reaction, it was discussed in more detail in Section 2.8.3. The Koning-Delaroche global optical model[138, 139] was used to calculate the d - ^{26}Si distorting potentials. A central real Woods-Saxon potential with a radius $r = 1.25$ fm, a spin-orbit term $V_{SO} = 6$ MeV and a diffuseness parameter $a_0 = 0.65$ fm was used, with the same geometry in the central interaction.

A suitable shell model orbital was chosen, dependent on the spin-parity of the final state, to describe the single particle nature of the final nucleus. Table 4.6 displays a summary of the extracted spectroscopic factors with their relevant shell model orbitals for the TWOFNR calculation and cross section information as described in Table 4.5. Uncertainties in theoretical cross sections have previously been determined to be up to 20%.

4.7.1 Comparison of non-resonant state spectroscopic factors

In general, the extracted spectroscopic factors from this study are in good agreement with those calculated from shell-model calculations and those determined from previous analog studies of the mirror ^{27}Al using $^{26}\text{Mg}(d,n)$ [186] and $^{26}\text{Mg}(^3\text{He},d)$ reactions [116, 187, 188]. In this study, shell-model calculations were performed by Alex Brown [189] from the National Superconducting Cyclotron Laboratory and are based on the USDB Hamiltonian within the sd shell-model space for states with a positive parity [143]

E_x / keV	E_γ / keV	J_n^π	σ / (μb)	nlj (ADWA)	$C^2S_{(d,p)}$
781	781	$1/2_1^+$	780(170)	$2s_{1/2}$	0.43(9)
957	957	$3/2_1^+$	610(140)	$1d_{3/2}$	0.11(3)
2163	2163	$7/2_1^+$	440(110)	¹	
2647	1690	$5/2_2^+$	300(90)	$1d_{5/2}$	0.05(2)
	2647				
2866	2866	$3/2_2^+$	1790(390)	$1d_{3/2}$	0.38(8)
4285	3328	$5/2_3^+$	380(140)	$1d_{5/2}$	0.06(2)
	4285				
5850	4893	$(3/2_2^-)^2$	491(130)	$2p_{3/2}$	0.06(2)
	5850				
	4893	$(7/2_4^+)^2$		¹	
	5850				
6027	5246	$3/2_3^-$	170(80)	$2p_{3/2}$	0.02(1)
6319	3671	$7/2_2^-$	2850(650)	$1f_{7/2}$	0.14(3)
	4156				
	6319				
6559	5778	$3/2_4^-$ ³	550(200)	$2p_{3/2}$	0.07(3)
	(6559)				
6586	5629	$5/2_8^+$	200(60)	$1d_{5/2}$	0.04(1)
7262 ⁴	7262	$(7/2_3^-)$	160(60)	$1f_{7/2}$	0.008(3)
7838	6881	$5/2_{14}^+$	≤ 168	$1d_{5/2}$	≤ 0.03
7909	7127	$3/2_5^-$	≤ 43	$2p_{3/2}$	≤ 0.01
		$3/2_{10}^+$		$1d_{3/2}$	≤ 0.01
8070	7112	$3/2_{12}^+$	≤ 14	$1d_{3/2}$	≤ 0.003
8140	7180	$1/2_7^+$	≤ 58	$2s_{1/2}$	≤ 0.09
		$1/2_3^-$		$2p_{1/2}$	≤ 0.02
8184	7402	$3/2_6^-$	≤ 15	$2p_{3/2}$	≤ 0.002

¹ Most likely populated via multi-step.

² Based on angular distribution coefficients reported in Ref. [165].

³ Parity assignment based on extracted cross section.

⁴ State reported in Ref. [167].

Table 4.6: Summary of the calculated spectroscopic factors for all observed states from the $^{26}\text{Si}(d,p)^{27}\text{Si}$ reaction. Also shown is the known or assumed spin-parities of these states and the orbitals used to describe the single particle nature of the state within TWOFNR.

and for the negative parity states, a WBP Hamiltonian including a $sd - pf$ Hamiltonian[190]. Table 4.7 displays a summary of all comparative spectroscopic factors in this study.

For states up to 5 MeV in energy, there are previously reported spin-parities and also good agreement with other comparative spectroscopic factor measurements. Except for the first 780 keV, $1/2^+$ state, these states will not be discussed in further detail here. This $1/2^+$ state is interesting after the recent publication of a $^{26m}\text{Al}(p,\gamma)^{27}\text{Si}$ study by S. Almaraz-Calderon *et al.*[169] which reported the spectroscopic factor into this state as 0.08(2). Adjusting for associated Clebsch-Gordon coefficients, this factor would equate to 0.16 within the (d,p) reaction, which is in discrepancy with this study. It is possible that this arises due to complications related to the $^{26}\text{Al}(p,\gamma)^{27}\text{Si}$ non-isomeric background subtraction performed by within that study.

E_x (keV)	J_n^π	$C^2S_{(d,p)}$	$C^2S_{(d,n)}$ [186]	$C^2S_{({}^3\text{He},d)}$ [116, 187, 188]	C^2S_{SM} [189]	Analog State in ^{27}Al (keV)
781	$1/2_1^+$	0.43(9)	0.41	0.50	0.41	844
957	$3/2_1^+$	0.11(3)	0.08	0.07	0.05	1014
2163	$7/2_1^+$		¹			2212
2647	$5/2_2^+$	0.05(2)	0.03	0.04	0.007	2735
2866	$3/2_2^+$	0.38(8)	0.47	0.63	0.32	2982
4285	$5/2_3^+$	0.06(2)	0.03	0.04	0.04	4410
5850	$(3/2_2^-)$	0.06(2)	¹		0.001	(6080)
	$(7/2_4^+)$		¹			(5961)
6027	$3/2_3^-$	0.02(1)	0.02	0.04	0.09	6159
6319	$7/2_2^-$	0.14(3)	0.22	0.20	0.23	6477
6559	$5/2_8^+ \ 3/2_4^-$	0.07(3)	0.07		0.12	6604
6586		0.04(1)	¹		0.002	(6767)
7262 ²	$(7/2_3^-)$	0.008(3)	¹		0.002	(7477)

¹ Seen in Ref. [186] but no C^2S reported.

² State reported in Ref. [167].

Table 4.7: Properties of observed excited states in ^{27}Si . Here compared to properties predicted by shell-model calculations and known mirror state properties in ^{27}Al .

The spin-parities and single neutron transfer orbitals for the 6.027, 6.319 and

6.586 MeV states in this study were taken from Ref., where they were assigned using the spin-parities from the mirror system, ^{27}Al [165]. The spectroscopic factors determined using these assignments are in good agreement with those from shell-model calculations, this study solidifies these assignments.

Both the 5.850 and 6.559 states were previously reported as $J^\pi = 3/2^+$ based on matching to the mirror ^{27}Al system [191]. The extracted cross sections from this study determine large spectroscopic factors using the $1d_{3/2}$ orbital which would be unfeasible for this reaction. Based on other possible state matching with the mirror system, a number of different spin-parity assignments were used within the TWOFNR reaction code and spectroscopic factors based on these assignments determined. As indicated in Table 4.7 assignments of $(3/2^-, 7/2^+)$ and $3/2^-$ were given for the 5.850 and 6.559 MeV states respectively, these assignments determine reasonable sized cross sections.

A γ -ray decay from the high excitation at 7.262 MeV was also observed within this study, this had been reported previously in work by Parikh *et al*[167] as an $l = 3$ transfer within the $^{28}\text{Si}(^3\text{He},\alpha)^{27}\text{Si}$ reaction and assigned potential spin-parities of $(5/2, 7/2)^-$. Based on the observed cross section in this study and comparing potential spin-parity spectroscopic factor determinations with those from shell-model calculation, the most likely assignment is $7/2^-$.

4.7.2 Relating resonant spectroscopic factors to the $^{26}\text{Al}(p,\gamma)^{27}\text{Si}$

No γ -ray decays were observed from states above the resonant threshold for the $^{26m}\text{Al} + p$ system, $E_x = 7.691$ MeV, this indicates that there are no strong single-particle states. As stated before there was enough evidence to place stringent upper limits on a number of possible resonant states, where there are excess counts in the region of their respective γ -ray decay. The 7.838 MeV state is interpreted as $5/2^+$ with a single neutron occupying the $1d_{5/2}$ orbital as previously assigned by G. Lotay *et al.*[165] and the theoretical cross section determined with a TWOFNR ADWA calculation. Ambiguity exists in the spin-parity assignment of the 7.909 MeV state, the study by Parikh *et al.*[167] determined a $l = 2$ transfer from ^{28}Si and as such a $(1/2, 3/2)^+$ was tentatively assigned whilst the G. Lotay *et al.*[165] study assigned a tentative $3/2^+$. This study has explored both parities of the $3/2$ spin for completeness. Parikh *et al.*[167] assigned a tentative $(3/2, 5/2)^+$ for the 8.070 MeV state An unpublished

proton decay study of ^{28}P performed at Texas A&M observed a strong proton decay branch into this state suggesting a low-spin level, as such this study has adopted $3/2^+$ for this state. G. Lotay *et al.*[165] observed the γ -ray decay from the 8.140 MeV state and identified this as a $1/2$ state with no given parity. This study makes no assignment of the parity, instead investigates the resultant spectroscopic factors from both parities. Finally, the spin-parity assignment from G. Lotay *et al.*[165] is assumed for the 8.184 MeV state.

E_x (keV)	E_r (keV)	J_n^π	C^2S^1 $^{26}\text{Si}(d,p)$	C^2S SM	C^2S^2 $^{26m}\text{Al}(p,\gamma)$
7838	146	$5/2_{14}^+$	≤ 0.03	0.0009	≤ 0.015
7909	218	$3/2_5^-$	≤ 0.01	0.05	≤ 0.005
		$3/2_{10}^+$	≤ 0.01	0.01	≤ 0.005
8070	378	$3/2_{12}^+$	≤ 0.003	0.003	≤ 0.0015
8140	448	$1/2_7^+$	≤ 0.09	0.02	≤ 0.045
		$1/2_3^-$	≤ 0.02	0.01	≤ 0.01
8184	492	$3/2_6^-$	≤ 0.002	0.004	≤ 0.001

$$^1 C^2 = 2/3$$

$$^2 C^2 = 1/3$$

Table 4.8: Properties of resonant states in $^{26m}\text{Al}(p,\gamma)^{27}\text{Al}$ system in comparison to those predicted from shell-model calculations. For the 218 and 448 keV resonances there still exists a parity ambiguity and as such both possibilities are presented here.

Table 4.8 shows that the upper limits set within this study are consistent with calculated shell-model spectroscopic factors and suggests that a more detailed study would provide direct observation. The factor C^2S is the product of the single-particle spectroscopic factor and the square of a Clebsh-Gordon coefficient. It is possible to relate between single-particle spectroscopic factors from different reactions using the relevant coefficients. In this study the relevant reactions $^{26}\text{Si}(d,p)$ and $^{26m}\text{Al}(p,\gamma)$ have the C^2 factors $2/3$ and $1/3$ respectively, so the astrophysical reaction of interest is related to this study by a factor of 2.

4.8 Determining Resonance Reaction Rate

As discussed in Section 2.3.2 the stellar reaction rate for a singular narrow resonance is defined as:

$$r_{aX} = N_a N_X \left(\frac{2\pi}{\mu kT} \right)^{3/2} \hbar^2 \cdot \exp \left(-\frac{E_R}{kT} \right) \cdot (\omega\gamma), \quad (4.15)$$

where $(\omega\gamma)$ and E_R can be determined from experiment. The resonance energy is determined from the excitation energy of a given state above the separation threshold and has been discussed previously. The resonance strength is determined through the spin-parities of a given state and the respective widths of the resonance. The assigned spin-parities of the states in ^{27}Si are discussed in Section 4.7.2 and will not be discussed further here. For the $^{26m}\text{Al}(p,\gamma)^{27}\text{Si}$ reaction there are three widths important for the resonance strength. These are the partial widths for the proton and γ -ray decays from the state, Γ_p and Γ_γ , and the total decay width of the state, Γ . The resonance strength of this reaction is determined by:

$$\omega\gamma = \omega \cdot \frac{\Gamma_\gamma \cdot \Gamma_p}{\Gamma}, \quad (4.16)$$

where Γ , the total decay width can be estimated from the lifetime of the state: $\Gamma = \hbar/\tau$, where τ is the lifetime of the state. The partial proton width is determined by:

$$2 \cdot \frac{\hbar^2}{mR^2} \cdot P_l \cdot C^2 S \cdot \theta_{sp}^2, \quad (4.17)$$

where m is the mass of the particle, R is the radius of the nucleus, P_C is the ‘‘penetration factor’’ which is defined as the probability of the particle penetrating the potential barrier that hinders the reaction and finally θ_{sp} is the dimensionless single-particle reduced width of the proton. Within this study P_C is calculated analytically for each state and θ_{sp} is taken from Ref. [149] and the values used for this reaction are 0.55, 0.7, 0.36 and 0.35 for the l -values 0, 1, 2 and 3 respectively. The partial γ -ray decay width in this study has either been assumed from shell-model calculations or determined from the difference between the total width and the proton partial width, given the $\Gamma = \Gamma_p + \Gamma_\gamma$ for this reaction. Table 4.9 summarises the estimated decay widths of the resonant states and their determined resonance strengths. From the determined resonance strengths it was possible to determine the reaction rates of these resonances

within a stellar environment of a given temperature, based upon Equation 2.40.

E_x (keV)	E_r (keV)	J_n^π	C^2S $^{26m}Al(p, \gamma)$	Γ_p (meV)	Γ_γ (meV)	$\omega\gamma$ (meV)
7838	146	$5/2_{14}^+$	≤ 0.015	4.9×10^{-6}	658	1.5×10^{-5}
7909	218	$3/2_5^-$	≤ 0.005	2.7×10^{-2}	658 ¹	0.054
		$3/2_{10}^+$	≤ 0.005	7.1×10^{-4}	960 ²	1.4×10^{-3}
8070	378	$3/2_{12}^+$	≤ 0.0015	0.16	510 ²	0.33
8140	448	$1/2_7^+$	≤ 0.045	683 ³	890 ²	385
		$1/2_3^-$	≤ 0.01	191	592 ¹	135
8184	492	$3/2_6^-$	≤ 0.001	45	120	65

¹ A lifetime lower limit of 1 fs has been assumed.

² Adopted from shell model calculations.

³ $C^2S = 0.01$ has been adopted from shell model calculations.

Table 4.9: Resonant strengths of states in $^{26m}Al(p,\gamma)^{27}Al$ system alongside their relevant partial widths. For the 218 and 448 keV resonances there still exists a parity ambiguity and as such both possibilities are presented here. The proton partial widths presented have been estimated using lifetimes from G. Lotay et al. unless otherwise noted.[165]

It is clear from Figure 4.26 that the dominant resonance contribution to the $^{26m}Al(p,\gamma)^{27}Si$ reaction will depend on the resolution on the spin-parity ambiguities that still exist. At extremely low stellar temperatures ($T < 0.8$ GK) the reaction rate is dominated by the 146 keV resonance. Should the 218 keV resonance be determined a $3/2^-$ state it will dominate the reaction rate at temperatures found in Asymptotic Giant Branch stars and classical novae environments, $0.1 < T < 0.3$ GK. However, if the 218 keV resonance is a $3/2^+$ state it will only be dominant across a small temperature range at ~ 0.22 GK. The spin-parity of the 448 keV level will affect the temperature range this state is dominant for. Either parity assignment will be dominant over a vast region of peak nova temperatures, $T > 0.3$ GK. This can extend down to the AGB/classic nova region above $T > 0.2$ GK dependent on the 218 keV spin-parity in relation and would make it the sole influential resonance across classical nova environments. These reaction rates within Figure 4.26 are upper limits and are approximately an order of magnitude lower than the upper limits stated in Ref [162] which are calculated from reaction rates of the $^{26}Al(p,\gamma)^{27}Si$ reaction. This indicates that this method of

calculation is unsuitable for this isomeric system. The reaction rates from Ref. [162] have subsequently used in nova nucleosynthesis calculations in Ref. [163] and in relation to those calculations this study would moderately increase the quantity of ^{26}Mg within these stellar environments.

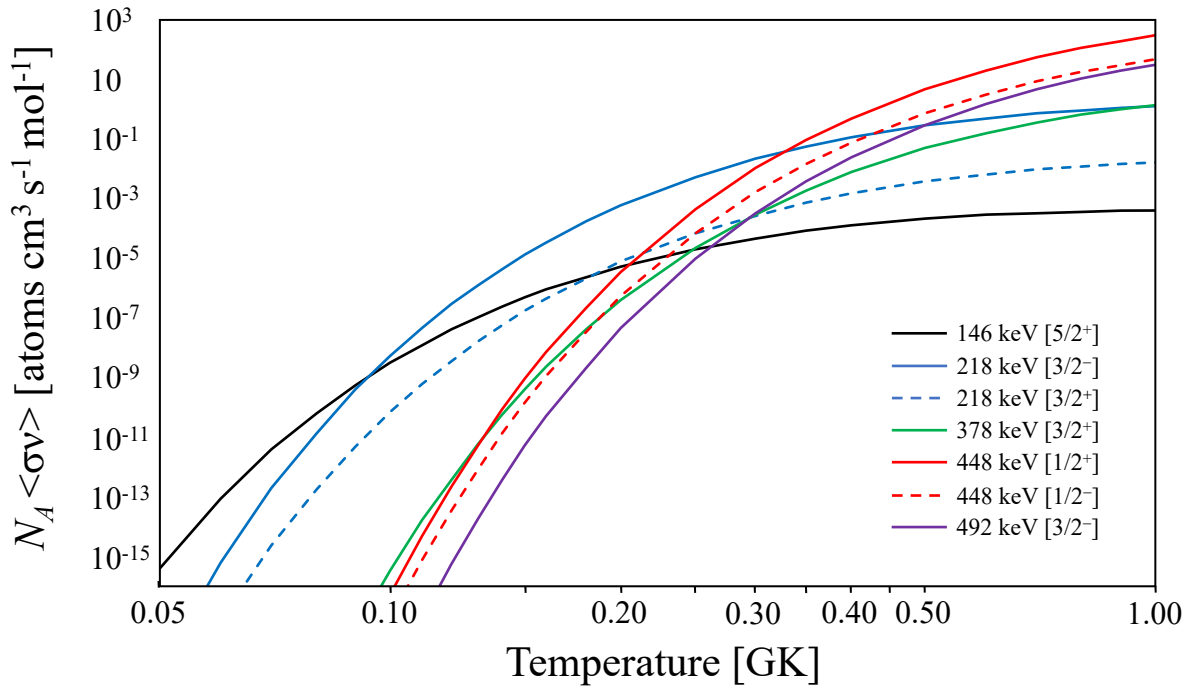


Figure 4.26: $^{26m}\text{Al}(p,\gamma)^{27}\text{Si}$ resonant reaction rate as a function of temperature determined by the extracted resonance strengths, assigned spin-parities and resonant energy as displayed in Table 4.9. Compiled by G. Lotay. [192]

Chapter 5

Conclusion

This present work focused on using (d,p) transfer reactions to indirectly determine astrophysical reaction information in the Mg-Al-Si region. Two independent studies were performed within this region to investigate stellar environments, including reactions involving Aluminium isotopes CSSN and AGB stars and involving Magnesium isotopes in Classical Novae and the weak s -process within main sequence stars.

The $^{22}\text{Ne}(\alpha,n)^{25}\text{Mg}$ reaction is a significant neutron breeding reaction thought to feed the weak s -process whilst the $^{22}\text{Ne}(\alpha,\gamma)^{26}\text{Mg}$ is a neutron poison reaction within the weak s -process, preventing the creation of the neutron flux that allows for neutron capture. States between 5 MeV and 6.5 MeV within ^{26}Mg are possible mirror state candidates for the $^{25}\text{Al}(p,\gamma)^{26}\text{Si}$ reaction thought to affect the nucleosynthesis abundances of Mg-Al-Si isotopes within Nova environments.

To that end the $^{25}\text{Mg}(d,p)^{26}\text{Mg}$ was studied in inverse kinematics using the TIARA array, four HPGe clover detectors and the MDM-2 magnetic spectrometer and Oxford focal plane detector at Texas A&M University. The original aim of the experiment was to identify and measure neutron partial widths of key resonant states above the neutron separation threshold within ^{26}Mg . This experiment was performed with a ^{25}Mg beam with 10 MeV/A energy, this was impinged upon a $\sim 197 \mu\text{g}/\text{cm}^{-2}$ deuterated-polyethylene target over a period of 86 hours. Heavy ^{26}Mg ejectile particles were separated from other beam-like species within the MDM-2 and stopped and analysed within the Oxford focal plane detector. This allowed for the measurement of coincident protons emitted by the $^{25}\text{Mg}(d,p)^{26}\text{Mg}$ reaction within the Hyball silicon detector of the TIARA array, whilst coincident γ rays were measured by 4 HPGe clovers

from the HYPERION array surrounding the target position.

Using data from the TIARA silicon detectors and coincident data from the HPGe clovers, a decay-scheme of the excited states populated by the $^{25}\text{Mg}(d,p)^{26}\text{Mg}$ reaction was observed. It was observed that the majority of states decayed through the first two excited states and the decays from these states are a constant within particle-gated γ -ray spectra. Angular distributions were constructed for all resolvable states and compared to theoretical angular distributions obtained using ADWA calculations. This allowed for the confirmation of l -transfer values and the determination of spectroscopic factors of the populated states from this reaction, which showed very good agreement with previously determined factors.

Whilst this reaction populated states up to 11 MeV of excitation energy, no states were observed above the neutron separation threshold and of relevance to the $^{22}\text{Ne}(\alpha,n)^{25}\text{Mg}$ reaction. This is a key result, as the experimental set-up had the capacity to measure states in this region, there is a large implication that there are no states within this region with a large γ -ray partial width.

A key state populated was the 6.125 MeV, 3^+ state within ^{26}Mg . This is thought to be the mirror of a key resonance state above the proton threshold within the $^{25}\text{Al}(p,\gamma)^{26}\text{Si}$ reaction. Using the spectroscopic factors of this state ($C^2S_{l=0} = 0.142$ & $C^2S_{l=2} = 0.302$) it was possible to determine the proton partial width of the resonant astrophysical state in the $^{25}\text{Al} + p$. Furthermore, this was used to determine the resonant strengths in this reaction system for the two previously reported resonance energies. These were found to slightly larger compared to previously reported strengths at both resonance energies.

Finally, a key conclusion to be made from this transfer is the implied low-lying negative parity state at 5.710 MeV excitation energy. This has been incorrectly assigned $(1,2)^+$ in some evaluations despite previous studies by Burlein *et al.* and Arciszewski *et al.* observing f -wave components within their angular distributions. This study highlights the need for further investigation of this state with an observed p -wave component needed to describe the known positive parity 5.715 MeV state, providing more evidence of this negative parity state. Shell-model calculations point towards this possible state being a 1^- . The mirror of this state within the $^{25}\text{Al} + p$ system would be within the Gamow window for this astrophysical reaction and could be a significant resonance state for the reaction.

The destruction of ^{26m}Al via (p,γ) reactions was thought to have a significant impact on the final abundances of the this nuclei region within CSSN and Wolf-Rayet AGB stars, where the temperature is hot enough for the ground state and isomeric state of ^{26}Al to communicate thermally. This reaction has been previously difficult to measure due to technical difficulties in producing an isomeric beam of ^{26}Al with relative purity from any ground state components.

For the first time, isospin symmetry has been utilized to mimic isomeric-state proton capture in astrophysical environments. In particular, the selective population of low-spin states in ^{27}Si , as well as the lack of contamination from unwanted beam components, make the present $^{26}\text{Si}(d,p)$ study a novel tool for studying $^{26m}\text{Al} + p$ resonances. Populating states with large single particle strengths through the $^{26}\text{Si}(d,p)^{27}\text{Si}$, information and the single particle strengths of the excited states in ^{27}Si could be related to the $^{26m}\text{Al}(p,\gamma)$ reaction.

The data for this measurement was collected by impinging a radioactive beam of ^{26}Si on a 9.1 mg/cm^{-2} thick CD_2 target. The γ -ray decays from this reaction was detected within the GRETINA HPGe array, whilst the ^{27}Si ejectile particles was separated and measured within the S800 spectrograph and its suite of focal plane detectors. This is currently the only measurement of its type looking for single particle states within ^{27}Si .

Using the γ -ray data from GRETINA gated upon ^{27}Si ions within the S800 focal plane, total reaction cross sections were determined by counting the total number of impinged ^{26}Si beam ions for a number of states up to 7.26 MeV excitation energy. A number of upper limits were placed based on excess counts observed in the same spectrum for states above this energy. From this total cross sectional measurement, spectroscopic factors were determined by comparisons to total cross sectional measurement from ADWA reaction codes.

The results demonstrate that there are no strong, single-particle states in the important energy region $E_r = 100 - 500 \text{ keV}$ and the new, stringent upper limits for resonance strengths indicate that the 218 and 448 keV resonances make the most influential contributions to the astrophysical $^{26m}\text{Al}(p,\gamma)$ reaction. Over the temperature range of AGB stars and classical novae, we find that the rate is significantly lower than the most recent theoretical estimates and thus, an increase in the abundance of ^{26}Mg in the ejecta of such environments is expected. In addition, we note that the $^{26m}\text{Al}(p,\gamma)$

reaction only becomes comparable to the $^{26g}\text{Al}(p, \gamma)$ reaction at temperatures ≥ 0.6 GK. Consequently, any effect on cosmic γ -ray emission is likely to be restricted to the highest temperature stellar scenarios, such as core collapse supernovae, where the situation is far more complex due to the allowed communication between ground and isomeric states of ^{26}Al , via thermal excitations. Nevertheless, further improvements are certainly still possible in constraining uncertainties in the $^{26m}\text{Al}(p, \gamma)$ reaction and we strongly encourage a direct measurement of the 448 keV resonance, as well as a definitive determination of the 218 keV resonance spin-parity.

Appendix A

Semiconductor Detectors

A.1 Charged Particles Detectors

A.1.1 Energy Loss of Charged Particles in Matter

The energy loss of positively charged particles within an absorbing medium is governed by Coulomb interactions between the particle and electrons of the absorber atoms. Multiple electrons within the medium can interact with the charged particle simultaneously, with the transfer of kinetic energy occurring until the particle has stopped or left the absorbing material. This transferred kinetic energy will either excite the absorber atoms or create electron-ion pairs within the medium. For charged particles the linear stopping power, S , is defined as the differential energy loss of the particle per unit distance, as given by Equation A.1.

$$S = -\frac{dE}{dx}. \quad (\text{A.1})$$

With a known charged particle and known absorbing material, this linear stopping power can be made more case specific, with the energy loss being described by the Bethe-Bloch formula, as given by Equation A.2.

$$-\frac{dE}{dx} = \frac{4\pi e^4 z^2}{m_0 v^2} N B \quad \text{where} \quad B = Z \left[\ln \frac{2m_0 v^2}{I} - \ln \left(1 - \frac{v^2}{c^2} \right) - \frac{v^2}{c^2} \right]. \quad (\text{A.2})$$

Where v and ze are velocity and charge of the incoming charged particle, m_0 is the electron rest mass, N and Z are the number density and atomic number of the medium and I is the average excitation and ionisation of the medium, usually

determined experimentally. At non-relativistic energies, i.e. $v \ll c$, only the first term within the B variable remains important. As can be seen within Equation A.2, the linear stopping power is inversely proportional to the kinetic energy of the particle. As a particle slows, it spends more time in the vicinity of any given electron within the absorber material causing it to lose more energy.

Whilst the velocity of charged particles remains large, with respect to the velocities of orbital electrons in the absorbing medium, the Bethe-Bloch formula remains valid. However, at low kinetic energies, charge exchange between the particle and medium becomes increasingly important. As positive ions travel through a medium, they collect electrons from the absorber atoms, eventually becoming neutral. This electron collection reduces the ion's charge and as such the energy loss of the ion. Equation A.2 can be re-arranged, multiplying the numerator and the denominator by m , to describe the proportional relationship between the energy loss in a small thickness of absorber material, ΔE , and the mass of the ion, the square of its charge and inversely to its kinetic energy.

$$\Delta E \propto \frac{mz^2}{E}. \quad (\text{A.3})$$

Charged particle detectors can utilise the transferral of kinetic energy from the particles to the electrons within the medium. In semi-conducting material the transferred energy promotes electrons into the conduction band, creating electron-hole pairs. In gas filled detectors, the energy ionizes electrons in the active detector volume. By applying an electric field across the active detector volume the charge from these liberated electrons or electron-hole pairs can be measured. An energy can be measured as this charge is proportional to the deposited energy in the material.

A.1.2 Semiconductor Diode Detectors

In order to create a semiconductor detector, a p-n junction must be formed. A p-n junction is created when p-type and n-type semiconducting material are in juxtaposition. The classification of p-type and n-type materials is based on whether there is a higher density of holes or electrons within them. Under normal conditions, i.e. no bias, there would be a charge equilibrium across this junction with the holes and electrons diffusing and recombining into its opposite respective material. This equilibrium cre-

ates a small natural depletion region where there is a high resistivity, no charge carriers and a space charge that creates an electric field that prevents further diffusion. This natural depletion region shifts the band gap structure of the semiconductor material and as such moves the Fermi level.

Applying a reverse bias electric field across a p-n junction widens the natural depletion region. As the n-side becomes more positive than the p-side, positive holes and negative electrons are attracted towards their opposite polarity terminals. When the depletion region extends across close to the entire width of the material it is “fully depleted”. For this to occur one of the junctions sides must be a heavily doped n^+ or p^+ layer and the other must be a high purity but mildly doped p^- or n^- layer. The numbers of p-type acceptors is much greater than n-type donors, therefore holes have a greater distance to travel than the electrons for recombination. Increasing the bias voltage increases the extent of the depletion region into the n-doped side. Increasing the bias voltage past the full depletion voltage of the material can cause irreversible damage to the diode.

This bias voltage also increases the charge carrier drift velocities within the detector and minimizes the probability of charge carrier recombination and/or trapping. Without this electric field only a small current is produced by ionizing radiation, on the order of $10 \mu\text{A}$, making measurements of the pulse difficult. Detector semiconductor materials are therefore chosen with properties of quick and efficient charge carrier collection, whilst producing minimal noise as a result of the leakage current created from the application of the electric field.

A.1.2.1 Dead Layer

A feature of semiconducting detectors is the “dead layer”, this is the heavily doped layer which becomes insensitive to charged particles. All charged particles lose some energy passing through this dead layer. For silicon detectors the high purity silicon sheets are typically n-type, a thin layer of heavily doped p^+ silicon is implanted onto one side. The depletion region does not extend into the p^+ layer and so does not constitute as part of the active area of the detector.

A.1.2.2 Silicon Detectors

It is very common for silicon detectors to be used for measuring energy and position of charged particles. It is possible to create large area multi-strip position-sensitive detectors which can cover a large solid angle, maximising statistics from even low intensity beams. Silicon only needs 3.26 eV at 300K to create an electron-hole pair, independent of radiation type and energy. Active areas of silicon detectors can be divided into electronically separated strips allow a higher precision of position and even the processing of high multiplicity events.

This experiment utilises two variants of silicon strip detectors (SSDs), namely double-sided silicon strip detectors (DSSSDs) and position-sensitive silicon strip detectors (PSSSDs). DSSSDs rely the front facing strips being perpendicular to those on the back side of the detector thus creating small pixels across the active area. PSSSDs have two anode outputs per strip, one at either end of the strip, the p-side is a resistive layer. This resistivity allows for the position along the strip to be calculated. The charge collected at each end of the strip as a fraction of the total charge is a function of the resistive division at the position r along the strip. PSSSDs are combined with offset resistors at either end of the strip, these ensure that hits at extreme ends of the strip have a measurable charge at the other extreme end.

A total charge Q deposited at position r on the strip will give two charge readings a and b at each end of the strip. These charges are proportional to the total charge deposited, strip position and the resistances of the strip and offset resistors:

$$a \propto Q \left[\frac{(1-r)R_0 + R_2}{R} \right] \quad (\text{A.4})$$

$$b \propto Q \left[\frac{rR_0 + R_1}{R} \right], \quad (\text{A.5})$$

where R_0 is the resistance across the strip, R_1 and R_2 that connect the strip to charge-sensitive preamplifiers. R is the total resistance of the strip, the sum of R_0 , R_1 and R_2 .

The total deposited energy can be recreated from the charge collected at each end of the strip. After gain matching the signals from each ends, the total deposited energy is simply the sum of the two signals. The hit position on the strip can also be determined from the difference in the gain-matched amplitudes.

$$E_{total} = g_a a + g_b b = E_{sum} \quad (\text{A.6})$$

$$p = \frac{g_a a - g_b b}{g_a a + g_b b} = \frac{E_{diff}}{E_{sum}} \quad (\text{A.7})$$

This position calculation has an energy dependent uncertainty. There is a fixed uncertainty related to the measurement of the charge at each end of the strip. There is also an inverse proportionality to the total energy deposited on the strip.

$$\Delta p \approx \frac{\Delta E_{diff}}{E_{sum}} \quad (\text{A.8})$$

A.1.2.3 Ballistic Deficit

The “ballistic deficit” is a necessary charge collection correction to the measured energy of charged particles within PSSSDs. This correction is a result of a non-constant charge collection time within shaping amplifiers. Shaping times of amplifiers in general require corrections for effects such as dead time and pile-up. If the charge time collection is relatively long it is possible for some of the resulting shaped pulse to have lost some of its amplitude. The long rise time of this process causes some loss of the originally collected charge. With DSSSDs this can be corrected simply with an additional gain correction because the charge collection time across the detector is constant.

The charge collected at either end of PSSSDs is dependent on the position the charged particle hits the resistive strip. If the incidence is near the centre of the strip, it will take a longer time for the charge to be collected at either end relative to an incidence near one of the strip ends. There is a differential charge collection time across the resistive strip. At the ends of the strip a majority of the charge is collected at end closest to the hit. However, in the middle the charge is approximately equally distributed to each end travelling half the length of the strip. So there is a greater percentage of charge lost for an incidence at the middle of the strip than at either end. The ballistic deficit correction will vary across the strip.

A.2 Gamma-ray Detectors

A.2.1 Interactions of Gamma Rays with Matter

How a γ -ray interacts with a material that it is travelling within is important in understanding the background that will be seen within the detector. A γ -ray has three main processes of interacting inside a material, which are dependent on the energy of the photon. These are photoelectric absorption, Compton scattering and pair production. Fig. A.1 shows the energy ranges over which these processes are dominant [83].

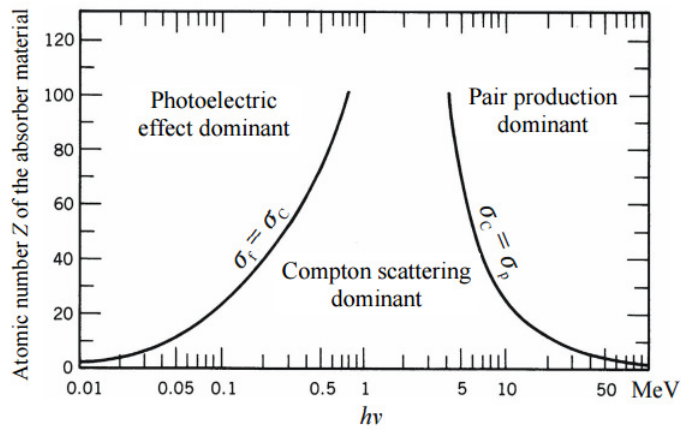


Figure A.1: The three γ -ray interactions with matter and their regions of dominance.

Taken from *Introductory Nuclear Physics* by Kenneth S. Krane [83]

A.2.1.1 Photoelectric Absorption

This process occurs at low energy (<100 keV) γ rays predominately. The photon is absorbed by an atomic orbital electron, ejecting it from the atom. The kinetic energy of the released electron is then the energy of the photon less the binding energy of the electron orbit [126]:

$$E_{e^-} = E_\gamma - B_e. \quad (\text{A.9})$$

The probability of such an event is hard to calculate precisely but it is known to be proportional to Z^4 and inversely proportional E_γ^3 with a discontinuity in probability around the binding energies of the electron orbitals [193]. It is given a linear absorption coefficient, τ , which is calculated from the photoelectric cross section like so:

$$\tau = 0.033^* \sigma_{cs}, \quad (\text{A.10})$$

where σ_{cs} is the cross section of the interaction. After emission, the valence space is then filled by electron re-arrangement with the emission of an X-ray or Auger electron.

A.2.1.2 Compton Scattering

Compton scattering is the process of a γ -ray scattering off of a free or nearly free electron. This process leaves a scattered electron (with some of the photon energy) and a less energetic γ -ray. Approximating the electron as free and at rest, the initial energy of the photon can be determined using the Compton-scattering formula:

$$E'_\gamma = \frac{E_\gamma}{1 + (E_\gamma/mc^2)(1 - \cos\theta)}. \quad (\text{A.11})$$

By integrating over all angles of the Klein-Nishina formula a cross section for the absorption of photons through the compton scattering process can be calculated. This is given by:

$$\sigma_c = \frac{\pi r_0^2}{\alpha} \left(\left[1 - \frac{2(\alpha + 1)}{\alpha^2} \right] \ln(2\alpha + 1) + \frac{1}{2} + \frac{4}{\alpha} - \frac{1}{2(2\alpha + 1)^2} \right), \quad (\text{A.12})$$

where, α is the photon energy in units of electron rest energy ($\alpha = E_\gamma/mc^2$) and r_0 is the classical electron radius ($r_0 = e^2/4\pi\epsilon_0 mc^2$). This cross section can be related to the linear Compton absorption coefficient, σ , by the following relationship:

$$\sigma = \sigma_c N Z. \quad (\text{A.13})$$

A.2.1.3 Pair Production

This is where a photon spontaneously creates an electron-positron pair. This process has a minimum threshold energy of 1.022 MeV which is the equivalent of the rest mass-energy needed to create the particle pair. It is dominant over the other two processes after 5 MeV [194]. The energy distribution of this process is:

$$E_\gamma = m_{e^+}c^2 + T_{e^+} + m_{e^-}c^2 + T_{e^-}. \quad (\text{A.14})$$

The probability of this process is given by the term, κ and is the summed probability of the process occurring in the field of an electron, κ_e , and the probability in the field of a nucleus, κ_n .

A.2.1.4 Gamma-Ray Attenuation Co-efficient

As γ rays pass through a material, the intensity follows an exponential attenuation with a distance through a material of x . The relationship is given as:

$$I = I_0 e^{-\mu x}, \quad (\text{A.15})$$

where I_0 is the initial intensity of the γ -ray. The term μ is known as the linear attenuation coefficient of the material, it is dependent on the effective charge of the nuclei within the material, Z_{eff} , as well as the density of the material, ρ , and the energy of the incoming γ -ray [195]. The coefficient is the sum of the probabilities of photoelectric absorption, τ , compton scattering, σ , and pair production, κ [91].

A.2.2 Germanium Detectors

The measurement of γ rays is altogether different from that of charged particles. As discussed in A.2.1 the probability of a γ -ray interaction is proportional to the Z of the material, therefore the detectors required to measure these γ rays are created using high Z materials. Due to the high mean free path of γ rays, they also require a large depletion region in order to maximize the photopeak efficiency. For a semi-conductor detector the depth or thickness of the depletion region is related to the voltage placed across the detector by the following equation:

$$d = \left(\frac{2\epsilon V}{\rho} \right)^{1/2}, \quad (\text{A.16})$$

where ϵ is the dielectric constant, V is the reverse bias voltage, and ρ is the charge density caused by impurities in the depletion region. It can be difficult to extend depletion regions beyond a few millimetres without electrical breakdown without semiconductors. To prevent this breakdown detectors whilst creating a thicker depletion region, the material used to create these detectors need to have higher purity. From equation A.16 it can be seen that this increased purity would allow a larger depletion region to be

created at a lower reverse bias voltage. It is now common to use high purity germanium detectors, or HPGe's, for γ -ray detection for all of the above reasons.

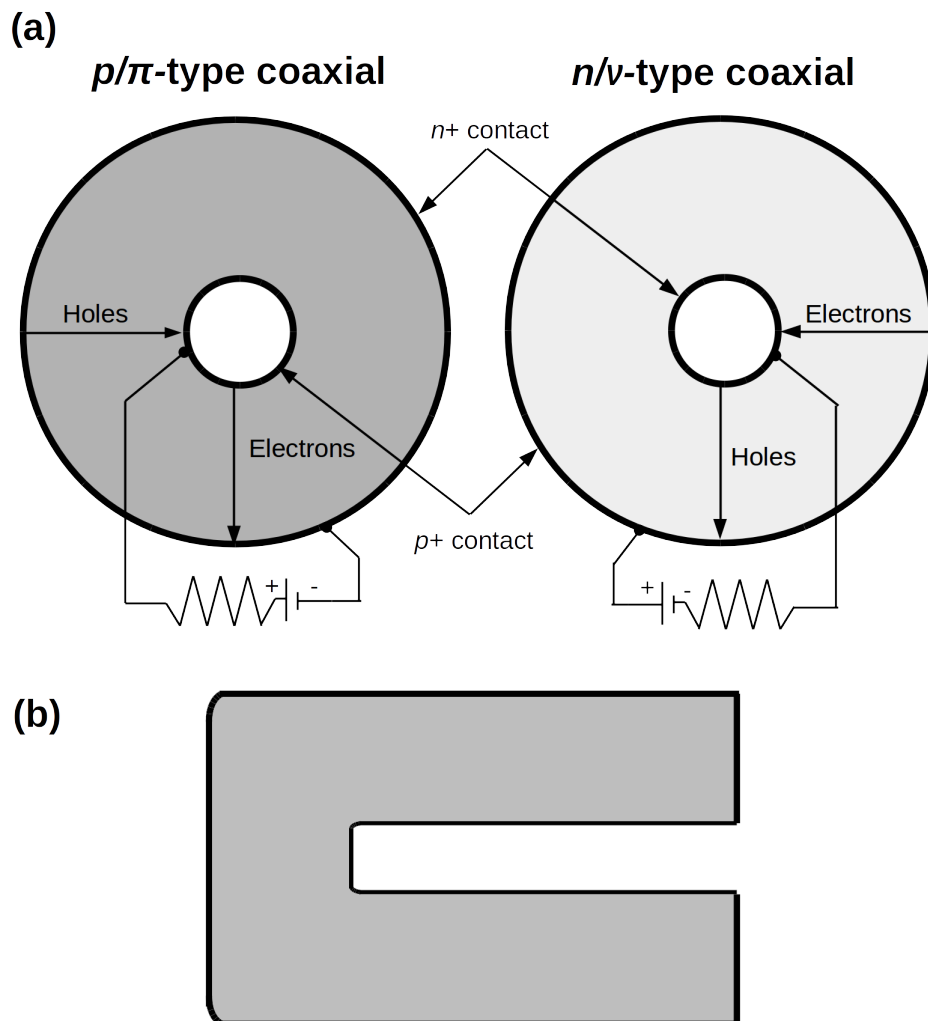


Figure A.2: Schematic diagram of the geometry of closed end coaxial High Purity Germanium detectors. (a) A cross-section through the depth of the crystals, the electrodes are connected to the inner and outer surfaces, maximizing the depletion volume. (b) A cross-section of the crystal perpendicular to the cylindrical axis of the detector.

There are several variations of germanium p-n junctions but the most common version in use for γ rays is the coaxial configuration, see figure A.2. In this format a cylindrical crystal of germanium with a central cylindrical hole is created. Two surface contacts are then created, one on the inner surface and one on the outer surface. One of them n^+ and one of them p^+ , with the arrangement of these contacts dependent on whether the germanium material is p-type or n-type. Coaxial germanium detectors are

not limited by the depletion depth of the semiconductor but instead are limited by the length of the crystal itself.

Germanium detectors need to be cooled down with liquid nitrogen to 77K and kept within a vacuum sealed chamber, otherwise these detectors would be unfeasible. With a very narrow band gap of 0.7 eV thermal excitations within the crystal are enough to create electron-hole pairs and become a saturating noise level. It has become commonplace to use composite germanium detectors, such as the four leaf clover detectors used within this experiment. These have a larger efficiency than singular detectors by allowing a number of single crystals, four in this case, to be treated as a group. This group can be electronically segmented allowing for an enhanced treatment of Compton scattered γ rays.

A.2.3 Add-back

As discussed above in Section A.2.1, gamma rays of certain energies have a higher probabilistic chance of compton scattering when interacting within a material. It is possible to reconstruct events of this nature by recombining multiple energies registered within the detection system. Events from multiple electronic readouts within a detection system can be used to add together multiple energies to recreate the original γ -ray energy. In order to do this the energy of the gamma rays and the emission angle of the first event is required.

A.2.4 Doppler Effects

The relative velocity between a γ -ray emitting nucleus and the measuring detector causes an observable Doppler shift. This shift has to be corrected for in the energy measurement of that γ -ray. This correction is related to the velocity of the nucleus, β , and the angle of the detector relative to the nucleus' velocity, θ , in the following equation:

$$E_{meas} = \frac{E_0}{\gamma(1 - \beta\cos\theta)}, \quad (\text{A.17})$$

where E_{meas} is the energy measured within the detector and E_0 is the γ -ray energy in the rest frame. At $\theta = 90$ the Doppler shift will be minimised, at $\theta > 90$ the γ -ray energy will be blue-shifted and at $\theta < 90$ the photons will be red-shifted. As detectors have a

finite angular range, it is impossible to apply this correction to the necessary level as to create an energy resolution comparable to that of a nucleus at rest. In general the correction is applied based on the median of the angular bin, whose size depends on the crystal range or the segmentation of the detector. A result of this is a phenomenon known as Doppler-broadening, where the measured γ -ray energy is smeared out. The better segmentation a γ -ray detector has the smaller this phenomenon effect is.

Bibliography

- [1] E. M. Burbidge, G. R. Burbidge, W. A. Fowler, and F. Hoyle, “Synthesis of the Elements in Stars,” *Rev. Mod. Phys.*, vol. 29, pp. 547–650, 4 Oct. 1957.
- [2] R. d. Atkinson, “Atomic Synthesis and Stellar Energy,” *The Astrophysical Journal*, vol. 73, p. 250, May 1931.
- [3] H. A. Bethe and C. L. Critchfield, “The Formation of Deuterons by Proton Combination,” *Phys. Rev.*, vol. 54, pp. 248–254, 4 Aug. 1938.
- [4] H. A. Bethe, “Energy Production in Stars,” *Phys. Rev.*, vol. 55, pp. 434–456, 5 Mar. 1939.
- [5] F. Hoyle, “The Synthesis of the Elements from Hydrogen,” *Monthly Notices of the Royal Astronomical Society*, vol. 106, p. 343, 1946.
- [6] P. W. Merrill, “Spectroscopic Observations of Stars of Class,” *The Astrophysical Journal*, vol. 116, p. 21, Jul. 1952.
- [7] K. Hirata, T. Kajita, M. Koshiba, *et al.*, “Observation of a neutrino burst from the supernova SN1987A,” *Phys. Rev. Lett.*, vol. 58, pp. 1490–1493, 14 Apr. 1987.
- [8] J. Davidson, H. Busemann, L. R. Nittler, *et al.*, “Abundances of presolar silicon carbide grains in primitive meteorites determined by NanoSIMS,” *Geochimica et Cosmochimica Acta*, vol. 139, no. Supplement C, pp. 248–266, 2014.
- [9] A. M. Davis, “Stardust in meteorites,” *Proceedings of the National Academy of Sciences*, vol. 108, no. 48, pp. 19 142–19 146, 2011.
- [10] C. J. Hansen, A. C. Andersen, and N. Christlieb, “Stellar abundances and presolar grains trace the nucleosynthetic origin of molybdenum and ruthenium,” *Astronomy and Astrophysics*, vol. 568, A47, 2014.
- [11] G. R. Huss, “The survival of presolar grains in solar system bodies,” *AIP Conference Proceedings*, vol. 402, no. 1, pp. 721–748, 1997.

- [12] K. Lodders, “Solar System Abundances and Condensation Temperatures of the Elements,” *The Astrophysical Journal*, vol. 591, no. 2, p. 1220, 2003.
- [13] K. Lodders, “Solar System Abundances of the Elements,” *Astrophysics and Space Science Proceedings*, vol. 16, p. 379, 2010.
- [14] H. E. Suess and H. C. Urey, “Abundances of the Elements,” *Rev. Mod. Phys.*, vol. 28, pp. 53–74, 1 Jan. 1956.
- [15] S. C. Trager, S. M. Faber, G. Worthey, and J. J. González, “The Stellar Population Histories of Early-Type Galaxies. II. Controlling Parameters of the Stellar Populations,” *The Astronomical Journal*, vol. 120, no. 1, p. 165, 2000.
- [16] Y. Komiya, T. Suda, and M. Y. Fujimoto, “Population III Stars Around the Milky Way,” *The Astrophysical Journal*, vol. 820, 59, p. 59, Mar. 2016.
- [17] M. Fraser, A. R. Casey, G. Gilmore, *et al.*, “The Mass Distribution of Population III Stars,” *Monthly Notices of the Royal Astronomical Society*, vol. 468, pp. 418–425, Jun. 2017.
- [18] D. Schaerer, “On the properties of massive Population III stars and metal-free stellar populations,” *Astronomy and Astrophysics*, vol. 382, no. 1, pp. 28–42, 2002.
- [19] D. Sobral, J. Matthee, B. Darvish, *et al.*, “Evidence for PopIII-like Stellar Populations in the Most Luminous Lyman- α Emitters at the Epoch of Reionization: Spectroscopic Confirmation,” *The Astrophysical Journal*, vol. 808, 139, p. 139, Aug. 2015.
- [20] B. D. Smith, J. H. Wise, B. W. O’Shea, *et al.*, “The first Population II stars formed in externally enriched mini-haloes,” *Monthly Notices of the Royal Astronomical Society*, vol. 452, pp. 2822–2836, Sep. 2015.
- [21] U. Maio, B. Ciardi, K. Dolag, *et al.*, “The transition from Population III to Population II-I star formation,” *Monthly Notices of the Royal Astronomical Society*, vol. 407, pp. 1003–1015, Sep. 2010.
- [22] *Hertzsprung-Russell Diagram*, Image Credit: Australian Telescope National Facility. [Online]. Available: https://www.atnf.csiro.au/outreach//education/senior/astrophysics/stellarevolution_postmain.html.
- [23] E. Hertzsprung, *Zeitschrift für wissenschaftliche*. 1905.

- [24] H. N. Russell, “Relations Between the Spectra and Other Characteristics of the Stars,” *Popular Astronomy*, vol. 22, pp. 275–294, May 1914.
- [25] F. H. Shu, “Self-similar collapse of isothermal spheres and star formation,” *The Astrophysical Journal*, vol. 214, pp. 488–497, Jun. 1977.
- [26] C. Hayashi, “Stellar Evolution in Early Phases of Gravitational Contraction.,” *Publications of the Astronomical Society of Japan*, vol. 13, 1961.
- [27] C. Hayashi, “Evolution of Protostars,” *Annual Review of Astronomy and Astrophysics*, vol. 4, no. 1, pp. 171–192, 1966.
- [28] S. International Astronomical Union. Symposium Geneva, . Jong Teive de, . Maeder André, *et al.*, *Star formation*, English, Conference Proceedings, 1977.
- [29] S. Chandrasekhar and S. Chandrasekhar, *An Introduction to the Study of Stellar Structure*, ser. Astrophysical monographs. Dover Publications, 1957.
- [30] E. G. Adelberger, A. García, R. G. H. Robertson, *et al.*, “Solar fusion cross sections. II. the *pp* chain and CNO cycles,” *Rev. Mod. Phys.*, vol. 83, pp. 195–245, 1 Apr. 2011.
- [31] W. A. Fowler, “Completion of the Proton-Proton Reaction Chain and the Possibility of Energetic Neutrino Emission by Hot Stars.,” *The Astrophysical Journal*, vol. 127, p. 551, May 1958.
- [32] A. Gavriluk, *Hydrogen Energy for Beginners*. Pan Stanford, 2013.
- [33] C. Iliadis, “Nuclear Burning Stages and Processes,” in *Nuclear Physics of Stars*. Wiley-VCH Verlag GmbH & Co. KGaA, 2015, pp. 349–568.
- [34] E. E. Salpeter, “Nuclear Reactions in Stars Without Hydrogen.,” *The Astrophysical Journal*, vol. 115, pp. 326–328, Mar. 1952.
- [35] H. Oberhummer, R. Pichler, and A. Csoto, “The triple-alpha process and its anthropic significance,” *ArXiv Nuclear Theory e-prints*, Oct. 1998.
- [36] F. C. Adams and E. Grohs, “Stellar Helium Burning in Other Universes: A Solution to the Triple Alpha Fine-Tuning Problem,” *Astroparticle Physics*, vol. 87, pp. 40–54, Jan. 2017.
- [37] S. E. Woosley, A. Heger, and T. A. Weaver, “The evolution and explosion of massive stars,” *Rev. Mod. Phys.*, vol. 74, pp. 1015–1071, 4 Nov. 2002.

- [38] G. M. Halabi, “Study of the Thermal Pulsation of AGB Stars,” *ArXiv e-prints*, Oct. 2014.
- [39] S. E. Woosley and T. A. Weaver, “The Evolution and Explosion of Massive Stars. II. Explosive Hydrodynamics and Nucleosynthesis,” *Astrophysical Journal, Supplement*, vol. 101, p. 181, Nov. 1995.
- [40] E. Chaisson and S. McMillan, *Astronomy Today*, ser. Pearson International edition. Pearson / Addison Wesley, 2008.
- [41] B. Pagel, *Nucleosynthesis and Chemical Evolution of Galaxies*. Cambridge University Press, 1997.
- [42] M. Lugaro, F. Herwig, J. C. Lattanzio, *et al.*, “s-Process Nucleosynthesis in Asymptotic Giant Branch Stars: A Test for Stellar Evolution,” *The Astrophysical Journal*, vol. 586, no. 2, p. 1305, 2003.
- [43] T. Rauscher, A. Heger, R. D. Hoffman, and S. E. Woosley, “Nucleosynthesis in Massive Stars with Improved Nuclear and Stellar Physics,” *The Astrophysical Journal*, vol. 576, no. 1, p. 323, 2002.
- [44] C. Abia, I. Domínguez, R. Gallino, *et al.*, “s-Process Nucleosynthesis in Carbon Stars,” *The Astrophysical Journal*, vol. 579, no. 2, p. 817, 2002.
- [45] S. Bisterzo, R. Gallino, F. Käppeler, *et al.*, “The branchings of the main s-process: their sensitivity to α -induced reactions on ^{13}C and ^{22}Ne and to the uncertainties of the nuclear network,” *Monthly Notices of the Royal Astronomical Society*, vol. 449, pp. 506–527, May 2015.
- [46] R. Reifarth, C. Lederer, and F. Käppeler, “Neutron reactions in astrophysics,” *Journal of Physics G Nuclear Physics*, vol. 41, no. 5, 053101, p. 053 101, May 2014.
- [47] C. Arlandini, F. Käppeler, K. Wisshak, *et al.*, “Neutron Capture in Low-Mass Asymptotic Giant Branch Stars: Cross Sections and Abundance Signatures,” *The Astrophysical Journal*, vol. 525, no. 2, p. 886, 1999.
- [48] M. Pignatari, R. Gallino, M. Heil, *et al.*, “The Weak s-Process in Massive Stars and its Dependence on the Neutron Capture Cross Sections,” *The Astrophysical Journal*, vol. 710, no. 2, p. 1557, 2010.

- [49] F. Käppeler, R. Gallino, S. Bisterzo, and W. Aoki, “The s process: Nuclear physics, stellar models, and observations,” *Rev. Mod. Phys.*, vol. 83, pp. 157–193, 1 Apr. 2011.
- [50] C. M. Raiteri, M. Busso, G. Picchio, and R. Gallino, “ s -Process Nucleosynthesis in Massive Stars and the Weak Component. II - Carbon Burning and Galactic Enrichment,” *The Astrophysical Journal*, vol. 371, pp. 665–672, Apr. 1991.
- [51] K. Lodders and S. Amari, “Presolar grains from meteorites: Remnants from the early times of the solar system,” *Chemie der Erde - Geochemistry*, vol. 65, no. 2, pp. 93–166, 2005.
- [52] E. Zinner, “Stellar Nucleosynthesis and the Isotopic Composition of Presolar Grains from Primitive Meteorites,” *Annual Review of Earth and Planetary Sciences*, vol. 26, no. 1, pp. 147–188, 1998.
- [53] T. Lee, D. A. Papanastassiou, and G. J. Wasserburg, “Correction [to “Demonstration of ^{26}Mg excess in Allende and evidence for ^{26}Al ,”]” *Geophysical Research Letters*, vol. 3, no. 2, pp. 109–112, Feb. 1976.
- [54] E. Gropman, E. Zinner, S. Amari, *et al.*, “Inferred Initial $^{26}\text{Al}/^{27}\text{Al}$ Ratios in Presolar Stardust Grains from Supernovae are Higher than Previously Estimated,” *The Astrophysical Journal*, vol. 809, no. 1, p. 31, 2015.
- [55] G. Srinivasan, J. N. Goswami, and N. Bhandari, “ ^{26}Al in Eucrite Piplia Kalan: Plausible Heat Source and Formation Chronology,” *Science*, vol. 284, no. 5418, pp. 1348–1350, 1999.
- [56] E. A. Samworth, E. K. Warburton, and G. A. P. Engelbertink, “Beta Decay of the ^{26}Al Ground State,” *Phys. Rev. C*, vol. 5, pp. 138–142, 1 Jan. 1972.
- [57] W. A. Mahoney, J. C. Ling, W. A. Wheaton, and A. S. Jacobson, “HEAO-3 Discovery of ^{26}Al in the Interstellar Medium,” *The Astrophysical Journal*, vol. 286, pp. 578–585, Nov. 1984.
- [58] W. Mahoney, J. Ling, A. Jacobson, and R. Tapphorn, “The HEAO 3 Gamma-Ray Spectrometer,” *Nuclear Instruments and Methods*, vol. 178, no. 2, pp. 363–381, 1980.

- [59] W. A. Mahoney, J. C. Ling, A. S. Jacobson, and R. E. Lingenfelter, “Diffuse galactic gamma-ray line emission from nucleosynthetic Fe-60, Al-26, and Na-22 - preliminary limits from HEAO 3,” *The Astrophysical Journal*, vol. 262, p. 742, Nov. 1982.
- [60] D. D. Clayton, “ ^{26}Al in the Interstellar Medium,” *The Astrophysical Journal*, vol. 280, pp. 144–149, May 1984.
- [61] V. Schoenfelder, H. Aarts, K. Bennett, *et al.*, “Instrument Description and Performance of the Imaging Gamma-Ray Telescope COMPTEL aboard the Compton Gamma-Ray Observatory,” *The Astrophysical Journals*, vol. 86, pp. 657–692, Jun. 1993.
- [62] R. Lin, B. Dennis, G. Hurford, *et al.*, “The Reuven Ramaty High-Energy Solar Spectroscopic Imager (RHESSI),” *Solar Physics*, vol. 210, no. 1, pp. 3–32, Nov. 2002.
- [63] Prantzos, N., “Radioactive ^{26}Al and ^{60}Fe in the Milky Way: Implications of the RHESSI Detection of ^{60}Fe ,” vol. 420, no. 3, pp. 1033–1037, 2004.
- [64] R. Diehl, C. Dupraz, K. Bennett, *et al.*, “COMPTEL Observations of Galactic ^{26}Al Emission,” *Astronomy and Astrophysics*, vol. 298, p. 445, Jun. 1995.
- [65] R. Diehl, H. Halloin, K. Kretschmer, *et al.*, “Radioactive ^{26}Al from Massive Stars in the Galaxy,” *Nature*, vol. 439, no. 7072, pp. 45–47, Jan. 2006.
- [66] I. R. Seitenzahl, F. X. Timmes, and G. Magkotsios, “The Light Curve of SN1987A Revisited: Constraining Production Masses of Radioactive Nuclides,” *The Astrophysical Journal*, vol. 792, no. 1, p. 10, 2014.
- [67] F. X. Timmes, S. E. Woosley, D. H. Hartmann, *et al.*, “ ^{26}Al and ^{60}Fe from Supernova Explosions,” *The Astrophysical Journal*, vol. 449, p. 204, Aug. 1995.
- [68] C. Winkler, T. J.-L. Courvoisier, G. Di Cocco, *et al.*, “The INTEGRAL Mission,” *A&A*, vol. 411, no. 1, pp. L1–L6, 2003.
- [69] D. M. Smith, “The Reuven Ramaty High Energy Solar Spectroscopic Imager Observation of the 1809 keV Line from Galactic ^{26}Al ,” *The Astrophysical Journal Letters*, vol. 589, no. 1, p. L55, 2003.
- [70] *Gamma-Ray Sky Maps*. [Online]. Available: <https://heasarc.gsfc.nasa.gov/docs/cgro/images/epo/gallery/skymaps/>.

- [71] S. Kikstra, Z. Guo, C. V. D. Leun, *et al.*, “Superallowed $^{26}\text{Al}^m(\beta^+ + \text{EC})^{26}\text{Mg}$ decay,” *Nuclear Physics A*, vol. 529, no. 1, pp. 39–52, 1991.
- [72] M. Limongi and A. Chieffi, “The Nucleosynthesis of ^{26}Al and ^{60}Fe in Solar Metallicity Stars Extending in Mass from 11 to 120 M_{\odot} : The Hydrostatic and Explosive Contributions,” *The Astrophysical Journal*, vol. 647, no. 1, p. 483, 2006.
- [73] C. Iliadis, A. Champagne, A. Chieffi, and M. Limongi, “The Effects of Thermonuclear Reaction Rate Variations on ^{26}Al Production in Massive Stars: A Sensitivity Study,” *The Astrophysical Journal Supplement Series*, vol. 193, no. 1, p. 16, 2011.
- [74] A. N. Nguyen and E. Zinner, “Discovery of Ancient Silicate Stardust in a Meteorite,” *Science*, vol. 303, no. 5663, pp. 1496–1499, 2004.
- [75] M. Wang, G. Audi, F. Kondev, *et al.*, “The AME2016 Atomic Mass Evaluation (II). Tables, Graphs and References,” *Chinese Physics C*, vol. 41, no. 3, p. 030 003, 2017.
- [76] W. Huang, G. Audi, M. Wang, *et al.*, “The AME2016 Atomic Mass Evaluation (I). Evaluation of Input Data; and Adjustment Procedures,” *Chinese Physics C*, vol. 41, no. 3, p. 030 002, 2017.
- [77] R. Saha, A. Markmann, and V. Batista, “Tunneling through Coulombic Barriers: Quantum Control of Nuclear Fusion,” vol. 110, May 2012.
- [78] G. Lotay, *Gamma-ray Spectroscopy Measurements for Nuclear Reactions in Novae*. University of Edinburgh: PhD Thesis, 2008.
- [79] C. Rolfs and W. Rodney, *Cauldrons in the Cosmos: Nuclear Astrophysics*. Chicago, USA: University of Chicago Press, 1988.
- [80] S. Courtin, D. G. Jenkins, G. Gruet, *et al.*, “STELLA Experiment: A Letter of Intent for ANDROMEDE,” Jun. 2016.
- [81] E. Wigner, *Proceedings of the Robert A. Welch Foundation Conferences on Chemical Research*, ser. Proceedings of the Robert A. Welch Foundation Conferences on Chemical Research v. 1. The Foundation, 1957.
- [82] W. Ormand and B. Brown, “Empirical Isospin-Nonconserving Hamiltonians for Shell-Model Calculations,” *Nuclear Physics A*, vol. 491, no. 1, pp. 1–23, 1989.

- [83] K. Krane, *Introductory Nuclear Physics*. John Wiley & Sons, 1988.
- [84] D. F. D. F. Jackson, *Nuclear Reactions*, eng. London: Methuen, 1970.
- [85] P. E. Hodgson, *Nuclear Reactions and Nuclear Structure*, eng, ser. The international series of monographs on physics. Oxford: Clarendon Press, 1971.
- [86] R. D. Woods and D. S. Saxon, "Diffuse Surface Optical Model for Nucleon-Nuclei Scattering," *Phys. Rev.*, vol. 95, pp. 577–578, 2 Jul. 1954.
- [87] K. Kikuchi, *Nuclear Matter and Nuclear Reactions*, eng. Amsterdam: North-Holland, 1968.
- [88] M. G. Mayer, "On Closed Shells in Nuclei. II," *Phys. Rev.*, vol. 75, pp. 1969–1970, 12 Jun. 1949.
- [89] O. Haxel, J. H. D. Jensen, and H. E. Suess, "On the "Magic Numbers" in Nuclear Structure," *Phys. Rev.*, vol. 75, pp. 1766–1766, 11 Jun. 1949.
- [90] R. F. Casten, *Nuclear Structure from a Simple Perspective*, eng, 2nd ed., ser. Oxford Studies in Nuclear Physics. New York ; Oxford: Oxford University Press, 2000.
- [91] J. Lilley, *Nuclear Physics - Principles and Applications*. New York, NY, USA: Wiley, 2001.
- [92] N. K. Glendenning, *Direct Nuclear Reactions*, eng. Washington ; London: World Scientific, 2004.
- [93] N. Austern, *Direct Nuclear Reaction Theories*, eng, ser. Interscience Monographs and Texts in Physics and Astronomy ; vol.25. New York ; London: Wiley-Interscience, 1970.
- [94] W. N. Catford, "What Can We Learn from Transfer, and How Is Best to Do It?" In *The Euroschool on Exotic Beams, Vol. IV*, C. Scheidenberger and M. Pfützner, Eds. Berlin, Heidelberg: Springer Berlin Heidelberg, 2014, pp. 67–122.
- [95] H. Enge, *Introduction to Nuclear Physics*, ser. Addison-Wesley series in physics. Addison-Wesley Pub. Co., 1966.
- [96] B. Cohen, *Concepts of Nuclear Physics*, ser. McGraw-Hill series in fundamentals of physics. Tata McGraw-Hill, 1971.

- [97] G. Satchler, “The Distorted-Waves Theory of Direct Nuclear Reactions with Spin-Orbit Effects,” *Nuclear Physics*, vol. 55, pp. 1–33, 1964.
- [98] R. M. Eisberg, *Fundamentals of Modern Physics*, eng. New York: Wiley, 1961.
- [99] W. Tobocman, “Numerical Evaluation of Deuteron Stripping Cross Sections and Polarizations,” *Phys. Rev.*, vol. 115, pp. 98–107, 1 1959.
- [100] S. S. M. Wong, *Introductory Nuclear Physics*, eng, 2nd ed. New York ; Chichester: J. Wiley, 1998.
- [101] M. Macfarlane and J. Schiffer, “IV.B.2 - Transfer Reactions Supported by the U.S. Atomic Energy Commission.,” in *Nuclear Spectroscopy and Reactions, Part B*, ser. Pure and Applied Physics, J. CERNY, Ed., vol. 40, Elsevier, 1974, pp. 169–194.
- [102] X. D. Liu, M. A. Famiano, W. G. Lynch, *et al.*, “Systematic extraction of spectroscopic factors from $^{12}\text{C}(\text{d},\text{p})^{13}\text{C}$ and $^{13}\text{C}(\text{p},\text{d})^{12}\text{C}$ reactions,” *Phys. Rev. C*, vol. 69, p. 064313, 6 2004.
- [103] *National Nuclear Data Center*, <http://www.nndc.bnl.gov/ensdf/>.
- [104] R. C. Johnson and P. J. R. Soper, “Contribution of Deuteron Breakup Channels to Deuteron Stripping and Elastic Scattering,” *Phys. Rev. C*, vol. 1, pp. 976–990, 3 Mar. 1970.
- [105] J. Gómez Camacho and A. M. Moro, “A Pedestrian Approach to the Theory of Transfer Reactions: Application to Weakly-Bound and Unbound Exotic Nuclei,” in *The Euroschool on Exotic Beams, Vol. IV*, C. Scheidenberger and M. Pfützner, Eds. Berlin, Heidelberg: Springer Berlin Heidelberg, 2014, pp. 39–66.
- [106] P. J. A. Buttle and L. J. B. Goldfarb, “Finite Range Effects in Deuteron Stripping Processes,” *Proceedings of the Physical Society*, vol. 83, no. 5, pp. 701–717, 1964.
- [107] M. Labiche, W. N. Catford, R. C. Lemmon, *et al.*, “TIARA: a large solid angle silicon array for direct reaction studies with radioactive beams,” *Nuclear Instruments and Methods in Physics Research A*, vol. 614, pp. 439–448, Mar. 2010.

- [108] E. Pollard and R. Humphreys, “Energy Levels of Mg^{26} and Si^{30} formed by Deuteron Bombardment,” *Phys. Rev.*, vol. 59, p. 466, 5 1941. DOI: 10.1103/PhysRev.59.464. [Online]. Available: <https://link.aps.org/doi/10.1103/PhysRev.59.464s>.
- [109] H. R. Allan, C. A. Wilkinson, and J. D. Cockcroft, “The Transmutation of Magnesium, Aluminium and Silicon by Deuterons,” *Proceedings of the Royal Society of London. Series A. Mathematical and Physical Sciences*, vol. 194, no. 1036, pp. 131–145, 1948.
- [110] H. R. Allan, C. A. Wilkinson, W. E. Burcham, and C. D. Curling, “Disintegration of Separated Isotopes of Magnesium by Deuterons,” *Nature*, vol. 163, no. 4136, pp. 210–210, 1949, ISSN: 1476-4687. DOI: 10.1038/163210a0. [Online]. Available: <https://doi.org/10.1038/163210a0>.
- [111] J. AMBROSEN, “Deuteron Reactions with Separated Magnesium Isotopes,” *Nature*, vol. 169, no. 4297, pp. 408–408, 1952, ISSN: 1476-4687. DOI: 10.1038/169408a0. [Online]. Available: <https://doi.org/10.1038/169408a0>.
- [112] P. M. Endt, J. W. Haffner, and D. M. Van Patter, “Magnetic Analysis of the $\text{Mg}^{25}(d,p)\text{Mg}^{26}$, $\text{Mg}^{26}(d,p)\text{Mg}^{27}$, and $\text{Mg}^{25}(d,\alpha)\text{Na}^{23}$ Reactions,” *Phys. Rev.*, vol. 86, pp. 518–522, 4 1952. DOI: 10.1103/PhysRev.86.518. [Online]. Available: <https://link.aps.org/doi/10.1103/PhysRev.86.518>.
- [113] J. R. Holt and T. N. Marsham, “An Investigation of (d, p) Stripping Reactions II: Results for the Isotopes of Magnesium,” vol. 66, no. 3, pp. 258–267, 1953. DOI: 10.1088/0370-1298/66/3/308.
- [114] N. Takano, “The Reaction $\text{Mg}^{25}(d, p)\text{Mg}^{26}$ in the Energy Range of Deuterons from 1.5 MeV to 3.0 MeV,” *Journal of the Physical Society of Japan*, vol. 16, no. 4, pp. 598–604, 1961. DOI: 10.1143/JPSJ.16.598.
- [115] R. B. Weinberg, G. E. Mitchell, and L. J. Lidofsky, “Deuteron Stripping Reaction on Mg^{25} ,” *Phys. Rev.*, vol. 133, B884–B892, 4B 1964. DOI: 10.1103/PhysRev.133.B884. [Online]. Available: <https://link.aps.org/doi/10.1103/PhysRev.133.B884>.
- [116] H. F. Lutz, D. W. Heikkinen, W. Bartolini, and T. H. Curtis, “Proton Transfer Reactions on ^{26}Mg and ^{30}Si via the Reactions $^{26}\text{Mg}(^3\text{He}, d)^{27}\text{Al}$ and $^{30}\text{Si}(^3\text{He}, d)^{31}\text{P}$,”

- Phys. Rev. C*, vol. 2, pp. 981–989, 3 1970. DOI: 10.1103/PhysRevC.2.981. [Online]. Available: <https://link.aps.org/doi/10.1103/PhysRevC.2.981>.
- [117] S. Hinds, H. Marchant, and R. Middleton, “The Angular Distributions of the (t, p) , (d, p) and (d, d) Reactions Leading to ^{26}Mg ,” *Nuclear Physics*, vol. 67, no. 2, pp. 257–270, 1965, ISSN: 0029-5582. DOI: [https://doi.org/10.1016/0029-5582\(65\)90801-1](https://doi.org/10.1016/0029-5582(65)90801-1). [Online]. Available: <http://www.sciencedirect.com/science/article/pii/0029558265908011>.
- [118] B. Čujec, “Studies of Mg^{25} , Mg^{26} , and Mg^{27} Nuclei with (d, p) Reactions,” *Phys. Rev.*, vol. 136, B1305–B1324, 5B 1964. DOI: 10.1103/PhysRev.136.B1305. [Online]. Available: <https://link.aps.org/doi/10.1103/PhysRev.136.B1305>.
- [119] C. Hamill, P. Woods, D. Kahl, *et al.*, “Study of the $^{25}\text{Mg}(d,p)^{26}\text{Mg}$ reaction to constrain the $^{25}\text{Al}(p,\gamma)^{26}\text{Si}$ resonant reaction rates in nova burning conditions,” *European Physical Journal A: Hadrons and Nuclei*, 2020.
- [120] D. Pringle, W. Catford, J. Winfield, *et al.*, “The Oxford MDM-2 Magnetic Spectrometer,” *Nuclear Instruments and Methods in Physics Research Section A: Accelerators, Spectrometers, Detectors and Associated Equipment*, vol. 245, no. 2, pp. 230–247, 1986.
- [121] J. Winfield, D. Pringle, W. Catford, *et al.*, “Focal Plane Detector for the Oxford MDM-2 Spectrometer,” *Nuclear Instruments and Methods in Physics Research Section A: Accelerators, Spectrometers, Detectors and Associated Equipment*, vol. 251, no. 2, pp. 297–306, 1986.
- [122] D. Youngblood, Y.-W. Lui, H. Clark, *et al.*, “Response of a resistive wire detector to 240 MeV alpha particles,” *Nuclear Instruments and Methods in Physics Research Section A: Accelerators, Spectrometers, Detectors and Associated Equipment*, vol. 361, no. 3, pp. 539–542, 1995.
- [123] A. Spiridon, E. Pollacco, B. Roeder, *et al.*, “Upgrade of the TAMU MDM-focal plane detector with MicroMegas technology,” *Nuclear Instruments and Methods in Physics Research Section B: Beam Interactions with Materials and Atoms*, vol. 376, pp. 364–368, 2016.

- [124] Y. Giomataris, P. Rebourgeard, J. Robert, and G. Charpak, “Micromegas: A high-granularity position-sensitive gaseous detector for high particle-flux environments,” *Nuclear Instruments and Methods in Physics Research Section A: Accelerators, Spectrometers, Detectors and Associated Equipment*, vol. 376, no. 1, pp. 29–35, 1996.
- [125] A. Spiridon, E. Pollacco, A. Saastamoinen, *et al.*, “A study in using MICROMEAS to improve particle identification with the TAMU-MDM focal plane detector,” *Nuclear Instruments and Methods in Physics Research Section A: Accelerators, Spectrometers, Detectors and Associated Equipment*, vol. 943, p. 162 461, 2019.
- [126] G. F. Knoll, *Radiation Detection and Measurement*. New York, NY, USA: Wiley, 2010.
- [127] T. A. Al-Abdullah, *Extracting The Asymptotic Normalization Coefficients in Neutron Transfer Reactions to determine the Reaction Rates for $^{22}\text{Mg}(p,\gamma)^{23}\text{Al}$ and $^{17}\text{F}(p,\gamma)^{18}\text{Ne}$* . Texas A&M University: PhD Thesis, 2007.
- [128] R. Hughes, J. Burke, R. Casperson, *et al.*, “The HYPERION particle- γ detector array,” *Nuclear Instruments and Methods in Physics Research Section A: Accelerators, Spectrometers, Detectors and Associated Equipment*, vol. 856, pp. 47–52, 2017.
- [129] S. Shepherd, P. Nolan, D. Cullen, *et al.*, “Measurements on a prototype segmented Clover detector,” *Nuclear Instruments and Methods in Physics Research Section A: Accelerators, Spectrometers, Detectors and Associated Equipment*, vol. 434, no. 2, pp. 373–386, 1999.
- [130] *Multi Instance Data Acquisition System*. [Online]. Available: <https://http://npg.dl.ac.uk/MIDAS/>.
- [131] A Matta, P Morfouace, N de Séréville, *et al.*, “Nptool: A simulation and analysis framework for low-energy nuclear physics experiments,” *Journal of Physics G: Nuclear and Particle Physics*, vol. 43, no. 4, p. 045 113, 2016. DOI: 10.1088/0954-3899/43/4/045113. [Online]. Available: <https://doi.org/10.1088/0954-3899/43/4/045113>.

- [132] H. Lutz and S. Eccles, “Study of the $^{25}\text{Mg}(d,p)^{26}\text{Mg}$ Reaction at $E_d = 8.0$ MeV,” *Nuclear Physics*, vol. 88, no. 3, pp. 513–522, 1966, ISSN: 0029-5582. DOI: [https://doi.org/10.1016/0029-5582\(66\)90410-X](https://doi.org/10.1016/0029-5582(66)90410-X). [Online]. Available: <http://www.sciencedirect.com/science/article/pii/002955826690410X>.
- [133] M. Burlein, K. S. Dhuga, and H. T. Fortune, “Spectroscopic Factors in $^{25}\text{Mg}(d,p)^{26}\text{Mg}$,” *Phys. Rev. C*, vol. 29, pp. 2013–2016, 6 1984. DOI: 10.1103/PhysRevC.29.2013. [Online]. Available: <https://link.aps.org/doi/10.1103/PhysRevC.29.2013>.
- [134] H. Arciszewski, E. Bakkum, C. V. Engelen], *et al.*, “The Dstructure of ^{26}Mg Investigated with the (d, p) Reaction,” *Nuclear Physics A*, vol. 430, no. 1, pp. 234–248, 1984, ISSN: 0375-9474. DOI: [https://doi.org/10.1016/0375-9474\(84\)90203-3](https://doi.org/10.1016/0375-9474(84)90203-3). [Online]. Available: <http://www.sciencedirect.com/science/article/pii/0375947484902033>.
- [135] S. S. Bhattacharjee, R. Bhattacharjee, R. Chakrabarti, *et al.*, “Nuclear structure study of ^{26}Mg following heavy-ion-induced fusion-evaporation reaction,” *Phys. Rev. C*, vol. 89, p. 024324, 2 2014. DOI: 10.1103/PhysRevC.89.024324. [Online]. Available: <https://link.aps.org/doi/10.1103/PhysRevC.89.024324>.
- [136] I. J. Thompson, *Computer Physics Reports*, vol. 7, 167 1988.
- [137] *J.A. Tostevin, University of Surrey version of the code TWOFNR (of M. Toyama, M. Igarashi and N. Kishida) and code FRONT (private communication).*
- [138] A. Koning and J. Delaroche, “Local and global nucleon optical models from 1 keV to 200 MeV,” *Nuclear Physics A*, vol. 713, no. 3, pp. 231–310, 2003, ISSN: 0375-9474. DOI: [https://doi.org/10.1016/S0375-9474\(02\)01321-0](https://doi.org/10.1016/S0375-9474(02)01321-0). [Online]. Available: <http://www.sciencedirect.com/science/article/pii/S0375947402013210>.
- [139] R. Johnson and P. Tandy, “An approximate three-body theory of deuteron stripping,” *Nuclear Physics A*, vol. 235, no. 1, pp. 56–74, 1974, ISSN: 0375-9474. DOI: [https://doi.org/10.1016/0375-9474\(74\)90178-X](https://doi.org/10.1016/0375-9474(74)90178-X). [Online]. Available: <http://www.sciencedirect.com/science/article/pii/037594747490178X>.
- [140] *W. N. Catford (private communication).*

- [141] B. Brown and W. Rae, “The Shell-Model Code NuShellX@MSU,” *Nuclear Data Sheets*, vol. 120, pp. 115–118, 2014, ISSN: 0090-3752. DOI: <https://doi.org/10.1016/j.nds.2014.07.022>. [Online]. Available: <http://www.sciencedirect.com/science/article/pii/S0090375214004748>.
- [142] S. M. Brown, W. N. Catford, J. S. Thomas, *et al.*, “Low-lying neutron fp -shell intruder states in ^{27}Ne ,” *Phys. Rev. C*, vol. 85, p. 011 302, 1 2012. DOI: 10.1103/PhysRevC.85.011302. [Online]. Available: <https://link.aps.org/doi/10.1103/PhysRevC.85.011302>.
- [143] B. A. Brown and W. A. Richter, “New “USD” Hamiltonians for the sd shell,” *Phys. Rev. C*, vol. 74, p. 034 315, 3 2006. DOI: 10.1103/PhysRevC.74.034315. [Online]. Available: <https://link.aps.org/doi/10.1103/PhysRevC.74.034315>.
- [144] M. Basunia and A. Hurst, “Nuclear Data Sheets for $A = 26$,” *Nuclear Data Sheets*, vol. 134, pp. 1–148, 2016, ISSN: 0090-3752. DOI: <https://doi.org/10.1016/j.nds.2016.04.001>. [Online]. Available: <http://www.sciencedirect.com/science/article/pii/S0090375216300011>.
- [145] Y. Parpottas, S. M. Grimes, S. Al-Quraishi, *et al.*, “Astrophysically important ^{26}Si states studied with the $(^3\text{He},n)$ reaction and the $^{25}\text{Al}(p,\gamma)^{26}\text{Si}$ reaction rates in explosive hydrogen burning environments,” *Phys. Rev. C*, vol. 70, p. 065 805, 6 2004. DOI: 10.1103/PhysRevC.70.065805. [Online]. Available: <https://link.aps.org/doi/10.1103/PhysRevC.70.065805>.
- [146] D. W. Bardayan, J. A. Howard, J. C. Blackmon, *et al.*, “Astrophysically important ^{26}Si states studied with the $^{28}\text{Si}(p,t)^{26}\text{Si}$ reaction. II. Spin of the 5.914-MeV ^{26}Si level and galactic ^{26}Al production,” *Phys. Rev. C*, vol. 74, p. 045 804, 4 2006. DOI: 10.1103/PhysRevC.74.045804. [Online]. Available: <https://link.aps.org/doi/10.1103/PhysRevC.74.045804>.
- [147] A. Barnett, D. Feng, J. Steed, and L. Goldfarb, “Coulomb wave functions for all real η and ρ ,” *Computer Physics Communications*, vol. 8, no. 5, pp. 377–395, 1974, ISSN: 0010-4655. DOI: [https://doi.org/10.1016/0010-4655\(74\)90013-7](https://doi.org/10.1016/0010-4655(74)90013-7). [Online]. Available: <http://www.sciencedirect.com/science/article/pii/0010465574900137>.

- [148] D. Clayton, *Principles of Stellar Evolution and Nucleosynthesis*. University of Chicago Press, 1983.
- [149] C. Iliadis, “Proton Single-Particle Reduced Widths for Unbound States,” *Nuclear Physics A*, vol. 618, no. 1, pp. 166–175, 1997, ISSN: 0375-9474. DOI: [https://doi.org/10.1016/S0375-9474\(97\)00065-1](https://doi.org/10.1016/S0375-9474(97)00065-1). [Online]. Available: <http://www.sciencedirect.com/science/article/pii/S0375947497000651>.
- [150] P. N. Peplowski, L. T. Baby, I. Wiedenhöver, *et al.*, “Lowest $l = 0$ proton resonance in ^{26}Si and implications for nucleosynthesis of ^{26}Al ,” *Phys. Rev. C*, vol. 79, p. 032 801, 3 2009. DOI: 10.1103/PhysRevC.79.032801. [Online]. Available: <https://link.aps.org/doi/10.1103/PhysRevC.79.032801>.
- [151] M. B. Bennett, C. Wrede, K. A. Chipps, *et al.*, “Classical-Nova Contribution to the Milky Way’s ^{26}Al Abundance: Exit Channel of the Key $^{25}\text{Al}(p,\gamma)^{26}\text{Si}$ Resonance,” *Phys. Rev. Lett.*, vol. 111, p. 232 503, 23 2013. DOI: 10.1103/PhysRevLett.111.232503. [Online]. Available: <https://link.aps.org/doi/10.1103/PhysRevLett.111.232503>.
- [152] L. Buchmann, M. Hilgemeier, A. Krauss, *et al.*, “The abundance of ^{26}Al in the MgAl cycle,” *Nuclear Physics A*, vol. 415, no. 1, pp. 93–113, 1984.
- [153] T. Wang, A. Champagne, J. Hadden, *et al.*, “Proton threshold states in ^{27}Si and the destruction of ^{26}Al at low stellar temperatures,” *Nuclear Physics A*, vol. 499, no. 3, pp. 546–564, 1989.
- [154] A. Champagne, B. Brown, and R. Sherr, “The $^{26}\text{Al}(p, \gamma)^{27}\text{Si}$ reaction at low stellar temperature,” *Nuclear Physics A*, vol. 556, no. 1, pp. 123–135, 1993.
- [155] R. B. Vogelaar, L. W. Mitchell, R. W. Kavanagh, *et al.*, “Constraining $^{26}\text{Al}+p$ resonances using $^{26}\text{Al}(^3\text{He},d)^{27}\text{Si}$,” *Phys. Rev. C*, vol. 53, pp. 1945–1949, 4 1996. DOI: 10.1103/PhysRevC.53.1945. [Online]. Available: <https://link.aps.org/doi/10.1103/PhysRevC.53.1945>.
- [156] C. Ruiz, A. Parikh, J. José, *et al.*, “Measurement of the $E_{\text{c.m.}} = 184$ keV Resonance Strength in the $^{26g}\text{Al}(p, \gamma)^{27}\text{Si}$ Reaction,” *Phys. Rev. Lett.*, vol. 96, p. 252 501, 25 Jun. 2006.

- [157] G. Lotay, P. J. Woods, D. Seweryniak, *et al.*, “Identification of Key Astrophysical Resonances Relevant for the $^{26g}\text{Al}(p,\gamma)^{27}\text{Si}$ Reaction in Wolf-Rayet stars, AGB stars, and Classical Novae,” *Phys. Rev. Lett.*, vol. 102, p. 162 502, 16 2009. DOI: 10.1103/PhysRevLett.102.162502. [Online]. Available: <https://link.aps.org/doi/10.1103/PhysRevLett.102.162502>.
- [158] V. Margerin, G. Lotay, P. J. Woods, *et al.*, “Inverse Kinematic Study of the $^{26g}\text{Al}(d,p)^{27}\text{Al}$ Reaction and Implications for Destruction of ^{26}Al in Wolf-Rayet and Asymptotic Giant Branch Stars,” *Phys. Rev. Lett.*, vol. 115, p. 062 701, 6 Aug. 2015.
- [159] S. D. Pain, D. W. Bardayan, J. C. Blackmon, *et al.*, “Constraint of the Astrophysical $^{26g}\text{Al}(p,\gamma)^{27}\text{Si}$ Destruction Rate at Stellar Temperatures,” *Phys. Rev. Lett.*, vol. 114, p. 212 501, 21 May 2015.
- [160] A. Kankainen, P. J. Woods, F. Nunes, *et al.*, “Angle-integrated measurements of the $^{26}\text{Al}(d,n)^{27}\text{Si}$ reaction cross section: A probe of spectroscopic factors and astrophysical resonance strengths,” *The European Physical Journal A*, vol. 52, no. 1, p. 6, 2016, ISSN: 1434-601X. DOI: 10.1140/epja/i2016-16006-5. [Online]. Available: <https://doi.org/10.1140/epja/i2016-16006-5>.
- [161] G. Lotay, P. J. Woods, M. Moukaddam, *et al.*, “High-resolution radioactive beam study of the $^{26}\text{Al}(d,p)$ reaction and measurements of single-particle spectroscopic factors,” *The European Physical Journal A*, vol. 56, no. 1, p. 3, 2020, ISSN: 1434-601X. DOI: 10.1140/epja/s10050-019-00008-8. [Online]. Available: <https://doi.org/10.1140/epja/s10050-019-00008-8>.
- [162] C. Angulo, M. Arnould, M. Rayet, *et al.*, “A compilation of charged-particle induced thermonuclear reaction rates,” *Nuclear Physics A*, vol. 656, no. 1, pp. 3 – 183, 1999, ISSN: 0375-9474. DOI: [https://doi.org/10.1016/S0375-9474\(99\)00030-5](https://doi.org/10.1016/S0375-9474(99)00030-5). [Online]. Available: <http://www.sciencedirect.com/science/article/pii/S0375947499000305>.
- [163] C. Iliadis, A. Champagne, J. José, *et al.*, “The effects of thermonuclear reaction-rate variations on nova nucleosynthesis: a sensitivity study,” *The Astrophysical Journal Supplement Series*, vol. 142, no. 1, pp. 105–137, 2002. DOI: 10.1086/341400. [Online]. Available: <https://doi.org/10.1086/341400>.

- [164] C. M. Deibel, J. A. Clark, R. Lewis, *et al.*, “Toward an experimentally determined $^{26}\text{Al}^m(p,\gamma)^{27}\text{Si}$ reaction rate in ONe novae,” *Phys. Rev. C*, vol. 80, p. 035 806, 3 2009. DOI: 10.1103/PhysRevC.80.035806. [Online]. Available: <https://link.aps.org/doi/10.1103/PhysRevC.80.035806>.
- [165] G. Lotay, P. J. Woods, D. Seweryniak, *et al.*, “ γ -ray spectroscopy study of states in ^{27}Si relevant for the $^{26}\text{Al}^m(p,\gamma)^{27}\text{Si}$ reaction in novae and supernovae,” *Phys. Rev. C*, vol. 80, p. 055 802, 5 2009. DOI: 10.1103/PhysRevC.80.055802. [Online]. Available: <https://link.aps.org/doi/10.1103/PhysRevC.80.055802>.
- [166] ———, “Erratum: γ -ray spectroscopy study of states in ^{27}Si relevant for the $^{26}\text{Al}^m(p,\gamma)^{27}\text{Si}$ reaction in novae and supernovae [Phys. Rev. C 80, 055802 (2009)],” *Phys. Rev. C*, vol. 81, p. 029 903, 2 2010. DOI: 10.1103/PhysRevC.81.029903. [Online]. Available: <https://link.aps.org/doi/10.1103/PhysRevC.81.029903>.
- [167] A. Parikh, K. Wimmer, T. Faestermann, *et al.*, “Production of ^{26}Al in stellar hydrogen-burning environments: Spectroscopic properties of states in ^{27}Si ,” *Phys. Rev. C*, vol. 84, p. 065 808, 6 2011. DOI: 10.1103/PhysRevC.84.065808. [Online]. Available: <https://link.aps.org/doi/10.1103/PhysRevC.84.065808>.
- [168] E. McCleskey, A. Banu, M. McCleskey, *et al.*, “Simultaneous measurement of β -delayed proton and γ decay of ^{27}P ,” *Phys. Rev. C*, vol. 94, p. 065 806, 6 2016. DOI: 10.1103/PhysRevC.94.065806. [Online]. Available: <https://link.aps.org/doi/10.1103/PhysRevC.94.065806>.
- [169] S. Almaraz-Calderon, K. E. Rehm, N. Gerken, *et al.*, “Study of the $^{26}\text{Al}^m(d,p)^{27}\text{Al}$ Reaction and the Influence of the ^{26}Al 0^+ Isomer on the Destruction of ^{26}Al in the Galaxy,” *Phys. Rev. Lett.*, vol. 119, p. 072 701, 7 2017. DOI: 10.1103/PhysRevLett.119.072701. [Online]. Available: <https://link.aps.org/doi/10.1103/PhysRevLett.119.072701>.
- [170] A. Kankainen, P. Woods, H. Schatz, *et al.*, “Measurement of key resonance states for the $^{30}\text{P}(p,\gamma)^{31}\text{S}$ reaction rate, and the production of intermediate-mass elements in nova explosions,” *Physics Letters B*, vol. 769, pp. 549–553, 2017, ISSN: 0370-2693. DOI: <https://doi.org/10.1016/j.physletb.2017.01.084>. [Online]. Available: <http://www.sciencedirect.com/science/article/pii/S0370269317301338>.

- [171] J. Al-Khalili and E. Roeckl, *The Euroschool Lectures on Physics with Exotic Beams*, ser. Lecture Notes in Physics v. 1. Springer Berlin Heidelberg, 2004.
- [172] *Fragmentation Facility, Credit - NSCL*. [Online]. Available: <https://www.nsl.msu.edu/public/virtual-tour.html>.
- [173] X. Wu, D. J. Morrissey, B. M. Sherrill, *et al.*, “Tracking studies and performance simulations of the nscl a1900 fragment separator,” *Proceedings of the 1997 Particle Accelerator Conference (Cat. No.97CH36167)*, vol. 1, 198–200 vol.1, 1997.
- [174] *A1900 Fragment Separator, Credit - NSCL*. [Online]. Available: <https://groups.nsl.msu.edu/a1900/overview/schematic.php>.
- [175] D. Bazin, J. Caggiano, B. Sherrill, *et al.*, “The S800 Spectrograph,” *Nuclear Instruments and Methods in Physics Research Section B: Beam Interactions with Materials and Atoms*, vol. 204, pp. 629 –633, 2003, 14th International Conference on Electromagnetic Isotope Separators and Techniques Related to their Applications.
- [176] J Yurkon, D Bazin, W Benenson, *et al.*, “Focal plane detector for the S800 high-resolution spectrometer,” *Nuclear Instruments and Methods in Physics Research Section A: Accelerators, Spectrometers, Detectors and Associated Equipment*, vol. 422, no. 1, pp. 291 –295, 1999.
- [177] G. W. Hitt, *The $^{64}\text{Zn}(t, ^3\text{He})$ charge-exchange reaction at 115 MeV per nucleon and application to ^{64}Zn stellar electron-capture*. Michigan State University: PhD Thesis, 2009.
- [178] M Berz, “COSY INFINITY reference manual,” Jul. 1990. DOI: 10.2172/6660243.
- [179] S. Paschalis, I. Lee, A. Macchiavelli, *et al.*, “The performance of the gamma-ray energy tracking in-beam nuclear array gretina,” *Nuclear Instruments and Methods in Physics Research Section A: Accelerators, Spectrometers, Detectors and Associated Equipment*, vol. 709, pp. 44 –55, 2013, ISSN: 0168-9002. DOI: <https://doi.org/10.1016/j.nima.2013.01.009>. [Online]. Available: <http://www.sciencedirect.com/science/article/pii/S0168900213000508>.

- [180] T. Lauritsen, A. Korichi, S. Zhu, *et al.*, “Characterization of a gamma-ray tracking array: a comparison of gretina and gammasphere using a ^{60}Co source,” *Nuclear Instruments and Methods in Physics Research Section A: Accelerators, Spectrometers, Detectors and Associated Equipment*, vol. 836, pp. 46 – 56, 2016, ISSN: 0168-9002. DOI: <https://doi.org/10.1016/j.nima.2016.07.027>. [Online]. Available: <http://www.sciencedirect.com/science/article/pii/S0168900216307434>.
- [181] D. Weisshaar, D. Bazin, P. Bender, *et al.*, “The performance of the γ -ray tracking array gretina for γ -ray spectroscopy with fast beams of rare isotopes,” *Nuclear Instruments and Methods in Physics Research Section A: Accelerators, Spectrometers, Detectors and Associated Equipment*, vol. 847, pp. 187 – 198, 2017, ISSN: 0168-9002. DOI: <https://doi.org/10.1016/j.nima.2016.12.001>. [Online]. Available: <http://www.sciencedirect.com/science/article/pii/S0168900216312402>.
- [182] J. Anderson, R. Brito, D. Doering, *et al.*, “Data acquisition and trigger system of the gamma ray energy tracking in-beam nuclear array (gretina),” *IEEE Transactions on Nuclear Science*, vol. 56, no. 1, pp. 258–265, 2009.
- [183] *L Riley et al. (to be published)*.
- [184] *D. Weisharr (private communication) (to be published)*.
- [185] *A. Gade (private communication)*.
- [186] J. Uzureau, A. Adam, and S. Joly, “Altitude des niveaux du noyau ^{27}Al par la réaction $^{26}\text{Mg}(d, n)^{27}\text{Al}$,” *Nuclear Physics A*, vol. 250, no. 1, pp. 163 –181, 1975, ISSN: 0375-9474. DOI: [https://doi.org/10.1016/0375-9474\(75\)90207-9](https://doi.org/10.1016/0375-9474(75)90207-9). [Online]. Available: <http://www.sciencedirect.com/science/article/pii/S0375947475902079>.
- [187] W. Bohne, H. Fuchs, K. Grabisch, *et al.*, “One-proton and two-proton stripping between ^{26}Mg , ^{27}Al and ^{28}Si ,” *Nuclear Physics A*, vol. 131, no. 2, pp. 273 –304, 1969, ISSN: 0375-9474. DOI: [https://doi.org/10.1016/0375-9474\(69\)90537-5](https://doi.org/10.1016/0375-9474(69)90537-5). [Online]. Available: <http://www.sciencedirect.com/science/article/pii/S0375947469905375>.

- [188] W. Alford, D. Cline, H. Gove, *et al.*, “A study of the $^{26}\text{Mg}(^3\text{He}, d)^{27}\text{Al}$ reaction,” *Nuclear Physics A*, vol. 130, no. 1, pp. 119–128, 1969, ISSN: 0375-9474. DOI: [https://doi.org/10.1016/0375-9474\(69\)90965-8](https://doi.org/10.1016/0375-9474(69)90965-8). [Online]. Available: <http://www.sciencedirect.com/science/article/pii/0375947469909658>.
- [189] *B.A. Brown (private communication)*.
- [190] E. K. Warburton and B. A. Brown, “Effective interactions for the $0p1s0d$ nuclear shell-model space,” *Phys. Rev. C*, vol. 46, pp. 923–944, 3 1992. DOI: 10.1103/PhysRevC.46.923. [Online]. Available: <https://link.aps.org/doi/10.1103/PhysRevC.46.923>.
- [191] G. Lotay, P. J. Woods, D. Seweryniak, *et al.*, “Identification of analog states in the $T = 1/2$ $A = 27$ mirror system from low excitation energies to the region of hydrogen burning in the $^{26}\text{Al}^{g,m}(p,\gamma)^{27}\text{Si}$ reactions,” *Phys. Rev. C*, vol. 84, p. 035802, 3 2011. DOI: 10.1103/PhysRevC.84.035802. [Online]. Available: <https://link.aps.org/doi/10.1103/PhysRevC.84.035802>.
- [192] *G. Lotay (private communication)*.
- [193] R. Evans, *The Atomic Nucleus*. New York: McGraw-Hill Companies, 1955.
- [194] A. Beiser, *Concepts of Modern Physics*. New York: McGraw-Hill Companies, 2003.
- [195] G. Pavlinsky, *Fundamentals of X-ray Physics*. Cambridge International Science Publishing, 2008.